Development and Modeling of Novel Battery Thermal Management Systems for Electric and Hybrid Electric Vehicles

A Thesis Submitted in Partial Fulfillment of

the Requirements for the Degree of Doctor of Philosophy

in

Mechanical Engineering

Submitted by

Maan Al-Zareer

Under the supervision of

Supervisor: Prof. Ibrahim Dincer

Co-supervisor: Prof. Marc A. Rosen

Faculty of Engineering and Applied Science

Mechanical Engineering Program

University of Ontario Institute of Technology

Oshawa, Ontario, Canada

April 2019

© Maan Al-Zareer, 2019

Thesis Examination Information

Submitted by: **Maan Al-Zareer**

Doctor of Philosophy in **Mechanical Engineering**

Thesis title: **Development and Modeling of Novel Battery Thermal Management Systems for Electric and Hybrid Electric Vehicles**

An oral defense of this thesis took place on April 5, 2019 in front of the following examining committee:

Examining Committee:

Chair of Examining Committee	Dr. Sayyed Ali Hosseini
Research Supervisor	Dr. Ibrahim Dincer
Research Co-supervisor	Dr. Marc A. Rosen
Examining Committee Member	Dr. Martin Agelin-Chaab
Examining Committee Member	Dr. Haoxiang Lang
University Examiner	Dr. Anatoli Chkrebtii
External Examiner	Dr. Cengiz Ozkan, University of California, Riverside

The above committee determined that the thesis is acceptable in form and content and that a satisfactory knowledge of the field covered by the thesis was demonstrated by the candidate during an oral examination. A signed copy of the Certificate of Approval is available from the School of Graduate and Postdoctoral Studies.

Abstract

Thermal management system is necessary to control the operating temperature of the lithium ion batteries in battery packs for electrical and hybrid electrical vehicles. This thesis studies, develops and models novel battery thermal management systems for the battery packs in hybrid electric vehicles and electric vehicles. The systems' thermal performances are assessed through thermal and electrochemical models. The performances of the proposed systems are investigated in terms of various performance measures including the maximum temperature in the pack and the temperature distribution throughout the battery pack and through each battery. The results show that pool based systems achieve better performance for cylindrical battery packs than for prismatic battery packs. For a pool system, covering 30% of the battery height reduces the maximum battery temperature by 28% to 40% depending on the fuel type for a high intensity cycle. To achieve 28% to 40% reduction in the prismatic battery maximum temperature from the case where there is no cooling, the pool system has to cover 80% of the battery height. The best performing system for prismatic battery packs is the tube based system, where the aluminum cold plate has tubes completely filled with coolant to maintain the battery temperature within range needed for the best performance possible by the system. The tube cold plate based system maintains 80% less coolant in the battery pack at a time than the direct contact pool based system while achieving a higher performance in terms of the maximum battery temperature and the maximum temperature difference across the battery pack. The response time for the proposed systems reached nearly 10 times faster than liquid and air systems proposed in the literature. Compared with the literature the pool based system response was 1.7% of the cycle time compared to around 17% for the cycle time for the mini channel cold plate cooling system.

Keywords: Lithium ion batteries; electric vehicles; hybrid electric vehicles; thermal management; cooling

Author's Declaration

I hereby declare that this thesis consists of original work of which I have authored. This is a true copy of the thesis, including any required final revisions, as accepted by my examiners.

I authorize the University of Ontario Institute of Technology to lend this thesis to other institutions or individuals for the purpose of scholarly research. I further authorize University of Ontario Institute of Technology to reproduce this thesis by photocopying or by other means, in total or in part, at the request of other institutions or individuals for the purpose of scholarly research. I understand that my thesis will be made electronically available to the public.

Maan Al-Zareer

Acknowledgments

I would like to express my gratitude to my supervisor Professor Ibrahim Dincer and my co-supervisor Professor Marc A. Rosen for their guidance, unlimited and continuous support. They have provided me with high courage and the support to work, produce and publish. Their support and confidence in me brought out the best in me and was one of the main sources of motivation during my research and studies. In addition, I would like to give special thanks to Prof. Ibrahim Dincer for not only being my supervisor but also for being my academic father that always wanted what is right for me and directed me towards all that allows me to grow to become a better person. I would like to extend my appreciation to my committee members: Professor Cengiz Ozkan as external examiner from University of California River side, Professor Anatoli Chkrebtii as university examiner, and the committee Dr. Martin Agelin-Chaab, and Dr. Haoxiang Lang for their valuable for their valuable feedback and constructive criticism to improve my thesis.

I would like to thank my father and mother for their unlimited and continuous support and encouragement. They always believed and trusted me. I would also like to thank all of my brothers Mohamed, Migdad, Moath, Isam and sisters Amal, Hawaa and Mai for their support.

Finally, special thanks goes to Ahmad Hasan for the kind support and motivation he provided throughout the years. I also would like to thank all my colleagues and friends at ACE 3030B for their support, Dr. Murat Demir, Dr. Muhammad Ezzat, Dr. Janette Hogerwaard, Zeynep Demir, Mohamed Ra'fat, Dr. Yusuf Bicer, Dr. Farrukh Khalid, Dr. Canan Acar, Abed Omran, Osamah Siddiqui, Haris Ishaq, Arda Yapicioglu, Eren Sevinchan, Anwar Hammad, Magd Dinali, Sherif Seif Eldin, Aida Farsi, Ahmed Ali, Khalid Al-Tayeb, and Khalid Al-Hamed.

Statement of Contributions

Part of the work described in Chapter 2 has been published as:

M. Al-Zareer, I. Dincer, M.A. Rosen, A review of novel thermal management systems for batteries, Int. J. Energy Res. (2018). doi:10.1002/er.4095

Part of the work described in Chapters 3, 4, and 5 has been published as:

M. Al-Zareer, I. Dincer, M.A. Rosen, Heat transfer modeling of a novel battery thermal management system, Numer. Heat Transf. Part A Appl. 73 (2018) 277–290. doi:10.1080/10407782.2018.1439237.

M. Al-Zareer, I. Dincer, M.A. Rosen, Transient analysis and evaluation of a novel pressurized multistage ammonia production system for hydrogen storage purposes, J. Clean. Prod. 196 (2018) 390–399. doi:10.1016/j.jclepro.2018.06.022.

M. Al-Zareer, I. Dincer, M.A. Rosen, Development and evaluation of a new ammonia boiling based battery thermal management system, Electrochim. Acta. 280 (2018) 340–352. doi:10.1016/j.electacta.2018.05.093.

M. Al-Zareer, I. Dincer, M.A. Rosen, Heat and mass transfer modeling and assessment of a new battery cooling system, Int. J. Heat Mass Transf. 126 (2018) 765–778. doi:10.1016/j.ijheatmasstransfer.2018.04.157.

M. Al-Zareer, I. Dincer, M.A. Rosen, A novel phase change based cooling system for prismatic lithium ion batteries, Int. J. Refrig. 86 (2018) 203–217. doi:10.1016/j.ijrefrig.2017.12.005.

M. Al-Zareer, I. Dincer, M.A. Rosen, Electrochemical modeling and performance evaluation of a new ammonia-based battery thermal management system for electric and hybrid electric vehicles, Electrochim. Acta. 247 (2017) 171–182. doi:10.1016/j.electacta.2017.06.162.

M. Al-Zareer, I. Dincer, M.A. Rosen, Performance assessment of a new hydrogen cooled prismatic battery pack arrangement for hydrogen hybrid electric vehicles, Energy Convers. Manag. 173 (2018) 303-319.

M. Al-Zareer, I. Dincer, M.A. Rosen, Novel thermal management system using boiling cooling for high-powered lithium-ion battery packs for hybrid electric vehicles, J. Power Sources. 363 (2017) 291–303. doi:10.1016/j.jpowsour.2017.07.067.

M. Al-Zareer, I. Dincer, M.A. Rosen, A Novel Approach for Performance Improvement of Liquid to Vapor Based Battery Cooling Systems, Energy Convers. Manag. 187 (2019) 191-204. https://doi.org/10.1016/j.enconman.2019.02.063

M. Al-Zareer, I. Dincer, M.A. Rosen, Development and Performance Assessment of an Evaporative Liquid Pool Based Battery Cooling System, Energy Convers. Manag. (under consideration for publication)

M. Al-Zareer, I. Dincer, M.A. Rosen, Comparative Assessment of New Liquid-to-Vapor Type Battery Cooling Systems, Energy. (under consideration for publication)

For all the journal articles mentioned above, I performed the majority of the modeling, simulation of the proposed systems, and writing of the manuscript.

Table of Contents

Thesis Examination Information ii
Abstract iii
Author's Declaration iv
Acknowledgments v
Statement of Contributions vi
List of Tables x
List of Figures xi
Nomenclature xix
Chapter 1: Introduction 1
1.1 Electric vehicles (EVs) 4
1.2 Hybrid electric vehicles (HEVs) 5
1.3 Plug-in hybrid electric vehicles (PHEVs) 9
1.4 Drive cycle 9
1.5 Motivation 10
1.6 Objectives 10
Chapter 2: Literature Review 12
2.1 Battery Thermal Management Systems (BTMSs) 14
2.2 Closing remarks from the literature review 33
Chapter 3: Development of Systems 37
3.1 Dependence on the Vehicle Drive Train 38
3.2 Independent on the Vehicle Drive Train 50
3.3 Closing remarks 54
Chapter 4: Analyses and Optimization 55
4.1 Electrochemical analysis 56
4.2 Thermodynamic and Heat Transfer Analysis 61
4.3 Optimization study 79
Chapter 5: Results and Discussion 84
5.1 Model Validation 84
5.2 Electrochemical performance results 87
5.3 Prismatic battery pack results 88

5.4 Cylindrical battery pack results 129
Chapter 6: Conclusions and Recommendations 174
6.1 Conclusions 174
6.2 Recommendations 175
References 177
Appendix 187

List of Tables

Table 1.1: Typical specifications of an electric vehicle that is usually used in the literature to perform electric vehicle drive cycle studies (date from [24]). 5
Table 1.2. Specification of an actual commercial EV integrated with a gasoline drive range extender (data from Von Helmolt and Eberle [23]). 6
Table 2.1. Main properties of rechargeable batteries used in EVs and HEVs 13
Table 2.2. Summary of novel air flow based BTMSs for lithium ion batteries. 15
Table 2.3. Detailed presentation of various design configurations proposed in the literature that are based on the air flow system. 16
Table 2.4. Summary of optimum configurations of battery pack size and shape and number of batteries for each configuration category. 20
Table 2.5. Summary of novel liquid based BTMSs for lithium ion batteries. 24
Table 2.6. Basu et al. [69] investigated results of the BTMS three main variables. 26
Table 2.7. Summary of novel PCM based BTMSs for lithium ion batteries. 32
Table 2.8. Systems and parameters used to investigate BTMS based on a heat pipe with PCM. (data from Zhao et al. [102]). 33
Table 2.9. Melting temperature, thermal conductivity and latent heat of various paraffin composites 34
Table 3.1. Summary of the five main proposed systems based on coolant type, and its applicability to work in EVs and HEVs. 37
Table 4.1. Summary of the five main proposed systems based on coolant type, and its applicability to work in EVs and HEVs. 80
Table 4.2. The upper and lower bounds of the variables of system 1. 81
Table 4.3. The upper and lower bounds of the variables of system 2. 82
Table 4.4. The upper and lower bounds of the variables of system 3. 82
Table 4.5. The upper and lower bounds of the variables of system 4. 83
Table 4.6. The upper and lower bounds of the variables of system 5. 84
Table 5.1. The input parameters of the hydrogen to the cold plate throughout the hydrogen cold plate design development and the main battery cooling system performance resulting from each design and input parameters in terms of the minimum and maximum temperature of the battery and the maximum temperature difference across the battery. 91

List of Figures

Figure 1.1 Breakdown of Canada's emissions in million tonne (Mt) CO_2 equivalent by sector, where the labeling on the graph inside the parentheses presents the following: (Mt CO_2 equivalent, percentage of the overall contribution) (Data from [1]). 1
Figure 1.2 Variations of the total GHG emissions in Canada with time, and the variation of the GHG emissions that are the product of the energy transport sector and the energy stationary combustion sector in Mt CO_2 equivalent (Data from [1]). 2
Figure 1.3 Breakdown of the energy transport emissions in Canada from 2005 to 2015 (Data from [1]). 3
Figure 1.4 A schematic diagram of the power flow and drive train arrangement of series HEVs. 7
Figure 1.5 A schematic diagram of the power flow and drive train arrangement of parallel HEVs. 7
Figure 1.6 A schematic diagram of the power flow and drive train arrangement of series-parallel HEVs. 8
Figure 2.1 Schematic of forced axial flow battery pack configuration, showing the designed flow direction, which is forced through the pack to flow in the axial direction of the batteries. 19
Figure 2.2 Variable contact area liquid based BTMS: (a) battery pack configuration and (b) different contact areas. 23
Figure 2.3 (a) Maximum temperature, and (b) temperature difference in the battery pack, for various coolant velocities and design parameter, the aluminum block length (data from Basu et al. [69]) 25
Figure 2.4 (a) Temperature distribution at several points in time through the discharging process. (b) Cross sectional view of the batteries in the pack during the discharging process for different thermal contact resistances at a constant discharge rate of 0.9C. (Modified from Basu et al. [69]). 28
Figure 2.5 (a) Schematic diagram of the proposed battery pack design of Wu et al.; (b) working principle of the heat pipe and PCM integrated battery cooling system. (Modified from Wu et al. [95]). 30
Figure 2.6 (a) Schematic diagram of the experimental setup used by Zhao et al. [98]; (b) working principle of the proposed oscillating heat pipes system. (Modified from Zhao et al. [98]). 30
Figure 2.7 Schematic diagram of the integrated shell and tube heat exchanger integrated with PCM for cylindrical battery cooling. 31
Figure 2.8 Variation of paraffin melting temperature and latent heat with length of the alkanes paraffin straight-chain, for various materials. 33
Figure 2.9 A schematic diagram summarizing the literature review on battery thermal management systems. 35
Figure 3.1 Schematic of the fuel cell based hybrid electric vehicle equipped with throttled hydrogen battery cooling system (note that the location of the vehicle drive train component are based on Toyota fuel cell vehicle Mirai [120]). 40

Figure 3.2 (a) Schematic diagram of the hydrogen cooled based cooling system for fuel cell vehicles and (b) overall dimensions of the considered prismatic battery. 40
Figure 3.3 Schematic diagram of ammonia based hybrid electric vehicle, for which the proposed boiling ammonia based cooling system is simulated. The electrical generator presented here is any device that can convert the ammonia vapor to electrical energy, for example with the ammonia fuel cell proposed in [28] or with internal combustion engine as proposed in [26,27]..... 41
Figure 3.4 Schematic of (a) considered prismatic battery including its dimensions, and (b) design of the battery pack integrated with the proposed ammonia based cooling system. 42
Figure 3.5 Schematic diagram of the ammonia based future hybrid electric vehicle in which the proposed boiling based battery cooling system is employed. 43
Figure 3.6 PSLA for cylindrical pack design, (b) dimensions of the thermal management system and the battery..... 44
Figure 3.7 Schematic of the pneumatic hybrid electric vehicle where the compressed air is used to partially power the vehicle and provide cool air to the battery cooling system. 45
Figure 3.8 Schematic of the propane based hybrid electric vehicle equipped with boiling based battery thermal management system..... 46
Figure 3.9 Schematic of the battery pack design that uses the proposed thermal management system: (a) pack design, (b) dimensions of the considered lithium ion prismatic battery and the thermal management system and the battery. 47
Figure 3.10 Schematic diagram of the hybrid electric vehicle on which the proposed battery thermal management system is employed. 48
Figure 3.11 Schematic of the battery thermal management system: (a) design, (b) dimensions of the cooling system and the battery. 49
Figure 3.12 Schematic diagram of the internal structure of the electric vehicle that uses the refrigerant based battery thermal management system..... 50
Figure 3.13 (a) Schematic of a single battery with a refrigerant R134a cold plate and how the recycling system keeps the loop of the coolant closed, and (b) a section cut showing the connection between the cooling plate and the battery. 51
Figure 3.14 (a) Three dimensional rendering of the working principle of the proposed cooling system (system 5 for cylindrical batteries). (b) batteries are separated by one battery radius, and (c) a compact design with 10% of a battery radius in one direction and 20% in the other direction..... 52
Figure 3.15 Schematic diagram of refrigerant R134a refrigerant based battery thermal management system for electric vehicles showing the working principle of the system. 53
Figure 4.1 Flow sheet of the modeling methodology used to assess the performance of the proposed system..... 55
Figure 4.2 Dimensions of the modeled and simulated lithium ion prismatic battery and the selected boundary conditions for the one dimensional electrochemical model..... 59

Figure 4.3 Dimensions of the modeled and simulated lithium ion cylindrical battery (battery type 18650) and the selected boundary conditions for the one dimensional electrochemical model. 60
Figure 4.4 Simulated domain and boundary conditions for the three dimensional heat and mass transfer model (for the optimum case) (The thermal contact properties as follows: surface roughness, asperities average height 1 μm, and the asperities average slope 0.4). 63
Figure 4.5 Proposed designs for the hydrogen cooled, aluminum cold plate considered in the thesis. The first two of the proposed designs have two hydrogen inlets and the remaining three have a single inlet cooled plate. 64
Figure 4.6 (a) Mesh independent study including a separate study on the number of mesh layers within the thickness of the battery and the cold plate based on the maximum temperature of the battery after a 100 seconds of charging the battery at 4C rate, (b) side view of the model showing the case with 10 extra mesh layers in both the cold plate and the battery (c) front view of the simulated model showing the variation of the selected mesh and (d) shows the back view of the model selected mesh. (note that the legend colors are based on the mesh cell size) 65
Figure 4.7 Three dimensional mass and heat transfer model, of design 1 of the ammonia boiling based battery thermal management system. 66
Figure 4.8 (a) Dimensions of the proposed design of the ammonia boiling based thermal management system, and (b) boundary conditions of the simulated three dimensional heat transfer model. 68
Figure 4.9 Boundary conditions and dimensions of (a) one dimensional electrochemical model, and (b) three dimensional mass and heat transfer model, and the integration between the two models (c) overall presentation of the connection between the one dimensional electrochemical and three dimensional heat and mass transfer models. 70
Figure 4.10 Effect of the mesh on the model results in terms of the battery maximum temperature and the propane vapor leaving the pack maximum temperature. 71
Figure 4.11 Schematic diagram of the R134a based cooling system for the prismatic battery pack showing (a) the front view of the section cut through the R134a cooling space and (b) is the top view. 72
Figure 4.12 Dimensions and boundary conditions of the simulated battery and cooling domain of the three dimensional heat and mass transfer model. 73
Figure 4.13 Mesh independence study (note that the e in the horizontal axis refers to 10 raised to the power of the number following the e latter). 74
Figure 4.14 Dimensions and boundary conditions of the simulated battery and cooling domains. (a) one dimensional model of the electrochemical reactions in a battery cell, (b) three dimensional heat and mass transfer model. 75
Figure 4.15 Mesh independence study 76
Figure 4.16 (a) Simulated domain in the heat and mass transfer model, (b) selected boundary conditions and (c) mesh plot of the variation of the mesh elements size in m^3.77
Figure 4.17 (a) The simulated domain location and size within the battery pack that is cooled by the proposed system. (b) Dimensions and boundary conditions of the two cases

considered for the three dimensional heat and mass transfer model (note that the text presented in blue color is to distinguish between the heat transfer boundary conditions and the fluid flow boundary conditions, which are in blue). 78
Figure 5.1 Comparison of the variation of the cell potential with the capacity of the cell at different discharge rates where the model considers $900\ \Omega.\mathrm{cm}2$ a film resistance on the negative electrode between the developed model and the experimental results done by Doyle et al [125]. 86
Figure 5.2 The boundary conditions of the simulated domain of Bolukbasi and Ciloglu [128] experimental setup to validate the developed boiling model.*Absolute pressure. . 87
Figure 5.3 Validation of the proposed boiling model for measuring the high heat rate of boiling. 87
Figure 5.4 The variation of the volumetric heat generation rate through a 600 seconds of charging and discharging cycle for the cycle rates of 3C, 4C, 5C, and 6C. 88
Figure 5.5 The variation of the volumetric heat generation rate through a 600 seconds of charging and discharging cycle for cycle rates of 6C for three different battery temperatures. 89
Figure 5.6 Temperature contours of half of the battery pack at the end of the 300 second discharging period. Negligible temperature differences are observed across the battery pack for a high power discharge rate of 7.5C. 90
Figure 5.7 Battery temperature distribution (in ^{o}C) due to the cooling of the aluminum cold plate for a hydrogen inlet temperature of 10°C and an inlet velocity of 0.02 m/s. (a) First design, (b) second design, (c) third design, (d) fourth design and (e) fifth design... 93
Figure 5.8 Variation with discharging and charging time of (a) battery maximum temperature and (b) maximum temperature difference within the battery. 94
Figure 5.9 Variation with discharging and charging time of the temperature distribution (in ^{o}C) on the surface of the battery with direct contact with the aluminum cold plate for the fifth design, for a hydrogen inlet temperature of 20°C and a speed of 0.01 m/s. Under each time frame of the battery surface temperature is the time from the start of the cycle in seconds. 95
Figure 5.10 The variation of the heat generation rate by the battery and the variation of the proposed system cooling rate through the 600 seconds of charging and discharging cycle at a rate of 4C (note that the cooling rate is calculated at a single contact surface between the battery and the cold plate) (total heat generated through the 600 second cycle is 8.17 kJ). 96
Figure 5.11 The variation of the heat transfer coefficient through the 600 seconds cycle with the hydrogen inlet velocity and inlet temperature at a cycle rate of 4C. 97
Figure 5.12 Comparison between the proposed cooling system in this thesis and selected air based, liquid based and evaporating based cooling systems. 97
Figure 5.13 Variation with discharging and charging time of (a) maximum temperature in the battery, (b) average temperature of the battery, and (c) temperature difference across the battery, for six cases of liquid ammonia pool height in the battery pack, ranging from 5% to 50% coverage of the front surface of the battery. 101

Figure 5.14 Shows a surface temperature difference with the saturation temperature of the cooling ammonia pool plot for the surface in contact with the pool and the surface in the middle of the battery through the discharging and charging time of a rate of 4C. ... 102
Figure 5.15 Temperature contours of the front surface (in contact with the ammonia pool) and the back surface (facing the neighboring battery) of a battery in the proposed pack design at the end of the 600 second discharging and charging cycle at 4C, for six cases of ammonia pool height 103
Figure 5.16 Variation with the discharging and charging time of maximum temperature, heat generation rate, total heat removed from the battery by the proposed cooling system, and fraction of the heat removed by the boiling ammonia, for fractions of the battery front surface covered by boiling ammonia pool of (a) 5%, (b) 10%, (c) 20%, (d) 30%, (e) 40%, and (f) 50%. Note that the figure starts at 20 seconds after discharging for better viewing of the curves. 104
Figure 5.17 Variation with discharging and charging time of (a) maximum temperature in the battery 106
Figure 5.18 Temperature contours on the front surface (in contact with the aluminum cold plate integrated with liquid ammonia tubes) and the back surface (facing the neighboring battery) of the battery in the proposed pack design at the end of the 600 second discharging and charging cycle at 4C, for six cases of number of tubes. 110
Figure 5.19 Variation with the discharging and charging time of maximum temperature, heat generation rate, total heat removed from the battery by the proposed cooling system, for various numbers of tubes. 111
Figure 5.20 Variation with the discharging and charging time of maximum temperature for the air based cooling system at a cycle rate 4C. 113
Figure 5.21 Variation of the maximum temperature difference across the battery through the discharging and charging cycle at a rate of 4C. 114
Figure 5.22 Temperature contours of the battery located at the center of the proposed pack the height of the propane pool (at saturation pressure of 8.5 bar) is varied, at the end of the discharging and charging cycle (i.e., at the end of the 600 second cycle). 116
Figure 5.23 Variation of (a) maximum temperature of the battery, (b) average temperature of the battery, (c) heat absorbed by the propane pool, and (d) volumetric heat generation rate by the batteries, for various propane pool heights and discharging and charging cycle times. 117
Figure 5.24 Effect of saturation pressure of the liquid propane pool on the temperature variation across the battery in terms of (a) maximum temperature difference, (b) average temperature, and (c) temperature contours on the surface of the battery (showing the surface facing the propane pool) (at the end of the 600 second cycle). 119
Figure 5.25 Effect of discharging and charging cycle rate on the temperature variation across the prismatic battery surface, where the upper row shows the surface in contact with propane pool and the bottom row shows the surface in contact with the neighboring battery (at the end of the 600 second cycle). 121
Figure 5.26 Effect of charging and discharging rates on the variation of the maximum temperature in the battery through the discharging and charging cycle. 122

Figure 5.27 Comparison of performance of the proposed boiling based cooling system with systems reported in the open literature [9,134]..... 123
Figure 5.28 The variation of the maximum battery temperature through the simulation cycle at a rate of 6C for the five different proposed cooling systems for prismatic batteries including two designs of the cold plate 125
Figure 5.29 The variation of the reduction of the battery maximum temperature by the pool and the tube based systems. 126
Figure 5.30 The variation of the maximum temperature difference across the battery for the five different proposed system including the two variation of the ammonia based system in addition to the case when there is no cooling system is used. 127
Figure 5.31 Variation of the maximum temperature of the prismatic battery when the tube based system with ammonia coolant and for other systems proposed in the literature, for a discharge cycle at a rate of 5C. 128
Figure 5.32 The variation of the maximum temperature of the battery prismatic battery when the tube based system with ammonia as the coolant and other systems proposed in the literature for a discharge cycle at a rate of 5C. 130
Figure 5.33 Electro-thermal performance of cooling system at a 9.0 bar saturation pressure of the PSLA. (a) Temperature difference throughout the battery, (b) maximum battery temperature, (c) specific heat generation rate, and (d) electrical potential. 131
Figure 5.34 Temperature contours of the middle section of the battery in the center of the pack for five cases of liquid propane height at the end of the cycle (at 600 s). 133
Figure 5.35 Battery temperature distribution with time during the charging and the discharging phases when 30% of the battery length is covered with liquid ammonia. .. 134
Figure 5.36 Effect of the saturation pressure of the PSLA partially covering the lithium ion batteries in the pack on the maximum temperature and the temperature difference in the battery..... 135
Figure 5.37 Effect of charging and discharging rates on the thermal performance of the cooling system 136
Figure 5.38 Maximum temperature (a), maximum temperature difference (b), specific thermal energy generated (c), and electric potential (d) of the lithium ion battery for various heights of the battery submerged in the liquid propane. 137
Figure 5.39 Temperature contours of the middle section of the battery in the center of the pack for the five cases of liquid propane height at the end of the cycle (at 600 s). 139
Figure 5.40 Temperature distribution variation with time during the charging and discharging phases, for 30% of the battery length covered with liquid propane. 140
Figure 5.41. Effect of pressure of the saturated liquid propane partially covering the lithium ion batteries in the pack on the maximum temperature and the temperature difference in the battery. 141
Figure 5.42 Four configurations of the cylindrical batteries in the pack and the top view of the simulated domain for each pack configuration, where the main operating parameter is the spacing between them (top view of the pack is used to demonstrate the spacing between the batteries for each configuration) 143

Figure 5.43 Thermal performance of the thermal battery management system under a charging and discharging cycle of 600 seconds at a 4C rate in terms of (a) battery maximum temperature and (b) battery maximum temperature difference. 144
Figure 5.44 Variation of the coolant volume fraction throughout the charging and discharging cycle for the four configuration considered at a charging and discharging rate of 4C..... 145
Figure 5.45 Temperature iso-surfaces (in ^{o}C) of the four configurations considered at time 590 s of the 600 s charging and discharging cycle at a rate of 4C (note that only the first configuration has it is own temperature legend, while the other three configurations has a single temperature legend shown on the right)..... 146
Figure 5.46 Variation of the battery maximum temperature and volume fraction (VF) of the liquid coolant surrounding the batteries in the pack throughout the charging and discharging cycle for three cycle rates and considering four configurations..... 147
Figure 5.47 Variation of the heat generation rate by the battery and the cooling rate by the battery for four spacing configurations throughout the charging and discharging cycle time for a cycle rate of (a) 4C, (b) 5C, and (c) 6C..... 148
Figure 5.48 Variation of the battery maximum temperature difference across the battery throughout the charging and discharging cycle for cycle rates of 4C, 5C, and 6C for (a) configuration 1, (b) configuration 2, (c) configuration 3, and (d) configuration 4..... 149
Figure 5.49 Variation with discharging and charging time of (a) maximum temperature in the battery, and (b) average temperature of the battery, for the six different cases of liquid R134a height in the battery pack. 151
Figure 5.50 Variation with charging and discharging time of battery maximum temperature for the cases when (a) 20%, (b) 40%, (c) 60%, and (d) 80% of the battery is covered with the liquid refrigerant pool..... 152
Figure 5.51 Variation with charging and discharging time of the difference in the breakdown of the heat transfer rate between the two proposed design configurations of the cooling system..... 153
Figure 5.52 Temperature contours of the battery when (a) 0%, (b) 20%, (c) 40%, (d) 60%, (e) 80% and (f) 100% of the battery surface is covered by liquid R134a. 155
Figure 5.53 Variation of battery temperature distribution over the charging and discharging cycle for the case when 20% of the battery surface is covered by liquid R134a. 156
Figure 5.54 Variation with charging and discharging time of battery average temperature for the cases when (a) 20%, (b) 40%, (c) 60% and (d) 80% of the battery is covered with the liquid refrigerant pool. 157
Figure 5.55 Temperature contours of the battery middle plane and outer surface for the four considered pool heights of the evaporating pool when the charging and discharging rates are (a) 6C, (b) 7C, and (c) 8C..... 159
Figure 5.56 Variation of the battery heat generation rate, and heat rate removed from the battery through boiling and through natural convection by the generated R134a vapor for the two compared designs for a liquid pool height of 20% and a cycle rate of (a) 6C, (b)

7C and (c) 8C, 40% and a cycle rate of (d) 6C, (e) 7C and (f) 8C, 60% and a cycle rate of (g) 6C, (h) 7C and (i) 8C, and 80% and a cycle rate of (j) 6C, (k) 7C and (l) 8C. 160
Figure 5.57 Variation of the battery heat generation rate, and heat rate removed from the battery through boiling and through natural convection by the generated R134a vapor, when (a) 0%, (b) 20%, (c) 40%, (d) 60%, (e) 80% and (f) 100% of the battery surface is covered by liquid R134a. 161
Figure 5.58 (a) Maximum temperature, average temperature and minimum temperature through the second test cycle, and (b) state of charge, voltage, current and operation power of a single battery in the pack. 163
Figure 5.59 (a) Maximum temperature, average temperature, cell electrical potential and cycle power for (a) three continuous multiples of the short test cycle and (b) Artemis motorway cycle. 165
Figure 5.60 The variation of the maximum temperature of the battery with the highest temperature in the battery pack through a charging and discharging cycle at a rate of 6C for 600 seconds, where systems 2, 4 and 5 are all simulated at the same pool height of 30% of the height of the battery. 166
Figure 5.61 The reduction percentage of the battery maximum temperature (relative to the case with cooling comes from the natural convection in an environment temperature) variation with time versus the charging and discharging cycle time for the three proposed systems. 167
Figure 5.62 Temperature versus enthalpy property plot of refrigerant R134a. 168
Figure 5.63 Temperature versus enthalpy property plot of ammonia. 168
Figure 5.64 Temperature versus enthalpy property plot of propane. 169
Figure 5.65 Variation of the maximum temperature difference across the cylindrical battery that has the highest maximum temperature in the battery pack, when cooled by various liquid-to-vapor phase change based thermal management systems. The initial temperature of the battery is 25°C. 170
Figure 5.66 Variation of the maximum temperature difference across the cylindrical battery that has the highest maximum temperature in the battery pack, when cooled by various liquid-to-vapor phase change based thermal management systems. The initial temperature of the battery is the saturation temperature of the coolant. 170
Figure 5.67 Variation of the energy efficiencies of liquid-to-vapor phase change thermal management systems for cylindrical batteries. The initial battery temperature is set to the saturation temperature of the coolant. 171
Figure 5.68 Performance compared of the proposed system against proposed systems from other studies for the thermal management of 18650 Li-ion battery packs at a discharge rate of 6.667C 172

Nomenclature

a	Specific interfacial area (m^2/m^3)
c_p	Specific heat capacity at constant pressure (kJ/kgK)
c_s	Concentration of lithium ions in the solid (mol/dm^3)
c	Salt concentration (mol/dm^3)
D	Salt diffusion coefficient (cm^2/s)
D_s	Lithium diffusion coefficient in the solid electrode (cm^2/s)
E	Open circuit voltage (V)
F	Faraday constant (96485 C/mol)
f	Activity coefficient
g	Gravitational acceleration (9.81 m/s^2)
I	Electrical current (A)
i_2	Superficial current density in the solution phase (mA/cm^2)
k	Thermal conductivity (W/m K)
L	Length (m)
n	Number of electrons
$\dot{Q}$	Heat rate (W)
Rs	Radius of the positive electrode (m)
S	Entropy (kJ/K)
$\bar{s}$	Specific entropy (J/molK)
t	Time (s)
T	Temperature (^oC or K)
U	Open circuit voltage (V)
V	Cell voltage (V)
V	Operating voltage of the battery (V)
υ	Velocity (m/s)
Greek letters	
ρ	Mass density (kg/m^3)
υ	Velocity (m/s)
ϵ	Volume fraction
ϕ	Electrical potential (V)
η	Electrode potential (V)
σ	Solid matrix electronic conductivity (S/cm)
Subscripts	
b	Battery
gen	Generation
i	Layer in the lithium ion battery
J	Joule heat
+	Positive electrode
1	Solid phase of the electrode
2	Solution phase of the electrode
Acronyms	
BTMS	Battery thermal management systems
EV	Electrical vehicle
GHG	Greenhouse gas
HEV	Hybrid electrical vehicle

IPCC	Intergovernmental Panel on Climate Change
ICE	Internal combustion engine
Li-ion	Lithium ion
PCM	Phase change material
PSLA	Pressurized saturated liquid ammonia

Chapter 1: Introduction

The environmental impact associated with fossil fuel consumption, mainly greenhouse gases and harmful air contaminants, are a global concern. According to the data presented by the Intergovernmental Panel on Climate Change (IPCC) in 2015, 28% of Canada's emissions is caused by the transportation sector consumption of fossil fuels as shown in Figure 1.1 [1].

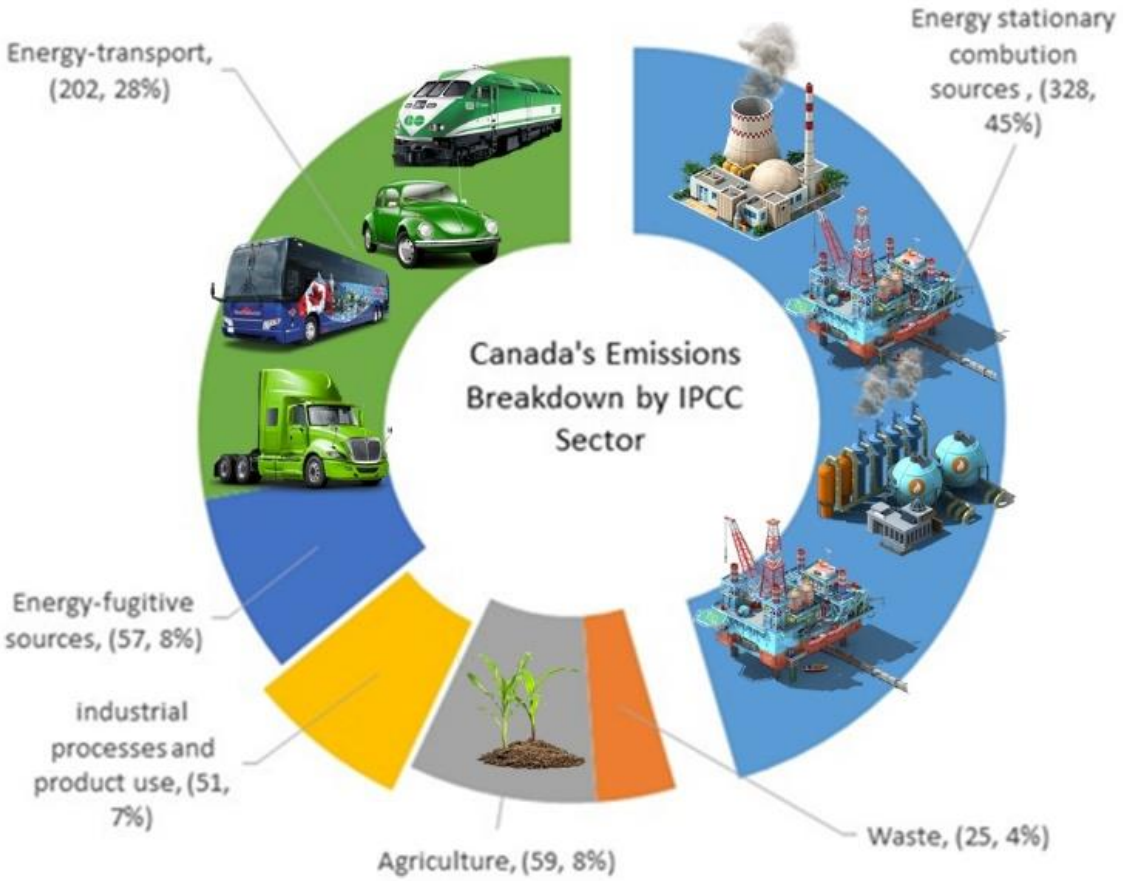

Figure 1.1 Breakdown of Canada's emissions in million tonne (Mt) CO_2 equivalent by sector, where the labeling on the graph inside the parentheses presents the following: (Mt CO_2 equivalent, percentage of the overall contribution) (Data from [1]).

Further details on the variation over time of the greenhouse gas (GHG) emissions in Canada are presented in Figure 1.2, where the variations of the total, energy transport and energy stationary combustion GHG emissions from 2005 to 2015 are shown. As shown in Figure 1.2 the GHG emissions produced by the transportation sector varied through the years 2005 to 2015, where in the earlier years of 2008 and 2009 it experienced a drop, where all the other years it experienced a raise or stayed constant. After ten years from 2005, the total GHG emissions and the energy stationary combustion in Canada was successfully reduced, however the GHG emissions released by the transportation sector increased from 195 Mt CO_2 equivalent to 202 Mt CO_2 equivalent (increased by 7 Mt CO_2

equivalent). The increase in the energy transport sector emissions highlights the urgent need to explore other practical solutions which are more environmentally benign transportation methods and technologies.

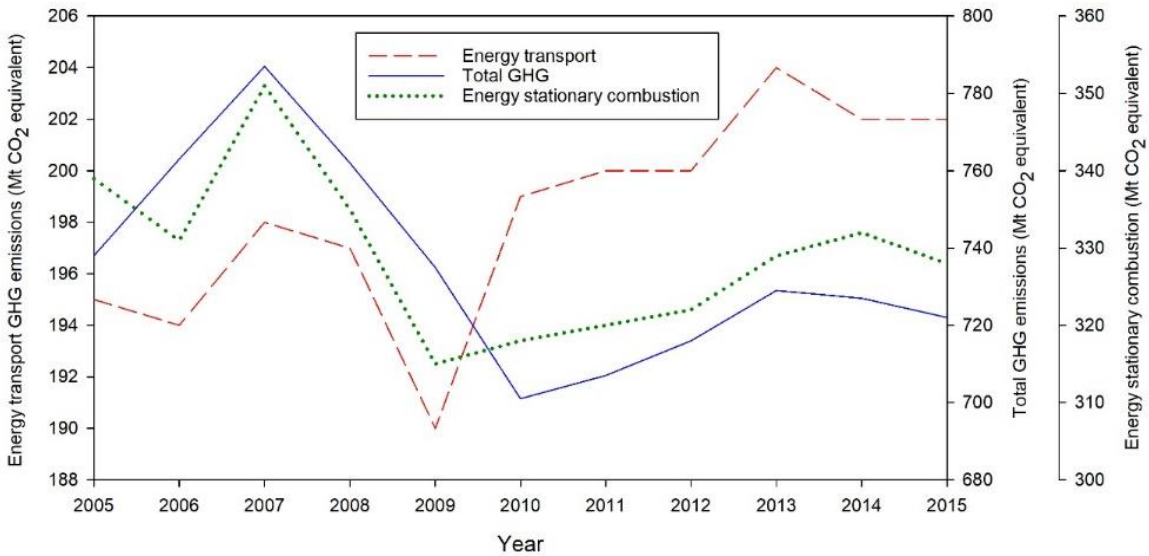

Figure 1.2 Variations of the total GHG emissions in Canada with time, and the variation of the GHG emissions that are the product of the energy transport sector and the energy stationary combustion sector in Mt CO_2 equivalent (Data from [1]).

The main contributor in the GHG emissions produced by the energy transport sector is the road transportation through the ten years from 2005 to 2015 as shown in Figure 1.3. Figure 1.3 shows the variation of the contribution of the main subsectors in the energy transport sector emissions in Mt CO_2 equivalent. As shown in Figure 1.3 the contribution of domestic aviation have decreased over the ten years from 2005 from releasing 8 million tonne of CO_2 equivalent in 2005 to 7 million tonne of CO_2 equivalent in 2015. Domestic navigation has also experienced a drop of 2 million tonne of CO_2 equivalent (from 6 to 4 million tonne of CO_2), so two of the main contributors have experienced a drop with time. However, the rail transport contribution has stayed constant through the years as shown in Figure 1.3. Finally, the road transportation with nearly around an average of 70% of the emissions of the energy transport sector, have increased over the last ten years from 2015, with an increase of 10 million tonne of CO_2 equivalent.

Having the road transportation, the main contributor in the emissions released by the energy consumed by the transportations sector this highlight the urgent need to explore other practical solutions which are more environmentally benign transportation methods and technologies. Note that the category ‘others’ shown in Figure 1.3 has a large percentage of the overall energy transport emissions. Others in Figure 1.3 refer to off road transportation. The pressure of the global warming and the governmental environment protection regulations that are related to the transportation sector have resulted in a global increase in the interest in electric vehicles (EVs) and hybrid electric vehicles (HEVs) [2]. For EVs and partially for HEVs their driving range, acceleration and the achieved speeds greatly depend on the energy content and performance of the battery pack.

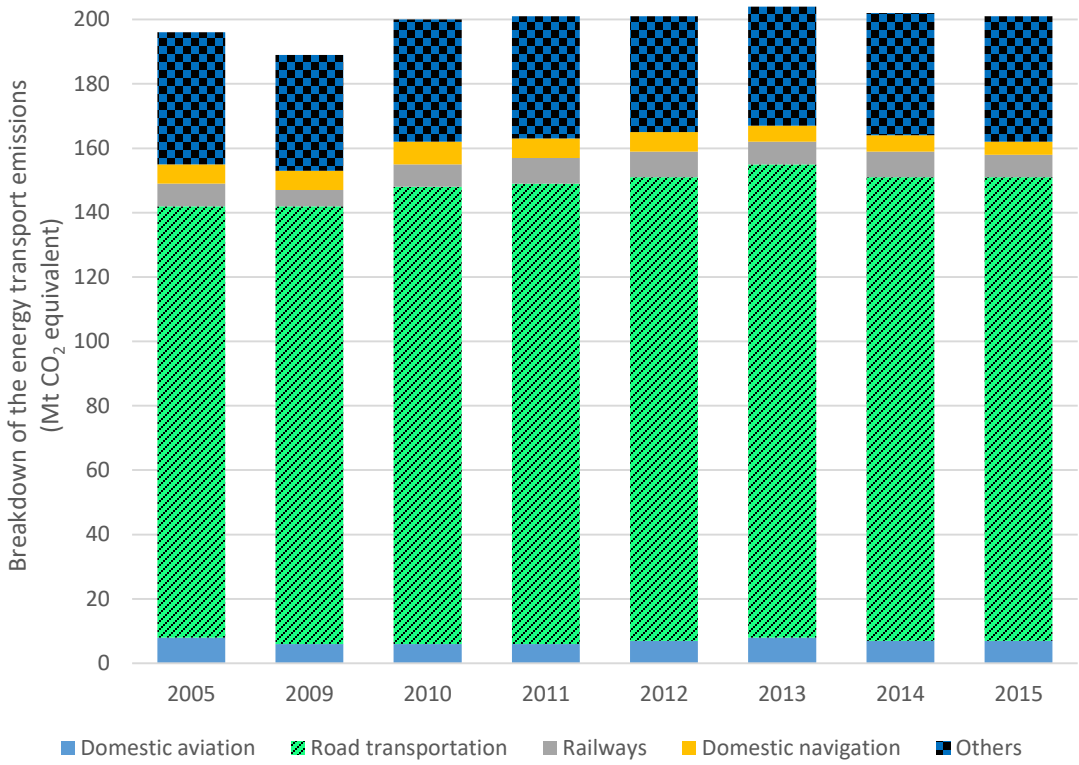

Figure 1.3 Breakdown of the energy transport emissions in Canada from 2005 to 2015 (Data from [1]).

However, for HEVs they are also supported by the fuel part of the vehicle drive chain. One of the most efficient energy storage technologies is the rechargeable lithium ion (Li-ion) batteries [3]. Li-ion batteries perform better than other rechargeable batteries in terms of having higher energy density, lower self-discharge rates, and does not suffer from the memory effect [4]. Other than the vehicle performance of EVs and HEVs, the safety and the life of the battery pack are also considered as a decisive factor in ensuring the success of EVs and HEVs [4]. In order to reduce the charging time (EV refueling), high charging rates are required, where the discharging rate determine the acceleration of the EVs and HEVs [5]. However, charging and discharging rates that the battery can receive and provide are limited by the battery operating temperature and the battery materials and the manufacturing technology used in making them. As a result, extensive research was dedicated towards improving the batteries' materials and manufacturing methods [3,6,7]. However, the other battery's performance decisive factor, which is the operating temperature and controlling it has received less attention was directed towards the development of battery thermal management systems [8].

Batteries generate heat when they are charging or discharging, which leads to an increase in the operating temperature of the battery if the generated heat was not removed. High operating temperatures can lead to safety issues such as thermal runaway and electrolyte explosion [9–13]. Research has shown that for Li-ion batteries (specifically Sony 18650 cell, which is the battery that was considered in here), as their operating

temperature increases away from the optimum operation range, the battery will suffer from capacity loss, which the capacity loss rate increases as the temperature increases for the same number of cycles [14]. For example, increasing the operating temperature of the battery from 25ºC to 50ºC, will increase the battery capacity loss by 100% for 300 cycles. Battery thermal management systems work to maintain the battery operating temperature from raising above or dropping below the optimum operation range, which means the battery thermal management system must cool the batteries at times and heat it up or insulate at other occasions. Regarding the heating function of the battery thermal management systems, battery packs are often insulated tightly and usually equipped with electric heating coils to raise the temperature of the battery pack [15,16]. The fact that battery thermal management systems (BTMS) uses electrical heating coils to prevent the battery pack temperature from dropping down indicates the importance of focusing on the cooling function of the BTMSs. Another important fact, which also highlights the importance of focusing on the cooling function of BTMS, is that generated heat when they are charged or discharged and that generated heat increases with the increase in the battery's internal resistance. Where the battery internal resistance increase as the temperature drops below the optimum operating battery temperature, which means cold batteries generates more heat and if that heat is not removed, the batteries will warm itself [17].

To better understand the vehicle battery temperature variation due to their heat generation rate it is important to understand the drive cycle of the electrified vehicles. The electrified vehicles can be classified into three groups, which are: electric vehicles (EVs), hybrid electric vehicles (HEVs) and plug-in hybrid electric vehicles (PHEVs). The coming subsections provide a detailed explanation of the drive train of these three categories.

1.1 Electric vehicles (EVs)

EVs uses power supplied from a single source, which are the batteries on board of the vehicle, other devices can also store the electrical energy in EVs such as capacitors. The power supplied from the batteries is directed to the electric motors of the vehicle, which in turn drive the wheels of the vehicle [18–21]. EVs takes an advantage of having electric motors driving the vehicle wheels in converting them into generator while breaking, which are cold regenerative breaking. The regenerative braking system helps the vehicle to reduce speed and stop quickly and at the same time they recharge the batteries. EVs have different methods to control the flow of electrical power from the batteries to the motors in the most effective and economic matter. The environmental impact associated with the fossil fuel combustion and the fact that fossil fuels have a finite nature have resulted in renewed interest in electric based transportation [22,23]. The EVs have the potential to reduce the GHG emissions since they can run on electricity from various sources, such as solar, wind, nuclear and also fossil fuels or any combinations of those. For the case where the electrical energy that derives the EVs comes from fossil fuel sources, it is still an advantage since stationary power production that are fueled with fossil fuels are more efficient than the on board internal combustion engines used in vehicles. Typical specifications of a EVs that usually used in the literature for drive cycle studies is presented in Table 1.1.

Table 1.1: Typical specifications of an electric vehicle that is usually used in the literature to perform electric vehicle drive cycle studies (date from [24]).

Parameter	Value
Vehicle mass	1720 kg
Conversion efficiency from inventor to motor	95%
Vehicles frontal area	2.39 m^2
Percent grade	1
Drag coefficient	0.38
Tire rolling resistance	0.015
Brake and steering coefficient	0.003
Regeneration coefficient	0.25
Battery to inverter efficiency	0.95
Motor to wheels efficiency	0.95
Battery cell capacity	12 Ah/m^2
Battery pack energy	25 kWh
Vehicle wheels dimensions	0.3 m (radius)

1.2 Hybrid electric vehicles (HEVs)

Hybrid electric vehicle (HEVs) are vehicles that utilize more than single energy source, where one of these source is electrical energy that derives an electrical motor, however the vehicle can also have a combustion engine or fuel cells [18–20]. HEVs that are fed with fossil fuels utilize small fossil fuel engines, which are more efficient and consequently gives a better range. Having a small engine and a battery pack that is charged with electrical gird will enhance the performance and reduce the overall vehicle environmental impact [25]. One of the other advantages that hybrid vehicles has over EVs is the range, or called range extenders. Range extenders are usually fossil fuel based engines that either produce electrical energy to drive the vehicle or charge the batteries. An example on the application of the range extenders utilized in commercial vehicles is presented in Table 1.2 where it list the specification of early model of Chevrolet Volt and the vehicle specifications are adapted from Von Helmolt and Eberle [23]. As presented in c, the range extender is gasoline fueled and it is an internal combustion engine with a size of 1.4-liter engine. HEVs can be categorized into three main configurations that are currently available in the market, and they are: series hybrid electric vehicles, parallel hybrid electric vehicles and series-parallel hybrid electric vehicles. Each of the three main categories of HEVs is discussed in the following subsections.

1.2.1 Series hybrid electric vehicle

Shown in Figure 1.4 is a schematic presentation of a series HEV. Figure 1.4 shows how the power train of the vehicle is connected. Figure 1.4 shows the drive train power flow for a series HEV with two energy sources, which are fuel and batteries. In series HEVs the wheels are powered by only electric motors, where the fuel is converted into energy through an internal combustion engine for the case of fossil fuels and the rotation energy is converted into electric energy by the help of an electric generator. The electrical energy produced by the electric generator is then used to charge the batteries or/and delivered to the motor to drive the vehicle [25].

This type of drive system usually provides a high performance capability for the vehicle. Such vehicles can utilize the high power output and high thermal efficiency of gas turbines (higher than internal combustion engines). In terms of the size of the engine and battery pack, series HEVs have larger battery pack and smaller engine than the parallel HEV. The configuration of the drive train of the series HEVs have made them more efficient in city driving compared to the parallel [25]. A practical example of series HEVs is the Chevrolet Volt, which is manufactured and sold by General Motors, and a brief presentation of Volt's specifications is presented in Table 1.2.

Table 1.2. Specification of an actual commercial EV integrated with a gasoline drive range extender (data from Von Helmolt and Eberle [23]).

Parameter	Value/specification
Drive system	Front wheel drive
Supporting system	Range extender
Charging via	Standard electrical wall outlet supplied from the grid
Dimensions	
Width	1798 mm
Length	4404 mm
Height	1430 mm
Wheelbase	2685 mm
Battery pack	
Cells	>220 cells
Battery type	Li-ion battery
Weight	180 kg
Length	1.8 m
Shape	T-shape
Power	Source of the vehicle full performance
Capacity	16 kWh (ca. 8 kWh usable)
Vehicle propulsion system	
Type	Electric
Motor type	Three phase induction motor
Maximum operating power	111 kW
Maximum torque	370 N.m
Range extender	
Type	Gasoline engine
Aspirated	Naturally
Size	1.4 Liter displacement
Power	53 kW
Overall vehicle performance	
Maximum speed	160 km/h
Acceleration	9 seconds from 0 to 100 km/h
Range	60 km and 500 km with a full gasoline tank

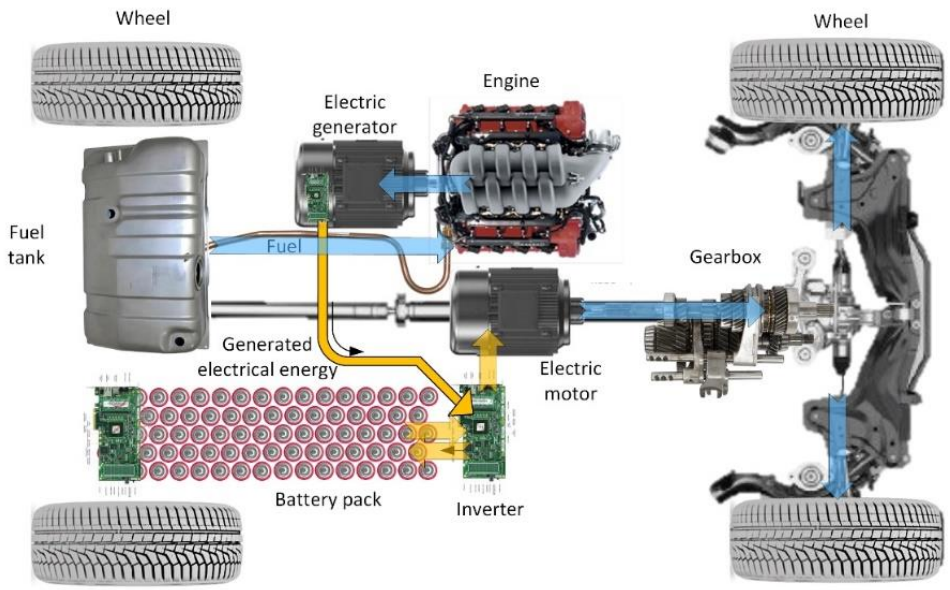

Figure 1.4 A schematic diagram of the power flow and drive train arrangement of series HEVs.

1.2.2 Parallel hybrid electric vehicle

Another arrangement of the HEVs drive train and power flow from the energy sources to the wheels is the parallel arrangement. A schematic diagram of the drive train of the parallel HEV and the power flow directions is shown in Figure 1.5. In the parallel arrangement both of the electric motor and the engine drive each of the axials of the vehicle as shown in Figure 1.5.

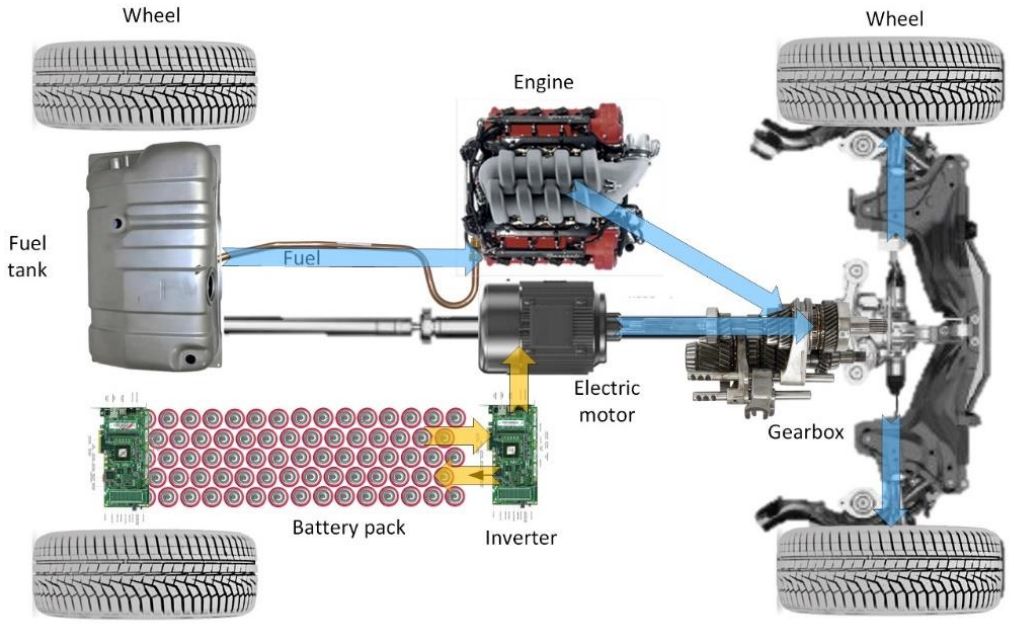

Figure 1.5 A schematic diagram of the power flow and drive train arrangement of parallel HEVs.

The electric motor in the parallel HEV driving the wheels can also be converted into a generator by treating the movement of the wheels as a resistance to generate electrical energy and charge the batteries. Having the electric motor treating the movement of the vehicle as a load to generate electrical energy, in addition it acts as a breaks to slow the vehicle down. One of the advantages to the parallel arrangement of HEVs is that the engine can be turned off while driving in the city and the vehicle can work as emission free vehicle [25]. Parallel HEVs can have a driving range around 650 km. Parallel arrangement of HEVs drive train and power distribution are often used in passenger cars, since the parallel arrangement is intended to enhance the vehicle performance. An example of the use of parallel arrangement in HEVs is Honda Civic, which uses an Integrated Motor Assist (IMA) system that coordinates the power supply for the energy sources it has. Other HEVs that has also a parallel arrangement is Honda Accord, Honda Insight.

1.2.3 Series-parallel (power split) hybrid electric vehicle

The most complicated design of the HEVs compared to the series and the parallel arrangement is the series-parallel (power split) HEV. In the series-parallel arrangement the power generated by the batteries and the engine can both or either drive the wheels, through the electric motors [25]. This configuration can also have a regenerative braking, which generate energy through slowing down the vehicles. A practical example of such vehicles that utilizes the series-parallel configuration of HEVs is Toyota Prius. Toyota's HEV drive and energy distribution system functions as a continuously variable transmission and achieve high efficiency and smooth power delivery. Brief description of the Toyota Prius, which has a series-parallel arrangement and utilizes an energy distribution system is presented in Table 1.3. Figure 1.6 shows the a schematic of the hybrid series-parallel electric vehicle and how it have the features of both series and parallel vehicles however it is equipped with the power split (PS) controller that allows the vehicle to switch between the two modes.

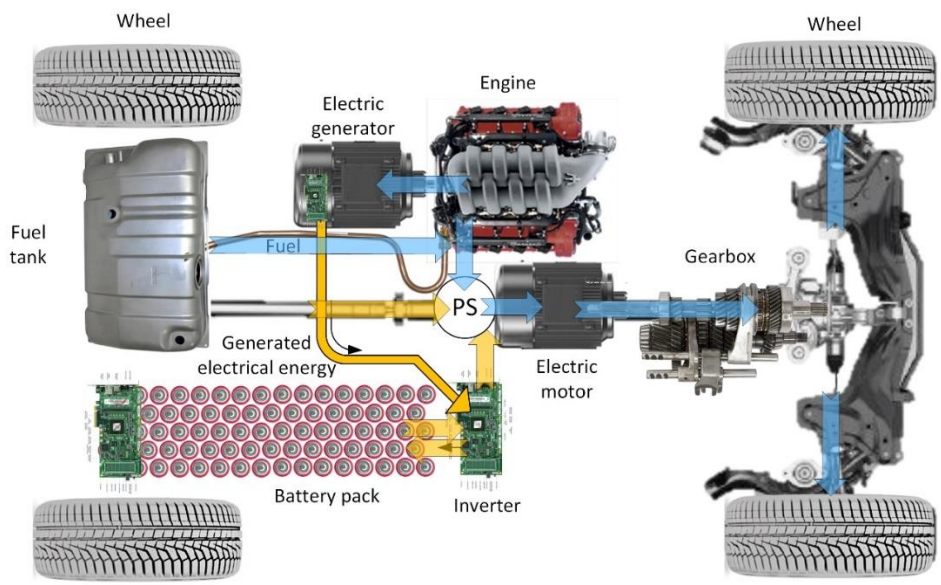

Figure 1.6 A schematic diagram of the power flow and drive train arrangement of series-parallel HEVs.

1.3 Plug-in hybrid electric vehicles (PHEVs)

Plug-in HEVs are HEVs but with a larger battery pack, where a large part of the driving power of the vehicle comes from the batteries and the batteries can be charged by plugging the vehicle to an electrical outlet. PHEVs have larger pure electric battery power supply range compared to the HEVs [25]. This means that the vehicle can be set to no emissions mode for a longer time duration and distance. PHEVs can also be referred to as charge-depleting range, for example so vehicles have a charge-depleting range of 16 km, while others may have 64 km. For the vehicle with a charge-depleting range of 64 km, if the vehicle moves a distance less than 64 km a day, then the vehicle will operate in charge-depleting mode [25].

Table 1.3. Brief description of the Toyota Prius, which has a series-parallel arrangement and utilizes an energy distribution system.

Parameter	Value/specification
Drive train	Front wheel drive
Power	121 hp
Gasoline engine	
Power	95 hp @ 5,200 rpm
Torque	142 N.m
Fuel tank	43 L
Electric motor	
Power	71 hp
Torque	163 N.m
Battery pack	
Battery type	Nickel-metal hydride
Energy	1.3 kWh
Voltage	202 V
Fuel economy	
City	4.3 L/100 km
Weight	1390 kg
Power to weight ratio	64.9 W/kg

1.4 Drive cycle

The pollutants emissions and fuel consumption for conventional vehicles are measured using standard driving cycles, such as the new European driving cycle (NEDC). However, vehicle manufacturing companies rely increasingly on a more realistic driving cycle such as the Artemis cycle. Through a more realistic driving cycle, the Artemis cycle emulates the actual performance of vehicles. There are three variations of the Artemis driving cycle: urban, motorway and road driving. Also, there are two versions of the motorway cycle, differing based on the maximum speed that the vehicle reaches in the cycle (130 km/h or 150 km/h). Detailed description of the drive cycle and its different modes for those which will be considered to evaluate the actual performance of the battery pack thermal management system or cooling system is presented in the analysis section of the thesis.

1.5 Motivation

The latest published research on thermal management systems is mostly on around optimizing the current methods for battery cooling such as air and liquid cooling systems. However, such systems performance is limited, and those limits can be determined through first and second laws of thermodynamics [26]. However, other energy saving and performance enhancement methods that are applied in other fields can be adapted into the thermal management of batteries, such as integration. Integration is done through various ways, such as using the vehicle fuel to cool the batteries and then use it to generate power. The example of using the fuel is applicable to hybrid electric vehicles. Other systems can also utilize the high heat transfer coefficient of boiling, while boiling is a phase change that has high potential of heat removal plus at a constant temperature.

All the previous examples and more are different methods to enhance the cooling performance of battery thermal management systems thus the performance of HEVs and EVs. The aim of this thesis to develop and model novel battery thermal management systems that will save energy, enhance the performance of EVs and HEVs and boost their market, and most importantly is to reduce the GHG emissions. Finally, the motivation for working on this thesis can be summarized in the following bullet points:

- There is an important need to reduce the EVs and HEVs battery operating temperature, including the maximum battery temperature and the maximum temperature difference across the battery to achieve a higher battery performance and vehicle performance as well through faster charging and discharging.
- There is an immediate need to reduce significantly environmental impact of fuel combustion in the transportation sector (to help mitigate global warming).
- A need to better understand the unexplored field of integrating the vehicle drive train and the battery cooling system to achieve higher cooling performance, energy savings and reduce space requirements of the cooling system.
- A need to better understand the unexplored high heat transfer rate of phase change from liquid to vapor (boiling) in battery cooling systems.

1.6 Objectives

The main objective of the thesis is to conceptually develop novel battery thermal management systems that achieve better performance than what is currently developed in the literature and analyze them comprehensively for practical applications. The specific objectives of the thesis study are detailed as follows:

- To develop novel battery thermal management systems for EVs and HEVs that will take advantage of the high heat transfer rate of the boiling (phase change) from liquid to vapor in the thermal management of the batteries, which can be integrated into vehicle drive train with the cooling system. The present systems are expected to:
    - attain better performance than the systems proposed in the literature, which are mainly the liquid- and air-based systems,
    - reduce the space requirement for the thermal management systems which will reduce in reduced overall weight and cost, and

    - reduce the carbon footprints of the thermal management systems in vehicles and make them more environmentally benign.
- To model, analyze and simulate the performances of the proposed battery thermal management systems, and comparatively evaluate them for practical applications. The following studies will in this regard be performed:
    - development of electrochemical models for cylindrical and prismatic batteries which are considered for the present thermal management systems,
    - validation of the developed electrochemical models with the experimental data published in the literature, in terms of cell voltage and battery capacity,
    - development of thermodynamic and heat transfer models for each thermal management system to cover the battery internal and external sections in the proposed systems,
    - validation of these developed thermodynamic and heat transfer models with the experimental data obtained from the literature, in terms of the boiling heat transfer fluxes, boiling surface temperatures, and the centerline temperatures of the batteries,
    - development of design, configuration and operation related strategies for the present battery thermal management systems,
    - examination of various charging and discharging rates including high intensity simulation cycles and drive cycles on the performances of the battery packs,
    - investigation of the effects of varying operating conditions and parameters on the performances of the proposed thermal management systems, and
    - evaluation of various design criteria, including geometry, on the performances of the thermal management systems.
- To perform an optimization studies on various design, geometry and operation related parameters of the proposed thermal management systems, using the iterative optimization methods of artificial neural network.
- To conduct comparative performance assessment studies of the battery thermal management systems in terms of temperature and heat transfer rate. Such studies include comparisons, evaluations and improvements of the efficiencies of the proposed thermal management systems by reducing the maximum prismatic and cylindrical battery temperatures and maximum temperature differences across these batteries.

Chapter 2: Literature Review

In the recent years and the recent advances in the lithium ion batteries have led to having them as the most promising electrical energy storage technology [3]. The main advantages that lithium ion batteries have over other rechargeable batteries but not limited to are: having higher energy density, has a bad memory effects, lower mass density and finally they have a lower self-discharge rates [4]. The main requirements of electric vehicles or the main two objectives electric vehicles have to achieve performance that is better than conventional gasoline vehicles are the long driving range and the high acceleration [5]. As known the starting point that gave the EVs the concentrated attention was the high performance EVs, which were able to achieve faster speeds and compete with high performance fuel based vehicles. The success in terms of acceleration, speed and efficiency of the high performance EVs and high performance hybrid electric vehicles (HEVs) have prompted the technology and the development of regular use EVs and HEVs.

Tesla Model S P100D is the first high performance electric vehicle and a production vehicle with a price tag that is comparable to the fuel vehicles. Tesla Model S P100D was able to achieve to go from 0 to 100 km/h in just 2.7 seconds [15]. Although, electric motors can provide instant torque and high acceleration, their top speed is limited compared to the gasoline vehicles. This was one of the motivations that led to the development of the hybrid high performance electric vehicles such as the Ferrari LaFerrari [27]. Hybrid high performance electric vehicles are those where they use the fuel to produce electrical power and the electric motor with its high torque capabilities to achieve a better performance. The performance of the electric vehicles including speed, acceleration and overall fuel consumption reduction have motivated and encouraged over the world the car manufactures to develop EVs and HEVs such as Tesla Model 3, Tesla Model X and others. As a results of the advances and the concentration from the car manufactures towards the electric vehicles, the research and development have been concentrated in developing the batteries technologies in terms of both manufacturing technology and material improvement. These are important factors for lithium ion batteries in determining the energy density, life cycle and allowable charging and discharging rates, and have been the subject of extensive investigations in the last few years [3,6,7]. However, the lithium ion batteries performance is sensitive to its thermal behavior, where relatively excessive temperature can result in degrading its performance to the level of failure and may reach to dangerous levels including explosions. However, battery thermal management has received less attention than manufacturing and material issues [8].

Doughty and Roth [28] highlighted the criticality of the thermal performance of the lithium ion batteries for performance. In order to assess the battery temperature effect on the capacity of the lithium batteries in terms of its life in terms of the cycle time Ramadass et al. [14] experimentally investigated the thermal performance of Sony 18650 at high temperatures. Ramadass et al. found that, at higher battery operation temperatures, the capacity fade of lithium ion cells accelerates. However, having high operating temperatures can result in overheating the batteries, which will eventually will lead to thermal runway if the generate heat was not removed effectively and properly [29–31]. Due to the importance of the operating temperature of the lithium ion battery on its performance and vehicle safety

and performance, improvements are needed in the thermal performance of the battery where two main ways of solving the thermal issues of the batteries are to reduce the heat generation rate or to increase the heat dissipation rate.

Charging or discharging the lithium ion battery to generate heat, which can be reduced by modifying the internal structure of the battery cell. The part of the battery that is responsible for the most of the heat generation by the battery happens on the cell electrode, which is mainly due to its resistance to the movement of the electrons and ions [3]. Due to the electrode generating most of the battery heat generation rate, reducing the size of the electrode through optimizing the internal battery design results in a better battery efficiency and thus less heat generation rate. Thus, battery heat generation rates are greatly reduced through optimizing the design of the electrode of the battery with the objective of minimizing its resistance to electron and ion flow. Reducing the electrode resistance is by reducing its thickness. However, increasing the dissipation rate of the heat generation rate can be accomplished without modifying the structure of the battery, i.e., by using an external procedure using a battery thermal management system (BTMS). The importance of BTMSs for achieving an optimum battery operating temperature and maintain it has been recognized by many researchers [32–34]. A BTMS can help relieve a lithium ion battery of the generated heat and keep its temperature within the optimum operation range, without structural or manufacturing modifications to the battery.

Table 2.1. Main properties of rechargeable batteries used in EVs and HEVs

Battery type	Specific energy (mass basis) (kJ/kg)	Specific energy (volume basis) (kJ/L)	Battery life (cycles)	Ref.
Zinc-air	828 [a]	968.4		[35]
Nickel-metal hydride	288			[36]
Lithium-ion	334.8	410.4	4000	[37]
	341.3			[38]
	432-468	720-1080		[36]
	540	1080	1000	[39]
	540-720	1656-2160 [b]	8-10 years	[40]
Nickel-iron	108-198	216-396	1200-4000	[35]
Nickel-zinc	216-234	432-468	100-300	[35]
Lead acid	108-180	216-360	400-600	[35]
	172.8		800	[41]

[a] Highest specific energy on mass basis
[b] Highest specific energy on volume basis

Regarding the second point mentioned earlier, which discussed increasing the heat removal rate from the battery, the main objective of that technique is to equalize the battery heat generation rate with the heat removal rate through the cooling system. However, with the attractiveness that method has over others, it has been noted that TMSs have received less attention by the research and development communities when compared with research on internal battery modifications. This part of the literature review will look in details in the air forced BTMSs, with special attention directed towards the configuration of the battery pack including but not limited to: the air delivery to the pack, batteries arrangement

in the pack and finally the simulation model used to simulate the thermal behavior of the proposed system. The main properties of rechargeable batteries used in EVs and HEVs are presented in Table 2.1. From Table 2.1 zinc-air battery specific energy on mass basis exceeds that of lithium ion batteries by 15% [35,40]. However, lithium ion batteries have the highest specific energy on volume basis, which is the main reason why EVs and HEVs manufacturers went with lithium ion batteries for their vehicles as shown in Table 2.1. Before going into more in details of thermal management systems and their different types including their main categories and the novel proposed systems, new and novel uses of the thermal behavior of the battery is presented. It was presented in Dong et al. [42], that the thermal behavior of the Li-ion batteries can be used as an indicator to enhance the performance of the electrochemical impedance spectroscopy of the battery itself.

The next section of the literature review chapter presents a review on the most recent and novel BTMS systems proposed in the literature, with special focus on the three main categories. The comparison between these systems and the details presented focuses on the development, simulation model and the investigation approach used to assess the performance of the proposed systems, such as experimental, simulation or combined approach.

2.1 Battery Thermal Management Systems (BTMSs)

Lithium ion battery manufacturing companies build batteries with fixed shapes and geometries since they have the ability to be used in a wide variety of applications, ranging from laptops to EVs. In some applications of the lithium ion batteries, high-powered charging and discharging currents are used, leading to excessive heat generation rates and possible excessive operating temperatures. These can increase battery frailty and safety hazards. To avoid excessive temperature, build up in high powered operated batteries, a BTMS needs to be integrated with the battery pack to maintain the battery operating temperature in the safe zone and preferably within the optimum operating temperature range. BTMS proposed in the literature considered various operating conditions and different battery geometries to achieve the optimum battery thermal performance. The proposed BTMSs in the literature can be categorized based on the nature of the coolant used in the system, which leads to having three main categories. The three main categories are: liquid based, air based, and phase change (PCM) based BTMS. Other systems that have been proposed in the literature that do not fall under any of the three main categories, are an integration of two or three main system categories. An example for an integrated BTMSs is the integration of PCM based systems with air or liquid cooling, where the PCM surrounds the batteries, while the air or the liquid cools down the PCM. With that configuration the PCM provide a uniform cooling to the battery to achieve high temperature uniformity while the high heat transfer coefficient of air and liquid cooling systems maintain the battery temperature within the optimum operation range. The coming subsections focus on each of the three main categories and on hybrid cooling models.

2.1.1 Air based BTMSs

The most adopted cooling technology in daily life is the air based cooling technology, which is used in various applications ranging from cooling the electronic internal components of computers to vehicle and residential applications [43–47]. The main reason behind the excessive use of air based cooling systems is the availability of air. Air based

systems can be categorized into two main categories, which are natural and forced air flow systems. Natural air flow convection based BTMS are the air system where the air flow into the battery pack occurs without consuming energy. However, forced air flow systems the air is forced to flow through the pack by a dedicated energy consuming system, which is known as forced air convection cooling based BTMS.

Table 2.2. Summary of novel air flow based BTMSs for lithium ion batteries.

Air flow system	Analysis method	Heat generation source	Battery type	Studied variables	Charging or/and discharging rates	Number of batteries in pack (simulated)	Ref.
Forced axial flow	CFD (ANSYS Fluent 14.5)*	2D pseudo electrochemical model	26650 $LiFePO_4$ (BAK International (Tianjin) Limited, China)	-Air flow velocity -Radial interval between batteries	Discharge 2C	36 (8)	Yang et al. [59]
Parallel forced air flow with secondary vent	CFD (differential equations are discretized and solved using SIMPLE algorithm)	From literature [44]	Prismatic battery with overall dimensions of 16 mm x 65 mm x 151 mm	-Inlet air temperature -Heat generation rate -Varying location of the secondary vent	Considered through the heat generation rate	12 each row (12)	Hong et al. [60]
Forced flow	Numerical and analytical models	Based on equation from the literature [56]	Sony-US18650	-Thickness of channel (for flat plate batteries) -Air Reynolds number -Distance between batteries (for cylindrical batteries)	Discharge at 2C	10 (10) batteries per cooling channel, 20 (20) batteries per cooling channel, and 30 (30) batteries per cooling channel	Xun et al. [18]
Forced flow	ANSYS Icepak 14.5	Obtained through experiments	18650 cylindrical battery	-Location of air inlet -Location of air outlet -Geometry of pack	Discharge at 1C, 2C and 3C	19 (19), 24 (24), 25 (25), and 28 (28)	Wang et al. [53]
Forced axial flow	CFD (ANSYS CFX) and experiments	Characterized using an accelerating rate calorimeter	Lithium Iron Phosphate (LFP) having the electric configuration of 12S2P	Mass flow rate of air	Charging at 1C, 3C and 5C	24 (24)	Saw et al. [17]

*Experimentally validated

Most of the proposed air based BTMS fall into the category of forced air convection systems, due to their high heat transfer coefficient and have the ability to maintain a constant heat transfer coefficient on the batteries in the pack. Some of the advantages that forced air based systems have over other cooling systems are the simple configuration, low

cost compared, ease of maintenance and ability to cool the batteries to the set temperature for most applications. The air based BTMSs proposed in the literature are usually proposed for moderate cooling requirements of the battery packs, which are those packs that are discharging or charged at low rates. The main differences that were found in air based thermal management systems proposed in the literature are three [2,10,55–59,45,48–54]:

(1) Air flow velocities
(2) Flow path
(3) Geometrical arrangement of the batteries in the pack

Some of the most recent and novel air based BTMSs for lithium ion batteries are presented in Table 2.2. Note that Table 2.2 summarizes these systems in terms of the analysis method, heat generation source, battery type considered in the study, the variables that were considered in the study, the nature of the simulation or test cycle and finally the number of the batteries in their proposed pack. Yang et al. [59] proposed an air cooling system for cylindrical lithium ion battery packs, where the battery type was 18650 lithium ion battery. The proposed configuration arranges the cylindrical batteries axially as shown in Table 2.3.

The main thermal performance measures that Yang et al. used to assess the performance of their proposed configuration are the pressure difference across the pack and the maximum temperature throughout the pack. The fluid behavior was also investigated in terms of velocity and pressure variations across the pack. The thermal performance of the battery was measured through three dimensional heat transfer and fluid flow modeling, where the heat generation rates are based on a user defined function program. The heat generation rates of Yang et al. were based on a pseudo two dimensional model of the electrochemical reactions.

Table 2.3. Detailed presentation of various design configurations proposed in the literature that are based on the air flow system.

Air flow system	Configuration	Details	Ref.
Axial air forced flow lithium ion battery pack, where batteries in the pack are arranged axially	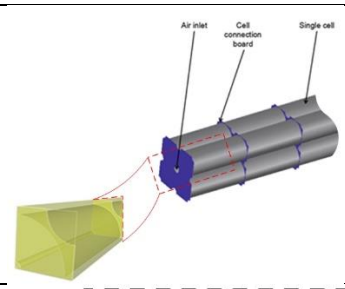	-Novel configuration of battery pack, where cylindrical batteries are arranged axially through the pack and air is forced through them using channels in the middle of the pack.	Yang et al. [59]
Parallel air cooled system	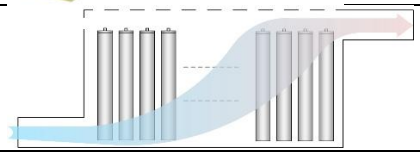	-Introduction of secondary air vents, where different locations were considered. -The lowest pack maximum temperature achieved was the first location shown in the figure (parallel to the inlet).	Hong et al. [60]

Various flow directions and configurations	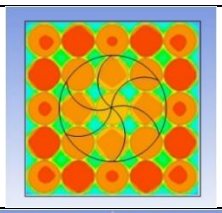	-Air flow is forced vertically through a square battery pack configuration. -Flow direction and location and pack size results in outer batteries having the highest temperatures.	Wang et al. [53]
	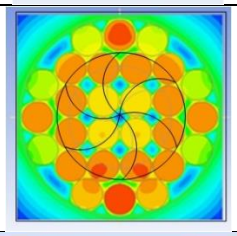	-Configuration has air flow in axial direction through a cylindrical pack. -Flow configuration results in batteries having lowest temperatures at outermost battery ring.	Wang et al. [53]
	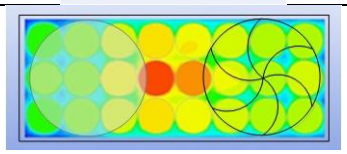	-Pack has a rectangular configuration, where flow inlet is at one side of the pack and outlet is at the other end. -Flow configuration has lower temperatures through the pack, however the battery in center of the pack has highest temperature.	Wang et al. [53]
Variations of inter-cell spaces	Zero spacing between the batteries 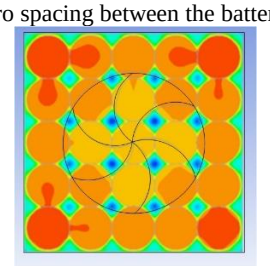	-Results in highest battery maximum temperature between the considered inter-cell spacing. -Exhibits highest temperature difference and average temperature in pack compared to other cases considered.	Wang et al. [53]
	Spacinig is 5.6% of battery radius 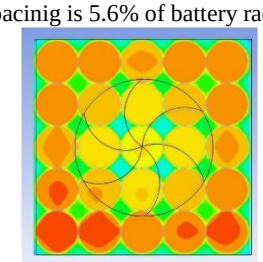	-Increasing the spacing between the batteries from zero to 5.6% of the battery radius will reduce the maximum temperature in the pack, the maximum temperature difference through the pack and the average temperature. -Having inter-cell space to be 5.6% of the battery radius will results in a lower pack average temperature than having large spacing of 33.3% of the battery radius	Wang et al. [53]
	Spacing is 22.2% of battery radius 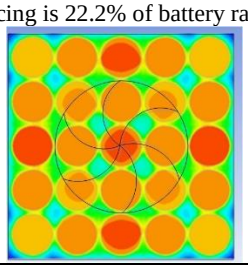	-Increase spacing to 22.2% of battery radius further reduces pack maximum temperature, maximum temperature difference through the pack, and pack average temperature. Exhibits a large drop compared to drop in average temperature.	Wang et al. [53]
	Spacing is 33.3% of battery radius 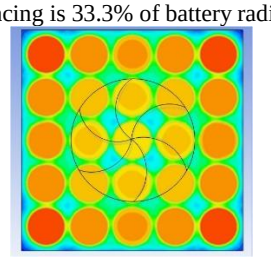	-Further increase of space from 22.2% to one third of battery radius has a negative effect on BTMS performance. -Maximum temperature, temperature difference and average temperature all increase.	Wang et al. [53]

The validation of their model was conducted experimentally, by comparing the results with a single battery axial cooling setup with the temperature variation of the battery subject to axial cooling. However, one of the disadvantages of the experimental procedure followed by Yang et al. [59] is that the temperature sensors where mounted on the batteyr surfaces by using a duct tape, which will reduce the cooling capabilities of the proposed system due to the thermal resistance of the duct tape. Most of the proposed air based BTMS fall into the category of forced air convection systems, due to their high heat transfer coefficient and have the ability to maintain a constant heat transfer coefficient on the batteries in the pack. Some of the advantages that forced air based systems have over other cooling systems are the simple configuration, low cost compared, ease of maintenance and ability to cool the batteries to the set temperature for most applications. The air based BTMSs proposed in the literature are usually proposed for moderate cooling requirements of the battery packs, which are those packs that are discharging or charged at low rates. The main differences that were found in air based thermal management systems proposed in the literature are three [2,10,55–59,45,48–54]:

(1) Air flow velocities
(2) Flow path
(3) Geometrical arrangement of the batteries in the pack

Some of the most recent and novel air based BTMSs for lithium ion batteries are presented in Table 2.2. Note that Table 2.2 summarizes these systems in terms of the analysis method, heat generation source, battery type considered in the study, the variables that were considered in the study, the nature of the simulation or test cycle and finally the number of the batteries in their proposed pack. Yang et al. [59] proposed an air cooling system for cylindrical lithium ion battery packs, where the battery type was 18650 lithium ion battery. The proposed configuration arranges the cylindrical batteries axially as shown in Table 2.3.

The main thermal performance measures that Yang et al. used to assess the performance of their proposed configuration are the pressure difference across the pack and the maximum temperature throughout the pack. The fluid behavior was also investigated in terms of velocity and pressure variations across the pack. The thermal performance of the battery was measured through three dimensional heat transfer and fluid flow modeling, where the heat generation rates are based on a user defined function program. The heat generation rates of Yang et al. were based on a pseudo two dimensional model of the electrochemical reactions.

Table 2.3 presents the various novel design configurations which have been considered by various researchers with the aim of reducing the maximum pack temperature, the maximum temperature difference through the pack and the average temperature. The details of the results are basically summarized for each configuration of the battery pack.

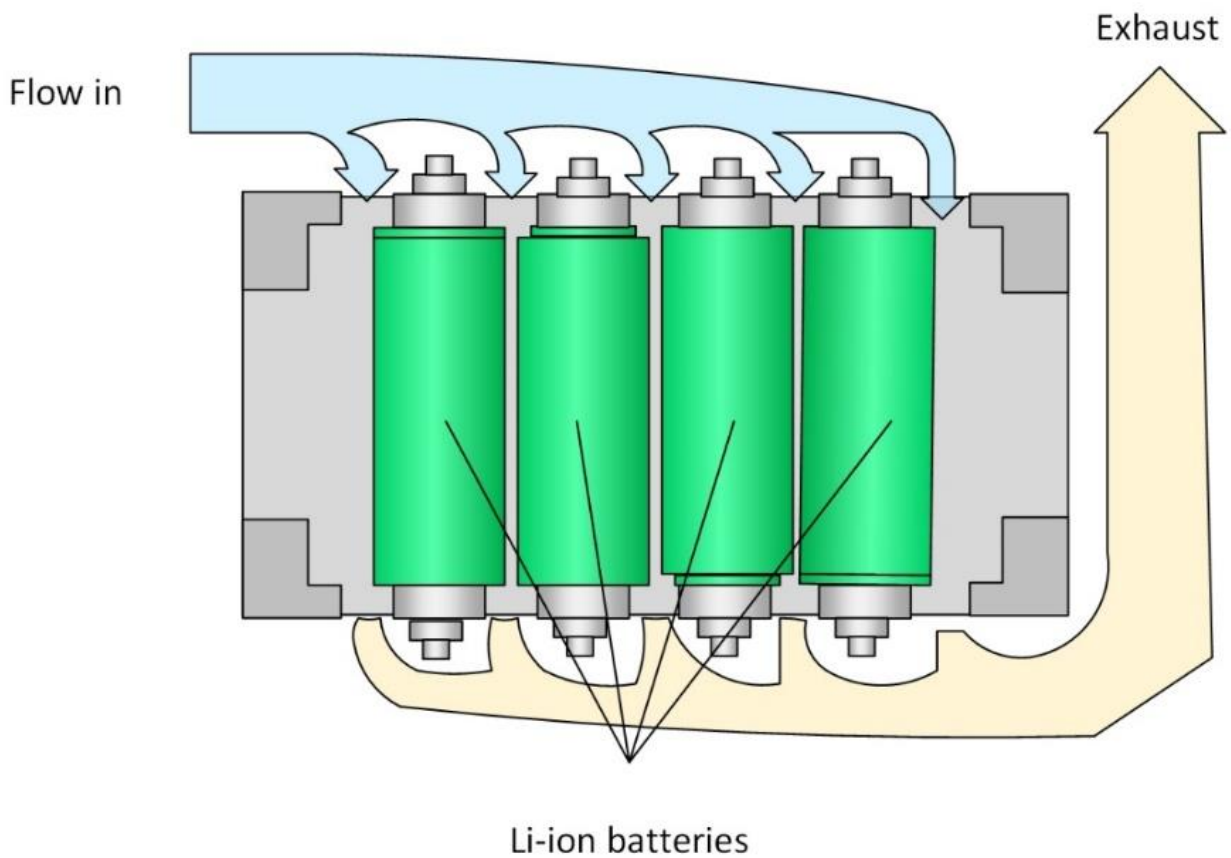

Figure 2.1 Schematic of forced axial flow battery pack configuration, showing the designed flow direction, which is forced through the pack to flow in the axial direction of the batteries.

The main parameters Yang et al. [59] considered through the assessment of the proposed forced air BTMS are the effect of the radial intervals between the batteries and the amount of air injected through the battery pack. All the different cases considered by Yang et al. had a common result in which the air velocity increases through the flow direction, due to the heat generation by the batteries in the pack. It is known that for a subsonic compressible flow, the addition of heat to the flow results in increasing the velocity until reaching the sonic conditions. The effect and the location of the air when it reaches the sonic conditions in the flow channel should be investigated. Yang et al. [59] found that for a specific air flux the radial interval has nearly a negligible effect on the maximum temperature in the battery, however the minimum temperature in the battery increases as the radial interval increases for all considered air fluxes. Saw et al. [10] proposed a novel design for forced air based BTMS for cylindrical lithium ion battery with the electrical configuration of 12S2P battery. The pack has 24 batteries, where they are arranged in two parallel rows of 12 cells each as shown in Fig. 1. Although the batteries are arranged side by side and the battery pack is characterized as parallel air flow pack, the novel configuration of the air delivery design of the pack produces an axial flow around the batteries. The thermal performance of the battery pack is investigated through three dimensional modeling of the 24 cells and the with supporting experimental studies. The

heat generation rate was obtained through an accelerating rate calorimeter for charging at a constant current rate.

In Saw et al. [10] work the main parameter that was investigated is the air mass flow rate entering the battery pack. They were able to identify the hot and cold spots in the pack and on the single battery surfaces. Saw et al. study concluded that as the air flow increases the cooling performance is improved while the pressure drop increases. In order to predict the transient performance of the battery pack through the use of their validated with the literature (in terms of trend) heat transfer coefficient correlation was used, where their developed Nusselt number and Reynolds number correlation is as follows:

$$\mathrm{Nu} = 0.0374\ \mathrm{Re}^{0.8014}\ [10] \tag{2.1}$$

This correlation was validated (in terms of trend) with data from the literature.

The cooling performance of the proposed battery cooling system by Saw et al. was measured under different charging rates. Their numerical model was also validated with a series of experimental studies. They concluded that for their proposed design a larger powered fan is required in order to achieve the required air mass flow rate input and maintain the batteries in the pack temperature under acceptable operating conditions. It is important to note that the proposed method in Saw et al. provide a simpler method to predict the transient thermal performance of a full battery pack, which is not viable for full transient simulation. Wang et al. [53] analyzed the performance of a lithium ion battery pack under wide different number of configurations of the location of the fan (provide forced air flow) and the air vent, which is the outlet. As shown in Fig. 2 the five different configurations of the location of the fan and the air vent of the battery pack. Wang et al. followed a similar approach to many other researchers [45,50–52] where the single battery is assumed to be a homogenous structure with an internal heat generation rate. In order to specify the thermal conductivity and the density and heat capacity of the homogenous battery assumption, the effective thermal conductivity and the effective density are calculated as follows [49]:

$$\rho c_p = \sum_i \rho_i c_{p,i} V_i \,/\, \sum_i V_i \tag{2.2}$$

Here, ρ is the density, c_p is the heat capacity, and V_i is the volume of the layer i. However, since the battery geometry is cylindrical then the effective thermal conductivity was calculated for both axial and radial direction. The main reason for calculating two effective thermal conductivities is based on the structure of the cylindrical lithium ion batteries. The cylindrical lithium ion battery is made of very thin sheets that are wrapped around a cylindrical rode to make a cylindrical structure. The effective thermal conductivity in the radial and axial directions are found as follows respectively [48]:

$$k_r = \sum_i L_i \,/\, \sum_i L_i/k_i \tag{2.3}$$

$$k_{ax} = \sum_i L_i/k_i \,/\, \sum_i L_i \tag{2.4}$$

Table 2.4. Summary of optimum configurations of battery pack size and shape and number of batteries for each configuration category.

Cell arrangement	Variable	Maximum temperature in pack (°C)	Maximum temperature difference in pack (°C)	Average battery temperature throughout pack (°C)
One row of 24 batteries (1×24)	Fan and exit location (Fan: top, exit: bottom)	40	11	35
Three rows of 8 batteries each (3×8)	Fan and exit location (Fan: top, exit: bottom)	39	7.0	34
Five rows of 5 batteries each (5×5)	Fan location (Fan: top, bottom, side)	34	3.0	33
Five rows of 5 batteries each (5×5)	Inter-cell spacing (1.0 mm)	34	3.0	33

Source: Wang et al. [53]

Wang et al. [53] used four indicators to measure the performance of the BTMS for the different number of battery pack size, shape and different locations for the air inlets and outlets from the pack. The four indicators that was defined by Wang et al. [53] are the maximum temperature in the battery pack, the maximum temperature difference through the pack, the batteries in the pack average temperature, and the space occupancy ratio. The space occupancy ratio is defined as the ratio of the volume of the batteries over the volume of the pack. For the performance measure indicators, the as the maximum temperature in the pack, the maximum temperature difference through the pack and the average cell temperature decrease the better cooling the BTMS is providing to the batteries. However, as the space occupancy ratio increases the better the BTMS is utilizing the space. For the different cooling configurations, the optimum performance for each category is shown in Table 2.4.

Xun et al. [56] investigated the cooling performance and the efficiency of multiple cooling configurations for the thermal management of battery packs for cylindrical lithium ion batteries and for flat plat battery models through both numerical and analytical models. Multiple configurations were proposed and the main operating parameters were considered. The heat generation in the study was based on a correlation that relates the internal resistance and the change of entropy of the battery with the state of charge as follows:

$$S_T = i^2 R - (T_b \, \Delta\bar{S} \, i)/nF \tag{2.5}$$

Here, i is the discharging current density (A/m^3), n is the number of electrons in the half electrochemical reaction, F is the Faraday constant, T_b is the temperature of the battery, R is the internal resistance of the battery and $\Delta\bar{S}$ is the change of entropy. The internal

resistance R of the battery can be written as a function of the state of charge (SOC) of the battery and its temperature as follows:

$$R = 2.258 \times 10^{-6} SOC^{-0.3952} \text{ at } T = 20^{o}C \quad (2.6)$$

$$R = 1.857 \times 10^{-6} SOC^{-0.2878} \text{ at } T = 30^{o}C \quad (2.7)$$

$$R = 1.659 \times 10^{-6} SOC^{-0.1692} \text{ at } T = 40^{o}C \quad (2.8)$$

Here, the internal resistance has the units of Ω/m^3. The change in entropy ΔS can also be expressed for several SOC values based on [54] as follows:

$$\Delta\bar{S} = 99.88\,SOC - 76.67 \quad (J/molK) \quad 0.00 \leq SOC \leq 0.77 \quad (2.9)$$

$$\Delta\bar{S} = 30 \quad (J/molK) \quad 0.77 \leq SOC \leq 0.87 \quad (2.10)$$

$$\Delta\bar{S} = -20 \quad (J/molK) \quad 0.87 \leq SOC \leq 1 \quad (2.11)$$

Xun et al. [56] carried on their investigation for number of different Reynolds numbers, where the results were compared and it was concluded that as the Reynolds number increases the maximum temperature in the pack decreases, however the temperature distribution through the pack becomes uneven. Xun et al. [56] investigated the effect of the air flow channel dimensions relative to the battery size and found that it can affect the average temperature of the pack which in turn may improve the temperature uniformity of the pack. Others considered the effect of the air channel dimensions such as Choi and Kang [46], where the channel size effect on the cooling performance of BTMS for a prismatic battery pack was investigated. Choi and Kang concluded that narrow channel thickness leads to a more lumped system behavior of the battery in the pack.

2.1.2 Liquid based BTMSs

Liquid cooling systems has been the most used and popular BTMS so far, and this popularity is shown where some of the major EV and HEV manufactures used liquid cooling system to maintain their batteries within the optimum operation range [16,61,62]. The first ever high performance EV was made by Rimac Automobili in Croatia, and they have implemented the liquid cooling system to maintain their batteries at the optimum operating conditions [63]. In this section, novel liquid based BTMSs are presented in details including system type, the novelty of the study, novelty of the proposed system, the analysis method, method used to obtain the battery heat generation rate, battery type, coolant material, studied variables, charging and discharging rates and battery pack configuration. A summary of the considered studies is presented in Table 2.5, which follows a brief description, conclusion and a recommendation the authors of the papers have presented.

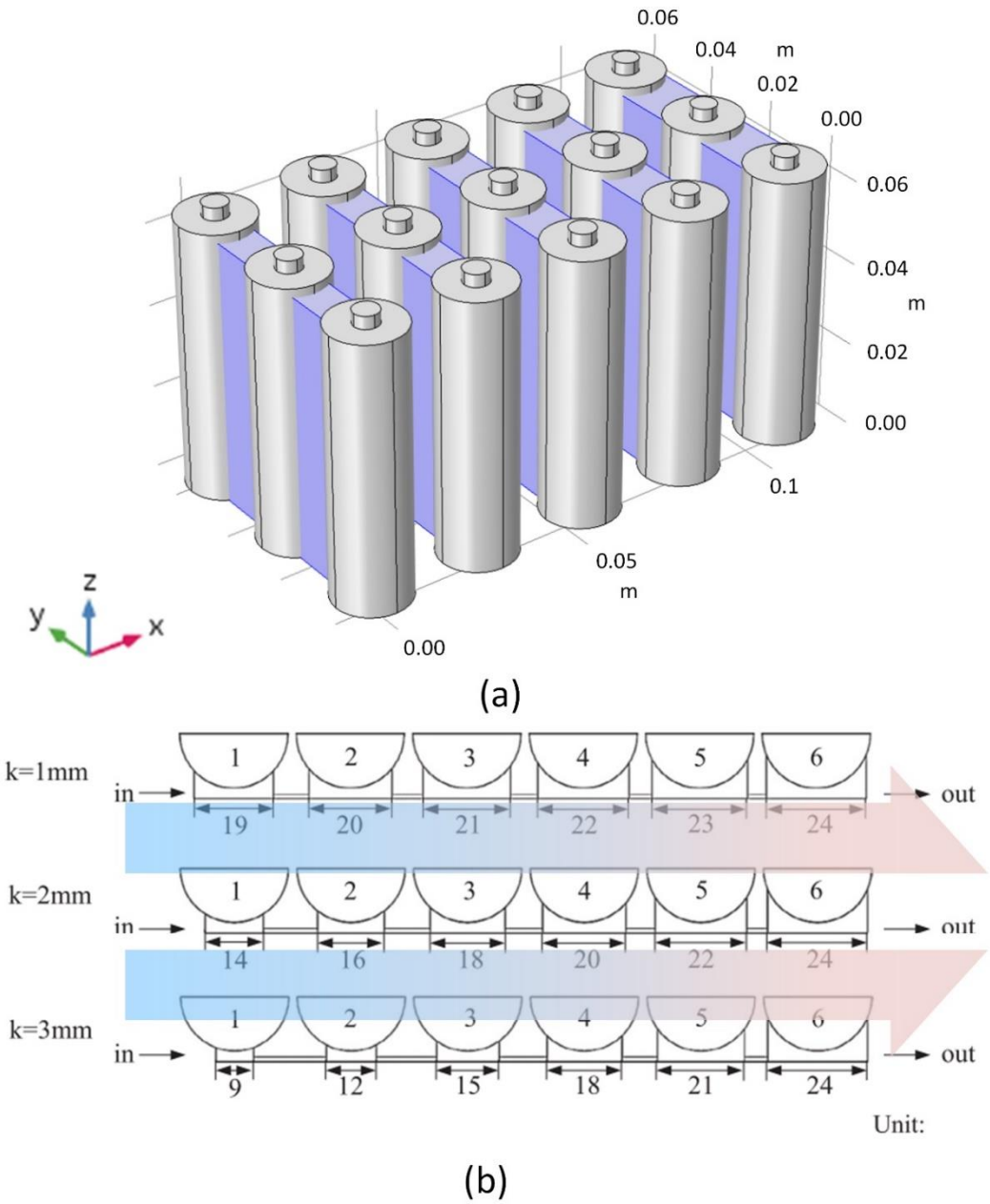

Figure 2.2 Variable contact area liquid based BTMS: (a) battery pack configuration and (b) different contact areas.

Rao et al. [64] proposed a novel liquid based BTMS, where the focus was on the cooling capabilities of the proposed system. The novelty of the proposed system based on Rao et al. is that the contact area, at which the heat is transferred from the battery to the coolant liquid is varied along the flow direction in the battery pack as shown in Figure 2.2. The coolant in the Rao et al. system flows inside cooling channels that receives the heat from the aluminum blocks that in contact with the batteries. The battery pack that was proposed by Rao et al. has six batteries along the flow direction of the coolant as shown in Figure 2.2(a).

Table 2.5. Summary of novel liquid based BTMSs for lithium ion batteries.

Liquid flow system	Novelty according to authors	Analysis method	Heat generation source	Battery type	Coolant material	Studied variables	Charging and/or discharging rate	Number of batteries in pack (simulated)	Ref.
With variable contact surface	Heat transfer area between batteries and coolant varies through the pack	CFD using ANSYS Fluent 14.5[a]	Modeling validated*	SONY 26650 (battery capacity 3 Ah)	Water (heat transfer block is aluminum)	-Aluminum block length (controls contact area) (k=1, 2, 3 mm) -Velocity of coolant flow (0.05, 0.1, 0.2 m/s)	3C	6 batteries along flow channel (3 [6 x 0.5])	Rao et al. [64]
Mini-channel cold plate	- Comprehensive investigation and simulation is conducted -k-ε model is used to simulate water flow in mini-channel	CFD -ANSYS ICEM for meshing -ANSYS Fluent (RANS model)	2D electrochemical model*	Large sized prismatic battery ($LiFePO_4$ 20.0 Ah)	Water	-Water inlet temperature (5, 15, 25ºC)	1C and 2C	Single battery (half with a symmetry boundary condition at center)	Panchal et al. [65]
Flow channels with aluminum conduction element	-Novel battery pack design -Developed a novel concept of thermal coefficient and demonstrated its efficacy	-Heat transfer model using StarCCM + 10.06.010*[a] - Electrochemical input by Battery Design Studio 10.06.010[b] -Supporting experiments	3D extension of the Pseudo 2D model (P2D)* [66–68]	Li-NCA/C 18650 (17.3 Ah)	Water (aluminum conduction element)	-Coolant flow rate (0.2, 0.02, 0.01 m/s) -Discharge current -Contact resistance (three cases)	0.6C, 0.9C, 1.8C, 2.7C	30 batteries with rows of 5 batteries (5)	Basu et al. [69]
Using liquid metal	First to use liquid metal as coolant in battery thermal management	Finite element methods using Fluent 6.3	Estimated by: $\dot{q} = 0.493\, I^2 + 0.2312\, IT$	Prismatic battery ($LiFePO_4$, 100 Ah, ZhongHang Li-ion Battery Co. Ltd, China)	Gallium (properties found in [70–72])	-Coolant material -Discharge rate -Coolant velocity	1C, 2C, 3C, 4C	24 batteries (2 [0.5 x 4])	Yang et al. [73]
Thermal silica plate	First to use thermal silica made plates as cold plates with embedded copper pipes	COMSOL*[d]	Calculated using $q = c_p m\, dT/dt$ and experimental results	Prismatic battery ($LiFePO_4$, 20 Ah)	Water	-Number of thermal silica plates (none, single side, double side) -Number of channels (1, 3, 5, 7) -Inlet flow rate (0.15, 0.25, 0.30. 0.35, 0.40) -Flow direction	Charged at 1C and discharged at 3C and 5C	Single battery and 2 silica liquid cooling plates	Wang et al. [74]

* Experimentally validated
a Maximum relative error in single battery temperature between the model and the experimental results is 2.4%
b Average error in temperature prediction is 0.2 K (less than 5%), maximum error is 0.5 K.
c Average accuracy of electrochemical model is 90%.
d Relative error did not exceed 0.6% of maximum battery temperature

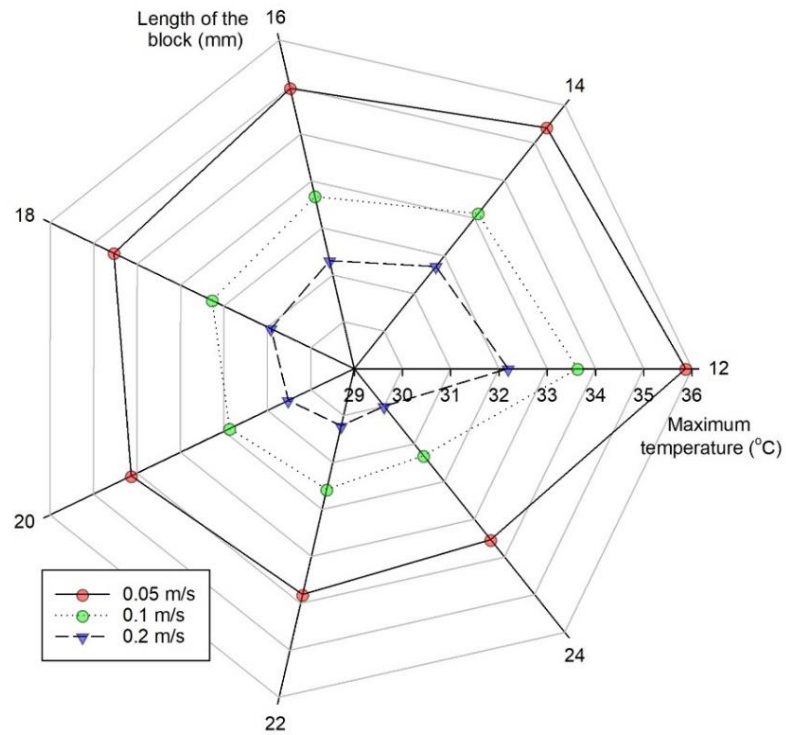

(a)

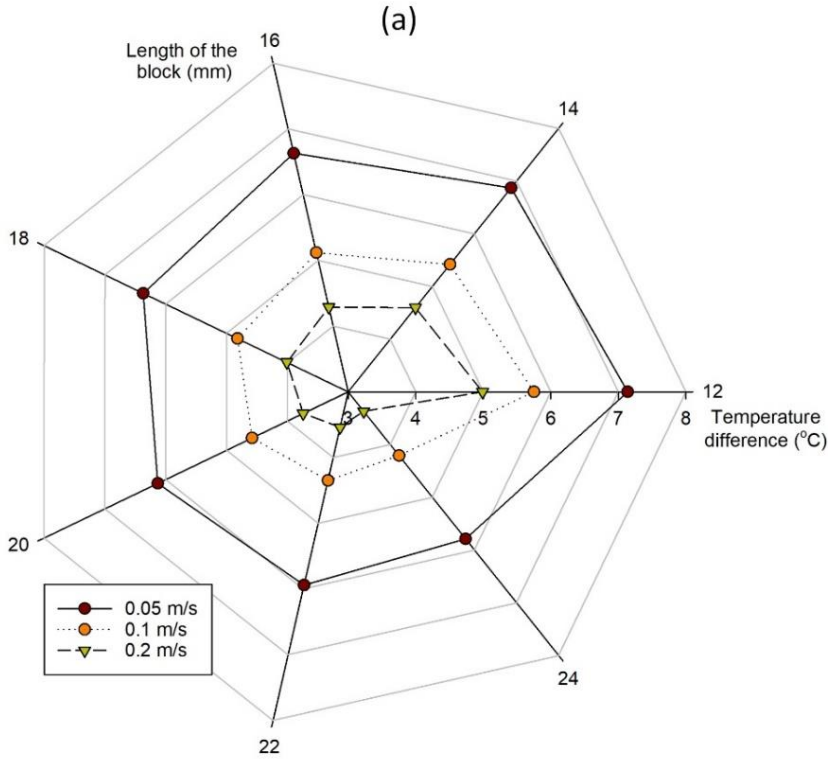

(b)

Figure 2.3 (a) Maximum temperature, and (b) temperature difference in the battery pack, for various coolant velocities and design parameter, the aluminum block length (data from Basu et al. [69])

In order to investigate the performance of their proposed system, Rao et al. simulated the proposed system on ANSYS Fluent 14.5, where the model was validated with experimental results at a discharge rate of 3C. Three different contact areas where considered as shown in Table 2.5. Rao et al. [64] reached to the conclusion that varying the contact area through the battery pack in the flow direction gives the battery pack higher temperature uniformity and lower maximum temperature at the same coolant flow velocity than the constant contact area packs.

The details of the results that Rao et al. reached with the different operating conditions that they considered are shown in Fig. 3. Where Fig. 3(a) shows the maximum temperature in the battery pack for various operating condition of coolant velocity and design parameter, the aluminum block length and Fig. 3(b) shows the temperature difference within the pack. Panchal et al. [65] investigated the thermal performance of the mini-channel cold plate system, with water as coolant for a large sized prismatic lithium ion battery. Panchal et al. [65] had previously considered the mini-channel cooling plate through extensive experimental and theoretical modeling [25,65,75,76]. The results of Panchal et al. [65] study was the following:

1- Increasing the discharging rate (C-rate) results in increasing the temperature distribution within the mini-channel cold plates.
2- Increasing the discharging rate (C-rate) results in increasing the temperature across the battery surface
3- The surface area closest to the electrodes had the highest recorded temperature across the battery surface.

Table 2.6. Basu et al. [69] investigated results of the BTMS three main variables.

Discharge current	Thermal contact resistance ($K.m^2/W$)	Coolant inlet velocity (m/s)	Total discharge time (s)	Maximum cell temperature (K)	Maximum heat generation rate (W)
0.9C	0.0025	0.01	3250	300.3	1.3
0.9C	0.0025	V	3250	$296.5 + (2.53\ V^{-0.0458})$	
1.8C	0.0025	0.01	1610	301.1	3.0
2.7C	0.0025	0.01	1065	303.1	4.0

Basu et al. [69] proposed a novel battery pack system that uses liquid cooling with an aluminum conducting element, where the method used was adapted from the heat pipe concept that is used for lithium ion pouch and prismatic batteries as shown in Fig. 4. Other advantages to the use of the conducting element is that it also acts as a separator between the batteries and the coolant, which avoids contact between the coolant and the electrical components in case of a failure such as a leakage in the coolant system. The geometric specification of Basu et al. system are: 1.5 mm thick aluminum conducting element, which are made of 44 mm height sheets, where the elements arms are separated with 11 mm and the cylindrical batteries are separated by 22 mm (measure between the centers of the neighboring batteries in each row) and the conducting elements are 38 mm apart [69]. The cooling channels are circular with a diameter of 9 mm housed in rectangular pipe with 3

mm flange thickness. As presented in Table 2.5, Basu et al. [69] investigated the effect of three system variables, where two are operating parameters and one is a design parameter. The first investigated variable was the discharge current, where they concluded that the cell temperature increases as the discharge current increases. With a starting battery pack temperature of 296.5 K, it was shown that the increase in the battery temperature can be approximated as having a linear relationship with the discharge rate. Where the other two variables were the coolant flow rate and the contact resistance. Note that for the thermal contact resistance three different values where considered, where the first is ideal case with zero contact resistance, the second case is having a thermal contact and the third is a normal contact resistance, the third case was also validated. The results of different combinations of these variables is presented in Table 2.6. As shown in Table 2.6, Basu et al. [69] presented the results numerically and xy plots for not all combinations of variables, where the results of the remaining combinations were presented in figures as shownin Figure 2.3. Figure 2.3 shows the effect the thermal contact resistance has on the temperature distribution through the batteries in the pack.

The results of various combinations of these variables are presented in Table 2.6. Basu et al. [69] results for the parametric studies they conducted for various operating and design parameters, including the length of the aluminum block are presented in graphically in Figure 2.3. Figure 2.3 is a web plot where each branch denotes a specific aluminum block length in mm, where the different shape and color points denotes different coolant inlet velocities and finally the inlet temperature varies throughout each branch in the plot. Figure 2.3 shows the geometry of the battery pack integrated with liquid and conducting element BTMS that Basu et al. [69] proposed. Figure 2.4 shows the effect the thermal contact resistance on the temperature distribution throughout the batteries in the pack.

Yang et al. [73] proposed the use of the liquid metal as a coolant to replace water in a liquid based BTMS. They concluded that, under similar flow conditions, higher temperature uniformity can be achieved in the battery pack with lower pumping power consumed when liquid metal is used compared to water. Other advantages of using liquid metal as a coolant are that it can handle large cooling loads in scenarios such as defects in cells, high power draws, and high environment temperatures. These advantages make it a promising option for BTMSs. However, a disadvantage associated with using liquid metal as a coolant is its high weight, due to the high density of liquid metals. Wang et al. [74] proposed a novel liquid based BTMS, where they also considered the vibrations and possible collusion between the batteries and the cold plates, which might leads to leakages. Wang et al. proposed the use of thermal silica made cold plates with copper pipes transporting the coolant (water) through the battery pack and thus cooling the batteries. One of their main goals is to avoid rigid objects collusion between the battery and the cold plate, and to take advantage of the high thermal conductivity of the silica plates.

The results of various combinations of these variables are presented in Table 2.6. Basu et al. [69] results for the parametric studies they conducted for various operating and design parameters, including the length of the aluminum block are presented in graphically in Figure 2.3. Figure 2.3 is a web plot where each branch denotes a specific aluminum block length in mm, where the different shape and color points denotes different coolant inlet velocities and finally the inlet temperature varies throughout each branch in the plot. Figure 2.3 shows the geometry of the battery pack integrated with liquid and conducting

element BTMS that Basu et al. [69] proposed. Figure 2.4 shows the effect the thermal contact resistance on the temperature distribution throughout the batteries in the pack.

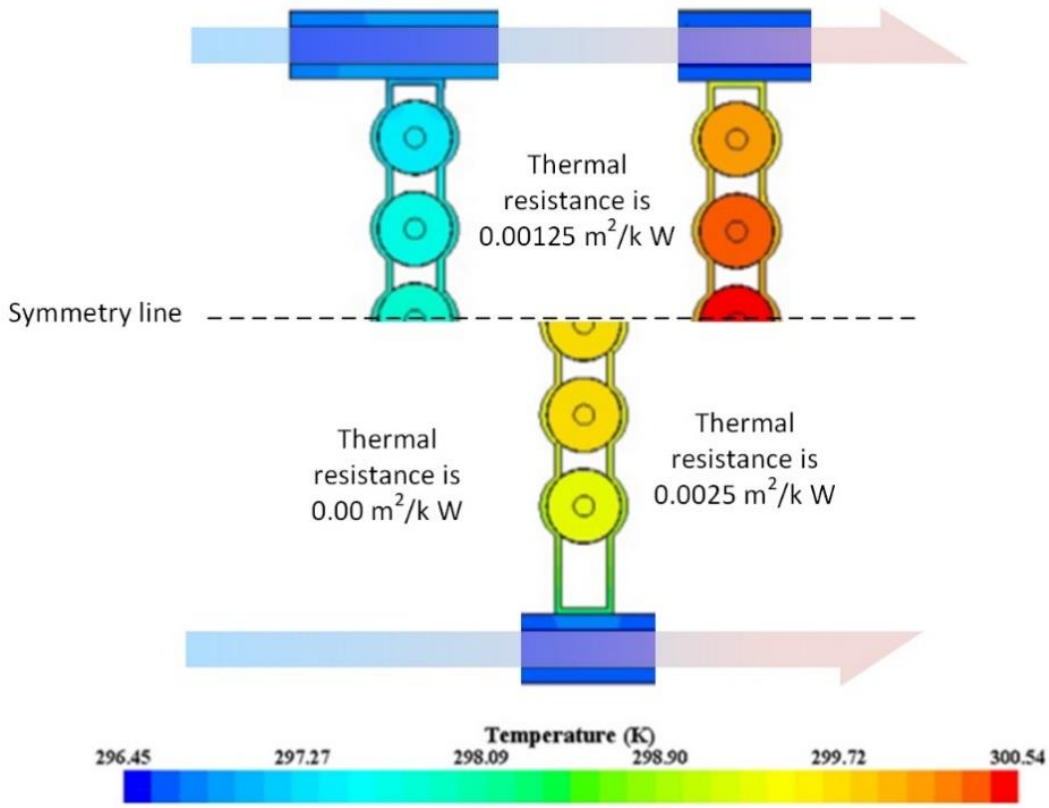

Figure 2.4 (a) Temperature distribution at several points in time through the discharging process. (b) Cross sectional view of the batteries in the pack during the discharging process for different thermal contact resistances at a constant discharge rate of 0.9C. (Modified from Basu et al. [69]).

Although BTMSs must be able to achieve optimum thermal operating conditions for the batteries to perform optimally, thermal runaway must also be controlled by the BTMS. Thermal runaway occurs when the temperature of the lithium ion batteries raise above the allowable operating conditions, which occur when the cooling system is unable to effectively remove the generated heat [6,77,78]. Xu et al. [79] proposed a mini channel liquid based cooling system that is designed on a battery modular level, where the proposed system performance was analyzed for sever conditions of internal short circuit. Internal short circuit in batteries can be the results of a manufacturing defects or/and vehicle collisions. Xu et al. [79] simulated a battery internal short circuit through employing nail penetration. Xu et al. concluded that their proposed system of mini channel cooling system was not able to cease the thermal runaway, however it was able to prevent battery fratricide, which results from the propagation of thermal runaway between the cells.

2.1.3 PCM based BTMSs

Liquid and forced air based BTMSs are active systems in which power assisted devices such as fan, compressor and pump are used to force the flow of the coolant through the battery pack [9,50,52,54,80]. Another type of management systems is the passive systems, in which the system is not supported with a power assisted devices and it does not require a control system to vary the system parameters to achieve the required cooling load [13,52,81–83]. An example on the passive cooling systems is phase change material (PCM) based BTMS. Although air and liquid based systems ware considered the most effective battery cooling methods, they have their drawbacks such as power consumption and complex system build up [84]. However, the passive PCM based systems have the advantages of large thermal energy storage and zero energy consumption. In the last decade many researchers have investigated the PCM based BTMS, where they performed experiments as well as simulations to assess the performance of such systems [85–88]. However, with the advantages the PCM based BTMS has, they have their own draw backs of low thermal conductivity and changes in the volume during phase change. One of the main methods that many researchers followed to overcome the PCM low thermal conductivity is adding to the PCM a high conductive material that will enhance the overall thermal conductivity of the BTMS, such as adding carbon fiber [89], carbon nanotubes [90], graphene [91,92], metallic foam/mesh [82,93] and metal particles [94]. Novel PCM based BTMSs were proposed to overcome the PCM low thermal conductivity of the PCM systems, where the most recently proposed are summarized in Table 2.7.

Zhang et al. [84] proposed a novel integration between a metal (aluminum) foam structure that houses a PCM (paraffin) , where the paper novelty was in proposing different metal foam structures and simulating it in a three dimensional model. Zhang et al. concluded that the use of a metal foam structure improves the overall thermal performance of the BTMS. Between the two metal foam structures, and with the porosity is constant for both having a larger interfacial surface area results in a better temperature uniformity in the battery pack. The metal foam flow resistance must be taken into consideration when designing the foam structure. Wu et al. [95] took advantage of both the large latent heat content of PCMs [83,96,97] and the high thermal conductivity of heat pipes [98,99]. Heat pipes were shown that they were able to provide a better cooling rate to the batteries better than the air and liquid cooling systems [100]. The integrated heat pipe and PCM based battery thermal management system that was proposed by Wu et al. is shown in Figure 2.5. Bai et al. [101] proposed a battery thermal management system that takes the advantage of the high cooling rate of liquid based cooling systems and the high temperature uniformity of the PCM based cooling systems, in what they refer to as PCM/water cooling plate system. Several design parameters were varied and their effect on the performance of the cooling system was investigated. The results showed that most of the heat generated by the battery was removed by the water that resides close to the battery electrodes, thus decreasing the battery maximum temperature. However, the PCM as shown in system schematic in Figure 2.5 was able to improve the temperature uniformity. Bai et al. proposed system was able to prevent thermal runway through the five continuous charge-discharge cycles.

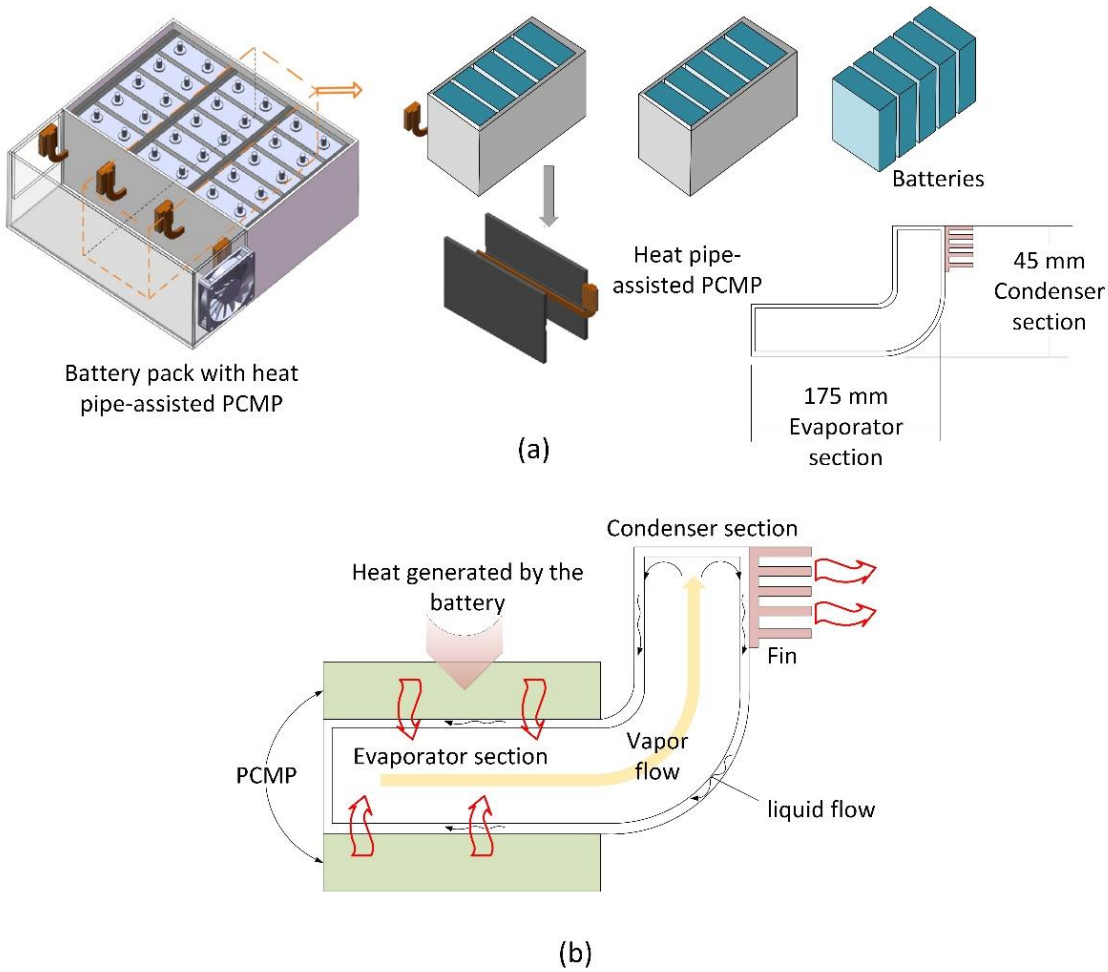

Figure 2.5 (a) Schematic diagram of the proposed battery pack design of Wu et al.; (b) working principle of the heat pipe and PCM integrated battery cooling system. (Modified from Wu et al. [95]).

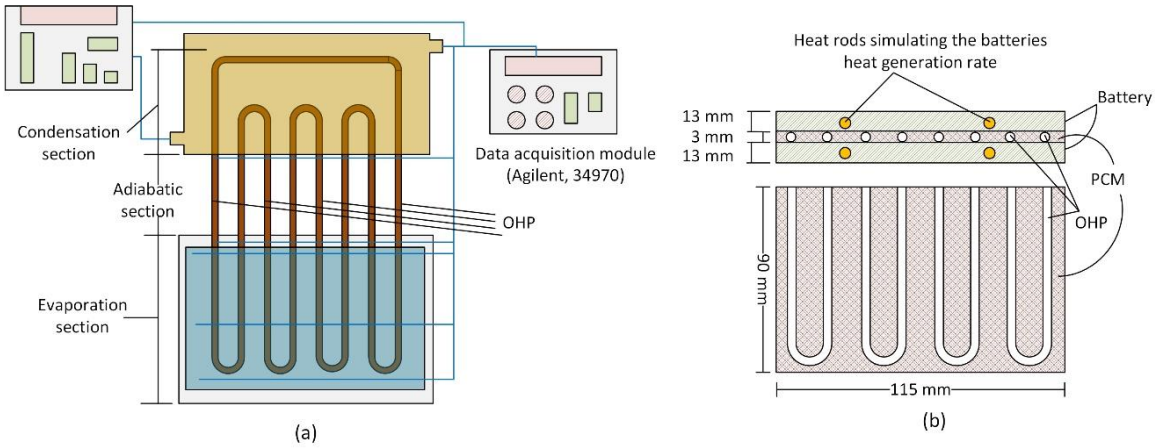

Figure 2.6 (a) Schematic diagram of the experimental setup used by Zhao et al. [98]; (b) working principle of the proposed oscillating heat pipes system. (Modified from Zhao et al. [98]).

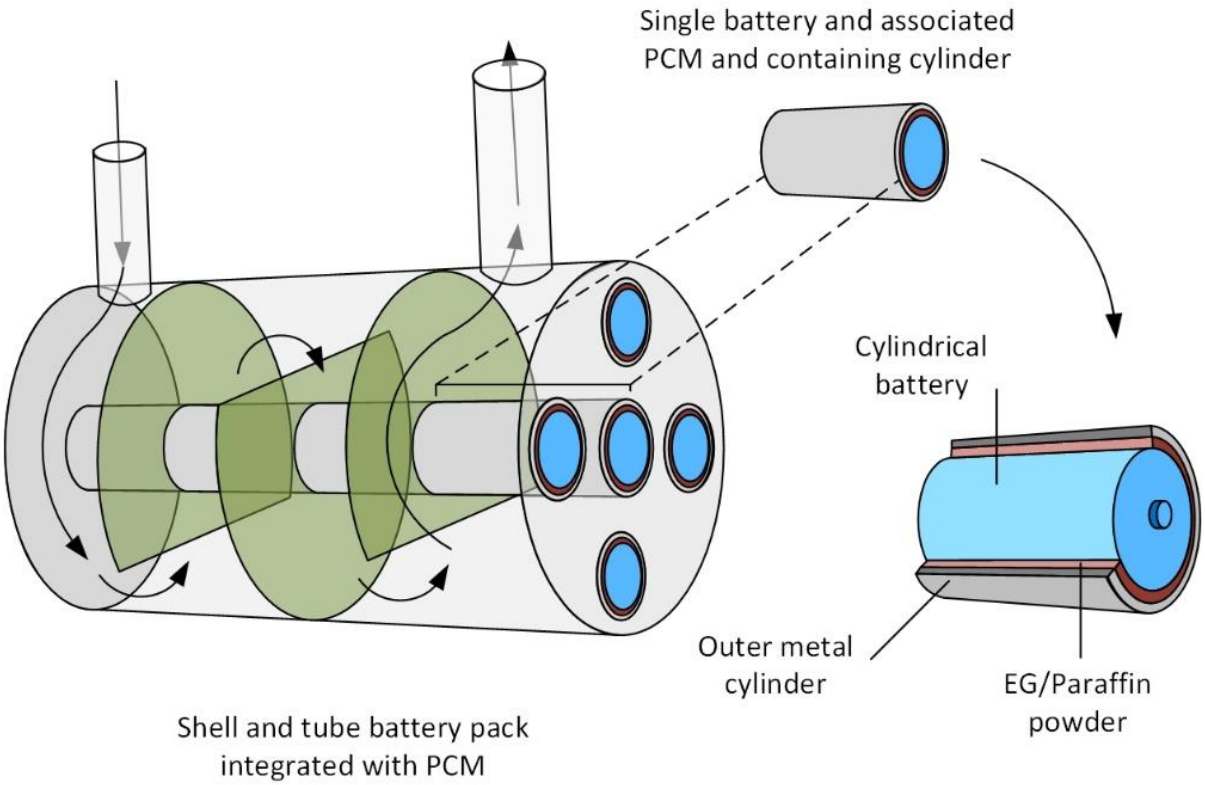

Figure 2.7 Schematic diagram of the integrated shell and tube heat exchanger integrated with PCM for cylindrical battery cooling.

Zhao et al. [102] investigated the performance of a BTMS coupled with a PCM and a heat pipe for cylindrical batteries. The coupled PCM and heat pipe system performed better than air based systems and PCM based systems for the same conditions. Zhao et al. reported a 33.6% reduction of the temperature difference by using PCM and a further temperature difference reduction can also be achieved through embedding the heat pipe into the PCM. The PCM with an embedded heat pipe is able to maintain a maximum temperature difference below 5°C for a longer period of time compared to air and PCM only based systems. Much of the research on PCM based cooling systems focused on integrating different cooling systems based on coolant type, as shown in Table 2.7. Most of the novel proposed PCM based BTMSs used paraffin wax as the PCM.

Figure 2.8 shows the variation of the melting temperature and the latent heat with the length of the alkanes paraffin straight-chain, for various materials. As shown in Figure 2.8 the melting temperature of the paraffin varies significantly with variation of the length of the main chain of the paraffin wax while only a small variation is observed in latent heat. Figure 2.8 The latent heat of the paraffin does not change notably as the length of the main straight-chain varies, which has led researchers to form paraffin composites in order to change its latent heat and thermal conductivity. Table 2.9 presents the thermal conductivity, latent heat and melting temperature of several composite paraffin based PCM.

Table 2.7. Summary of novel PCM based BTMSs for lithium ion batteries.

PCM system	Novelty according to authors	Analysis method	Heat generation source	Battery type	PCM	Studied variables	Charging or/and discharging rates	Number of batteries in pack (simulated)	Ref.
Composite PCM with open-cell metal foam skeleton	Designing a metal foam skeleton where PCM is embedded in the skeleton, and simulating it in 3D	Heat and mass transfer model simulated in COMSOL Multiphysics*	Constant heat flux		Paraffin (metal foam is made from aluminum)	-Metal foam skeleton design (two designs) -Use the metal foam (with and without) -Pore size			Zhang et al. [84]
Heat pipe assisted	Integration of heat pipes and PCM	Experimental with a battery testing system (BTS-50V120A-NTF, Shenzhen Neware Electronics Co. Ltd, China)	Experimental	Prismatic batteries (3.2 V/12 A h)	-Paraffin -Paraffin/EG	-Discharge rate -PCM -With and without PCM	1C, 3C and 5C (discharge)	Lab scale battery pack of five commercial batteries	Wu et al. [95]
PCM/water cooling-plate	Integration of liquid cooling and PCM cooling	A 2D network equivalent circuit [103]	2D electro-thermal model	$LiFePO_4$/C: -$170 \times 230 \times 12\ (\mathrm{mm}^3)$ -40 Ah	Properties: -$c_p = 2000 \frac{\mathrm{J}}{\mathrm{kg}}.\mathrm{K}$ -Latent heat = 247,000 J/kg - k = 0.151 W/m.K -$\rho = 778\ \mathrm{kg/m^3}$ -viscosity = 0.01kg/m.s	-Size of the cooling plate -Space between batteries -Mass flow rate Flow direction -Melting point of PCM	2C (discharge)	5 (1)	Bai et al. [101]
Tube-shell battery pack with composite PCM	Tube-shell Li-ion battery pack with a passive thermal management system using composite PCM	-Model*: using ANSYS FLUENT, where the meshing in GAMBIT - Experiments	Heat generation model proposed by Bernardi et al. [104]	Cylindrical lithium ion battery	Commercial paraffin wax (Rubitherm RT44HC) and EG as the promoter (composite with 16 wt.% EG)	Effect of baffles on improving heat transfer of air fluid	3C and 5C discharge	-25 in experiment $(1/2 \times 25)$	Jiang et al. [105]
Oscillating heat pipe assisted	Integrating a PCM with oscillating heat pipe	-Experimental (experimental setup is shown in Figure 2.6)	-Experiments where heating rods simulate the heat generation	Battery surrogates was used with a heating element	Paraffin with a melting point of 41 ± 1 °C	-Heating powers -Battery surrogate terminal direction -OHP[a] placement	Presented by the heating element power (20, 25, 30, 35 40, 45 W)	Stacked rectangular pack (2 batteries and one cooling PCM with oscillating heat pipe	Wang et al. [98]
Heat pipes	Coupling PCM with heat pipes	-Experimental setup with battery substitutes	-Experiments where heating rods simulate the heat generation	Battery substitutes cylindrical in shape	20% paraffin/EG composites	Refer to Figure 2.9	Presented by the heating element power (5, 10, 15, 20, 25, 30, 35, 40 W)	12 cylindrical batteries (12 tested experimentally)	Zhao et al. [102]
PCM with air cooling	Integrating PCM with air cooling that passes through porous structure -Unsteady mathematical model was developed	-Experimental and through an unsteady mathematical model	-Mathematical model* -Experiments	Lithium titanate battery, 2.3 V and 10 Ah with a thermal conductivity of 5.22 W/(m.K) (dimensions of 6.1 x 203 x 127 mm^3)	n-Eicosane with purity of 99% was	-Thermal resistance -Initial temperature -Melting temperature -Ambient temperature	2C, 3C, 4C charge/discharge rates	12 batteries and	Shi et al. [106]

* Experimentally validated
a Oscillating heat pipe (OHP)

Table 2.8. Systems and parameters used to investigate BTMS based on a heat pipe with PCM. (data from Zhao et al. [102]).

Configuration	Air velocity (m/s)
Air cooling	0, 4.3, 6.3, 9.3
PCM without heat pipe	0
PCM coupled with heat pipe	0, 2.3, 6.3 (passing through condenser of heat pipes)

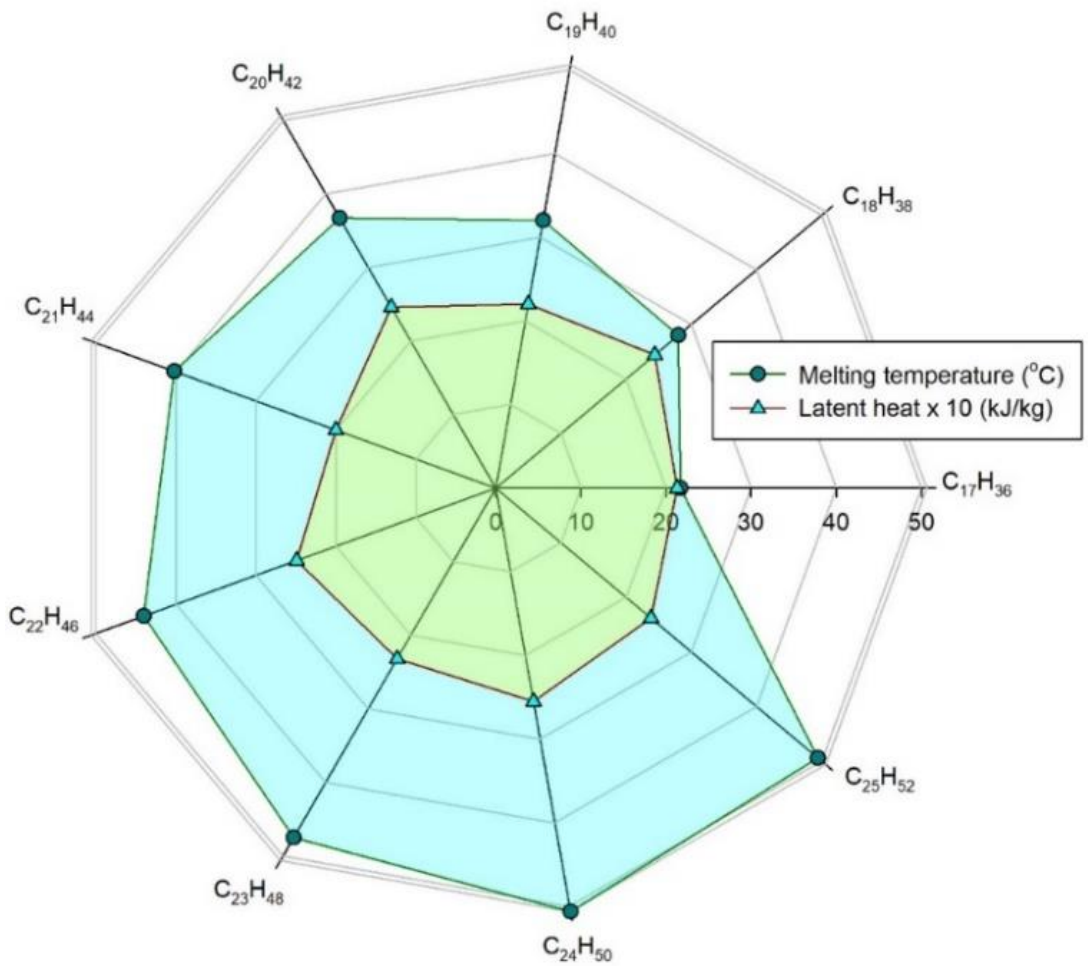

Figure 2.8 Variation of paraffin melting temperature and latent heat with length of the alkanes paraffin straight-chain, for various materials.

2.2 Closing remarks from the literature review

Battery performance is greatly affected by operating temperature, and the successful control of that temperature improves performance, ensures safe operation and extends lifespan. Please note that large portions of the text presented here in this chapter are taken from my published paper [107].

Table 2.9. Melting temperature, thermal conductivity and latent heat of various paraffin composites

PCM (additive mass fraction)	Melting temperature (^oC)	Thermal conductivity (W/m^2 K)	Latent heat (kJ/kg)	Ref.
Paraffin	46-48	$0.12 - 0.21$	173.4	Kandasamy et al. [108]
Paraffin/SFG75 composite (5%)	56-58	0.316 ± 0.005		Lachheb et al. [109]
Paraffin/SFG75 composite (10%)	56-58	0.409 ± 0.01		
Paraffin/SFG75 composite (15%)	56-58	0.569 ± 0.023		
Paraffin/SFG75 composite (20%)	56-58	0.906 ± 0.026		
Paraffin/graphite waste composite (5%)	56-58	0.289 ± 0.012		
Paraffin/graphite waste composite (10%)	56-58	0.342 ± 0.012		
Paraffin/graphite waste composite (15%)	56-58	0.383 ± 0.008		
Paraffin/graphite waste composite (20%)	56-58	0.428 ± 0.021		
Paraffin (75%)/PSC (25%)	56.3	0.387	165.16	Xiangfa et al. [110]
Paraffin (60%)/HDPE (40%)	68.3	0.28	51.59	Zhang et al. [111]
Paraffin (60%)/HDPE (20%)/APM (20%)	74.7	0.29	50.58	
Paraffin (60%)/HDPE (15%)/APM (25%)	81.5	0.34	51.70	
Paraffin (60%)/HDPE (20%)/APM (15%)/EG (5%)	68.8	0.51	51.10	
Paraffin (60%)/HDPE (15%)/APM (20%)/EG (5%)	73.6	0.85	50.58	
Paraffin (98%)/EG (2%)	41.1	0.40	192.6	Sarı and Karaipekli [111]
Paraffin (96%)/EG (4%)	41.0	0.52	188.0	
Paraffin (93%)/EG (7%)	40.7	0.68	181.9	
Paraffin (90%)/EG (10%)	40.2	0.82	178.3	

HDP: high-density polyethylene, APM: ammonium polyphosphate.

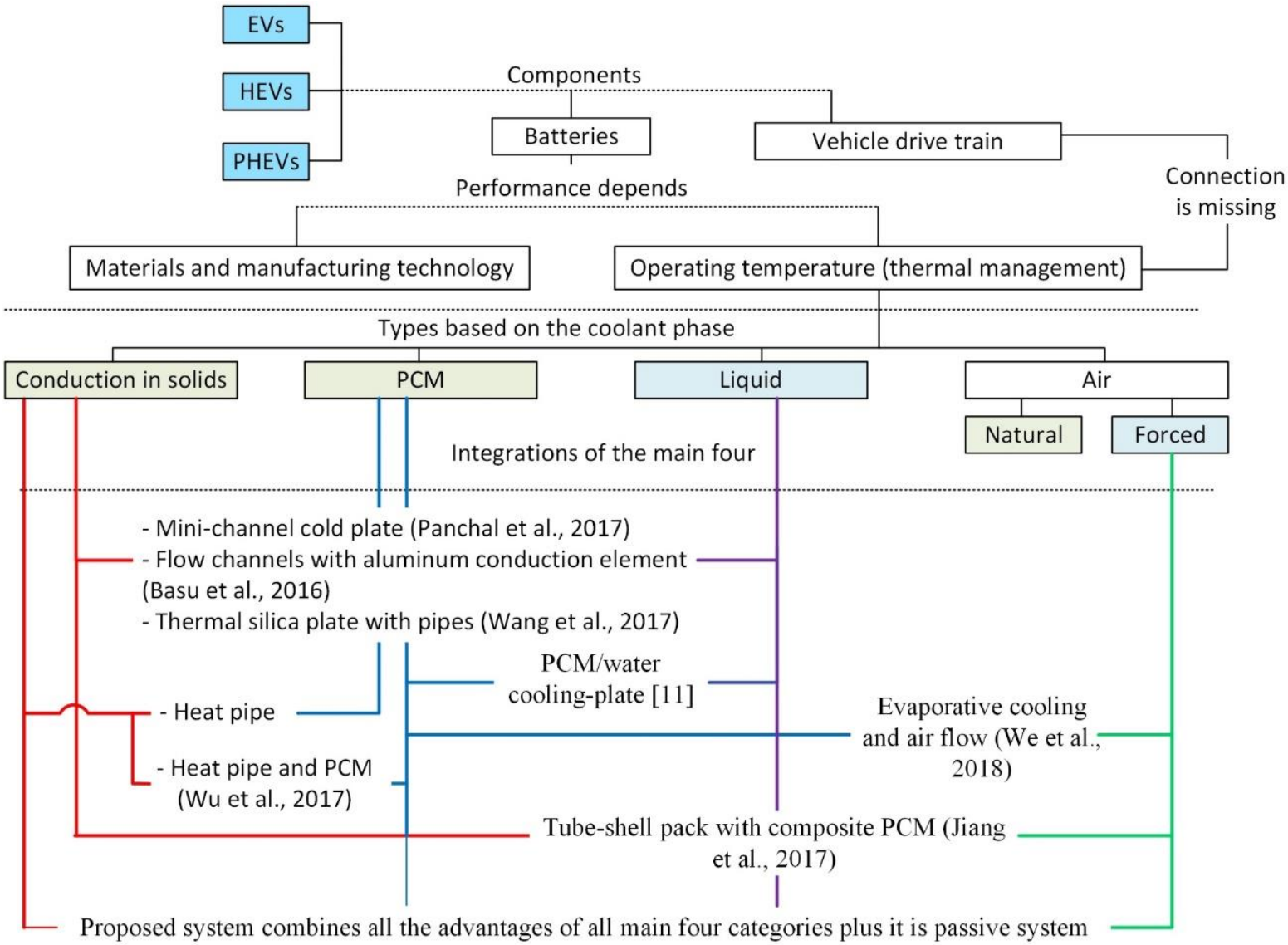

Figure 2.1 A schematic diagram summarizing the literature review on battery thermal management systems.

There are three main categories of battery thermal management systems (BTMSs): air, liquid and phase change material (PCM) based. Air based cooling systems are usually cheaper and more environment friendly during operation, but their cooling ability is less than that for liquid cooling systems such as those used in Tesla vehicles. However, liquid based BTMSs consume more energy than the other BTMSs, and use space within the vehicle for auxiliary components. PCM based systems have the advantages of being passive and requiring no power assisted devices. However, PCM systems have some disadvantages, including low thermal conductivity, and thus are often unable to remove heat from batteries when necessary. Researchers have focused on improving the characteristics and behavior of the three main BTMSs in various ways. Most of these studies have used simulation. This thesis summarizes in detail the latest BTMSs for each of the main types of BTMSs and also discusses a new category of BTMS that integrates it with the drive train. The novelty in air based BTMSs lies mainly in the air delivery method to the batteries in the pack, where the impact direction of the incoming air and the batteries has been the focus of many studies. The impact direction of the air is controlled mainly by proposing novel routes the air can follow into the pack with minimum pressure losses, although new configurations and arrangement of the batteries in the pack are also proposed. The results show that the impact direction is one of the main determining factors of the maximum temperature and temperature uniformity in the pack.

In liquid based BTMSs, the focus has been directed towards ensuring high temperature uniformity throughout the pack, by reducing the thermal gradient, which is formed in the flow direction of the liquid coolant. The type of coolant is one of the varied parameters, while other variations focused on controlling the contact area or heat transfer area between the coolant and the batteries. The goal of controlling the contact area is to ensure a lower contact area for the batteries at the start of the pack to those at the end, to ensure equal heat transfer rate for all batteries.

Overcoming the low thermal conductivity of PCM based systems has been a main focus of research on PCM based BTMSs. A wide variety of novel PCM integrations has been proposed, aimed at increasing the system's thermal conductivity. Variations in materials and use of composite heat pipes, solid meshes and integration with air and liquid based systems, are considered.

Finally, the literature review chapter is summarized graphically in Figure 2.9. Figure 2.9 starts with highlighting the fact all of the EVs, HEVs, and PHEVs share the same two main components, which are batteries and vehicle derive train. The performance of the batteries depends on both the battery material and manufacturing technology, and the battery thermal performance. The function of battery thermal management systems is to maintain the operating temperature of the battery within the optimum operation range. Figure 2.9 then categories the available battery thermal management systems into the main four system types developed in the literature. The categories are based on the nature of the coolant. For each of these BTMSs main advantages and disadvantages are listed within the schematic. In the literature these categories were combined in novel systems to achieve a better performance and these systems are presented graphically with line connections between these systems. Finally, the graphic connects the drive train of the vehicle with the cooling system and highlights the gap in the literature and how it can be fixed.

Chapter 3: Development of Systems

The focus of this chapter is to describe the various proposed designs of the novel battery thermal management systems, which were summarized in the objectives of the thesis. The proposed system will be divided into two main categories. The first category is for those proposed systems that are vehicle specific. A vehicle specific system is a system where the proposed battery thermal management system is an integrated part of the specific vehicle type drive train. The second category of proposed battery thermal management systems are those who are independent on the vehicle drive train and that they can be used in all applications were the thermal performance of the battery needs to be controlled.

In this chapter, five battery thermal management systems are proposed and their novelty and working principle are explained in details. There are five different proposed systems, where some of them are based on the concept of single phase flow through either cooling channels or directly through the battery, while others are based on two phase flow and a heat transfer medium between the coolant and the battery. Others are based on a static boiling pool that can either have a direct contact with the batteries or have a heat transfer medium. Others will be passive in their cooling while others are active, where also the active systems a passive case study is considered for them. The five proposed battery thermal management systems are summarized in Table 3.1. These systems are proposed and developed to accommodate the different types of HEVs that have the possibility of using their fuel as a coolant and also uses the novel BTMSs category proposed in this thesis in both HEVs and EVs.

Table 3.1. Summary of the five main proposed systems based on coolant type, and its applicability to work in EVs and HEVs.

System	Coolant	Applicable for EVs	Type of HEVs	Detailed description is presented in section
1	H_2	No	Fuel cell HEV	3.1.1.1
2	NH_3	No	Future NH_3 fueled HEV	3.1.1.2
3	Air	Applicable[1]	Pneumatic HEV	3.1.1.3
4	Propane		Propane fueled HEV	3.1.2.1
5	R134a[2]	Applicable for all	Applicable for all	3.2

[1] For EVs that uses a compressor to achieve the required air flow rate, or natural due to the movement of the vehicle
[2] The type of refrigerant can also be varied

While having Table 3.1 describing the different proposed systems in this thesis, where they are summarized in terms of the coolant, applicability of the cooling system to the vehicle category, and which specific vehicle category it works for. However, more details on each system is provided next including the systems properties and specifications are presented next. Note that I was able to publish many of the proposed system in this

thesis as can be found in the following references [11,107,112–116] and thus portions of these papers are used in this chapter and following chapters.

3.1 Dependence on the Vehicle Drive Train

As mentioned part of the introduction of this chapter, the following section groups the proposed battery thermal management systems that are an integrated part of the vehicle drive train. Having the proposed system as an integrated part of the vehicle drive train makes it dependent on the drive train components, such as the type of fuel used. This section will include subsections that discuss each proposed system and specify the vehicle drive train specifications on which the proposed system is dependent. Usually vehicle drive train specific systems are proposed for HEVs, where they are designed to recover energy losses and insure effective, efficient, and safe thermal management system.

3.1.1 Carbon free fuel as refrigerant

This section presents the proposed battery thermal management systems that are part of the vehicle drive train specific systems. These systems are specific for HEVs that runs on carbon free fuels. The carbon free fuels that are considered are hydrogen and ammonia. Hydrogen fueled HEVs are usually called fuel cell vehicles, since the hydrogen is converted into electrical energy by oxidizing the hydrogen in the fuel cell. Fuel cell vehicles are available and sold commercially by Toyota, where the fuel cell vehicle is Toyota Mirai. Other carbon free fuels such as ammonia, which is often used as a chemical medium to store hydrogen in more compact and cost effective way. HEVs that are fueled with ammonia are still in the research and development stage, however research publications are showing a very promising performance [117,118].

The next subsections provide more details on the proposed battery thermal management systems and how they are specific for different HEVs drive train. The subsection will start by providing a brief description and literature review on the type of the vehicle that the specific BTMS is designed for, and why such cooling system is required. Then the proposed cooling system (BTMS) is described in details including the working principle and how it is better and different than currently operating systems and how its performance and the working principle of the cooling system and how it is integrated with the drive train of the HEV.

3.1.1.1 System 1

The recent development and launch of the hydrogen fueled HEV by Toyota, which called Mirai [119], has shown its advantages over the fossil fuel based HEVs and EVs. However, in hydrogen fueled HEV, fuel cells are supported with batteries in order to aid the fuel cell during acceleration and achieve more smooth driving experience. However, the batteries in the hydrogen vehicle, requires cooling to maintain safe operation and high performance. Since most of the studies in the literature were concerned with the cooling performance of the BTMSs, rather than their heating abilities, since the heat function of the BTMS is often provided by an electrical heater, this system will propose a BTMS, however the focus will be directed towards the system cooling abilities.

BTMS configuration for prismatic battery pack

The proposed system uses the fuel of the fuel cell vehicle or hydrogen fueled vehicle to cool the batteries, where the hydrogen is later injected into the fuel cell. The compressed

hydrogen is passes first through the expander, which will lead to power generation, reduce the pressure of the hydrogen leading to a low temperature hydrogen that is ready for battery cooling. Since the temperature of the hydrogen coming out of the expander might be very low for cooling batteries, i.e. it might cold shock the batteries, it is assumed that the connecting channels between the expander exit and the inlet to the pack are long enough to heat it up.

The hydrogen fueled HEV carries highly compressed hydrogen, which is throttled down to the operating temperature of the fuel cell, where it is used to produce electrical energy to run the electric motors and drive the vehicle or charge the batteries. The hydrogen is usually stored in high pressure cylinders, with pressure reaching around 700-875 bar and a total of 5 kg of hydrogen for Toyota Mirai [120]. However, the fuel cell operating pressure is usually selected to be 2 bar and an operating temperature within the range 30-80°C, which leads to a fuel stack overall energy and exergy efficiencies of 43.0% and 43.8% respectively at an exchange current density of 1150 A/cm^2 [121]. To achieve the fuel cell stack required performance, hydrogen is usually throttled down from the tank pressure to the operating pressure of the fuel cell. However, fuel cell vehicles such as Toyota Mirai also uses batteries to achieve the required vehicle performance such as high rates of accelerations since the fuel cell dynamic response is slow compared and they are usually running on a constant power. Running the fuel cell on constant power means that for accelerations or other high power demanding activities the batteries are used to supply the surplus to the power generated by the fuel cell stack. Also the batteries are charged with the excess power for cases where the required power load is less than that generated by the fuel cell stack. Batteries in the fuel cells are also used to benefit from regenerative breaking. Through the operation of the fuel cell vehicles, the batteries are charged and discharged at different stages. When batteries are charged and discharged, they generate heat, which will cause the operating temperature of the batteries to raise unless the generated heat is removed. This thesis propose a hydrogen based cooling system for fuel cell vehicles. The proposed cooling system uses a turbo expander to reduce the pressure of the hydrogen from the tank pressure to the operating pressure that will results in the required hydrogen velocity through the battery pack. The expanded hydrogen leaves the expander at a very low temperature, which is then fed to the battery pack cooling system, which heats up while cooling the batteries in the pack to maintain its operation temperature within the optimum operating conditions. The heated hydrogen exiting the battery pack is either fed directly to the fuel cell stack or stored temporary in a storage tank before it is fed to the fuel cell stack. A schematic presentation of the hybrid fuel cell vehicle that is integrated with the proposed cooling system is shown in Figure 3.1. Having the hydrogen slightly heated above the ambient temperature as it is fed to the fuel cell achieves the required operating conditions, according to Ezzat and Dincer [121].

Figure 3.2a shows a schematic diagram of a prismatic battery pack integrated with the proposed cooling system including the overall dimensions of the battery pack. In the battery pack, the prismatic batteries are arranged to have a consistent arrangement of two batteries followed by a hydrogen cold plate.

The cold hydrogen (the hydrogen exiting the turbo expander) enters the battery pack from the bottom right corner as shown in Figure 3.2a, where it fills the supply channel with a pressurized cold hydrogen. The cold hydrogen flow through the cold plate, where it

cools the battery and gets heated. Note that there is no direct contact between the cooling hydrogen and the battery at any point through the cooling process, where aluminum cooling plate is used to conduct the heat between the hydrogen and the battery as shown in Figure 3.2b. The heated hydrogen is collected in the collection channel located on the top left corner of the battery. The heated hydrogen is carried through the collection channel to outside the battery pack, where it then sent to the intermediate or temporary storage tank shown in Figure 3.1. The hydrogen cold plate, where the hydrogen flow inside it is made of aluminum with thickness equal to the thickness of single prismatic battery, which is 7 mm. Where the overall dimensions of the considered prismatic li-ion battery are shown in Fig. 2b are based on the prismatic battery considered in Chen et al. [103].

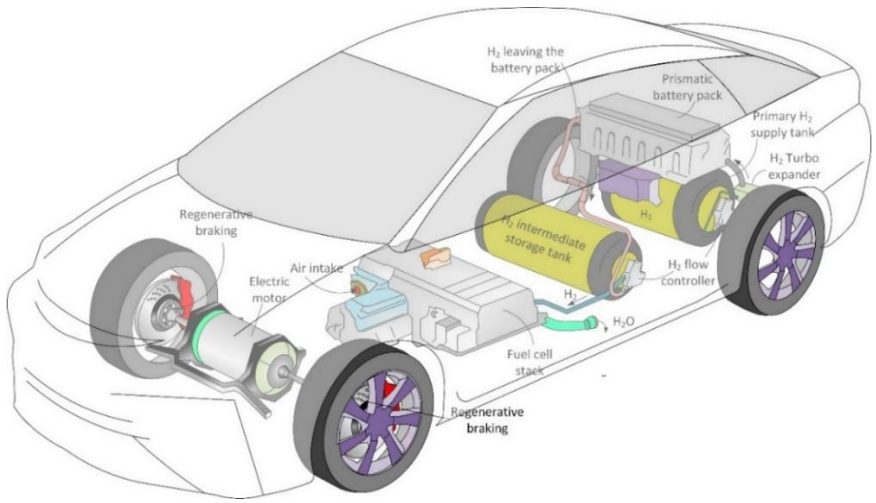

Figure 3.1 Schematic of the fuel cell based hybrid electric vehicle equipped with throttled hydrogen battery cooling system (note that the location of the vehicle drive train component are based on Toyota fuel cell vehicle Mirai [120]).

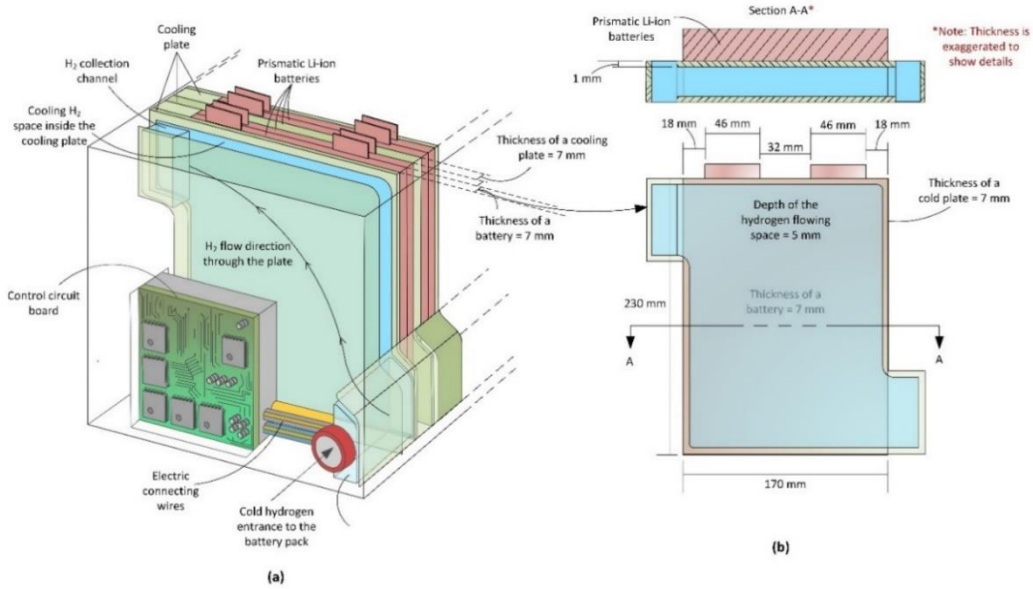

Figure 3.2 (a) Schematic diagram of the hydrogen cooled based cooling system for fuel cell vehicles and (b) overall dimensions of the considered prismatic battery.

Regarding the design of the cooling plate of the hydrogen cooled battery pack, five different designs were considered by changing the volume of the cooling hydrogen channel in the cooling plate. First the five generated designs aim to vary the contact time of the cooling hydrogen and the different parts of the battery through the thin aluminum cooling plate. Where the aim is to reduce gradually with different design the contact time between the hydrogen and the battery at the location were the cooling hydrogen enters and increase it at the exit of the cooling plate. The different designs were simulated for the highest battery heat generation rate for a 300 seconds of discharging and 300 seconds of charging at a current rate of 4C in a steady state conditions. A charging current of 1C will be able to completely charge an empty battery in one hour, and a discharging current of 1C will completely discharge a fully charged battery in one hour, where the battery capacity is 1Ah. Regarding the operating conditions, the hydrogen temperature entering the battery pack is varied through the varying the exit pressure of the turbo expander and insulation of the hydrogen pipe to heat up the hydrogen from the surrounding environment (assumed constant at 25°C).

BTMS configuration for cylindrical battery pack

This section will propose a battery pack integrated with a cooling system that utilizes the cold hydrogen that is produced when the highly compressed hydrogen in the fuel tank is reduced to the fuel cell operating pressure. Where the cold hydrogen will be used to maintain the operating temperature of a cylindrical battery pack within the optimum operating range. The design will have to accommodate the nature of the arrangement of the cylindrical batteries in the pack.

The proposed design will be designed to avoid the cooling hydrogen in having a direct contact with the batteries. Such configuration can be developed to have a heat exchanger between the cold hydrogen and forced or natural flow of air. The air exiting the heat exchanger will be at a cold temperature enough to cool the batteries to a temperature within the optimum operation range.

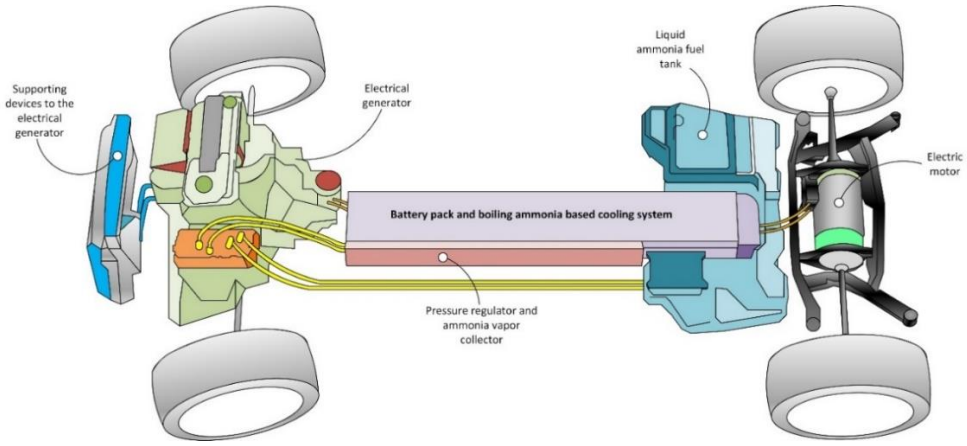

Figure 3.3 Schematic diagram of ammonia based hybrid electric vehicle, for which the proposed boiling ammonia based cooling system is simulated. The electrical generator presented here is any device that can convert the ammonia vapor to electrical energy, for example with the ammonia fuel cell proposed in [28] or with internal combustion engine as proposed in [26,27].

3.1.1.2 System 2

These type of systems are proposed as novel PCM based battery thermal management system design, in which the phase change material is ammonia. The PCM changes phase from liquid to vapor by absorbing part or all of the heat generated by the battery. The performance of the proposed design is assessed in terms of the thermal characteristics of the lithium ion batteries in the battery pack. The proposed system is intended for the use in future hybrid electric vehicles that use a carbon free ammonia as a fuel.

Such vehicles are intended to be environmentally benign and are under development and investigation at the University of Ontario Institute of Technology [117,122,123]. The proposed system has advantages of liquid cooling systems, in terms of high heat transfer rate, the air cooling systems, in terms of not requiring supporting systems to reject heat and reuse the coolant, and typical phase change systems, in terms of constant phase change temperature

BTMS configuration for prismatic battery pack

Figure 3.3 shows a schematic diagram of a future ammonia based HEV. The ammonia fuel is converted to electrical energy to either drive the vehicle, contribute to the overall electrical requirements of the vehicle or charge the batteries. In the proposed BTMS, liquid ammonia from the vehicle tank is sent to the battery pack where it absorbs the heat generated by the batteries and produces ammonia vapor.

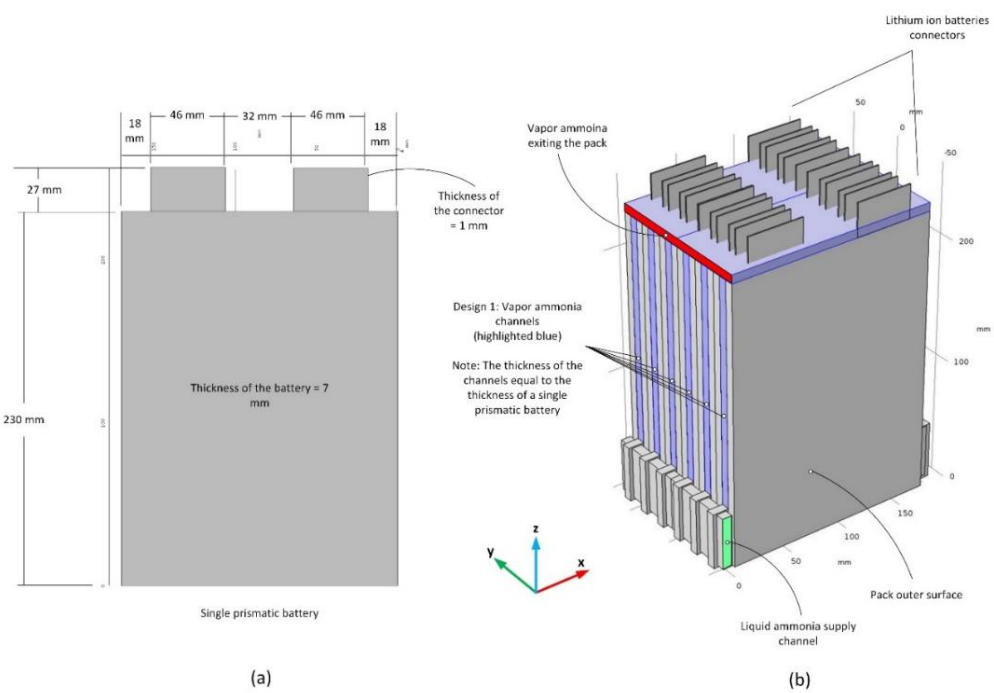

Figure 3.4 Schematic of (a) considered prismatic battery including its dimensions, and (b) design of the battery pack integrated with the proposed ammonia based cooling system.

The vapor ammonia produced by the boiling is collected through a pressure regulator and a vapor collection system, where the vapor is sent to the ammonia fueled based electrical generation system. The ammonia based electrical generation system can

be for example ammonia fueled internal combustion engine or ammonia fed fuel cell system based HEV proposed by Ezzat and Dincer [117]. The proposed system working principle is illustrated in Figure 3.4 where a pool of liquid ammonia is either in direct or indirect contact with the surfaces of a battery in the pack. The batteries are arranged so that after each two batteries there is a cooling space where the ammonia pool is located and the ammonia vapor is allowed to travel upward through the pack. The proposed system is based on pool boiling of liquid ammonia, where the batteries are partially submerged in the boiling ammonia pool. The ammonia pool boils by absorbing the heat generated by the battery, cooling the battery and releasing ammonia vapor. Due to gravity and the pressure regulator and vapor ammonia collector device, the ammonia vapor travels up the pack cooling the uncovered part of the battery. The vapor ammonia is collected and then sent to the ammonia electrical generator, which produces electrical energy that is used to charge the batteries, drive the electrical motor, or supplement the electrical power coming from the batteries for driving the vehicle. Figure 3.4(a) illustrate how the internal structure of the ammonia based HEV is connected and how the ammonia from the fuel tank is sent to the battery pack to cool them and the generated vapor is sent to the fuel vehicle engine. Figure 3.4(b) shows the overall dimensions and geometry of the proposed boiling ammonia based cooling system, which are adapted from Chen et al. [103]. It is seen in Figure 3.4(b) that the produced ammonia vapor leaves the pack from one of the sides of the pack. Also, the design of the proposed battery pack and cooling system shown in Figure 3.4 is observed not to depend on a specific number of batteries in each pack and instead to be very flexible.

BTMS configuration for cylindrical battery pack

Figure 3.5 shows a future ammonia based HEV vehicle that runs on using heat from ammonia combustion and electrical energy stored in batteries.

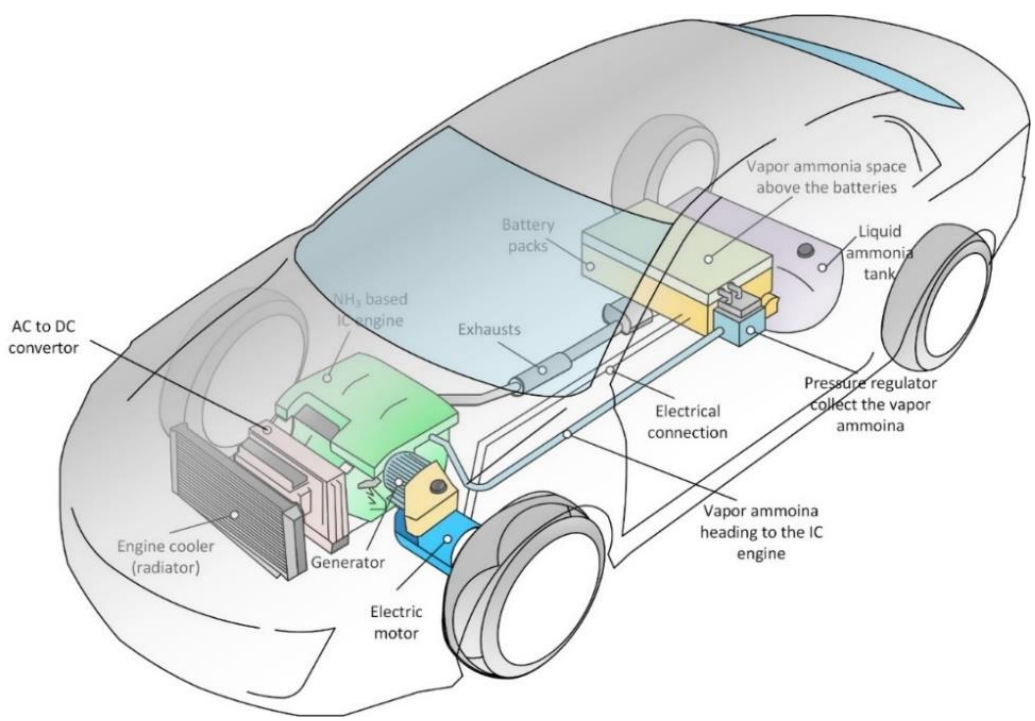

Figure 3.5 Schematic diagram of the ammonia based future hybrid electric vehicle in which the proposed boiling based battery cooling system is employed.

In the proposed battery thermal management system, the pressurized liquid ammonia is used first to maintain the temperature of the battery in the optimum operation range, by absorbing the thermal energy generated by the batteries and evaporating. Then, the ammonia vapor is sent to the ammonia internal combustion engine (IC). The IC engine with an electrical generator produces electrical power, which is either stored or used directly to drive the vehicle via the electrical motor. In HEVs, and EVs the lithium ion batteries are grouped in packs. The proposed pressurized ammonia based battery cooling system is shown in Figure 3.6(a). Cylindrical 18650 lithium ion batteries are used here, arranged in a rectangular pattern and partially submerged in pressurized saturated liquid ammonia (PSLA). The PSLA absorbs the heat generated by the cells as it evaporates, maintaining the temperature of the battery. The heat generated by the battery cells are removed by ammonia via two heat transfer modes: boiling (for the area of the battery covered by PSLA) and forced convection (for the ammonia vapor transferring heat from the unsubmerged part of the battery). The evaporation of the PSLA generates ammonia vapor that flows along the uncovered part of the battery and cools it. It then passes through a pressure regulator and into a collection tank. After a specific amount of ammonia vapor accumulates in the collection tank, the ammonia vapor is then sent to the IC engine, which generates electrical power. Figure 3.6(b) provides the dimensions of the battery pack shown in Figure 3.6(a).

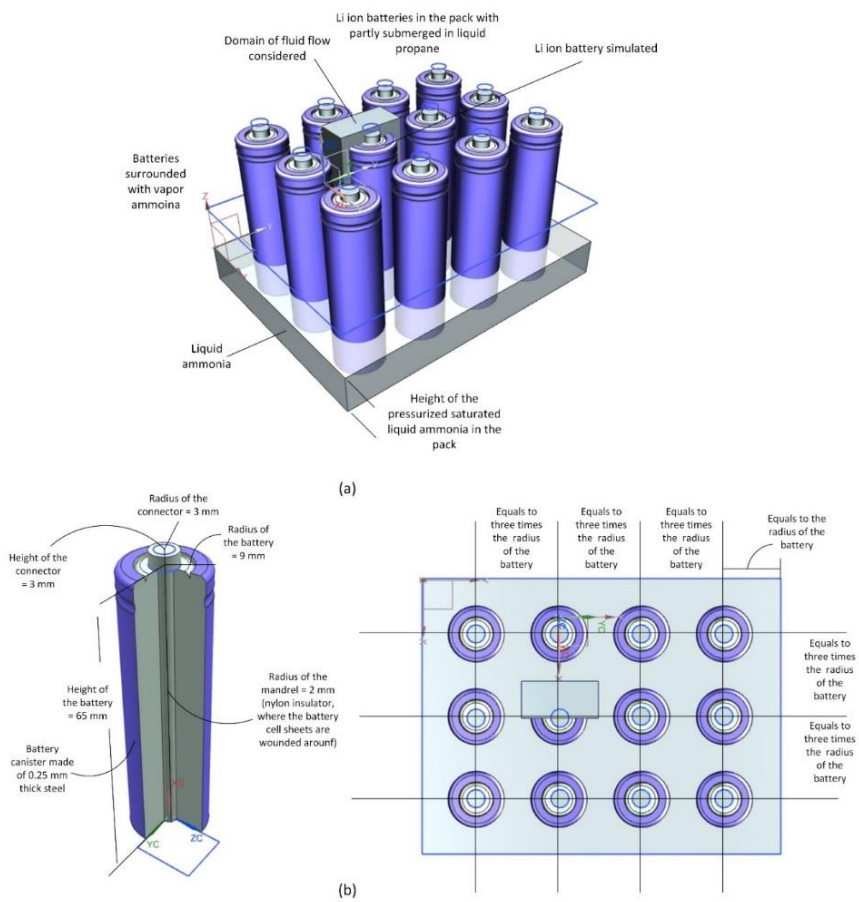

Figure 3.6 PSLA for cylindrical pack design, (b) dimensions of the thermal management system and the battery.

3.1.1.3 System 3

In the process of providing alternatives to the conventional fossil fuel vehicles. Alternative vehicle systems are electric vehicles (EVs), which are fuelled with electrical energy recovered from batteries, and pneumatic vehicles are fuelled with work produced when the compressed air pressure is reduced through a turboexander. However, due to the driving range limits of EVs and pneumatic vehicles, hybrid electric vehicles (HEVs) were introduced to reduce the overall harmful emissions and achieve longer driving range than EVs and air based vehicles. An air based HEV is a promising technology, in which pneumatic motors and electric motors fuelled with compressed air and batteries receptivity was proposed in the literature. In air based HEVs, batteries are often cooled using battery cooling system similar what is being used in EVs, which often reduces the vehicle performance due to the energy and space consumption by such systems. This thesis proposes a new novel battery cooling system, in which the batteries are cooled by the expanded compressed air through the pneumatic motors. The proposed system saves energy and space by taking advantage of the drive train of air based HEV.

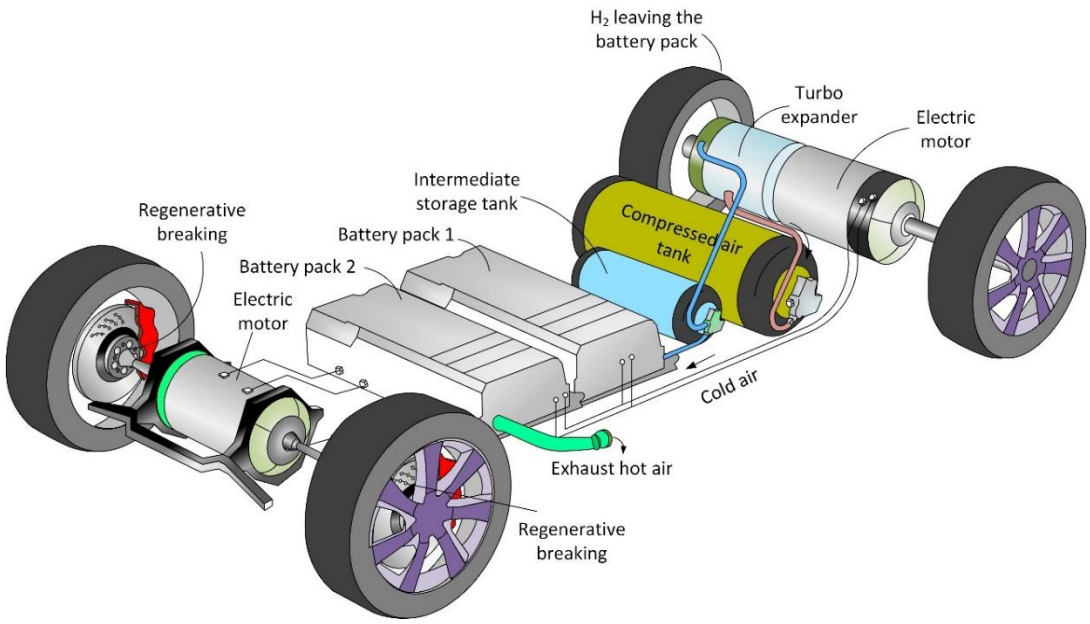

Figure 3.7 Schematic of the pneumatic hybrid electric vehicle where the compressed air is used to partially power the vehicle and provide cool air to the battery cooling system.

The pack will be designed to utilize the cold air supplied from the turboexpander, which generate a driving power to drive the vehicle. In this section two different proposed design will be applicable for both battery packs of prismatic and cylindrical batteries. Note that the battery pack design for both the prismatic and cylindrical cooling are those the same developed and optimized for the hydrogen cooling system where the reader can refer to section 3.1.1.1 for more details. Note that the results of the air system will be presented in the conclusion and the results and discussion with the hydrogen forced flow system.

3.1.2 Fossil fuels as refrigerant

HEVs such as Chevrolet Volt uses gasoline as the fuel part of the hybrid system, other HEVs uses different types of the fossil fuels, such as propane. Propane and other fossil

fuels have a phase change temperature around an ambient temperature at moderate pressures. This advantage will help in reducing the energy consumption caused by the cooling system and save space while achieving a better performance. This section will propose various battery pack designs that will utilize the vehicle fuel in cooling the batteries; later they are consumed by the engine to produce power.

3.1.2.1 System 4

In this section, PCM based battery thermal management systems are proposed, where the PCM is propane and phase change occurs between the liquid and vapor phases, is evaluated for cooling prismatic lithium ion batteries. The cooling system that utilizes propane is proposed for HEVs that use propane as an energy source along with electrical energy supplied by the batteries. Having the PCM change phase from liquid to vapor results in a much higher heat transfer coefficient compared to air and liquid cooling systems; thus the PCM based cooling system has the advantage of the high heat transfer coefficient of liquid systems and the simplicity of air systems. The high heat transfer coefficient is due to the pool boiling of the propane to cool the batteries. The propane vapor is later collected and used to produce electrical power through the internal combustion engine part of the HEV, reducing the overall vehicle emissions significantly.

BTMS configuration for prismatic battery pack

The propane based HEV uses the propane vapor as the fuel feed to the internal combustion engine to produce electrical power, for either charging the batteries or direct use in driving the vehicle by with the electric motor. The propane based HEV is shown in Figure 3.8, where the prismatic battery pack is seen to be located close to the pressurized liquid propane tank. In the proposed battery thermal management system, saturated liquid propane is used to maintain the temperature of the batteries in the pack within the optimum operation temperature range by absorbing thermal energy generated by the batteries and evaporation.

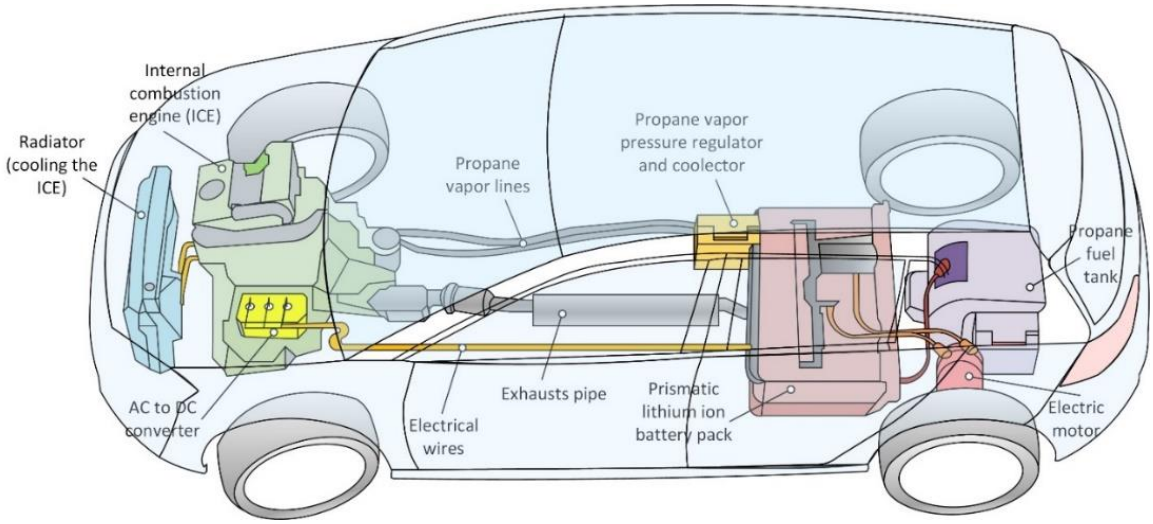

Figure 3.8 Schematic of the propane based hybrid electric vehicle equipped with boiling based battery thermal management system.

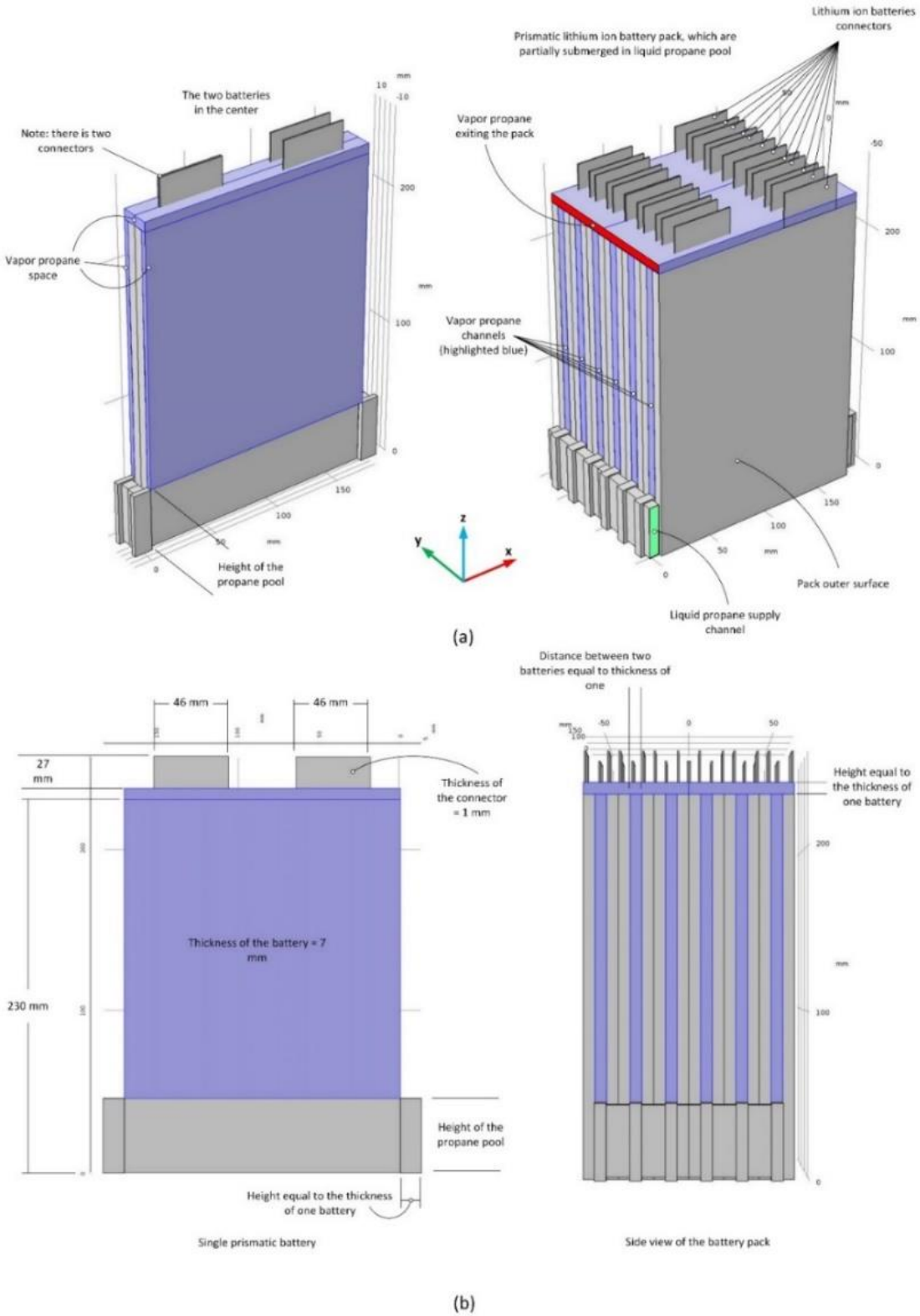

Figure 3.9 Schematic of the battery pack design that uses the proposed thermal management system: (a) pack design, (b) dimensions of the considered lithium ion prismatic battery and the thermal management system and the battery.

The lithium ion prismatic battery pack shown in Figure 3.8 is connected to a propane vapor collector and a pressure regulator, which collects the propane vapor and discharges the collected propane vapor to the internal combustion engine (ICE) via the injector at its operating pressure. Other components in the HEV shown in Fig. 1 are the AC to DC converted, and the vehicle radiator that cools the ICE of the vehicle. Having the propane in the slightly superheated state as it is fed to the ICE increases the engine combustion efficiency, according to Rowley [124]. Rowley proposed using the exhaust thermal energy to evaporate gasoline so it is injected into the engine in vapor form. Rowley's experiments showed that the overall fuel combustion efficiency increased by 5.5 kilometers per liter of fuel when the gasoline was injected in the vapor phase. Rowley also considered the case where gasoline vapor is first converted to propane vapor through a conversion device and then fed to the engine.

BTMS configuration for cylindrical battery pack

Figure 3.10 shows a schematic diagram of the HEVs in which the proposed battery thermal management system is to be used. The liquid propane which is the fossil fuel part of the HEV is used first for cooling then for combustion to produce electrical power that either charges the batteries or drives the vehicle. In HEVs the batteries are grouped in battery packs. Figure 3.11(a) shows the schematic diagram of the propane based thermal management system proposed in this thesis. The cylindrical batteries are arranged in an array format where part of the cylindrical batteries are submerged in the liquid propane.

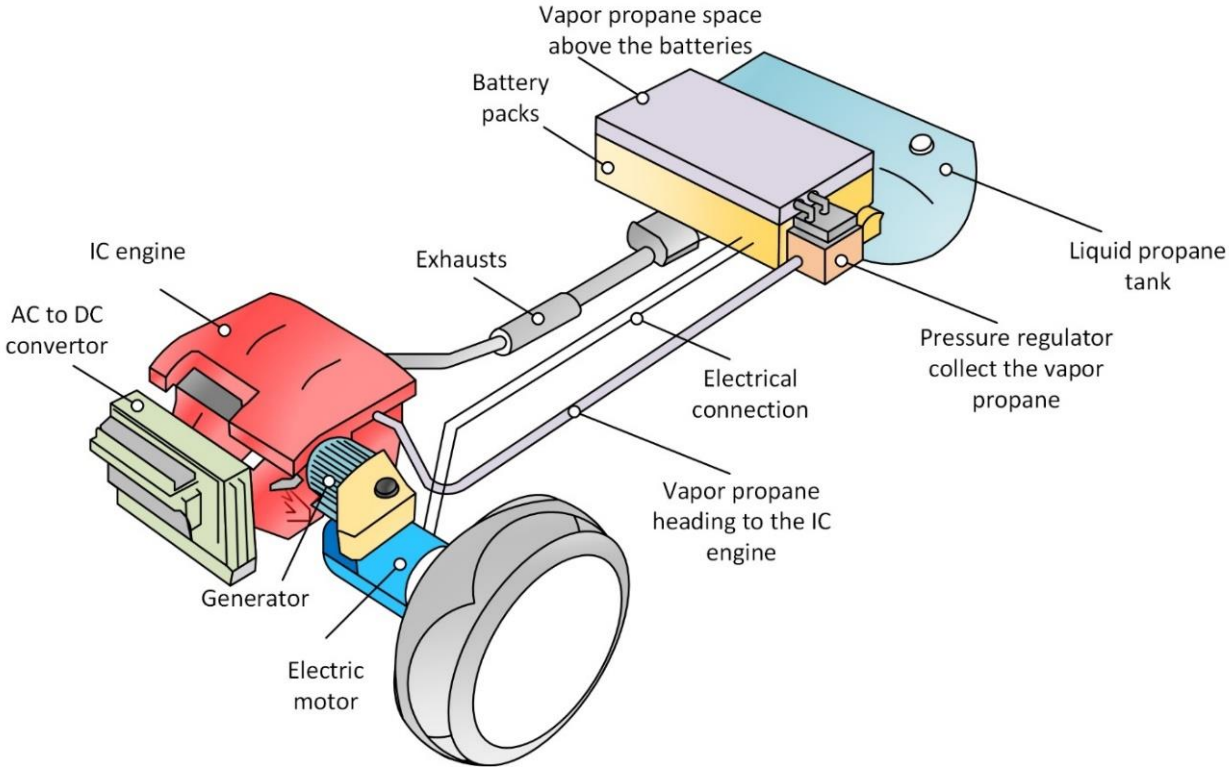

Figure 3.10 Schematic diagram of the hybrid electric vehicle on which the proposed battery thermal management system is employed.

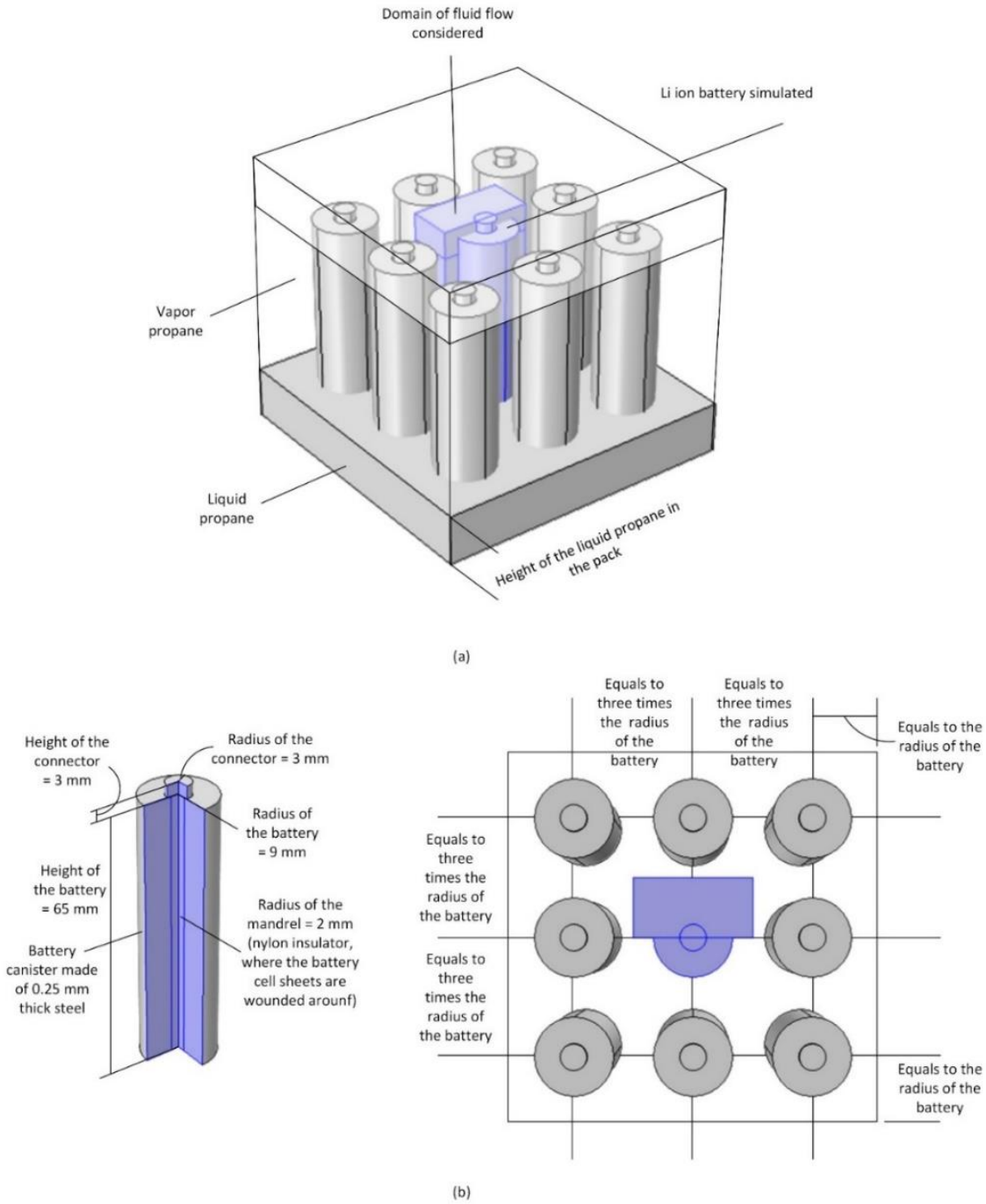

Figure 3.11 Schematic of the battery thermal management system: (a) design, (b) dimensions of the cooling system and the battery.

The thermal energy generated by the cells is transferred to the propane, which cools the batteries in the pack. The thermal energy generated by the cells is removed by the surrounding propane via two heat transfer modes. The first mode involves boiling the liquid propane, where the level of the propane in the battery pack is maintained by the propane tank in the HEV. The propane in the vapor phase, which results from boiling of the liquid propane produces an upward flow due to the buoyancy force and the pressure difference

made by the propane injectors, which inject the vapor propane into the combustion chambers of the electrical generator in the HEV. Before the propane injectors there is a regulator tank that stores the propane vapor before sending it to the injectors. The upward flow of the vapor propane in the battery pack cools the reaming part of the batteries that are not submerged in the liquid propane. There are a total of nine batteries in the battery pack considered in this thesis.

3.2 Independent on the Vehicle Drive Train

This section is discussing the development of novel battery cooling systems that are not vehicle drive train specific, where they can be used to maintain the operating temperature of any battery pack in any vehicle including EVs and HEVs.

3.2.1 Halocarbons as refrigerants

Halocarbons can be categorized into five main categories, which are Chlorofluorocarbons (CFCs) and Bromofluorocarbons (BFCs), Hydrochlorofluorocarbons (HCFC), Hydrofluorocarbons (HFCs), Azeotropic mixtures and Zeotropic mixtures. The HFCs are one of the most commonly used refrigerants in air conditioning systems in vehicles, and residential applications. In this section, an independent battery cooling system on the vehicle drive train that utilizes the Halocarbons is proposed, where the halocarbons are used to cool the batteries and then recycled to be used again.

3.2.1.1 System 5

In this section, the aim of the proposed system designed for EVs, is to exploits the advantages of boiling based BCSs. In the proposed system the batteries in the pack are partially submerged in the coolant, R134a. The PCM selected is refrigerant R134a, which boils to produce vapor and cools the batteries in the pack. The generated vapor is slightly superheated by cooling of the unsubmerged part of the battery in the pack. Then superheated vapor is condensed by the vehicle cabin cooling system.

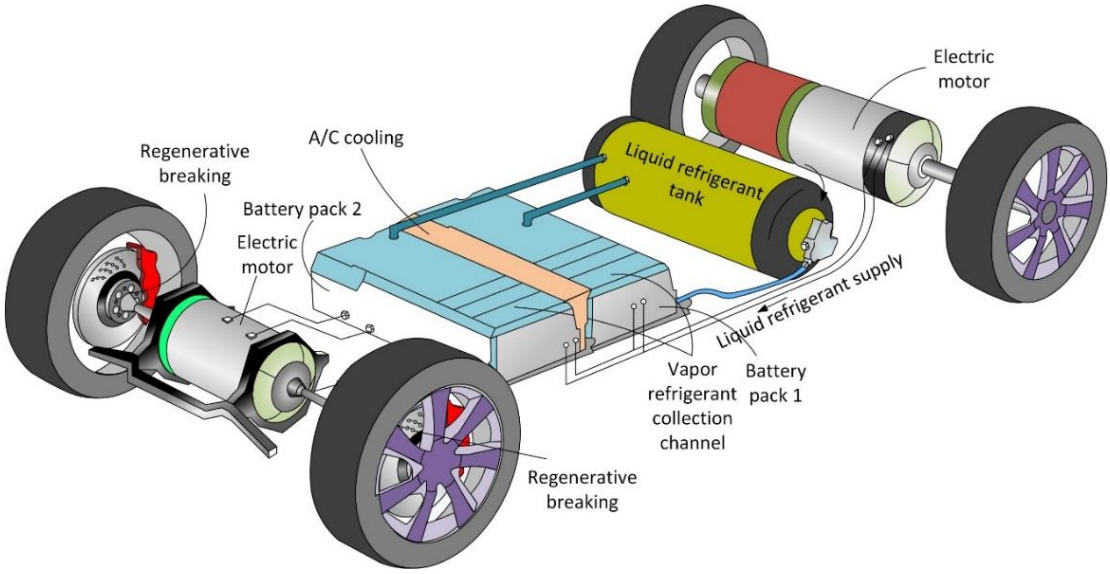

Figure 3.12 Schematic diagram of the internal structure of the electric vehicle that uses the refrigerant based battery thermal management system.

The performance of the proposed BCS is investigated through a charging and discharging cycle of 600 seconds (300 seconds each). The selected performance measures include the thermal characteristics of the lithium ion batteries in the battery pack. The aim is to propose a BCS that uses refrigerant cooling in EVs. Figure 3.12 shows a schematic diagram of the internal structure of an electric vehicle with the refrigerant based thermal management system installed to maintain the thermal performance of the batteries within the acceptable operation range. In Figure 3.12 it shows that the refrigerant supply tank supply the coolant to the battery pack at a specified pressure. The battery packs have the upper collection chamber that collect the vapor refrigerant where it cooled and recycled into the pack again.

BTMS configuration for prismatic battery pack

System 5 configuration to cool battery pack that are prismatic in shape will be proposed in this subsection. One of the designs of the battery cooling system that uses the liquid refrigerant pool is similar in geometry to the system 4 design as shown in Figure 3.9.

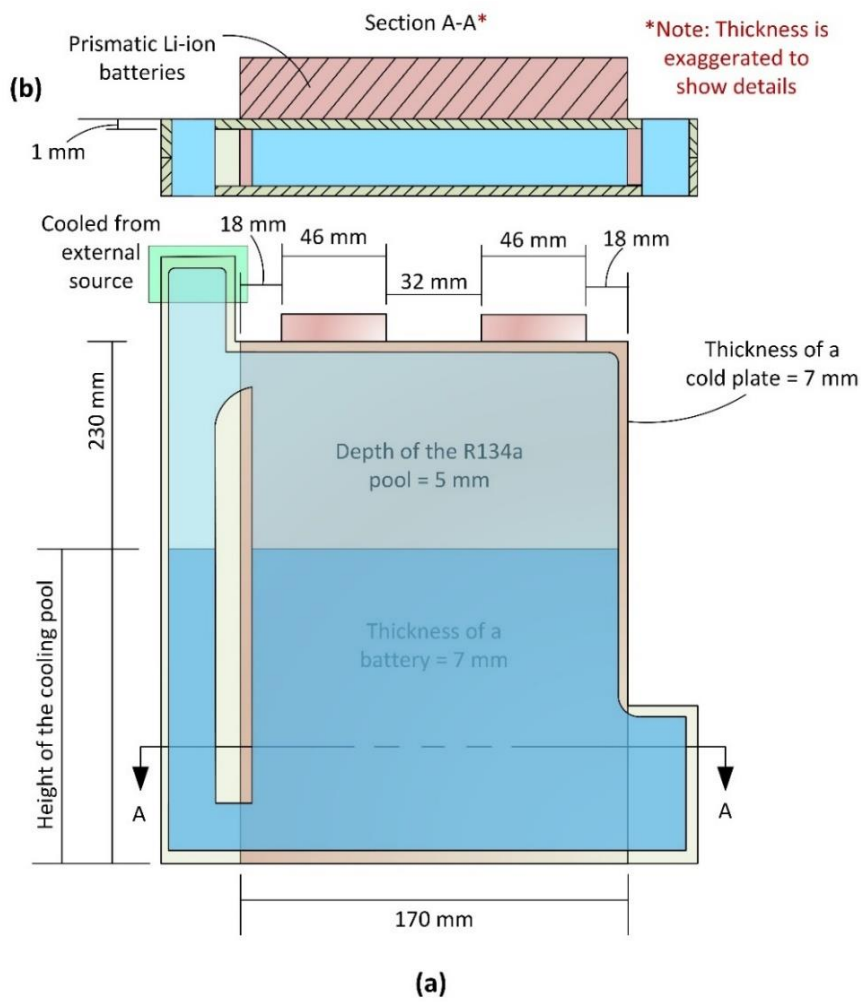

Figure 3.13 (a) Schematic of a single battery with a refrigerant R134a cold plate and how the recycling system keeps the loop of the coolant closed, and (b) a section cut showing the connection between the cooling plate and the battery.

However the R134a design features a recycle channel where the vapor R134a is cooled to condensation through the use of the external cooling source such as the environment air when the environment temperature is lower than the saturation temperature of the pool at the selected operating pressure. Another source of cooling is the air conditioning system of the vehicle. The schematic of the R134a based prismatic battery pack cooling system is shown in Figure 3.13. Figure 3.13 shows that the height of the pool in the pack where it can be also varied based on the control system for the supply. Note also the way the cooling plate that houses the liquid refrigerant it can also be a passive coolant supply system.

BTMS configuration for cylindrical battery pack

A schematic diagram of the proposed refrigerant based battery cooling system (BCS) for EV battery packs is shown in Figure 3.14. Figure 3.15 shows a perspective and three views of the proposed refrigerant based BCS for the case where the batteries in the pack are cylindrical.

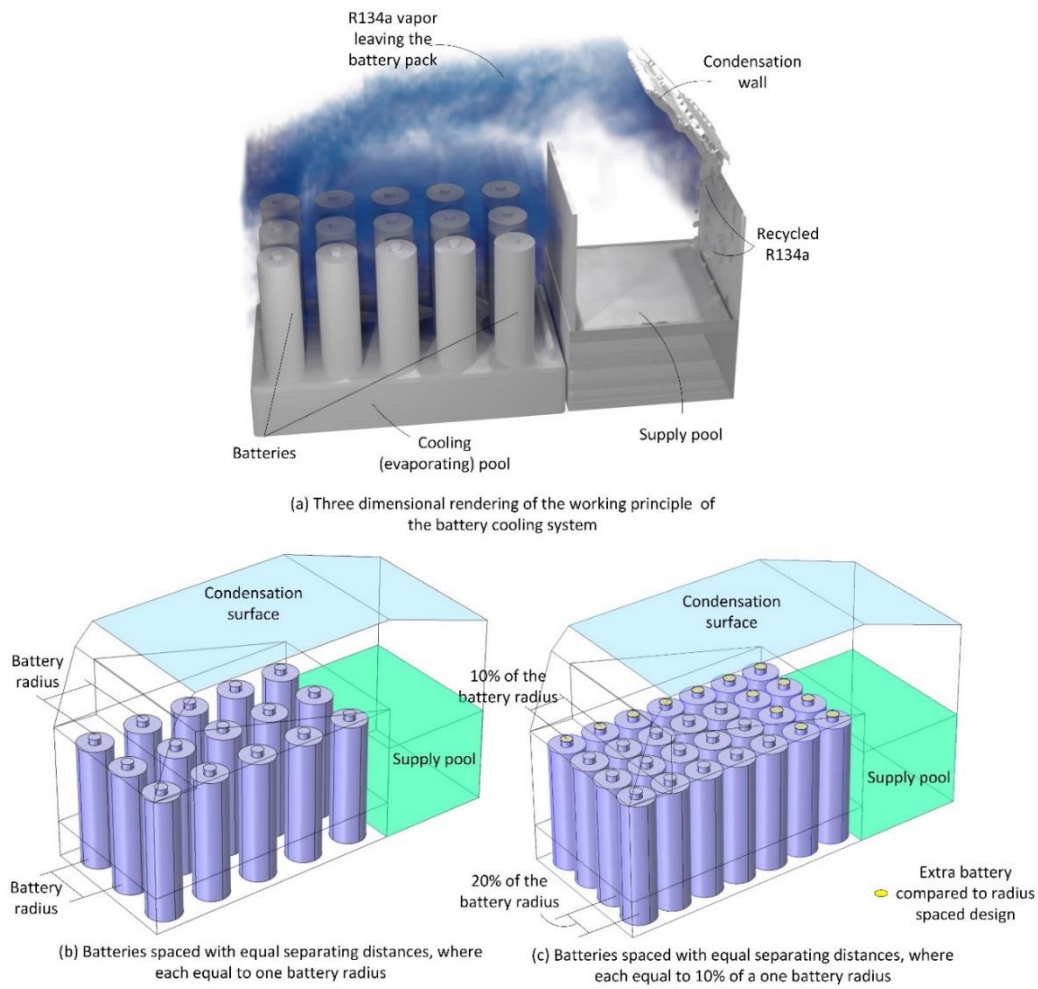

Figure 3.14 (a) Three dimensional rendering of the working principle of the proposed cooling system (system 5 for cylindrical batteries). (b) batteries are separated by one battery radius, and (c) a compact design with 10% of a battery radius in one direction and 20% in the other direction.

The BCS refrigerant is R134a. Note that the type of refrigerant used in the proposed BCS does not have the limitation of needing to be the same as the fuel used in the HEV. The detailed working principle of the proposed BCS is illustrated in Figure 3.15. The refrigerant R134a is supplied in the liquid phase from a pressurized tank. The liquid refrigerant partially or fully surrounds the batteries in the pack, and the refrigerant height in the pack is maintained by a liquid height controller. The liquid refrigerant is in a direct contact with the surface of the batteries as shown in Figure 3.15. When the batteries in the vehicle pack are charged or discharged, their temperature rises due their heat generation. This causes the refrigerant surrounding the batteries to start to boil by absorbing part of the generated heat by the batteries, which in turn cools the batteries in the pack. The generated refrigerant vapor is superheated by cooling the uncovered part of the battery through natural convection. Then the superheated R134a vapor leaves the pack and enters a return channel. The return channel with the car air conditioning system condenses the R134a. The R134a condensate is returned to the R134a tank for reuse in cooling the batteries. The saturation temperature is selected to be 30°C, for which the corresponding saturation pressure is 771 kPa. This saturation temperature is selected to maintain the pack temperature within the optimum operation range and to permit use ambient air or vehicle cabin cooling air to condense the evaporated R134a.

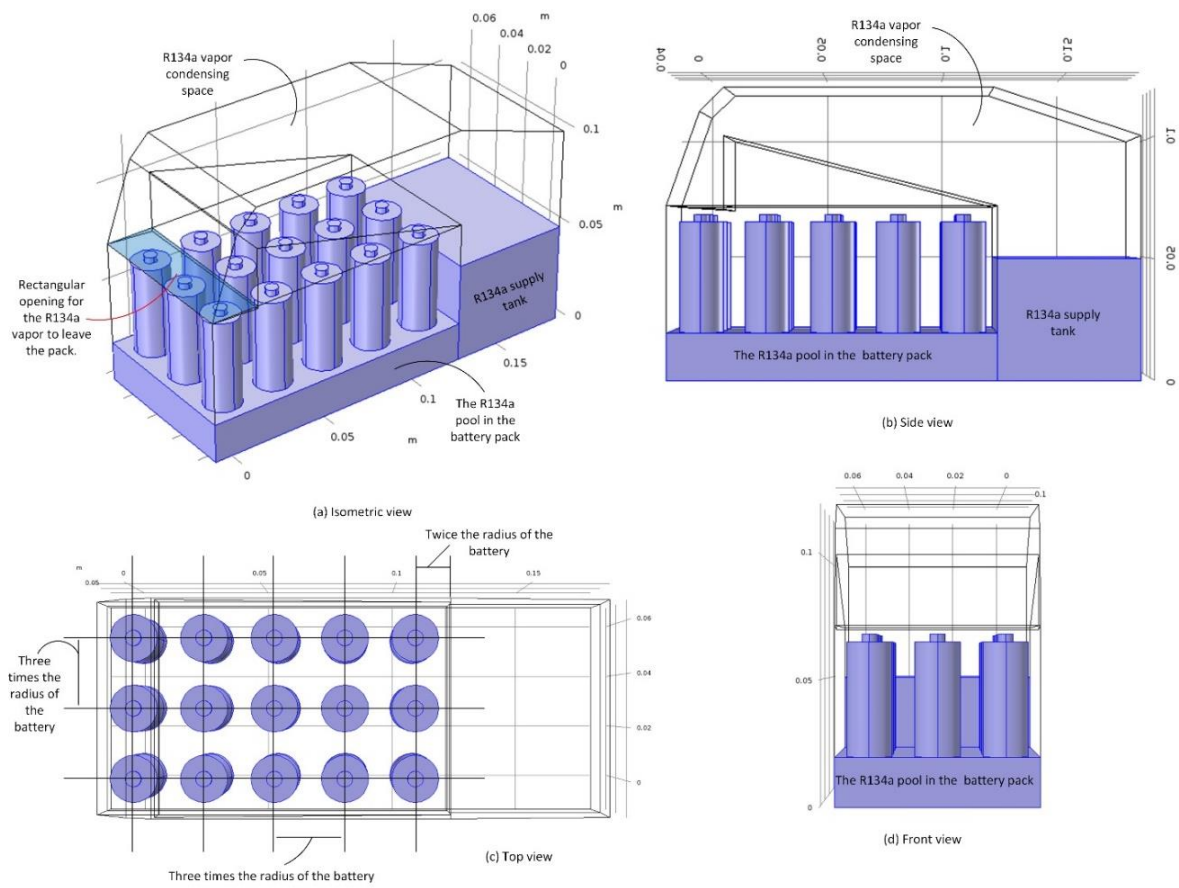

Figure 3.15 Schematic diagram of refrigerant R134a refrigerant based battery thermal management system for electric vehicles showing the working principle of the system.

3.3 Closing remarks

This chapter have focused on describing the various proposed designs of the novel battery thermal management systems, which were summarized in the objectives of the thesis. The proposed systems were divided into two main categories based on their role in the vehicle drive train. The first category is for those proposed systems that are vehicle specific. A vehicle specific system is a system where the proposed battery thermal management system is an integrated part of the specific vehicle type drive train. The second category of proposed battery thermal management systems are those who are independent on the vehicle drive train and that they can be used in all applications were the thermal performance of the battery needs to be controlled. The following two chapters (4 and 5) present the details of the developed model on COMSOL Multiphysics.

Chapter 4: Analyses and Optimization

The performance of the proposed battery thermal management systems are analyzed and optimized in this chapter. In order to analyze and then optimize the proposed systems, the battery and the proposed thermal management system are model, simulated and analyzed in Comsol Multiphysics and Engineering Equation Solver (EES). The performance is measured through an integrated electrochemical and heat and mass transfer model. This chapter first introduces the built models, the electrochemical and heat transfer models, then the environmental effect of the proposed systems are considered and finally the optimization study including the method, objective functions and the variable ranges are discussed.

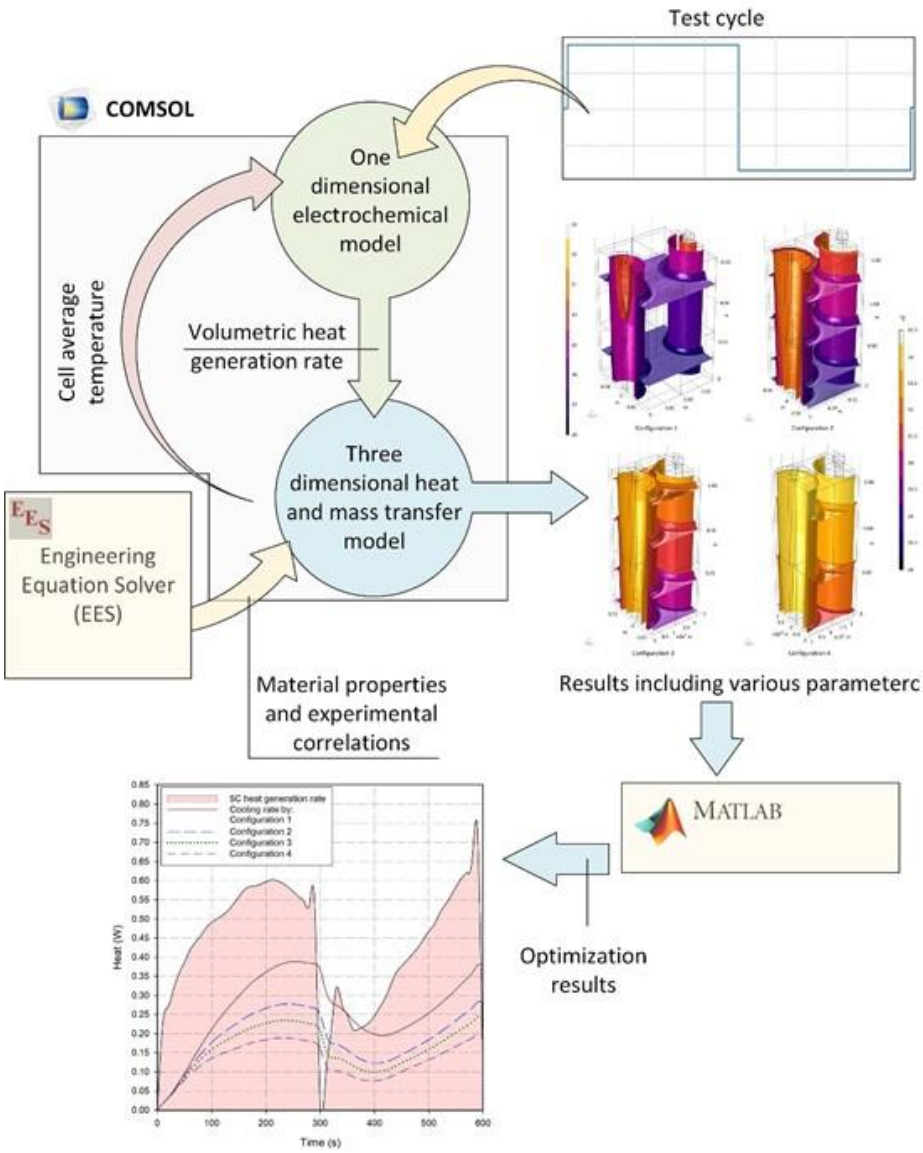

Figure 4.1 Flow sheet of the modeling methodology used to assess the performance of the proposed system.

All the proposed systems share the same modeling methodology of using two models with different physics simulated simultaneously to accurately and computationally cost effective the performance of the battery pack and thermal management system and flow sheet of this modeling methodology is presented in Figure 4.1. As shown in Figure 4.1 the electrochemical model receives the simulation cycle in terms of the cycle current or the power drawn or delivered to the battery pack. As shown in Figure 4.1 the model starts with the drive test cycle, which can be presented in terms of intense charge and intense discharge or through a realistic drive cycle. The simulation test cycle can be in power required to charge or the power absorbed from the batteries to drive the vehicle or the charging and discharging current as shown in the top right corner of the flow chart. The electrochemical model simultaneously sends the volumetric heat generation rate per each second or solution step to the heat transfer and fluid flow model, which sends the average cell temperature back to the electrochemical model. As mentioned earlier a set of material properties as well as heat transfer correlations are generated by EES and used in the heat transfer and fluid flow model as shown in Figure 4.1. The results regarding the thermal performance of the battery pack are generated from the heat transfer and fluid flow model, where those related to the electrochemical performance of the pack such as the state of charge of the battery are generated by the electrochemical model. The optimization is carried out with the help of Matlab and the optimization results are presented throughout the analysis and results of the proposed systems.

4.1 Electrochemical analysis

This section presents the electrochemical modeling and model development process, where the model is built to analyze the electrical performance of the batteries in the pack. The electrochemical model of the battery provide the heat generation rate produced by the battery as a results of its electrochemical reactions and its internal resistance to the current flow. The heat generation is one of the links between the two main models, the electrochemical and heat and mass transfer models. The two models together are used to simulate the performance of the proposed systems. The other link between the two models will be temperature of the battery, which is determined by the heat and mass transfer model and then transferred to the electrochemical model. In the literature, the main goal of the electrochemical model of the battery is evaluate the variable heat generation rate. Various methods were proposed in the literature to evaluate the transient heat generation rate of the battery other than simulating the actual performance of the battery electrochemically. This chapter will start by presenting the properties of the batteries considered in this thesis, including material, thermophysical properties, and geometric properties. Then it will list assumptions considered for the modeling the battery electrochemically. Following the assumption is the electrochemical modeling procedure, steps and governing equations and finally the results from the electrochemical model are validated with experimental and simulation results published in the literature.

In the previous section it was presented that the heat generation depends on the electrochemical properties and reaction occurring in the battery during the charging and discharging of the battery. This section summarizes the governing equations of the developed one dimensional electrochemical model, which is used to find the heat generation rate during the charging and discharging process, which is fed to the three dimensional heat and mass transfer model. Further details of the electrochemical model

including the description of the material properties of different parts of the battery can be found elsewhere [67,68,125].

4.1.1 Prismatic battery electrochemical model

As mentioned earlier and presented in Figure 4.2, the positive and negative porous electrodes separated with the separator make the layered structure of a single battery cell. A pseudo-homogeneous mixture describes the porous electrode structure, which consist of polymer matrix, conductive filler, active insertion material and non-aqueous liquid electrolyte [67,68,125]. The separator in the battery cell is a multicomponent structure of a plasticized electrolyte. The separator plasticized electrolyte is made of five different species and they are two liquids, an anion, a cation and a polymer, where more details on their properties and their thermophysical behavior during the charging and discharging can be found elsewhere [67,68,125]. The one dimensional electrochemical model governing equations can be summarized in terms of the variation of the salt concentration through the battery cell electrodes and separator. The salt concentration in the electrode solution phase varies with time as follows:

$$\frac{\partial b_s}{\partial t} = \left(\nabla \cdot (D_s \nabla b_s) + (aj_n + aj_n t_+^0) - \frac{i_2 \cdot \nabla t_+^0}{F}\right) \tag{4.1}$$

where b_s is the salt concentration, t is time, D_s is the salt diffusion coefficient, a is the specific interfacial area, i_2 is the superficial current density and j_n is the pore wall flux of lithium ions. The subscript + refers to the positive electrode and – refers to the negative electrode. The specific interfacial area and the pore wall flux of lithium ions are related as follows:

$$a = \frac{1}{F} \nabla \cdot \frac{i_2}{j_n} \tag{4.2}$$

where the superficial current density (i_2) is expressed as follows:

$$i_2 = -k\nabla\phi_2 + \left(\frac{2kRT}{F} + \frac{2kRT}{F} \cdot \frac{\partial \ln f_\pm}{\partial \ln b_s}\right)(1 - t_+^0)\nabla \ln b_s \tag{4.3}$$

Here, k presents the electrolyte ionic conductivity, R is the universal gas constant, T the absolute temperature, F is Farday's constant, which has a value of 96,587 C/mol, f is the activity coefficient, and ϕ is the electrical potential of the electrode solution phase. The effective electrolyte ionic conductivity (k) can be presented in terms of the phase volume fraction and the effective conductivity of the liquid/salt/polymer system as follows:

$$k = \epsilon^{3.3} k_0 \tag{4.4}$$

where ϵ is the volume fraction of the liquid/salt/polymer and k_0 is conductivity of the liquid/salt/polymer system, which can be presented as a function of the salt concentration temperature, and the solvent ratio of ethylene carbonate (EC) to dimethyl carbonate (DMC). For a liquid/salt/polymer system with 2:1 v/v mixture of EC to DMC at a temperature of 25°C, its conductivity is calculated as follows:

$$k_0 = 4.1253 \times 10^{-4} + 5.007 \times 10^{-3} b_s - 4.7212 \times 10^{-3} b_s^2 + 1.5094 \times 10^{-3} b_s^3 - 1.6018 \times 10^{-4} b_s^4 \tag{4.5}$$

Since the above equation is a correlation then, the units that should be used are, b_s is the salt concentration in mol/dm^3 and the resulting conductivity is in S/cm. However, for liquid/salt/polymer systems with 1:2 v/v mixture of EC to DMC, which is used in several $LiPF_6$ cells, the conductivity can be defined as follows:

$$k_0 = 1.0793 \times 10^{-4} + 6.7461 \times 10^{-3} b_s - 5.2245 \times 10^{-3} b_s^2 + 1.3605 \times 10^{-3} b_s^3 - 1.1724 \times 10^{-4} b_s^4 \quad (4.6)$$

The relationship between the composite electrode solid matrix superficial current density and its electrical potential can be presented as follows:

$$i_1 = -\sigma \nabla \phi_1 \quad (4.7)$$

where i_1 is the superficial current density, ϕ_1 is the electrode potential and σ is the solid matrix electronic conductivity. The lithium concentration in the electrode solid matrix can be expressed as follows:

$$\frac{\partial b_{Li}}{\partial t} = D_{Li} \left[\frac{2}{r} \frac{\partial b_{Li}}{\partial r} + \frac{\partial^2 b_{Li}}{\partial r^2} \right] \quad (4.8)$$

where D_{Li} is the lithium diffusion coefficient of lithium through the solid phase of the composite electrode. The dimension in through the thickness of the battery cell layers is denoted as r, which the same dimension the developed one dimensional electrochemical model is considered. Note that r is selected arbitrary to present that direction and it does not refer to a cylindrical coordinates, rather it is in the same as the y direction shown in Figure 4.2.

The governing equations defining the solution and solid phases of the composite electrodes are related through boundary condition and the Butler-Volmer kinetics expression. The boundary condition used to relate the two phases of the electrode is on the outer surface of the electrode and it can be written as follows:

$$\frac{\partial b_s}{\partial r} = -j_n / D_{Li} \quad (4.9)$$

where r here is the same cell dimension used in equation (19), and j_n is the pore wall flux of lithium ions.

The Butler-Volmer kinetics expression can be written as follows:

$$\left(\frac{j_n}{H}\right) + (b_s)^{0.5}(b_i - b_{Li})^{0.5}(b_{Li})^{0.5} \exp\left(-\frac{F}{2RT}(\eta - V_{oc})\right) = (b_s)^{0.5}(b_i - b_{Li})^{0.5}(b_{Li})^{0.5} \exp\left(\frac{F}{2RT}(\eta - V_{oc})\right) \quad (4.10)$$

where b_{Li} is the lithium concentration in the solid, b_i is the salt concentration in layer i, η is the electrode potential and V_{OC} is the open circuit voltage. H presents the product of the forward and backward reaction constants, which are raised to the power that are derived from the charge transfer coefficient at the electrode surface. The electrode potential is calculated as follows:

$$\eta = \phi_1 - \phi_2 \quad (4.11)$$

where ϕ_1 and ϕ_2 are the electrical potential of the solid and solution phases of the composite electrode. The parameter H is related to concentration of different species including the lithium ions and the insertion process exchange current density of the insertion process (i_o) through the following equation:

$$i_o = FH(b_s)^{0.5}(b_t - b_{Li})^{0.5}(b_{Li})^{0.5} \tag{4.12}$$

where b_t is the maximum slat concentration in the intercalation material.

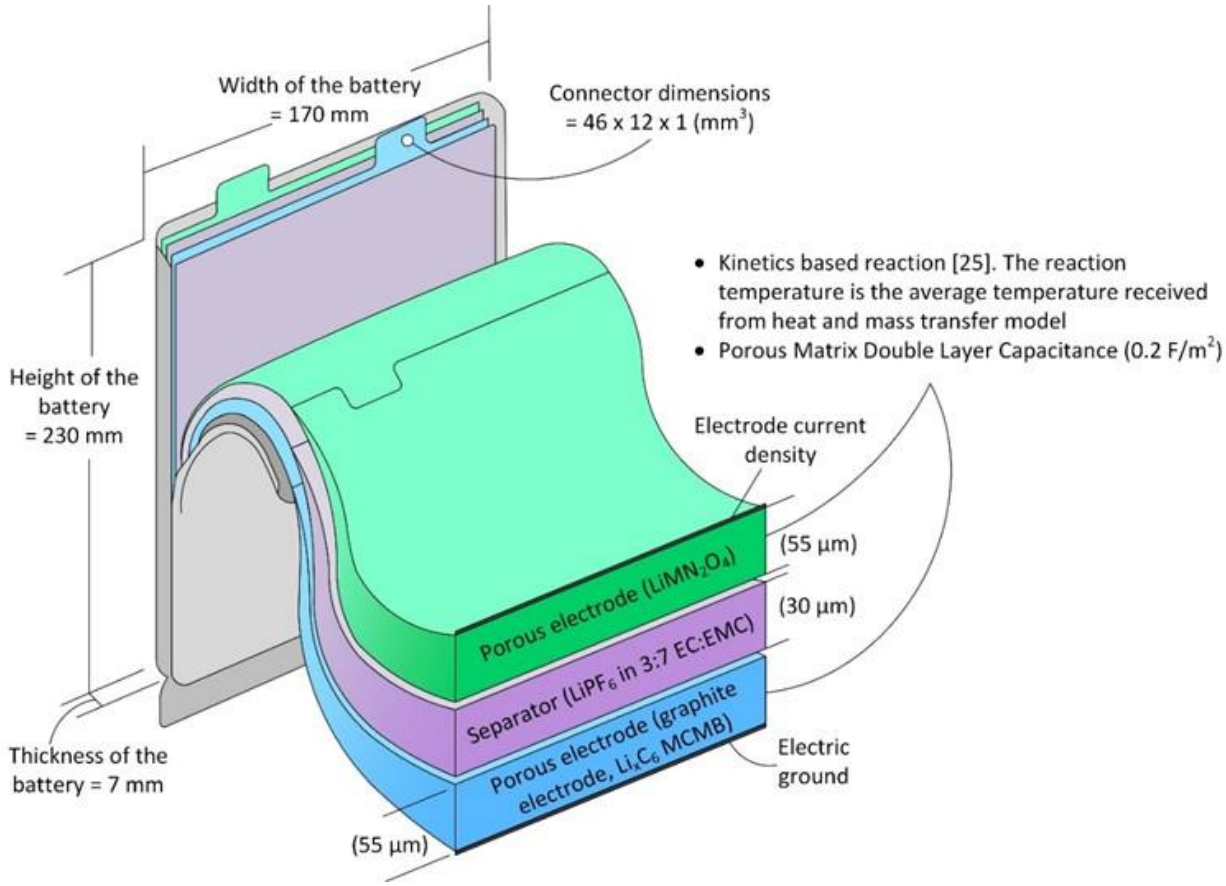

Figure 4.2 Dimensions of the modeled and simulated lithium ion prismatic battery and the selected boundary conditions for the one dimensional electrochemical model.

4.1.2 Cylindrical battery electrochemical model

The electrochemical reactions occur in the active part of the battery, which consists of sheets wound around a nylon mandrel to form a cylindrical structure as shown in Figure 4.3. There are three types of sheets that make up the active part of the battery: the porous positive electrode, the separator and the porous negative electrode. The cylindrical structure that forms the active part of the battery is incased in a metallic canister, which is 0.25 mm thick and made from steel. Figure 4.3 illustrates the cylindrical Li-ion battery considered in this thesis, as well as detailed dimensions of the battery.

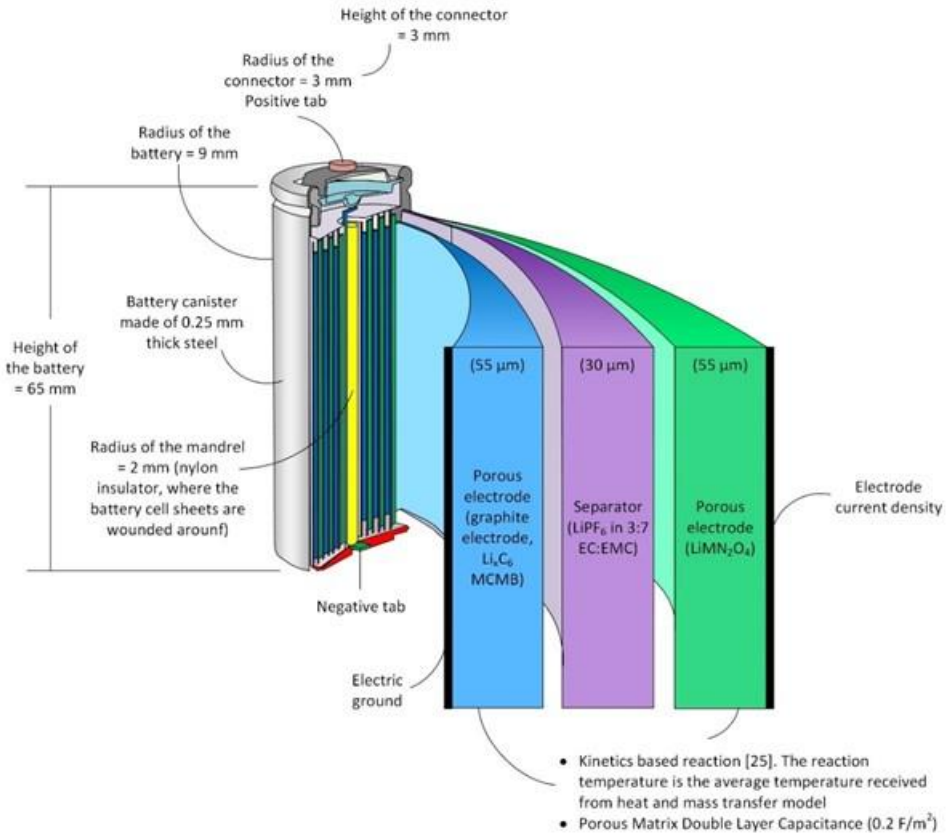

Figure 4.3 Dimensions of the modeled and simulated lithium ion cylindrical battery (battery type 18650) and the selected boundary conditions for the one dimensional electrochemical model.

The battery consists of a number of cells. Each cell consists of three main layers: the positive and negative electrodes which are separated with a slightly thinner layer called the separator as shown in Figure 4.3. The thickness of each layer in the cell is on the order of ten of micrometers, while the layers have a height close the battery height and a length that can span tens of centimeters. The electrochemical reactions occurring in the battery can be assumed to occur only in one dimension, through the thicknesses of the layers. This assumption is based on the large difference between the thickness of the battery cell and other two cell dimensions. Other researchers have considered the same assumption due to small percentage difference in the results between the one dimensional and two and three dimensional models [116,125].

The electrochemical reactions that occur in the batteries are one source of heat generation in the batteries, and the other is the internal resistance of the battery. Note that, for either source to start producing heat, the battery has to be charging or discharging. The electrochemical model of the battery is developed to investigate its electrical and thermal behavior. The thermal effect is presented in terms of the heat generation rate and the effect of battery temperature on the electrical performance of the battery. This section summarizes the electrochemical model developed for the cylindrical battery, where only these changes to fit the cylindrical mode are considered here where for those that are similar to the prismatic model are omitted from this section since it is included earlier in the

prismatic battery electrochemical model; further details on the model can be found elsewhere [125].

The lithium concentration in the solid matrix of the electrode can be expressed as follows:

$$\frac{\partial b_{Li}}{\partial t} = D_{Li}\left[\frac{2}{r}\frac{\partial b_{Li}}{\partial r} + \frac{\partial^2 b_{Li}}{\partial r^2}\right] \tag{4.13}$$

where b_{Li} is the lithium ion concertation in the electrode solid matrix and D_{Li} is the diffusion coefficient of lithium through the electrode solid matrix.

The next step is to define the boundary conditions and the relations between the solid and the solution phases of the cell electrode. The Butler-Volmer kinetics expression is used to relate the electrode's two phases, as follows:

$$\left(\frac{j_n}{H}\right) + (b_s)^{0.5}(b_i - b_{Li})^{0.5}(b_{Li})^{0.5}\exp\left(-\frac{F}{2RT}(\eta - V_{oc})\right) = (b_s)^{0.5}(b_i - b_{Li})^{0.5}(b_{Li})^{0.5}\exp\left(\frac{F}{2RT}(\eta - V_{oc})\right) \tag{4.14}$$

where V_{oc} is the open circuit voltage, b_i is the salt concentration in layer i, η is the electrode potential and H is the parameter that connects the concentration of different species such as the lithium ions with the insertion process exchange current density (i_o) as follows:

$$i_o = FH(b_s)^{0.5}(b_t - b_{Li})^{0.5}(b_{Li})^{0.5} \tag{4.15}$$

The boundary condition at the electrode outer radius also is used in relating the two phases of the electrode. This boundary condition can be expressed as follows:

$$\frac{\partial b_s}{\partial r} = -j_n/D_{Li} \tag{4.16}$$

Here, the electrode potential in equation (4.17) is calculated based on the electric potential of the two phases of the electrode as follows:

$$\eta = \phi_1 - \phi_2 \tag{4.17}$$

where ϕ_1 and ϕ_2 refer to the electrical potentials of the solid phase and the solution phase.

4.2 Thermodynamic and Heat Transfer Analysis

This section presents the development of the three dimensional heat and mass transfer analysis, where the section is divided into two subsections, the first presents the equations and the modeling methodology for the prismatic battery and then within that subsection the boundary conditions for the simulated domain are presented for each system model.

4.2.1 Prismatic battery model

Throughout the charging, discharging or resting (not charging nor discharging) processes, the temperatures throughout the battery and the cooling system vary with time. The variation of the temperature through the battery pack including batteries and cooling system at any instant of time can be found with the energy rate balance equation, which can be written as follows [126]:

$$\left(\frac{\partial \rho_b}{\partial t} \cdot \frac{\partial c_{p,b}}{\partial t} \cdot \frac{\partial T_b}{\partial t}\right) = \nabla \cdot \left(k_b(\frac{\partial T_b}{\partial x} i + \frac{\partial T_b}{\partial y} j + \frac{\partial T_b}{\partial z} k\right) + \dot{Q}_{gen} \quad (4.18)$$

Here, ρ denotes density, T temperature, k thermal conductivity, cp specific heat capacity and $\dot{Q}_{gen}$ heat generation rate. The subscript b refers to the battery. Each battery cell is made of three layers, which result in different thermal conductivities in the x, y and z directions. Using the x, y, and z directions shown in Figure 4.9 for developing the thermal conductivity equations, the thermal conductivity of the battery can be expressed in the three dimensions as follows:

$$k_x = \sum(L_i k_i) / \sum L_i \quad (4.19)$$

$$k_y = \sum L_i / \sum(L_i / k_i) \quad (4.20)$$

$$k_z = \sum(L_i k_i) / \sum L_i \quad (4.21)$$

Here, L_i is the dimension of layer i in the direction at which the thermal conductivity is calculated, and the thermal conductivity of layer i is referred to as k_i.

The specific heat capacity and the density of the battery's multilayer structure can be expressed respectively as follows:

$$c_{p,b} = \frac{\sum(L_i \times c_{p,i})}{\sum L_i} \quad (4.22)$$

$$\rho_b = \frac{\sum(L_i \times \rho_i)}{\sum L_i} \quad (4.23)$$

The heat rate generated by the battery while discharging or charging is due to the internal resistance of the battery and the chemical reactions occurring within it [54]. The battery heat generation rate can therefore be written as follows:

$$\dot{Q}_{gen} = \dot{Q}_{ec} + \dot{Q}_J = -T\Delta S \frac{I}{nF} + I(E - V) \quad (4.24)$$

Here, E is the open circuit voltage and V is the operating voltage of the battery, I is the charging or discharging current, T is the temperature of the battery, ΔS is the change in entropy associated with the electrochemical reactions, and n is the number of electrons in in the balanced electrochemical half reaction.

4.2.1.1 System 1 and system 3

In this section the model and the set boundary conditions for both systems 1 and 3 since both are using the same cooling plate design of the flow of the coolant which is the hydrogen and air in system 1 and system 3 respectively. This section introduces the design procedure of the cold plate for the hydrogen and air based systems, including the design and development procedure.

The mesh and the boundary conditions used in the three dimensional heat and mass transfer model are presented in Figure 4.10 for one of the five designs; however, the boundary conditions presented in Figure 4.5 are used in all the different proposed designs. The inlet boundary condition is set as a velocity boundary condition where the temperature of the hydrogen entering the pack is also set as a temperature boundary condition. The battery in the three dimensional heat and transfer model is modeled based on its outer

dimensions and the selected material for the battery domain is a custom material with calculated thermophysical properties as presented in the governing equation section. Based on the nature of the proposed cooling system, a single battery with half of a cooling plate equipped with symmetry boundary conditions constitutes the three dimensional heat and mass transfer model simulated domain.

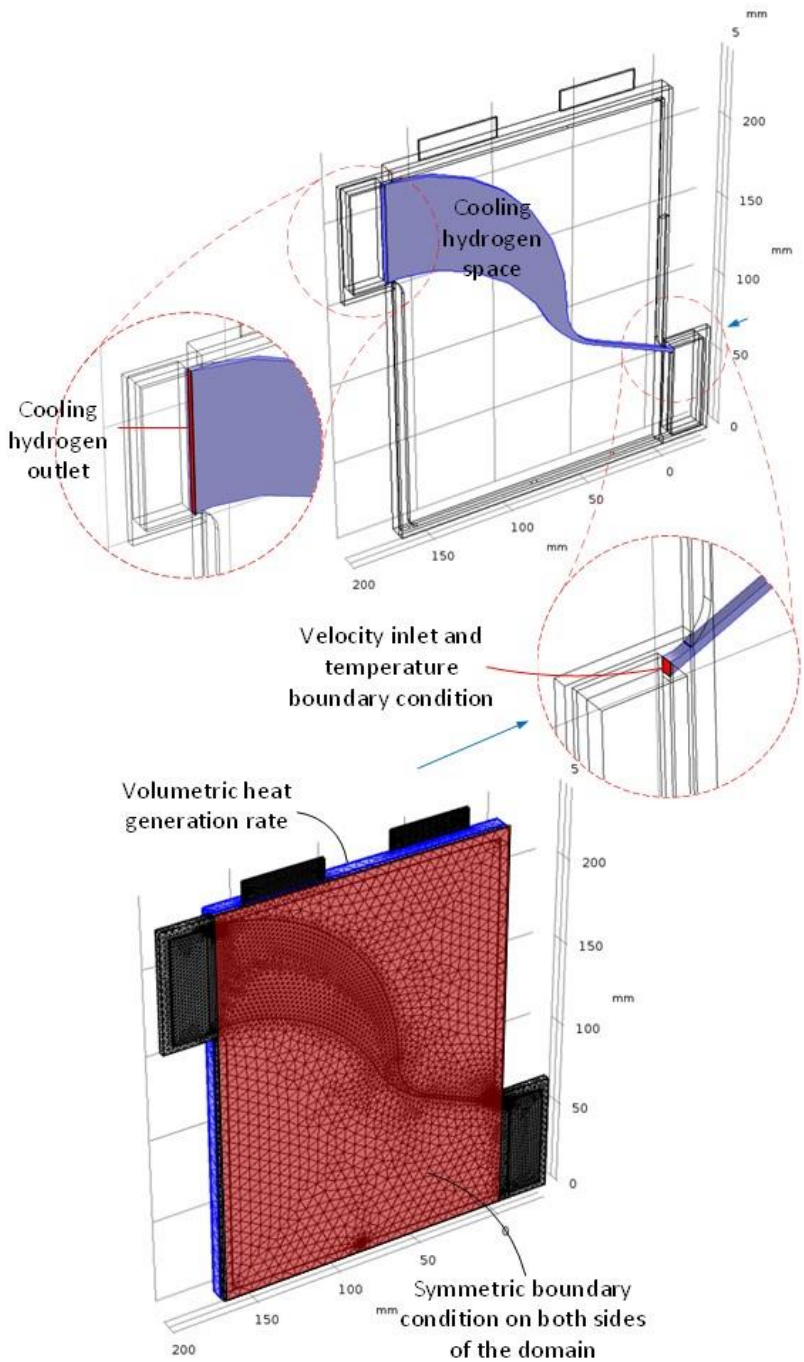

Figure 4.4 Simulated domain and boundary conditions for the three dimensional heat and mass transfer model (for the optimum case) (The thermal contact properties as follows: surface roughness, asperities average height 1 μm, and the asperities average slope 0.4).

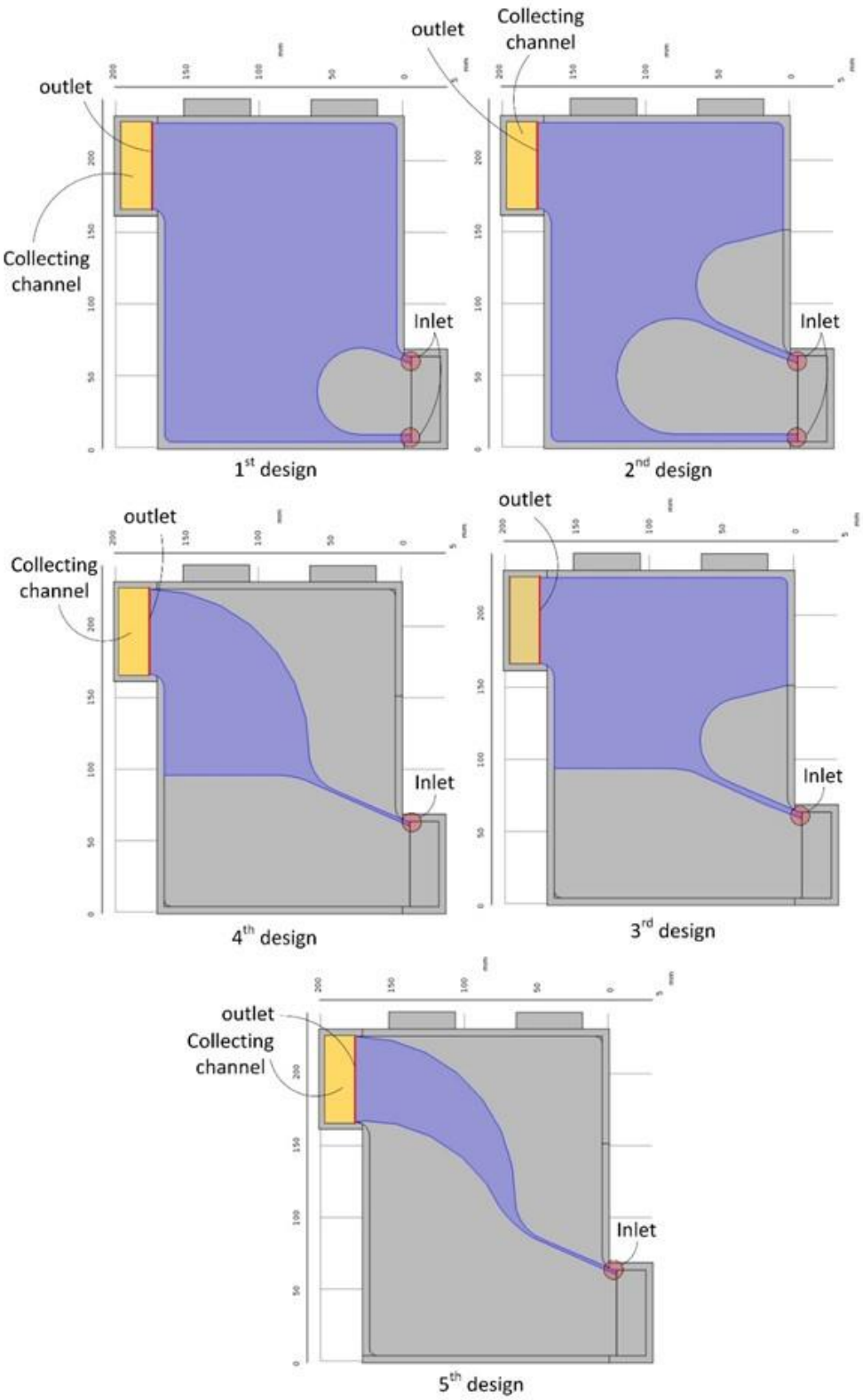

Figure 4.5 Proposed designs for the hydrogen cooled, aluminum cold plate considered in the thesis. The first two of the proposed designs have two hydrogen inlets and the remaining three have a single inlet cooled plate.

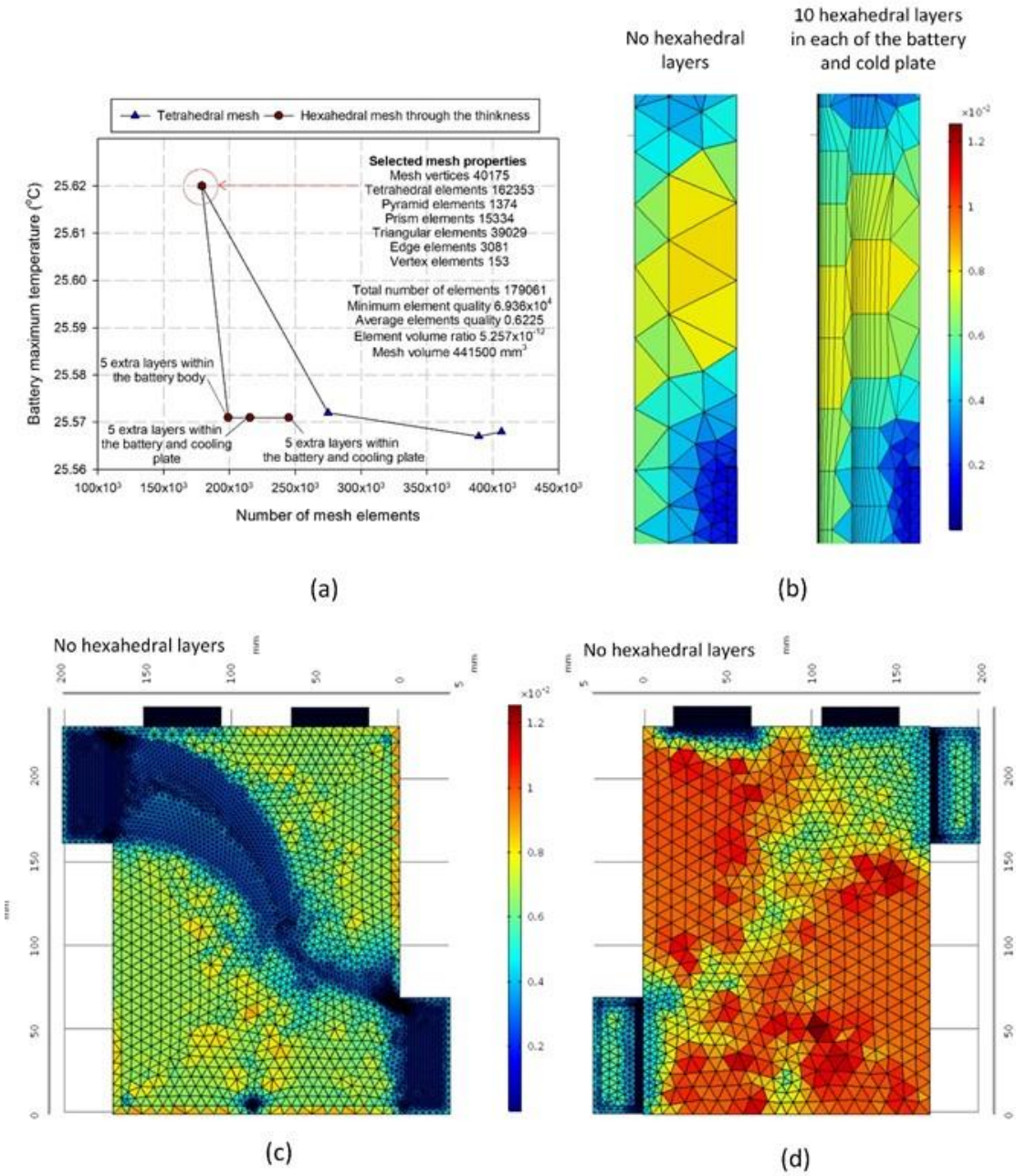

Figure 4.6 (a) Mesh independent study including a separate study on the number of mesh layers within the thickness of the battery and the cold plate based on the maximum temperature of the battery after a 100 seconds of charging the battery at 4C rate, (b) side view of the model showing the case with 10 extra mesh layers in both the cold plate and the battery (c) front view of the simulated model showing the variation of the selected mesh and (d) shows the back view of the model selected mesh. (note that the legend colors are based on the mesh cell size)

A grid independent study is carried out on the proposed model to ensure that the model is not sensitive to and hence independent of the mesh. A set of four different meshes were considered as shown in Figure 4.6 with the smallest mesh considered is 179081

tetrahedral mesh elements to a maximum of 406718 tetrahedral mesh elements. Fig. 5(a) shows that further increase of the mesh elements more than 179061 will lead to a change less than 0.2% in the battery maximum temperature at a rate of 4C charging current and for 100 seconds. Due to such a small change, a mesh of 179061 elements is considered for the rest of the study. In addition, Figure 4.6(a) includes a mesh independent study concerning the number of hexahedral mesh layers through the thickness of the battery and the aluminum cold plate. As shown in Figure 4.6(a) the increase in the number of hexahedral mesh layers within the thickness of the battery from zero hexahedral layers to 5 within the battery itself caused a change of 0.19% in the battery maximum temperature after 100 seconds of charging at a 4C rate. Figure 4.6(b) shows a mesh comparison on the thickness of the battery from the top view for the case with no hexahedral mesh layers and the fourth case of 10 hexahedral elements within the thickness of the battery and the cold plate. Here, Figure 4.6(b) with no hexahedral layers shows that mesh of the first considered appropriate mesh size (the first point in Figure 4.6(a)). It is important to note that increasing the mesh layers within the battery thickness resulted in reaching a mesh independency with less number of mesh elements compared to enhancing the overall mesh quality of the simulated domain. Furthermore, Figure 4.6(c) shows graphical details on the mesh structure and elements size distribution throughout the simulated domain from the front surface showing the hydrogen flow channel, and Figure 4.6(d) shows the mesh structure but on the opposite side to what Figure 4.6(c) shows.

4.2.1.2 System 2

System 2 is the ammonia based system, where the prismatic design is varied as a part of the optimization study and both designs are presented in this section, they are explained and the selected boundary conditions are presented as well.

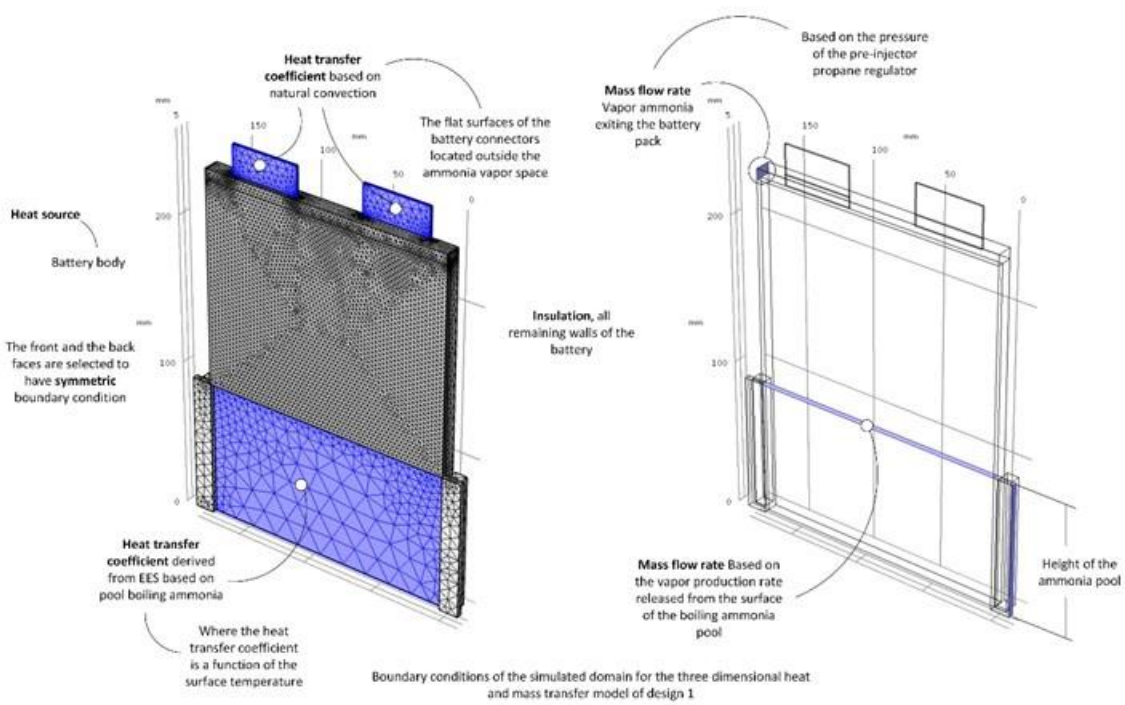

Figure 4.7 Three dimensional mass and heat transfer model, of design 1 of the ammonia boiling based battery thermal management system.

The first design is the direct contact pool design where the boiling ammonia pool is in direct contact with the surface of the battery and the second design uses a smaller amount of ammonia however it is confined in a cooling plate or it can also be referred to cold plate in the form of tubes inside the cold plate. Each of the designs are presented next in details.

Figure 4.7 shows the heat and mass transfer simulated domain considered from the battery pack presented earlier in the system description chapter. In the three dimensional heat and mass transfer model, the ammonia vapor flows from the surface of the boiling ammonia pool upward due to buoyancy and mainly due to the pressure regulator and vapor collection device. The pressure regulator and the ammonia vapor collector ensures a constant pressure inside the battery pack and also collects the ammonia vapor until specific amounts are attained that are used by the electrical generator to produce electrical energy. The ammonia vapor entering the vapor domain is saturated, at the same temperature as the boiling ammonia pool.

The first boundary condition selected is an inlet mass flow rate, applied to the surface of the ammonia pool based on the evaporation rate of the ammonia as it cools the battery by absorbing generated heat. When the ammonia vapor reaches the upper part of the pack it leaves from one side to the collection channel leading to the vapor collector and pressure regulator. The surface that connects the vapor space to the collection channel is selected as the outlet boundary condition as shown in Figure 4.7. A heat flux based on an input heat transfer correlation is selected as the boundary condition for the surface of the battery in direct contact with the boiling ammonia pool. The correlation is based on the surface temperature of the battery that it is in direct contact with the pool, as the pool boiling starts at a surface temperature 5°C higher than the boiling temperature of the ammonia pool at a specified pressure. As long as the temperature of the battery surface is within 5°C of the saturation temperature of the ammonia pool, natural convection heat transfer occurs. A laminar flow model is used to describe the flow of the ammonia vapor through the vapor channels between the batteries and above the pool. The laminar model is chosen for the vapor flow corresponding to the low Reynolds number of the generated ammonia vapor, where the Reynolds number is calculated with the characteristic length equal to the hydraulic diameter of the flow channel. Since the ammonia vapor flow rates vary continuously throughout the discharging and charging cycle of the battery, the selection of the laminar flow model was based on the maximum Reynolds number experienced in the flow channel. The pressure of the ammonia pool in the battery pack is set to 9.0 bar, so as to be similar to the ammonia HEV tank pressure and to have a saturation temperature (21.5^{o}C) below the ambient temperature (25°C) [127]. The cooling ability of the proposed system is assessed through a discharging and a charging cycle of 600 seconds divided equally at a rate of 4C, which is four times the rate required to discharge or charge the battery completely from a 100% to 0% state of charge in one hour.

The second design where the boiling ammonia is not in direct contact with the battery surface is presented next, where the ammonia pool is kept inside the cold plate in tubes as shown next.

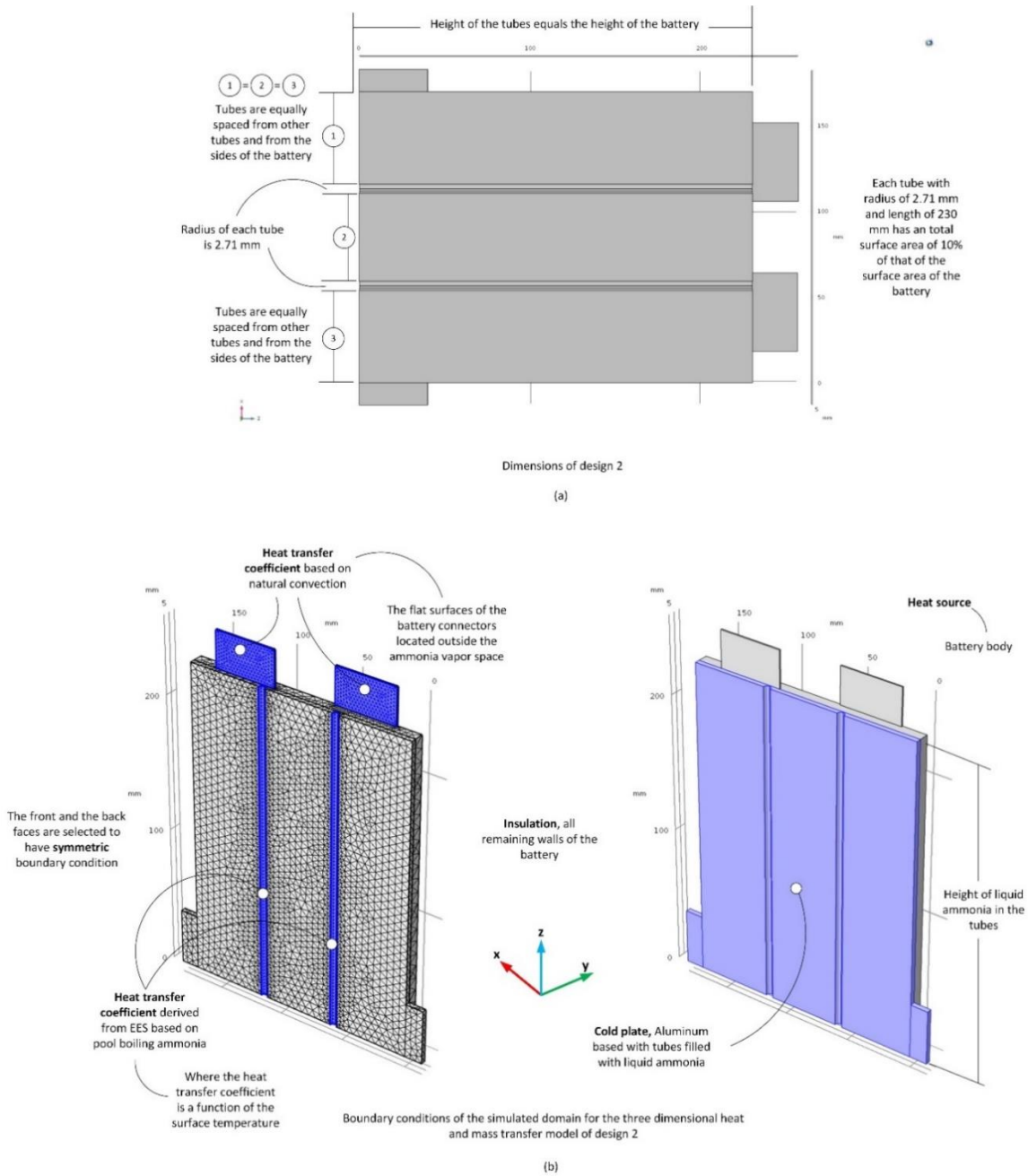

Figure 4.8 (a) Dimensions of the proposed design of the ammonia boiling based thermal management system, and (b) boundary conditions of the simulated three dimensional heat transfer model.

Due to the symmetric configuration of the batteries and the cold plates in the pack, as shown in the system description chapter, only a single battery and half of a cold plate equipped with symmetric boundary conditions is simulated. A transient three dimensional heat transfer model is used to assess the performance of the proposed cooling system, as shown in Figure 4.8(b). The dimensions of the structure of the aluminum cold plate with embedded liquid boiling stagnant liquid ammonia is shown in Figure 4.8 (a). The diameter

of each tube in the cold aluminum plate is selected so that half of the surface area of the tube is equal to 5% of the front surface of the battery. The tubes in the cold plate are distributed at equal distances. The boiling of ammonia in the tubes is assumed to be pool boiling, since the relative motion of the vapor produced and the surrounding liquid is mainly due to buoyancy effect. The heat transfer coefficient for the surface of the tube is set as the heat transfer coefficient of pool boiling, and is a function of the surface temperature of the tube.

The correlation is based on the surface temperature of the battery that it is in direct contact with the stagnant liquid ammonia, as the pool boiling starts at a surface temperature 5°C higher than the boiling temperature of the stagnant liquid ammonia at a specified pressure. Symmetric boundary conditions are selected for the surface of the battery in contact with the neighboring battery and the surface at the middle of the cold aluminum plate. The connectors of the battery are considered to be subject to natural convection with the surrounding air. The boundary conditions used for the three dimensional heat transfer model are illustrated in Figure 4.8(b).

The stagnant liquid ammonia filling the tubes in the aluminum cold plate are at a pressure of 9.0 bar, so the corresponding saturation temperature (21.5^{o}C) is lower than the ambient temperature of 25°C [127]. The proposed BCS is assessed for a 600 second discharging and charging cycle at a rate equal to 4C. A current of 4C is four times the current that would completely discharge or completely charge a battery with a capacity of C Ah within an hour.

4.2.1.3 System 4

The boundary conditions used for the one dimensional electrochemical model and the three dimensional mass and heat transfer model are presented in Figure 4.9(a) and Figure 4.9(b), respectively. The three dimensional model developed here simulates the heat and mass phenomena in the battery itself, the propane pool and the propane vapor generated. Note that one of the key advantages of the COMSOL Multiphysics software is that it can simulate in a single domain more than a physical one, which means that the temperature variations in the propane and the battery can simultaneously be simulated. In the three dimensional model, the propane vapor enters the propane vapor space shown in Figure 4.9 from the surface of the liquid propane pool in the battery pack as shown in Figure 4.9, where the proposed cooling system is described. The propane vapor entering the vapor space between the batteries is a saturated vapor, so its temperature is that of the boiling propane pool. The surface of the propane pool was selected as an inlet boundary condition as shown in Figure 4.9(b), where the inlet flow rate is selected based on the evaporation rate from the boiling propane pool. The propane vapor is collected through a channel along the pack leading to the pressure regulator and propane collector. The inlet to the collection channel is set to be the outlet of the vapor domain between the batteries as shown in Figure 4.9(b). The surface of the battery pack that is covered by propane liquid is set to have a heat flux boundary condition, where the heat transfer coefficient is based on the vertical plane pool boiling correlation imported from EES when the battery temperature is 5°C higher than the saturation temperature of the liquid propane pool. However, when the temperature of the battery surface submerged in the propane pool is higher than its saturation temperature, but with a temperature difference less than 5°C, then natural convection heat transfer correlation imported from EES is used.

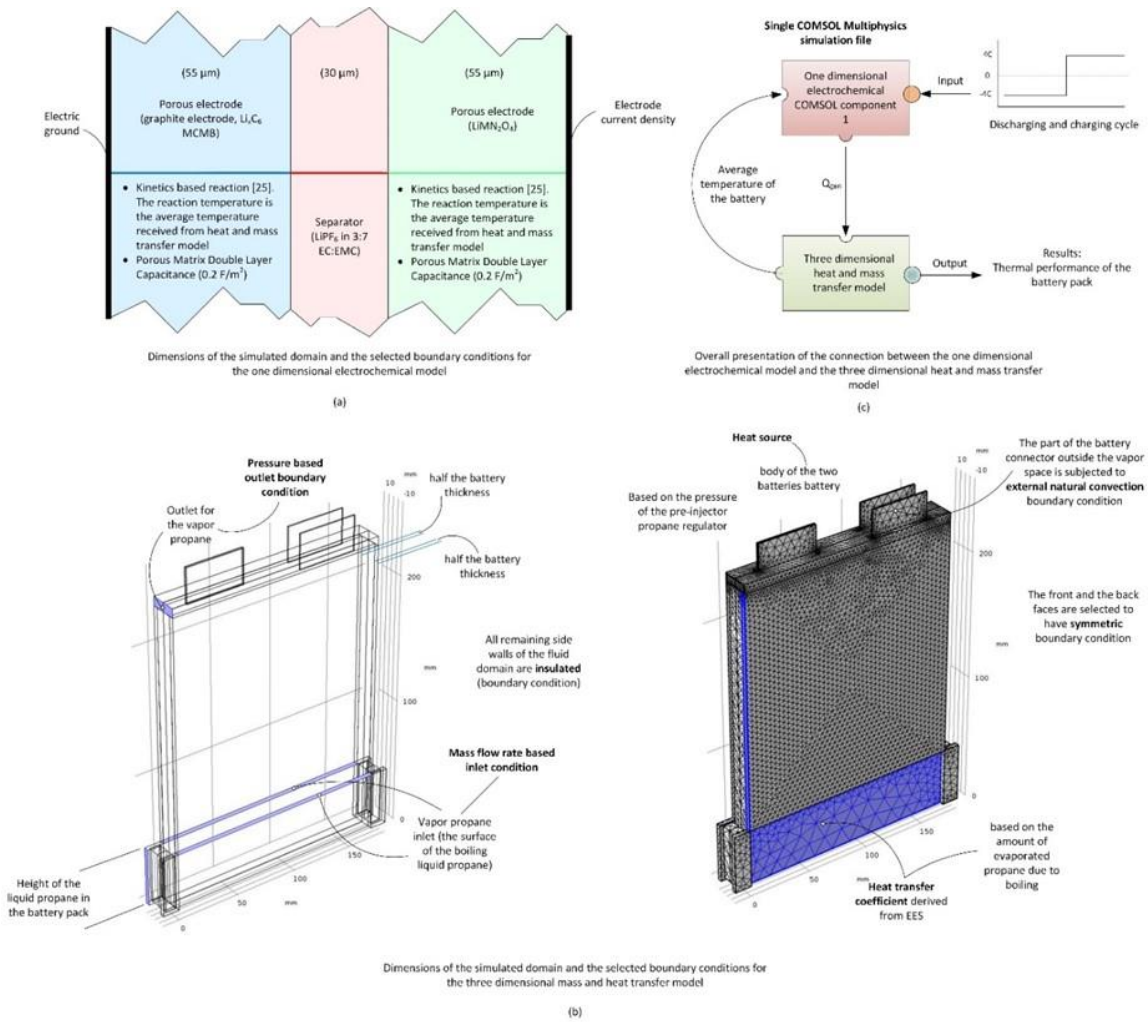

Figure 4.9 Boundary conditions and dimensions of (a) one dimensional electrochemical model, and (b) three dimensional mass and heat transfer model, and the integration between the two models (c) overall presentation of the connection between the one dimensional electrochemical and three dimensional heat and mass transfer models.

The flow of the vapor phase of the propane is modeled as laminar flow, since the Reynolds number is calculated to be far below the critical Reynolds number. The Reynolds number of the propane vapor is calculated based on internal flow, where the inlet area is the surface of the propane pool in the pack. The Reynolds number for the propane vapor varies continuously as the mass flow rate of the propane vapor flowing through the rectangular channel where the battery pack is accommodated. It also changes throughout the charging and discharging cycles as calculated by

$$\mathrm{Re} = \frac{\rho V D_h}{\mu} \tag{4.25}$$

where the D_h is the hydraulic diameter, μ is the dynamic viscosity, ρ is the density, and V is the mean velocity. The highest velocity of the propane vapor through the discharging and charging steps occurs at the end of the cycle with an average value of 0.0375 m/s, which results in a Reynolds number of 130.8.

The pressure of the propane pool surrounding the batteries in the pack is selected to be 8.5 bar, based on the saturation temperature of 20.8°C, so that when the surface temperature of the battery slightly increases the propane pool starts boiling. The ambient temperature considered in this study is equal to 25°C [127]. The performance of the battery pack cooling system is investigated by discharging the batteries in the pack for 300 seconds and then charging for 300 seconds consecutively at a rate of 4C, which is four times the rate at which the battery capacity will be completely discharged or charged in one hour. In order to ensure that the model results are independent on the number of elements in the mesh, a grid independence test was performed. The grid independence test, in this regard, considered the variation of the maximum temperature of the battery and the maximum temperature of the vapor propane in the battery pack with the variation of the mesh quality of the developed model. It is found that increasing the number of mesh elements beyond 159,794 elements results in an increase in the maximum temperature by 0.003% as shown in Figure 4.10.

Regarding the maximum temperature of the vapor propane, it will remain constant for a mesh with higher number of mesh elements than 159,794. Out of the selected 159,794 mesh elements, a total of 120,257 are dedicated for the propane space, while the remaining is for the battery.

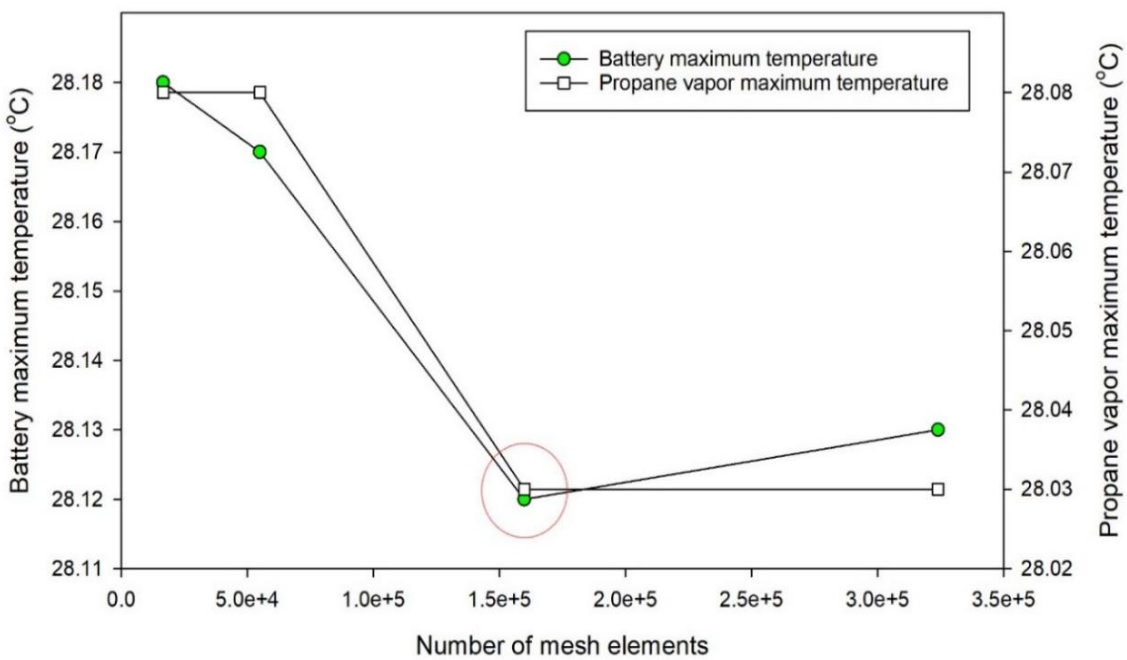

Figure 4.10 Effect of the mesh on the model results in terms of the battery maximum temperature and the propane vapor leaving the pack maximum temperature.

4.2.1.4 System 5

The prismatic battery boundary conditions are presented in Figure 4.11 where the schematic is used to show the selected boundary conditions to make it easier for the reader to understand the selected boundary conditions and the set parameters. Unlike the propane and the ammonia based systems the boiling is simulated through the phase change domain rather than using the experimental correlations.

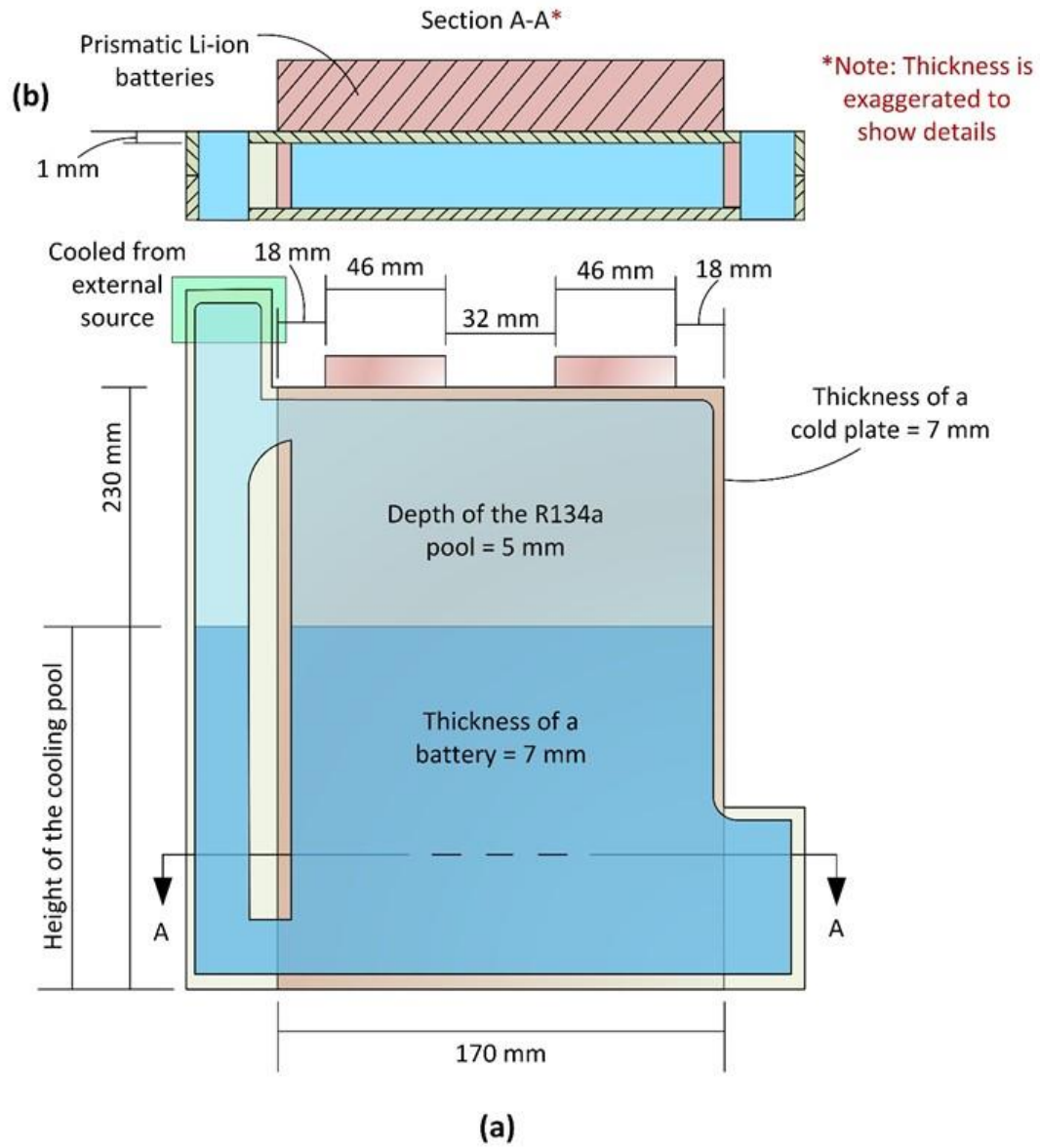

Figure 4.11 Schematic diagram of the R134a based cooling system for the prismatic battery pack showing (a) the front view of the section cut through the R134a cooling space and (b) is the top view.

Note that for the details for the selected and used boundary conditions for simulating the refrigerant based battery thermal management system used for prismatic battery packs are the same as those used in Figure 4.9.

4.2.2 Cylindrical battery model

The governing equations of the thermodynamics and heat and mass transfer model are similar to those presented in section 4.2.1, which is the governing equations for the thermodynamics and heat and mass transfer model of the prismatic battery. The only difference will be in the equations used to calculate the battery overall thermal conductivity

of the battery in the different directions, which are calculated based on the cylindrical coordinates rather than the prismatic coordinates as follows:

$$k_r = \frac{\sum L_i}{\sum (L_i/k_i)} \tag{4.26}$$

$$k_z = \frac{\sum (L_i \times k_i)}{\sum L_i} \tag{4.27}$$

where k_r and k_z are the overall thermal conductivities of the battery in the radial and axial directions, which are calculated through the thermal conductivity of each layer k_i, and the thickness of each layer L_i.

The coming subsections presents the boundary conditions used to model each of the thermodynamics and heat and mass transfer model of each system. Note that system 1 and system 3 which are the air and the hydrogen based systems for the cylindrical configuration they are not simulated since the novelty in these systems does not require the simulation of the cylindrical battery packs.

4.2.2.1 System 2

To better understand the cooling effect provided by the PSLA based cooling system, the simulated domain, its dimensions and the boundary conditions used in the simulation are shown in Figure 4.12. Due to the vertical motion of the ammonia vapor in the pack, all batteries are expected to have matching temperature distributions. Not all the thermophysical properties for ammonia in the gas phase are available in COMSOL library, so missing properties are imported from Engineering Equation Solver (EES).

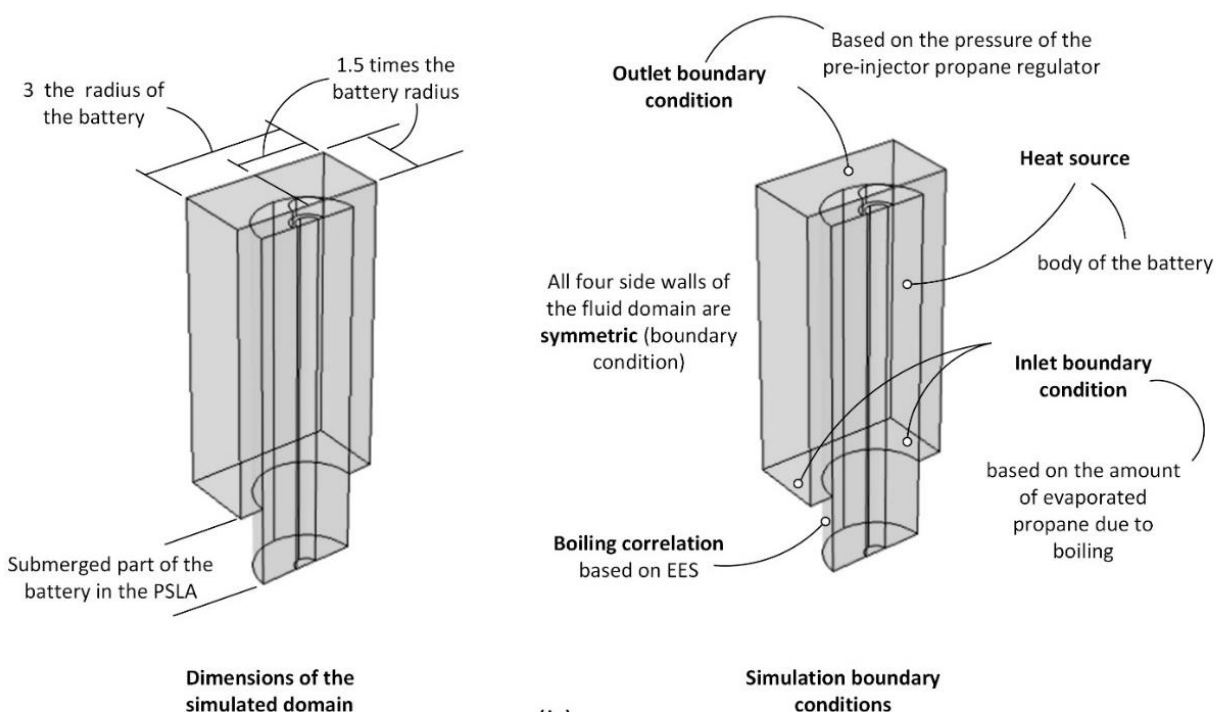

Figure 4.12 Dimensions and boundary conditions of the simulated battery and cooling domain of the three dimensional heat and mass transfer model.

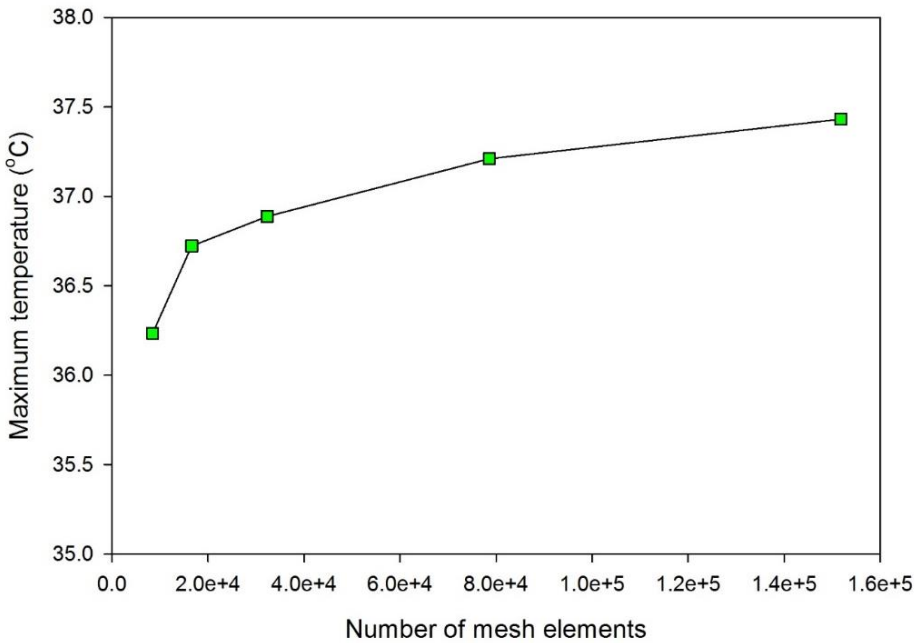

Figure 4.13 Mesh independence study (note that the e in the horizontal axis refers to 10 raised to the power of the number following the e latter).

In the heat and mass transfer model, ammonia becomes a vapor at the surface of the PSLA as shown in Figure 4.12, which presents the boundary conditions used in the developed model. The mass flow rate and the inlet temperature of the ammonia vapor are based on the boiling temperature and the amount of evaporated ammonia from the PSLA. The upper surface of the selected domain that is shown in Figure 4.12 is selected as the outlet boundary condition since the ammonia vapor flowing upward is collected by the pressure regulator. The submerged portion of the Li-ion battery in the PSLA is selected as a convection heat transfer boundary condition, where the boiling heat transfer coefficient is defined by a nucleate boiling correlation imported from Engineering Equation Solver (EES) for battery surface temperatures 5ºC above the saturation temperature of PSLA. For cases when the battery surface temperature is less than 5ºC above the saturation temperature, the free natural convection correlation is used from EES. The part of the battery not covered by liquid is taken to be subject to a convection heat transfer boundary condition, at the battery surface.

Two pressure values of the PSLA are considered here: 9.0 bar and 10.0 bar. These correspond to saturation temperatures of 21.5ºC and 24.9ºC respectively. Both pressure values give a saturation temperature slightly below the ambient temperature considered in this study (25ºC) [127]. The model insensitivity to the mesh is ensured by performing a mesh independence study where the sensitivity of the maximum temperature of the battery at the end of the charging process on the mesh is examined (see Figure 4.13). That figure shows that as the number of the mesh elements reaches 151,793 the maximum temperature changes by less than 0.6%. The charging and discharging durations are 600 seconds in total, 300 seconds each with a high charging and discharging rate of 7.5C simulating the high power demand in HEVs. The battery initial charged state is set to 10%.

4.2.2.2 System 4

For the cylindrical battery pack that uses propane as the coolant two different studies were carried out one using a correlation to simulate the boiling while the other one uses a phase change validated boiling simulation to further investigate the model to carry out the optimization for the proposed system. The boiling correlation based model is presented first including the set boundary conditions and then followed by the boiling validated model.

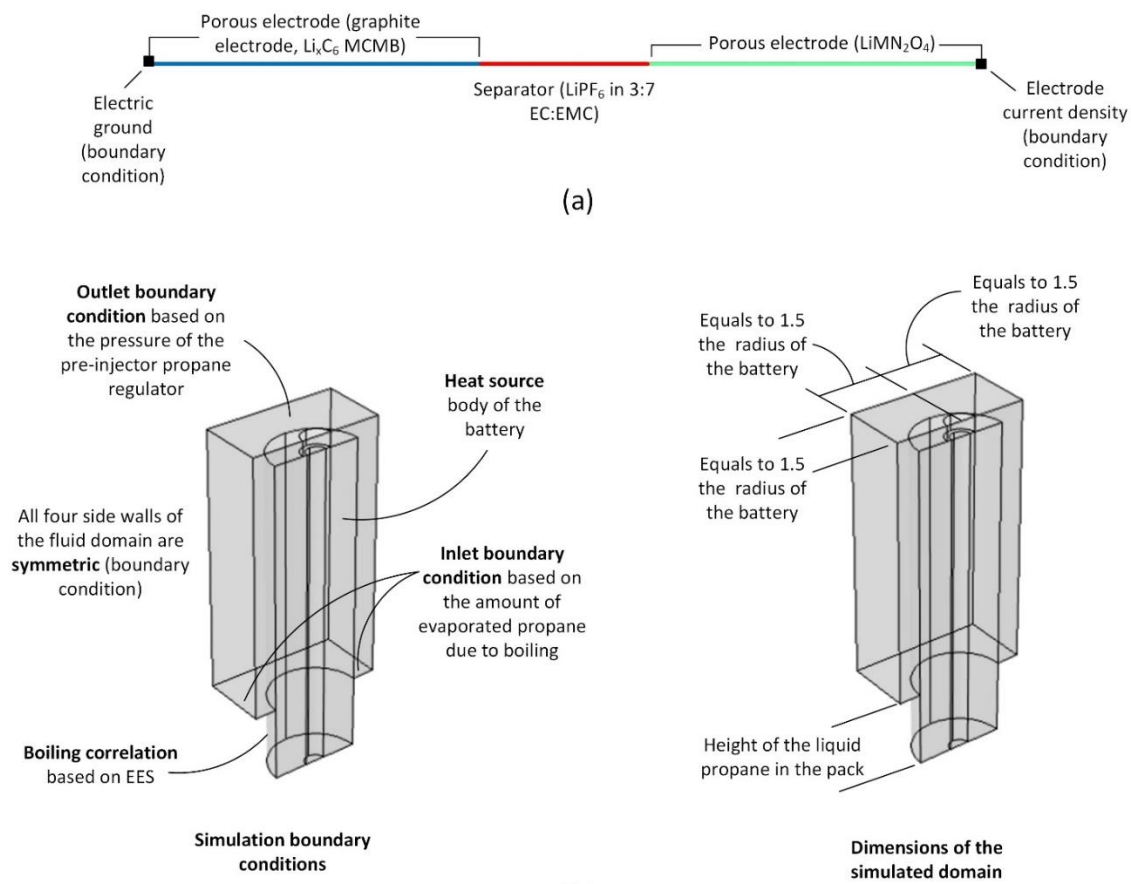

Figure 4.14 Dimensions and boundary conditions of the simulated battery and cooling domains. (a) one dimensional model of the electrochemical reactions in a battery cell, (b) three dimensional heat and mass transfer model.

Only half of a single battery with its surrounding is considered due to the selection of symmetric boundary conditions as shown in Figure 4.14. The flow derives from boiling the liquid propane and the propane vapor rises due to two forces: buoyancy and the pressure difference. Due to the vertical motion of the propane vapor, all the batteries in the pack are expected to have the same temperature distribution. Liquid and vapor propane thermophysical properties are a function of temperature and they are available in COMSOL library.

The dimensions, material properties, kinetics of the electrochemical reactions and parameters of the Li-ion battery considered in this thesis are adapted from Doyle et al.

[125]. The boundary conditions used to define the one dimensional model are shown in Figure 4.14.

The inlet mass flow for the propane vapor is selected based on the surface of the liquid propane, where the value of the mass flow rate depends on the amount of propane evaporated during boiling and the outlet conditions are those at the upper outlet boundary condition, as shown in Figure 4.14. The submerged portion of the battery surface is modeled with a convection boundary condition and a heat transfer coefficient defined by a nucleate boiling correlation. The correlation used here is generated in Engineering Equation Solver (EES) for a surface temperature 5ºC above the boiling temperature of the liquid propane with free natural convection at lower surface temperatures. The remaining part of the battery surface is considered to be subject to convective heat transfer. The pressure of the liquid propane is 8.5 bar, which corresponds to a saturation temperature of 293.75 K. This pressure was selected at slightly below the tank pressure (9 bar) to give a saturation temperature slightly below the optimum operating temperature for the battery (25ºC) [127]. An independent analysis of the sensitivity of the maximum temperature of the batteries to the mesh (number of elements) was carried and the results are shown in Fig. 4, where the number of mesh elements selected is seen to be 151,793. The battery was charged for 300 seconds and then discharged for 300 seconds, with charging and discharging currents of 7.5C and starting with a state of charge of 10%.

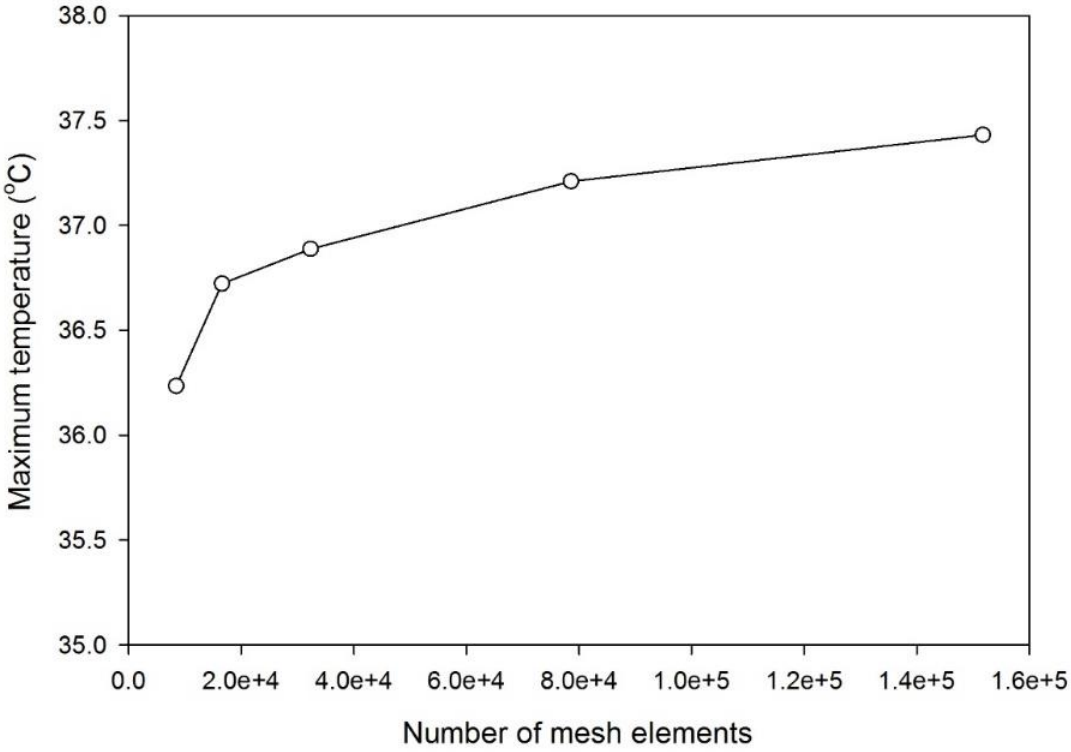

Figure 4.15 Mesh independence study

The simulated heat and mass transfer domain and the selected boundary conditions are shown in Figure 4.16(a) and Figure 4.16 (b). Figure 4.16 (c) shows the variation of the mesh element sizes throughout the simulated domain. Note that both the vapor space and

the battery electrical connections are not included in the simulated domain due to previously mentioned reasons. The volumetric heat generation rate that results from the one dimensional electrochemical model is fed to the three dimensional heat and mass transfer battery model.

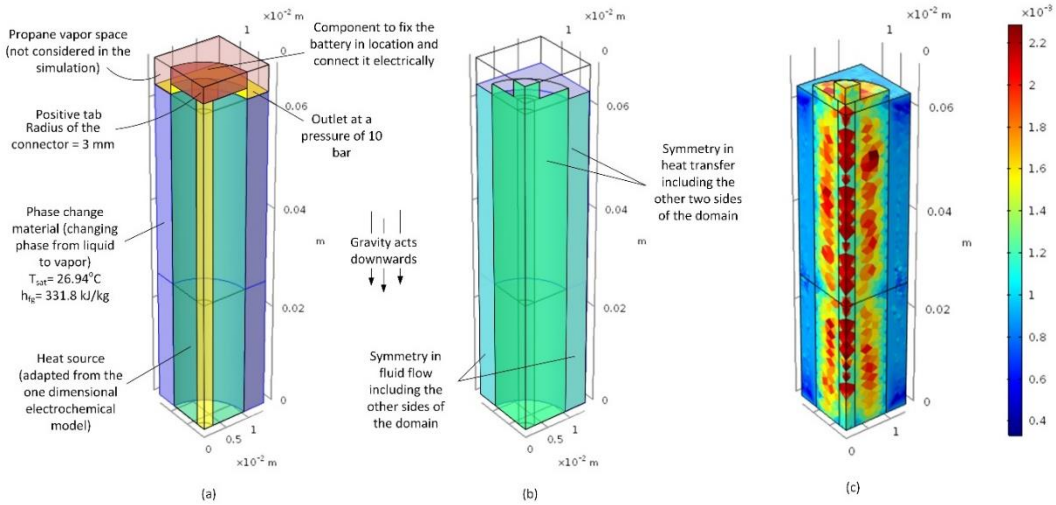

Figure 4.16 (a) Simulated domain in the heat and mass transfer model, (b) selected boundary conditions and (c) mesh plot of the variation of the mesh elements size in m^3.

4.2.2.3 System 5

It was earlier shown in section 5.2 through various studies that ELP based BCSs have a high temperature uniformity throughout the battery pack. That and the symmetric configuration of the battery pack allows only half of a single battery and its surrounding domain to be simulated as shown in Figure 4.17. Figure 4.17 also gives the dimensions of the simulated domain for the two designs of the pack. The second part of the modeling is the heat and mass transfer model, which is modeled and simulated in three dimensions. The heat and mass transfer model communicates with the one dimensional electrochemical model by sending the battery average temperature to the electrochemical model and receiving the volumetric heat generation rate from the electrochemical model. The simulated domain and the selected boundary conditions are shown in Figure 4.17(b), where the location and the size of that domain within the battery pack is shown in Figure 4.17(a). As shown in Figure 4.17(b) the boiling correlation is applied to the battery surface that is submerged in the liquid refrigerant pool, where the correlation is a function of that surface temperature. Note that when the temperature difference between the saturation temperature of the refrigerant and the battery surface is less than 5°C then refrigerant evaporates due to heat gain through natural convection between the liquid and the battery surface. The symmetric boundary condition is applied to the side walls of the refrigerant domain as shown in Figure 4.17(b) to account for the heat generated by the neighboring batteries. In the heat and mass transfer model, modeling the flow as either laminar or turbulent depends on the Reynolds number of the R134a vapor, which is calculated based on the internal flow formula, where the inlet area of the flow is taken as the surface of the liquid R134a pool in the pack.

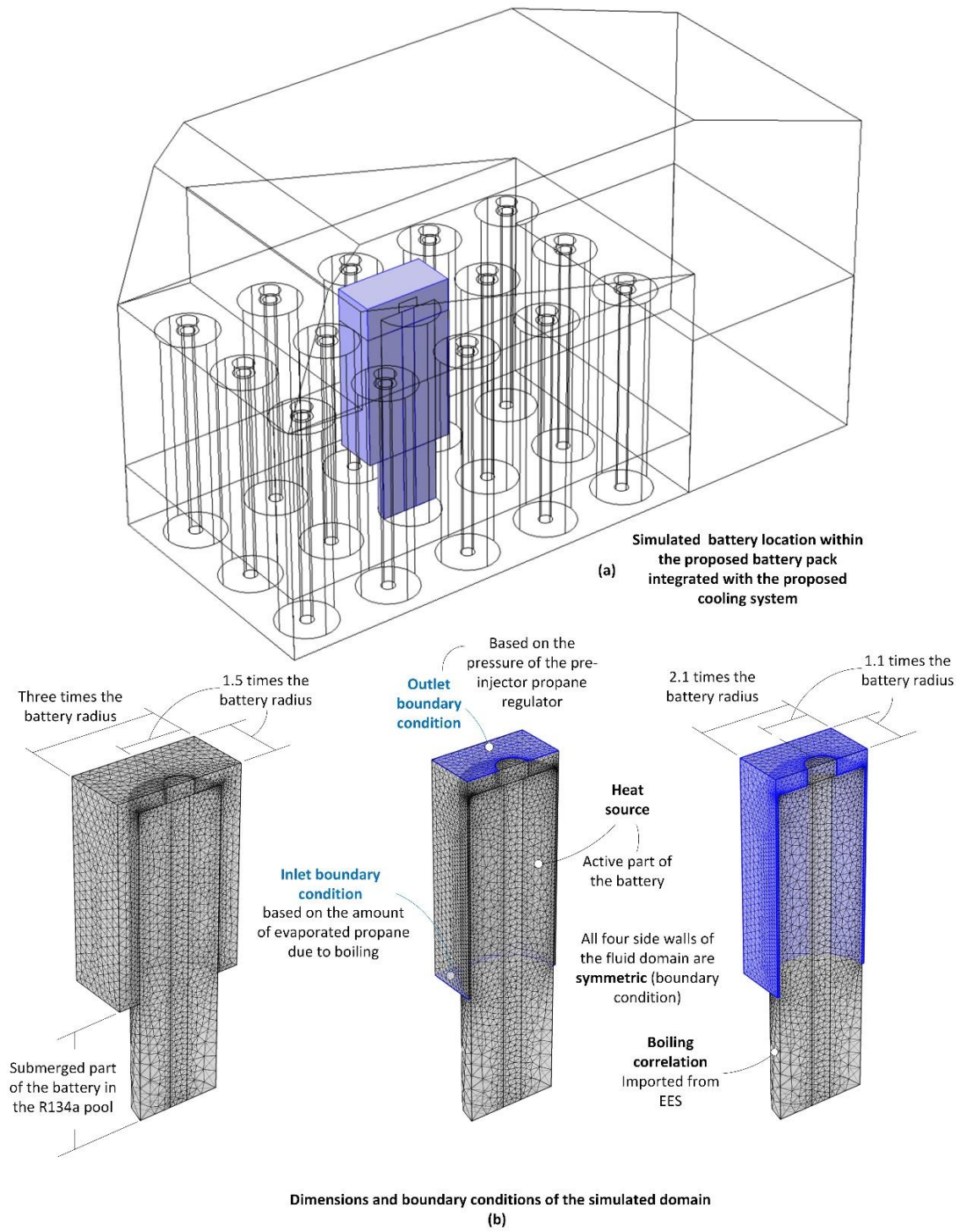

Figure 4.17 (a) The simulated domain location and size within the battery pack that is cooled by the proposed system. (b) Dimensions and boundary conditions of the two cases considered for the three dimensional heat and mass transfer model (note that the text presented in blue color is to distinguish between the heat transfer boundary conditions and the fluid flow boundary conditions, which are in blue).

The flow rate of the vapor R134a varies through the charging and discharging cycles continuously, which means the decision on whether the flow Reynolds number passes the critical value or not has to be determined based on the maximum achievable flow rate. From all the variations of the system and operating parameters considered, the configuration that is expected to achieve the highest Reynolds number is: 8C charging and discharging cycle rate, the liquid pool covers 80% of the battery and the compact design of the two designs considered. The formula used to calculate the Reynolds number is as follows:

$$\mathrm{Re} = \frac{\rho V D_h}{\mu} \tag{4.28}$$

where ρ is the density, V is the vapor mean velocity, D_h is the hydraulic diameter and μ is the dynamic viscosity. The highest velocity the R134a vapor achieves through 600 seconds, 8C charging and discharging cycle is 9.23 mm/s which results in a Reynolds number of 172, which is away below the critical Reynolds number for internal flow. Then the flow of the R134a vapor is modeled as laminar.

4.3 Optimization study

The proposed systems are optimized by using the Genetic Algorithm model. The Genetic Algorithm was selected to optimize the proposed system due to a number of reasons, one of these reasons being it can be used to optimize a large number of variables for non-linear systems. Another reason is that the genetic Algorithm model work through the different variables to find the global extrema (maximum and minimum points) and avoid being tricked with the local extrema points. A third reason is that most of the modeling and simulation software have an embedded Genetic Algorithm models that can be used easily without the need to program it from scratch. In comparison with the traditional optimization methods, the genetic method generates the different possible points in parallel, rather than from a single point. In addition, the genetic algorithm does not require derivative information or other auxiliary knowledge, only the corresponding fitness levels and the objective function affect the direction of the research. Due to the many advantages the method has, the method is selected to optimize the proposed system.

The Genetic algorithm can be defined as an optimization tool that is based on the natural selection in the concept of evolution. The algorithm starts with a setoff population of individual solution and then during each following step through the optimization process it continuously changes the population of the individual solutions. The method the algorithm goes through to generate different populations is by first randomly selecting individuals from the current population of solutions and then use those which were selected randomly as parents of the next population of solutions. The final results of the optimization or the final population of solutions that corresponds to the optimized solution is called the Pareto optimum points, which are the optimum of the objective function. A Pareto point is defined as the optimum point allocations when there is no way of improving it for any of the objectives without worsening any of the other objectives.

There are five different proposed systems, where some of them are based on the concept of single phase flow through either cooling channels or directly through the battery, while others are based on two phase flow and a heat transfer medium between the

coolant and the battery. Others are based on a static boiling pool that can either have a direct contact with the batteries or have a heat transfer medium. Others will be passive in their cooling while others are active, where also the active systems a passive case study is considered for them. Due to the specific operating conditions and features, each system has its own objective function and constrains as listed in Table 4.1.

Table 4.1. Summary of the five main proposed systems based on coolant type, and its applicability to work in EVs and HEVs.

System	**Objectives**	**Constraints**
System 1 and 3	-Pack average and maximum temperature -Battery average and maximum temperature -Temperature difference across the pack and the battery -Mass flow rate of the coolant	-Pressure of the coolant -Initial temperature of the coolant -Cooling channel geometry
System 2, 4 and 5	-Pack average and maximum temperature -Battery average and maximum temperature -Temperature difference across the pack and the battery -Mass flow rate of the NH_3	-Pressure of the coolant -Height of the liquid pool in the pack -Cooling plate design -Geometry of the cooling plate -Nature of the contact between the coolant and battery -Number of cooling plates per batteries

4.3.1 System 1

System 1, is a hydrogen cooled metallic made cold plate, where the compressed hydrogen is throttled from the tank pressure to a specific operating pressure, which will be the hydrogen pressure at the cold plate inlet. The hydrogen temperature at the inlet, and the hydrogen flow channel shape and size are the different variables that can be changed in the proposed system. Where the main objectives of the functions are to have minimum temperature difference across the battery, a maximum temperature in the pack is within the optimum operation range, minimum temperature difference through the pack and with the minimum possible hydrogen flow rate. The function of system 1 considered parameters in the optimization in terms of other system operating parameters can be written as follows:

$$\left(T_{pack}, T_{battery}, \Delta T_{pack}, \Delta T_{battery}, \dot{m}_{H_2}\right) = f(P_{H_2}, T_{H_2}, \text{Channel geometry}) \qquad (4.29)$$

Here, T_{pack} refers to the temperature of the battery pack, $T_{battery}$ refers to the temperature of the battery with the maximum temperature in the pack, ΔT_{pack} maximum temperature difference within the pack, $\Delta T_{battery}$ the maximum temperature difference within a single battery that has the maximum temperature difference in the pack and $\dot{m}_{H_2}$ refers to the mass flow rate of the hydrogen entering the cooling plate. P_{H_2} is the pressure of the hydrogen entering the cooling system and T_{H_2} is the temperature of the hydrogen entering

the pack. The variables are varied within the allowable range bounded by the upper and lower limits that are listed in Table 4.1.

Table 4.2. The upper and lower bounds of the variables of system 1.

Variable	Lower limit	Upper limit	Units
P_{H_2}	20	700	bar
T_{H_2}	-140	50	ºC
Channel geometry	Pipe with radius equal to the inlet	Full plate with borders thickness of 2 mm	

4.3.1 System 2

System 2 is an ammonia based battery thermal management system proposed for future ammonia fueled HEVs that are under investigation at the University of Ontario Institute of Technology. The liquid ammonia in the tank is used to cool the batteries and then used to generate power through the engine of the vehicle, where it can be an internal combustion engine or a fuel cell or other devices. The variables of the system depend on the cooling configuration of the proposed battery thermal management system, where pool based system have the following variables: pool height, thickness of the pool, direct or indirect contact, pressure of the ammonia pool, number of batteries between each cooling plate and the shape and size of the pool. The main objectives are to have minimum temperature difference across the battery, minimum maximum temperature in the pack, minimum temperature through the pack and minimum consumption of the ammonia tank. The objective function of system 2 can be written as follows:

$$\left(T_{pack}, T_{battery}, \Delta T_{pack}, \Delta T_{battery}, \dot{m}_{NH_3}\right) = f(P_{NH_3}, h_{NH_3}, \text{cooling plate design}, t_{NH_3}, N) \tag{4.30}$$

Here, $\dot{m}_{NH_3}$ is the mass flow rate of the liquid ammonia going to the battery pack, h_{NH_3} is the height of the liquid ammonia pool, t_{NH_3} is the thickness of the pool, and N is the number of batteries between the cooling plates.

The variables are varied within the allowable range bounded by the upper and lower limits that are listed in Table 4.3.

Table 4.3. The upper and lower bounds of the variables of system 2.

Variable	Lower limit	Upper limit	Units
P_{NH_3}	2	10	bar
h_{NH_3}	5% of the battery height	100% of the battery height	%
Cooling plate design	Vertical pipe with a radius large enough to have a negligible capillary effect	Full plate with borders thickness of 2 mm	
t_{NH_3}	50% of the battery thickness	300% of the battery thickness	%
Nature of the contact	Direct contact	Indirect contact	
Number of batteries (N)	1	10	

4.3.2 System 3

System 3 is an air based battery thermal management system proposed for pneumatic HEVs, where the compressed air is throttled from the tank pressure to a specific operating pressure in the vehicle main driver, the vehicle turboexpanders produces the driving power of the vehicle and as a result the expander produces a cold air that can be used to maintain the temperature of the battery pack within the optimum operation range. The variables of the system include the air inlet temperature to the pack, the channel shape and size in the cold plate and the number of batteries between the cooling plates. Where the main objectives of the functions are to have minimum temperature difference across the battery, minimum maximum temperature in the pack, minimum temperature through the pack and minimum hydrogen flow rate. The objective function of system 3 can be written as follows:

$$\left(T_{pack}, T_{battery}, \Delta T_{pack}, \Delta T_{battery}, \dot{m}_{Air}\right) = f(P_{Air}, T_{Air}, \text{Channel geometry}, N) \qquad (4.31)$$

Here, $\dot{m}_{Air}$ refers to the mass flow rate of the air entering the cooling plate. P_{Air} is the pressure of the air entering the cooling system and T_{Air} is the temperature of the air entering the pack.

The variables are varied within the allowable range bounded by the upper and lower limits that are listed in Table 4.4.

Table 4.4. The upper and lower bounds of the variables of system 3.

Variable	Lower limit	Upper limit	Units
P_{Air}	10	200	bar
T_{Air}	-50	50	ºC
Channel geometry	Pipe with radius equal to the inlet	Full plate with borders thickness of 2 mm	

4.3.3 System 4

System 4 is a liquid propane based battery thermal management system proposed for propane fueled HEVs. The liquid propane in the tank is used to cool the batteries and then used to generate power through the engine of the vehicle, which is an internal combustion engine. The variables of the system depend on the cooling configuration of the proposed battery thermal management system, where pool based system have the following variables: pool height, thickness of the pool, direct or indirect contact, pressure of the ammonia pool, number of batteries between each cooling plate and the shape and size of the pool. The main objectives are to have minimum temperature difference across the battery, minimum maximum temperature in the pack, minimum temperature through the pack and minimum consumption of the ammonia tank. The objective function of system 4 can be written as follows:

$$\left(T_{pack}, T_{battery}, \Delta T_{pack}, \Delta T_{battery}, \dot{m}_{C_3H_8}\right) = f(P_{C_3H_8}, h_{C_3H_8}, \text{geometry}, t_{C_3H_8}, N) \quad (4.32)$$

Here, $\dot{m}_{C_3H_8}$ is the mass flow rate of the liquid propane going to the battery pack, $h_{C_3H_8}$ is the height of the liquid propane pool, $t_{C_3H_8}$ is the thickness of the pool, and N is the number of batteries between the cooling plates.

The variables are varied within the allowable range bounded by the upper and lower limits that are listed in Table 4.5.

Table 4.5. The upper and lower bounds of the variables of system 4.

Variable	Lower limit	Upper limit	Units
$P_{C_3H_8}$	2	10	bar
$h_{C_3H_8}$	5% of the battery height	100% of the battery height	%
Cooling plate design	Vertical pipe with a radius large enough to have a negligible capillary effect	Full plate with borders thickness of 2 mm	
t_{NH_3}	50% of the battery thickness	300% of the battery thickness	%
Nature of the contact	Direct contact	Indirect contact	
Number of batteries (N)	1	10	

4.3.4 System 5

System 5 is a liquid refrigerant based battery thermal management system proposed for all different types of vehicles that uses a battery pack as a part of the driving system. The liquid refrigerant in the tank is used to cool the batteries, where its evaporation temperature is set to a value that will allow it to condense at ambient temperature and then goes back to the supply pool. The variables of the system depend on the cooling configuration of the proposed battery thermal management system, where pool based system have the following variables: pool height, thickness of the pool, direct or indirect contact, pressure of the refrigerant pool, number of batteries between each cooling plate and the shape and size of the pool. The main objectives are to have minimum temperature difference across the battery, minimum maximum temperature in the pack, minimum temperature through the pack and minimum consumption of the ammonia tank. The objective function of system 5 can be written as follows:

$$\left(T_{pack}, T_{battery}, \Delta T_{pack}, \Delta T_{battery}, \dot{m}_{ref}\right) = f(P_{ref}, h_{ref}, \text{geometry}, t_{ref}, \text{contact}, N) \quad (4.33)$$

Here, $\dot{m}_{ref}$ is the mass flow rate of the liquid refrigerant going to the battery pack, h_{ref} is the height of the liquid refrigerant pool, t_{ref} is the thickness of the pool, and N is the number of batteries between the cooling plates. The variables are varied within the allowable range bounded by the upper and lower limits that are listed in Table 4.6.

Table 4.6. The upper and lower bounds of the variables of system 5.

Variable	Lower limit	Upper limit	Units
P_{ref}	2	10	bar
h_{ref}	5% of the battery height	100% of the battery height	%
Cooling plate design	Vertical pipe with a radius large enough to have a negligible capillary effect	Full plate with borders thickness of 2 mm	
t_{ref}	50% of the battery thickness	300% of the battery thickness	%
Nature of the contact	Direct contact	Indirect contact	
Number of batteries (N)	1	10	

Chapter 5: Results and Discussion

In this chapter, the results of the proposed battery thermal management systems are presented in this chapter, where the chapter first starts with validating the developed models with experimental results from the literature. Where the validation is done for both parts of the model including the electrochemical and heat transfer and mass flow models. Then the chapter goes in analyzing each of the proposed systems, analyzing first the systems applied to prismatic battery packs and then when the systems are applied to cylindrical battery packs. Finally, for each battery geometry that is considered the performance is compared and the best performing systems are compared to those that were published in the literature. Note that the optimization studies are presented throughout the thesis through the analysis of each of the proposed models and those parameters performing the best are reported as well.

5.1 Model Validation

This section in the results and discussion chapter deals with the validating the models developed to investigate the performance of the proposed novel battery pack systems. First the section starts with validating the electrochemical model of the battery with the literature then the section will continue to validate the boiling modeling and simulation proposed in this thesis that is used as the heart of the simulation of the three of the proposed systems. The boiling in this thesis will be simulated on two forms of surfaces that are the surfaces of the batteries or the contact cold plate between the battery and the boiling pool. These surfaces are the cylindrical surface and the prismatic surface. So the boiling validation is carried out for both surfaces with experimental results from the literature.

5.1.1 Electrochemical modeling results

The battery electrochemical model is built as was presented in section 4.1, where it presents the building of the battery electrochemical model. The validation of the electrochemical model is done through the comparison between the variation of the cell potential against the attainable capacity for the cell at various discharge rates produced by the developed battery electrochemical model with the experimental results published in Doyle et al [125]. Multiple discharge rates were considered varying from a low discharge rate of 0.1C up to a discharge rate of 2C. Figure 5.1 shows the comparison between the results produced by the simulation and those experimental results from Doyle et al. [125] work. As shown in Figure 5.1 the model accurately predicts the electrochemical behavior of the lithium ion battery cell considered in this thesis.

The developed model in COMSOL simulating the experiment done in [128] is presented in Figure 5.2. Note that Figure 5.2 is contracted by revolving a two dimensional system model since the geometry and the boundary conditions are axially symmetric. Most studies that are concerned with predicting the pool boiling behavior concentrate on the interference between the forming bubbles and the liquid surrounding them [129–131]. However, in these studies the focus on the nucleation sites of the bubbles, the shape of the nucleation sites, their number and their distribution as well makes the model complicated and specific to material, geometrical and temperatures limitations. In this thesis, a boiling

model is developed that does not depend on the nucleation sites properties, where its main goal is to model with correlations accuracy the high boiling heat transfer rate.

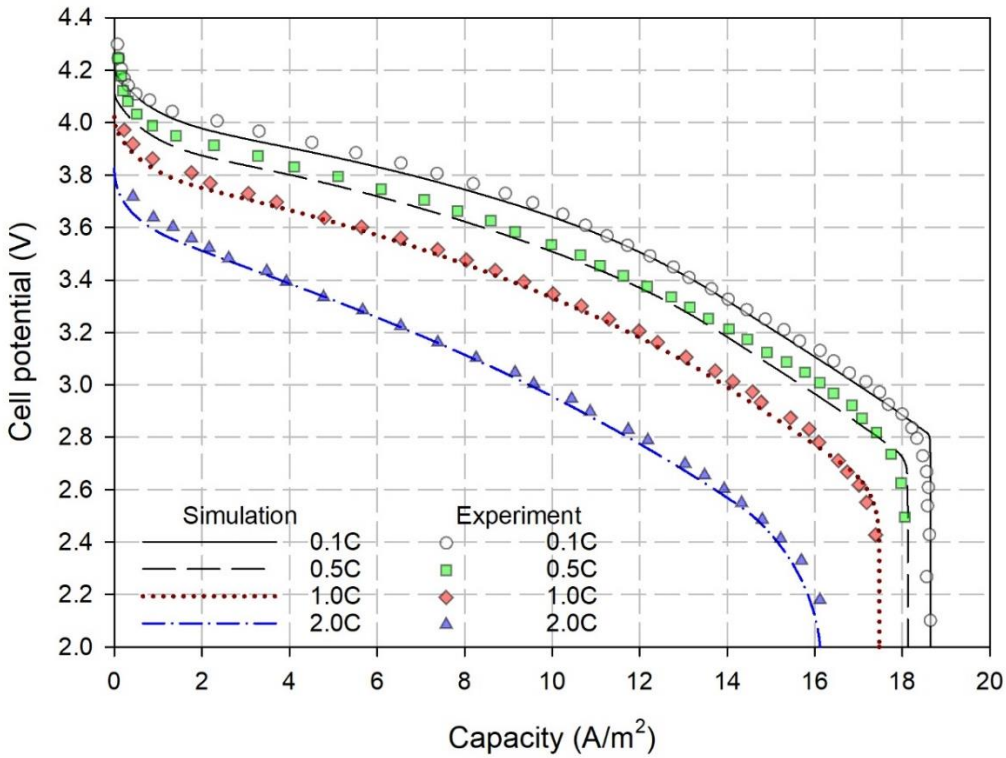

Figure 5.1 Comparison of the variation of the cell potential with the capacity of the cell at different discharge rates where the model considers $900\ \Omega.\mathrm{cm}^2$ a film resistance on the negative electrode between the developed model and the experimental results done by Doyle et al [125].

5.1.2 Boiling modeling results of the battery

Due to the lack of experimental research on the boiling heat transfer rate of vertical cylindrical metallic surface, however there are number of experimental studies concerning close geometry to the battery with metallic surface under high heat rate of water boiling. The boiling model is validated with water boiling high heat transfer rate on a metallic vertical cylindrical surface experimental results done by Bolukbasi and Ciloglu [128]. Bolukbasi and Ciloglu [128] investigated the heat transfer rate of boiling for a cylindrical surface with a semi-spherical bottom to prevent a premature collapse of the vapor film. A wide range of superheat temperatures of the cylindrical object relative to the boiling temperature of the pool were tested in [128], ranging from 500ºC to around 0ºC. The model shown in Figure 5.2 is validated with the experimental results in [128] using different flow physics modeling techniques, including laminar and different models of Reynolds-averaged Navier–Stokes equations (RANS) model. Figure 5.3 shows the results of the different considered flow physics models including the mesh independent study. As shown in Figure 5.3(a) and (b), the laminar model achieves the lowest average error than the other considered models. It shown in Figure 5.3(a) that the laminar model achieves an average error of 14.9% with the experimental data, which is acceptably accurate compared to the

published correlations and developed model especially with the high flexibility of the model [132,133].

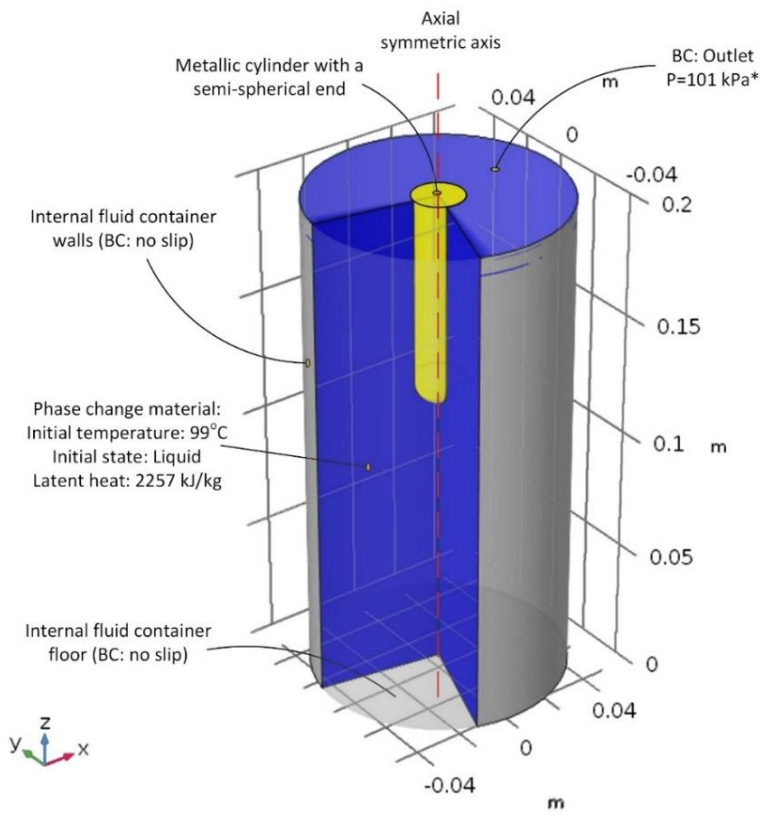

Figure 5.2 The boundary conditions of the simulated domain of Bolukbasi and Ciloglu [128] experimental setup to validate the developed boiling model.*Absolute pressure.

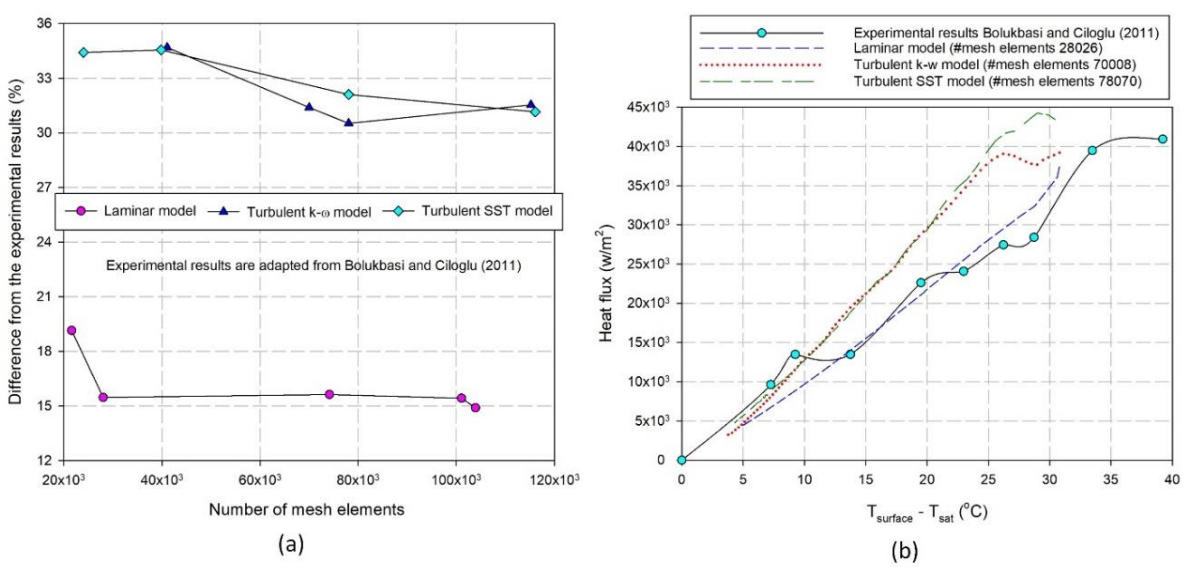

Figure 5.3 Validation of the proposed boiling model for measuring the high heat rate of boiling.

5.2 Electrochemical performance results

This section presents the results of the electrochemical model mainly the variation of the heat generation rate with the variation of the charging and discharge cycle rate and with the variation of the battery average temperature. Note that during the simulations that considers the variation of the battery average temperature, the battery average temperature is set constant throughout the 600 seconds simulation cycle. However, for the case where the effect of the charging and discharging cycle rate on the heat generation rate the average battery temperature is set constant to 298 K.

5.2.1 Cycling rate effect on the battery performance

The variation of the volumetric heat generation rate with the variation of the charging and discharging cycle rate throughout a charging and discharging cycle for 600 seconds is presented in Figure 5.4. Figure 5.4 considers four different cycle rates of 3C, 4C, 5C, and 6C. As shown in Figure 5.4, as the cycle rate increases it leads to increase in the heat generation rate.

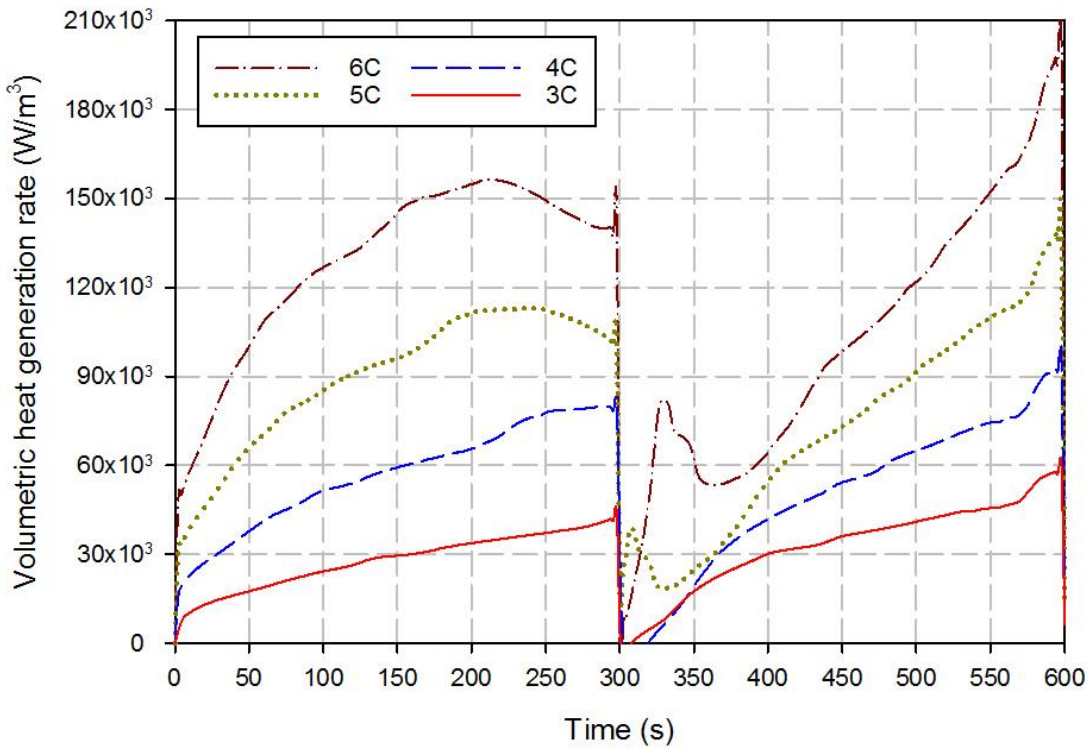

Figure 5.4 The variation of the volumetric heat generation rate through a 600 seconds of charging and discharging cycle for the cycle rates of 3C, 4C, 5C, and 6C.

5.2.2 Temperature effect on the battery performance

The effect of the battery temperature on the heat generation rate of the battery is investigated for a high a cycle rate of 6C in this section. The study considers three various battery temperature, which are 25ºC, 35ºC and 55ºC, where the temperatures are set to be constant for the entire one dimensional electrochemical model and for the entire cycle. The

results of the effect of the variation of the battery temperature on the volumetric heat generation rate is shown in Figure 5.5. Figure 5.5 shows the variation of the battery volumetric heat generation rate through a 600 seconds of charging and discharging cycle for cycle rates of 6C for three different battery temperatures 25ºC, 35ºC and 55ºC. As shown in Figure 5.5 as the battery temperature decreases the heat generation increases. What causes the heat generation to increase when the battery temperature decreases is that when the battery temperature decreases the thermal resistant of the battery increases and as since the battery internal resistant is one of the main reasons for the heat generation of the battery then the heat generation will increase with the decrease in the battery maximum temperature.

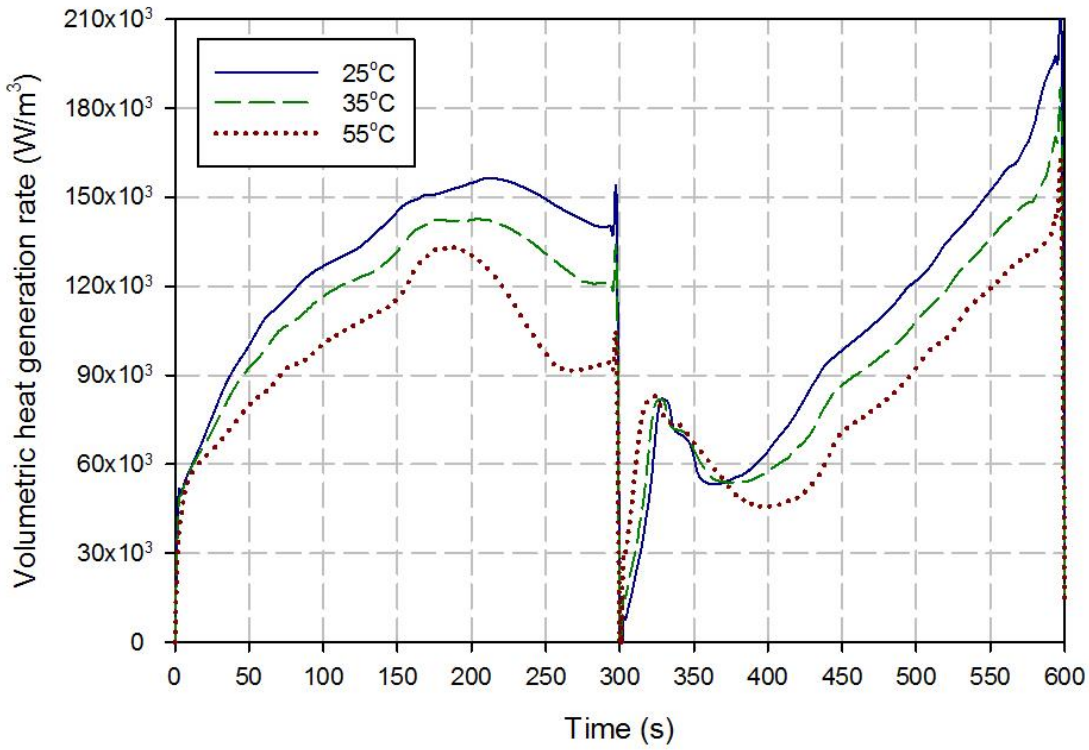

Figure 5.5 The variation of the volumetric heat generation rate through a 600 seconds of charging and discharging cycle for cycle rates of 6C for three different battery temperatures.

5.3 Prismatic battery pack results

In this section the results of the proposed battery pack thermal management systems are presented in this section of those that are proposed for the prismatic batteries. Before starting to simulate the proposed systems, the variation of the temperature through the battery pack needs to be investigated first, since it will determine the size of the models that are used to investigated the performance of the proposed systems in various configurations of operating parameters.

The considered battery pack contains 12 prismatic lithium ion batteries as shown in Figure 3.9, and temperature uniformity throughout the pack is desirable to avoid performance degradation and an inability to deliver the required power. In order to

investigate the performance of the boiling based cooling system on the temperature variations across the battery pack, all batteries in the pack must be simulated. Simulating the full pack of 12 batteries is a computationally expensive and unrealistic especially if negligible lost in accuracy occurs if smaller number of batteries were simulated and the symmetric boundary condition is utilized.

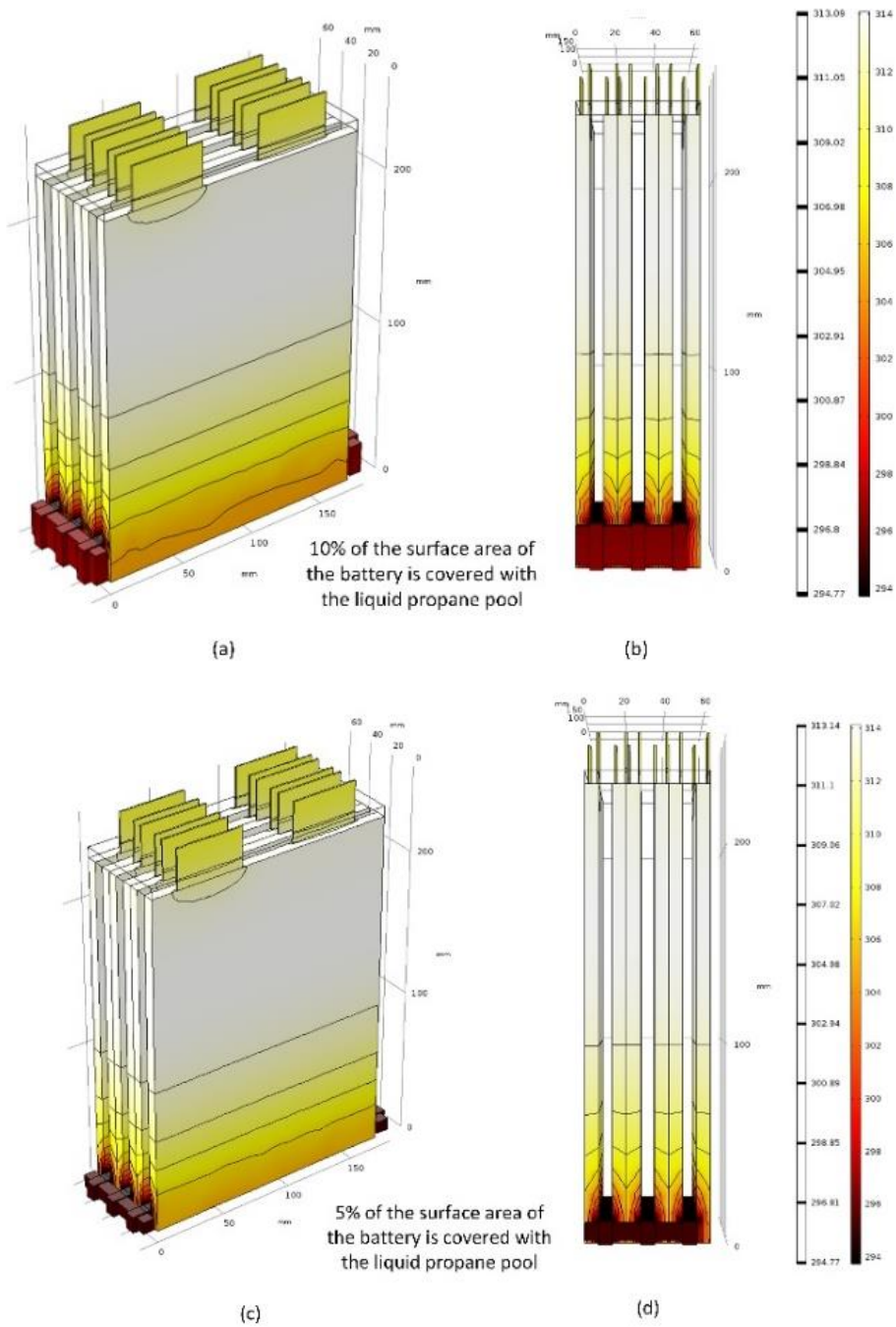

Figure 5.6 Temperature contours of half of the battery pack at the end of the 300 second discharging period. Negligible temperature differences are observed across the battery pack for a high power discharge rate of 7.5C.

The performance of the battery pack is evaluated at a high power discharge current of 7.5C for a duration of 300 seconds for two heights of the propane pool in the pack. In the first case the propane liquid pool covers 5% of the surface area of the battery and in the second case 10%. The temperature contours of half of the battery pack at the end of the high power discharge period (i.e., after 300 seconds) are shown in Figure 5.6 for the two cases. Note that the temperature contour is plotted for half of the battery pack to show the temperature distribution on the middle of the pack battery face. It is observed that six batteries in the pack for both propane pool heights exhibit temperature differences of less than one degree Celsius, reflecting the high level of temperature uniformity that the proposed cooling system can provide in the battery pack. Given these results, the symmetric boundary conditions and a smaller simulated domain (a single battery and a half of propane pools) can capture the performance of the battery pack cooled with the proposed cooling system.

5.3.1 System 1 results

The design parameter considered is the hydrogen cooled space in the aluminum made cold plate, where the design is varied based on the resulting temperature distribution, maximum temperature, minimum temperature and the maximum temperature difference. The methodology of changing the design of the cold plate is to reduce the flow space size for the areas where cold temperatures are achieved and increase it for the areas where high temperatures are present. For the best performing design in terms of the above mentioned criteria, further analysis is carried out considering the full cycle in a transient analysis for various operating parameters.

a) Steady state heat transfer results

For each design, three hydrogen inlet temperatures are considered. One is the lowest possible temperature the system can draw from the pressurized tank while the other two temperatures are selected to be 10°C and 20°C. The latter two values are selected to obtain a battery operating temperature within the optimum operation range. The designs are developed and upgraded based on the battery temperature contours plot, where the aim is to reduce the hydrogen flow area close to the low temperature portions of the battery and increase it where the battery experiences high temperatures. The first design features two inlets for the hydrogen with an overall flow velocity of 0.02 m/s as shown in Figure 4.4 and presented in Table 5.1.

The first design of the cold plate has an aluminum block separating the two inlets to avoid shocking the battery from the hydrogen supply channel side. The first cases of the inlet temperature of -140°C exhibit a maximum temperature difference of 50.2^{o}C (Table 5.1). Note that the presented maximum temperature difference is not the expected maximum temperature difference in the transient test, which is expected to be much lower than the steady state. The difference between the two cases is due to the case that the heat generation rate is considered constant and equals to nearly the maximum heat generation rate in a 600 seconds cycle and rate of 4C, but it is used to guide the design process. Note that the main reason for considering the lowest temperature possible based on the pressure of the supply tank is to investigate the behavior of the temperature difference across the pack, which is reflected in the transient study that presents and investigate the actual performance of the battery pack. To investigate the sensitivity of the first design to the

cooling hydrogen supply temperature, the other two temperatures are considered. For inlet hydrogen temperatures of 10°C and 20°C, the maximum temperature difference through the battery increased in both cases to 51.4°C, as seen in Table 5.1. This increase in temperature difference can be explained by pointing out that the flow of hydrogen temperature reaches a point where it can no longer cool the battery in comparison with the -140°C temperature inlet, which has a larger temperature difference to drive the heat transfer. For cases where the inlet temperatures to the first design are 10°C and 20°C, the battery temperature the hydrogen outlet are 71.5°C and 81.5°C respectively. Although these temperatures are not valid for the transient case, which simulates actual cooling system performance, they are used to compare and improve the design, particularly the shape of the channel.

Table 5.1. The input parameters of the hydrogen to the cold plate throughout the hydrogen cold plate design development and the main battery cooling system performance resulting from each design and input parameters in terms of the minimum and maximum temperature of the battery and the maximum temperature difference across the battery.

	Input parameters			Results		
Design number	Hydrogen inlet temperature (°C)	Hydrogen inlet velocity (m/s)	Inlet Area (mm^2)	Minimum battery temperature (°C)	Maximum battery temperature (°C)	Maximum temperature difference (°C)
1	-140	0.02	25	-128.6	-78.4	50.2
1	10	0.02	25	20.07	71.5	51.4
1	20	0.02	25	30.07	81.5	51.4
2	-140	0.02	25	-129	-88.1	40.9
2	10	0.02	25	21.0	61.9	40.9
2	20	0.02	25	31.0	71.9	40.9
3	-140	0.02	11.22	-113.2	-71.7	41.5
3	10	0.02	11.22	35.8	78.3	41.5
3	20	0.02	11.22	46.8	88.3	41.5
4	-140	0.02	8.16	-110.8	-71.9	38.9
4	10	0.02	8.16	39.2	78.1	38.9
4	20	0.02	8.16	49.2	88.1	38.9
5	10	0.02	8.16	38.8	76.2	37.4
5	20	0.02	8.16	48.8	86.2	37.4

The results are obtained through a steady state simulation of the proposed cooling system with a volumetric heat generation rate of 90,000 W/m^3 (24.6 W), which is 95% of the maximum heat generation rate by the battery under a discharge and charge current rate of 4C. Reynolds number for all 15 cases is less than 2300.

Figure 5.7a shows the temperature contours of the front and back faces of the battery being cooled with the first design cold plate, when the inlet temperature is 10°C. One case is shown only since the three cases exhibit very similar temperature differences across the battery. From the temperature distribution on the front and the back face of the battery, the lowest temperature is concentrated near the inlet of the hydrogen. For the first design the temperature increases to nearly the double that at the end of the aluminum block located at the hydrogen supply channel. In the second design the blockage area is stretched

and another block is placed to allow the cold hydrogen to reach the area near the collection channel faster, so as to reduce the temperature difference across the battery. The results of the second design are listed in Table 5.1.

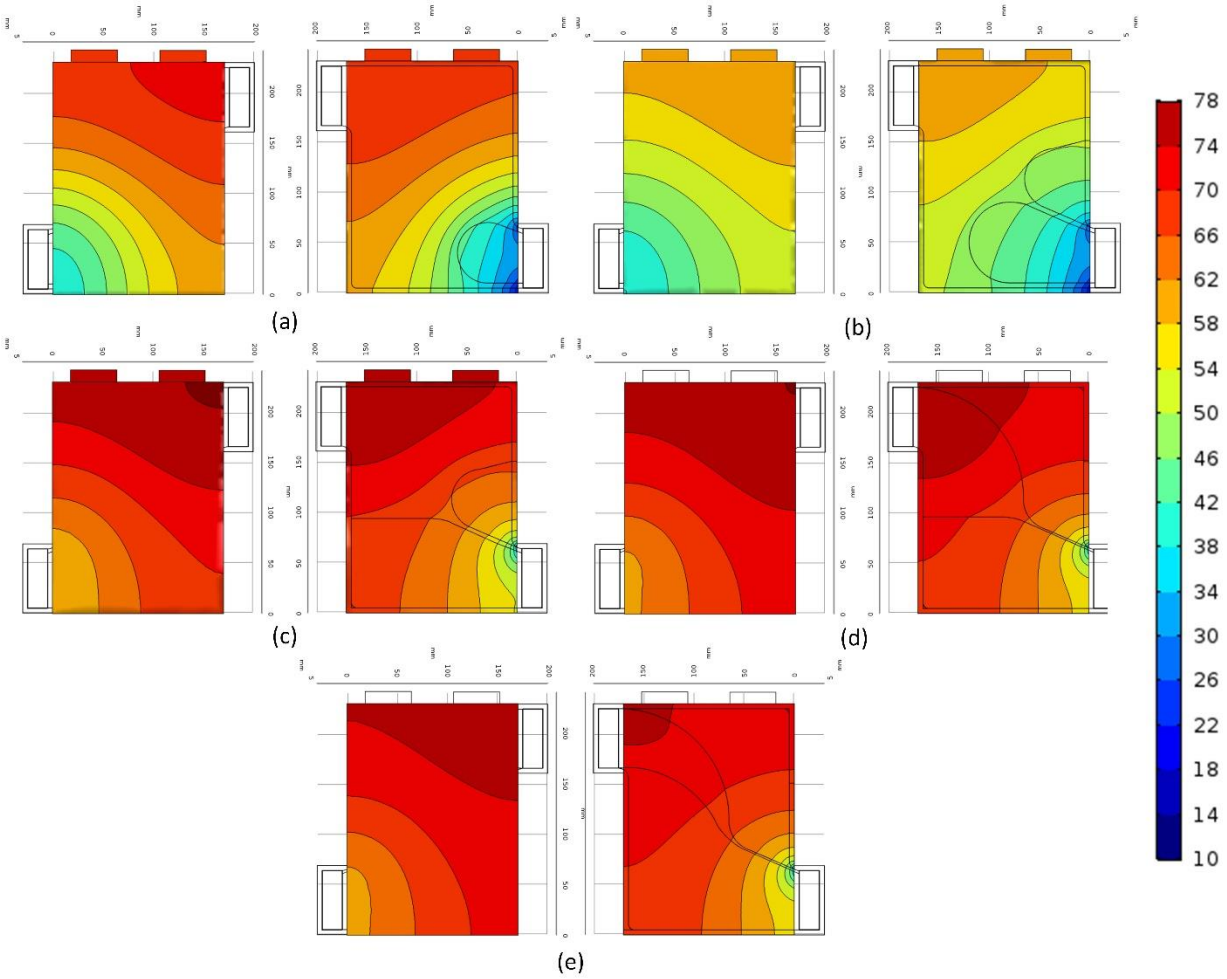

Figure 5.7 Battery temperature distribution (in ^{o}C) due to the cooling of the aluminum cold plate for a hydrogen inlet temperature of 10°C and an inlet velocity of 0.02 m/s. (a) First design, (b) second design, (c) third design, (d) fourth design and (e) fifth design.

The second design was able to successfully reduce the temperature difference by 10.5^{o}C, from 51.4^{o}C to 40.9^{o}C, as presented in Table 5.1. The temperature distribution on the surface of the battery cooled by the second design of the cold plate is shown in the temperature contour plot of Figure 5.7b. Figure 5.7b shows how the redesign of the cold plate redirects the flow of hydrogen away from the inlet area and allows colder hydrogen to reach the other end of battery, which improves the temperature variation with respect to the first design. Another noticeable result with the redesign of the cold plate is that the temperature difference across the battery is not affected by the temperature of the cold hydrogen. Following a similar design strategy, and from the fact that the lower part of the battery is colder than the top the third design has one hydrogen inlet and the bottom part of the plate is completely blocked, as shown in Figure 5.7. The results for the third design are presented in Table 5.1. The maximum temperature difference across the battery increases

with the third design from 40.9^{o}C to 41.5^{o}C, as seen in Table 5.1. The third design is not able to reduce the maximum temperature difference across the battery, and in addition the minimum and maximum temperatures increase. Figure 5.7c shows the temperature distribution across the front and the back surfaces of the battery cooled by the third design of the cold plate.

The main goal of blocking the lower inlet to the cold space is to allow the hydrogen to reach the other end of the battery with a colder temperature, so that the overall temperature difference across the battery is reduced. However, the improvement in the thermal performance of the BTMSs due to blocking the lower inlet in third design did not achieve the needed results, mainly due to the space above the aluminum block inserted at the top. Since the increase in temperature difference is less than 1°C and since the temperature distribution seems promising for further redesign with the same strategy, the design is further modified to introduce the fourth design, which is shown in Figure 4.4. In the fourth design the flow space for hydrogen is reduced by expanding the top aluminum block and make it cover the top right corner of the battery. Blocking the top right corner of the battery improves the temperature distribution of the battery by reducing the maximum temperature difference across the battery to 38.9^{o}C, as seen in Table 5.1. Further improvement from the third to the fourth design is noticed in the minimum temperature and maximum temperature reductions.

The improvements in the fourth design relative to third are negligible reduction in the maximum temperature, and a slight drop is noticed in the minimum temperature of the battery. Figure 5.7d also shows the temperature distribution over the surface of the battery that results from use of the fourth cold plate design. Filling the top right corner of the cold plate was able to expand the cold bands further in the direction of the collection channel.

The final design is the fifth design shown in Figure 4.4, where the size of the hydrogen flow space within the cold plate is reduced. The fifth design features the smallest hydrogen flow space and a single coolant inlet. Note that only two cases of hydrogen inlet temperature are considered. The results of the fifth design in terms of minimum, maximum and temperature difference are presented in Table 5.1. It therefore shows a further reduction compared to the fourth design in the maximum temperature difference across the battery, which drops from 38.9^{o}C to 37.4^{o}C. Compared to the fourth design the fifth design of the cold plate also results in a reduction in the maximum temperature of the battery from 78.1^{o}C to 76.2^{o}C, where the minimum temperature also reduced from 49.2^{o}C to 48.8^{o}C, as seen in Table 5.1.

Figure 5.7(e) shows the battery temperature distribution due to the cooling of the fifth design cold plate. The battery temperature distribution shown in Figure 5.7(e) is improved from fourth design, where the maximum temperatures on both sides of the battery are almost the same and having the hydrogen cooling space narrower improves the battery surface temperature.

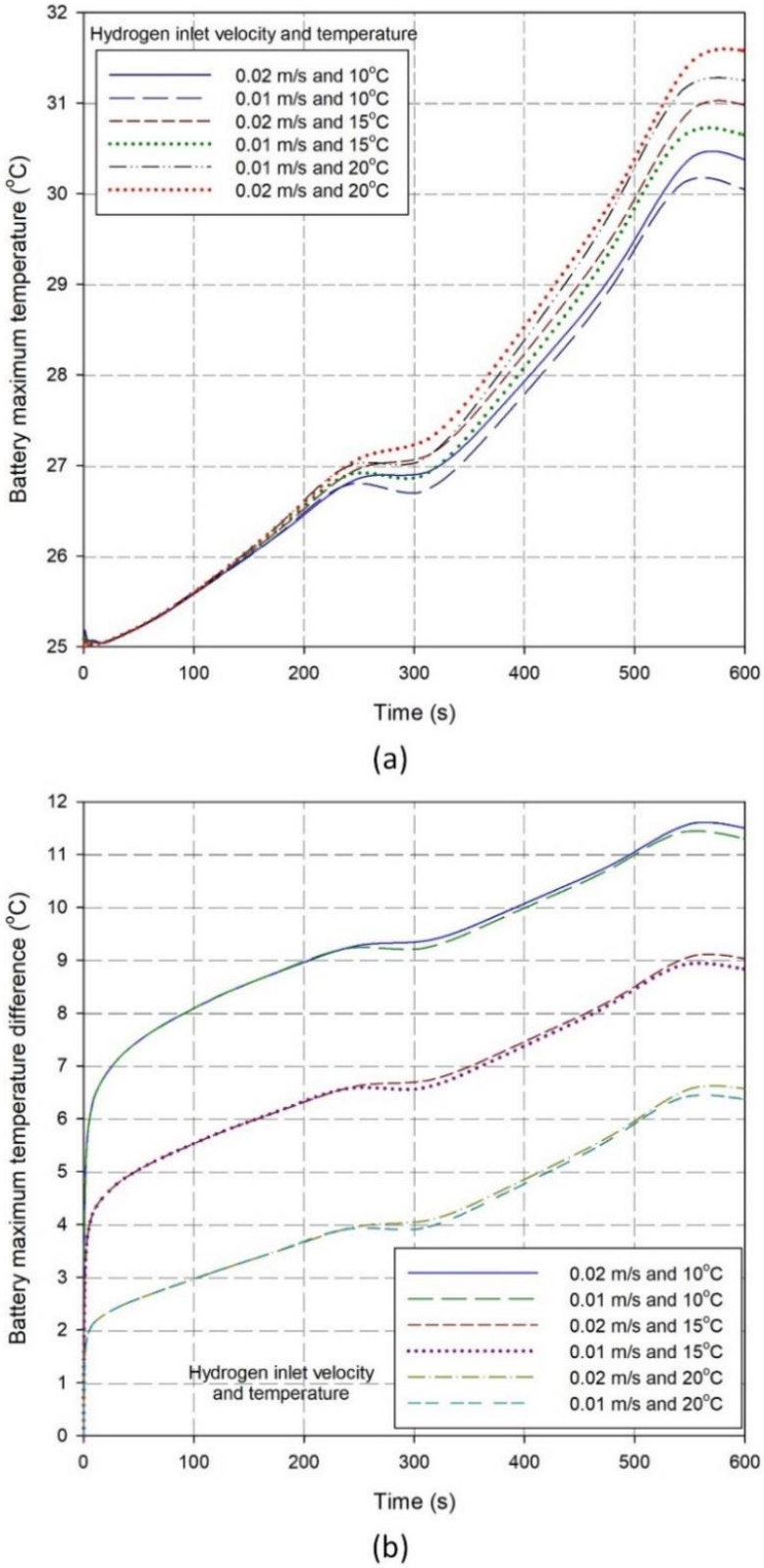

Figure 5.8 Variation with discharging and charging time of (a) battery maximum temperature and (b) maximum temperature difference within the battery.

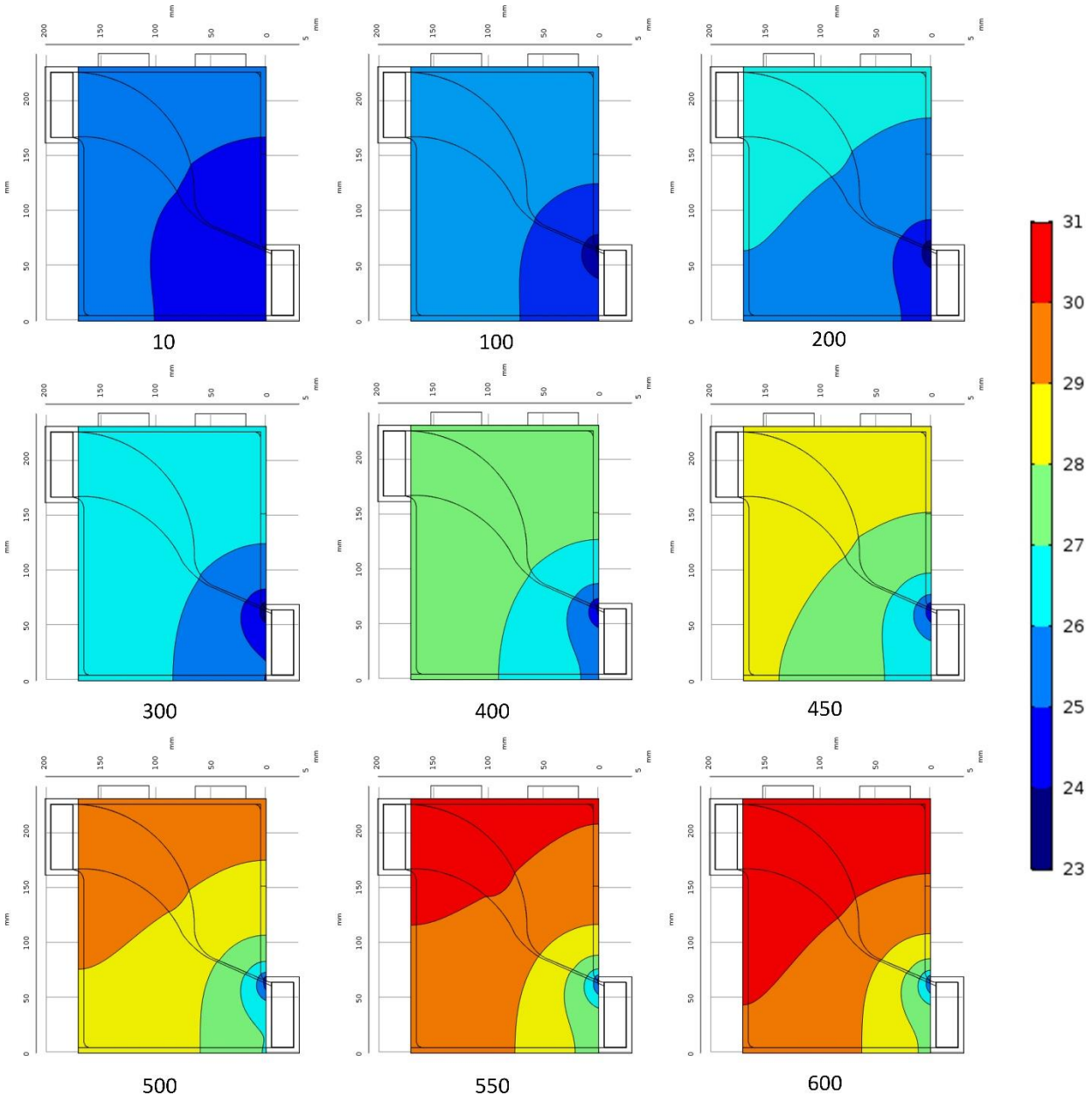

Figure 5.9 Variation with discharging and charging time of the temperature distribution (in ^{o}C) on the surface of the battery with direct contact with the aluminum cold plate for the fifth design, for a hydrogen inlet temperature of 20°C and a speed of 0.01 m/s. Under each time frame of the battery surface temperature is the time from the start of the cycle in seconds.

Although it might seem that the fifth design is a downgrade from the second design considering the maximum and minimum temperatures, reducing the temperature difference by distributing the cooling heat rate over the battery surface raises those temperatures. Since the fifth design proved to provide the best performance in terms of maximum temperature and maximum temperature difference across the battery, it is selected as the final design for the hydrogen based aluminum made cold plate in this thesis.

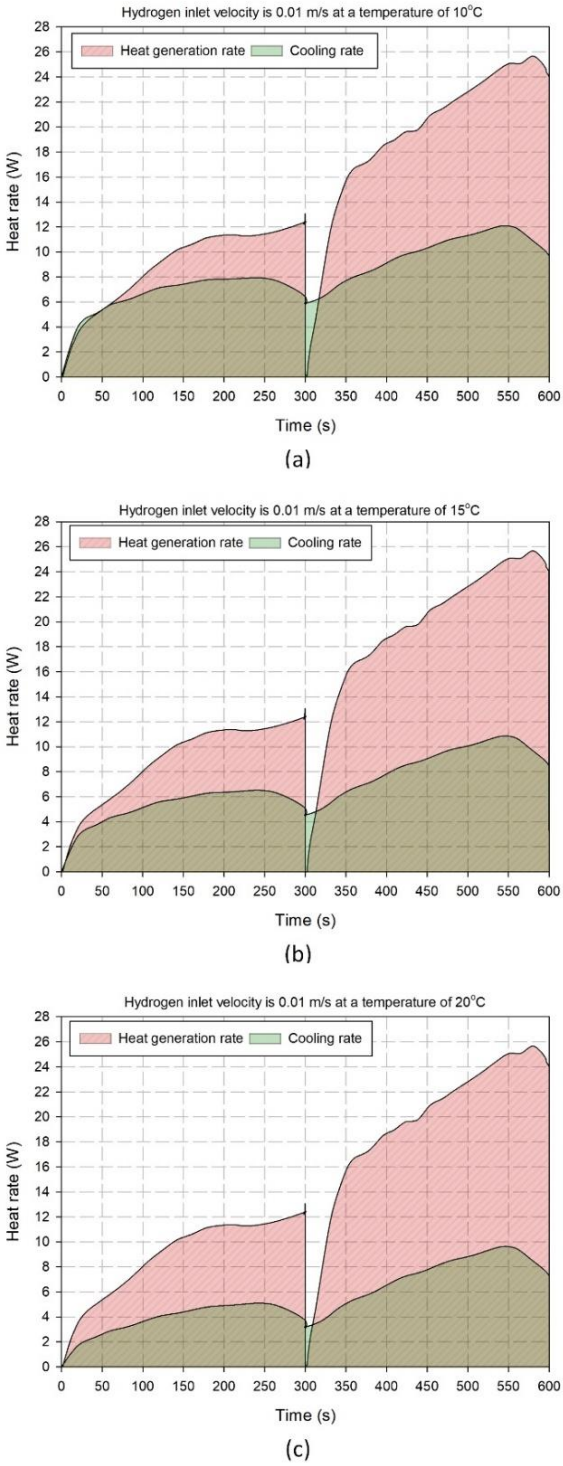

Figure 5.10 The variation of the heat generation rate by the battery and the variation of the proposed system cooling rate through the 600 seconds of charging and discharging cycle at a rate of 4C (note that the cooling rate is calculated at a single contact surface between the battery and the cold plate) (total heat generated through the 600 second cycle is 8.17 kJ).

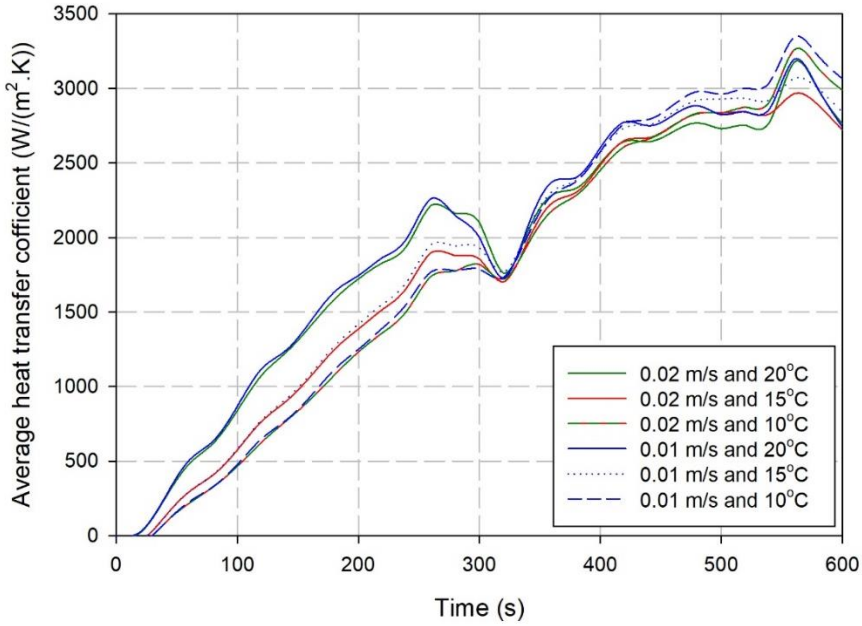

Figure 5.11 The variation of the heat transfer coefficient through the 600 seconds cycle with the hydrogen inlet velocity and inlet temperature at a cycle rate of 4C.

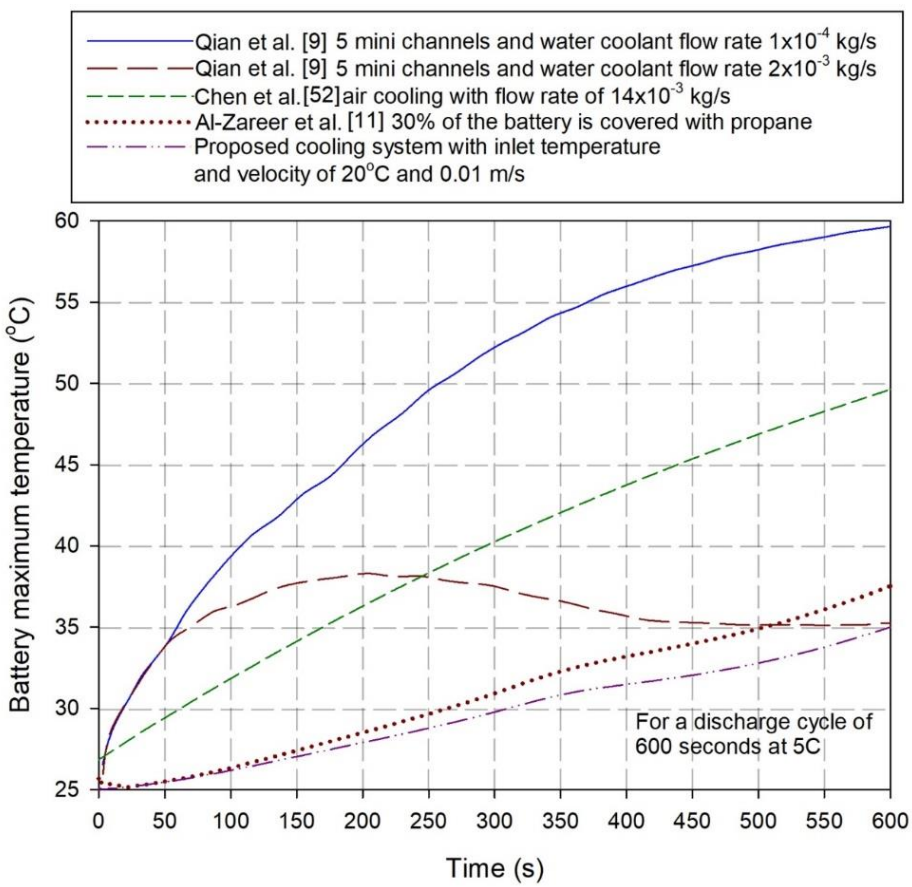

Figure 5.12 Comparison between the proposed cooling system in this thesis and selected air based, liquid based and evaporating based cooling systems.

b) Transient heat transfer results

In this section, the performance of the proposed cooling system is investigated through a transient approach resembling an actual battery operation and their operating conditions, where the battery is discharged at a rate of 4C for 300 seconds and then it is charged with a rate of 4C in 300 seconds. Note that 1C corresponds to a current density of 12 A/m^2. The testing cycle used here has been used earlier [11,25,75,76,134–136]. Several variables are varied to investigate the effect of various operating parameters including the hydrogen inlet velocity and inlet temperature. Two velocities (0.01 m/s and 0.02 m/s) and three hydrogen inlet temperatures (10°C, 15°C and 20°C) are considered. Figure 5.23a show the variation of the battery maximum temperature and the maximum temperature difference across the battery which is shown in Fig. 7b. Increasing the inlet temperature of hydrogen to the cold plate increases the maximum battery temperature for most of the cycle (from the 100th second to the end of the cycle as shown in Figure 5.23(a)). The effect of increasing the hydrogen inlet temperature on the maximum temperature of the battery increases with as the time through the test cycle. The effect of the cooling hydrogen inlet temperature on the maximum temperature of the battery becomes noticeable (i.e., a temperature difference of more than 0.5^{o}C) half away through the cycle. For the three considered temperatures, two velocities are taken into consideration and their effect on the battery maximum temperature is shown in Figure 5.23a. The lower velocity exhibits better performance than the higher velocity, however this is not generalized and is specific for the considered velocities. Having a lower velocity results in reducing the cooling effect at the hydrogen inlet side, since the velocity is a major factor in determining the heat transfer coefficient. Having a lower cooling effect at the inlet side allows cooler hydrogen to reach the other side of the battery, thus reducing the maximum temperature of the battery.

Figure 5.23b shows that as the inlet temperature increases the overall temperature difference across the battery reduces. Although a higher inlet temperature leads to higher battery maximum temperature, the difference is small compared to the large reduction in the temperature difference across the battery. The effect of the inlet temperature on the maximum temperature difference through the battery is negligible as shown in Figure 5.23b. The velocity effect on the maximum temperature is negligible compared to the effect of the temperature, within the considered ranges. Figure 5.9 shows the temperature contours through the test cycle for the surface of the battery that is in direct contact with the cold plate.

The results of the maximum temperature of the battery can be better understood with the help of Figure 5.10, which shows the variation of the heat generated by a single battery and the variation of the cooling rate provided by the cold plate for that single battery throughout the charging and discharging cycle. It is important to further note that Figure 5.10 shows for three cases only of the six different considered cases since the flow rates considered effect is almost negligible in terms of the maximum temperature difference across the battery. It is shown that the reduced temperature inlet reduces the heat generated more by the cooling hydrogen and the cold plate.

Further research results about the performance of the proposed system is exhibited in Figure 5.11, where the variation of the average heat transfer coefficient of the forced convection between the flowing hydrogen and the cold plate surface is presented. As shown

in Figure 5.11, the heat transfer coefficient varies slightly with the inlet velocity at a constant temperature. However, it is more sensitive to the temperature rather than the velocity. The achieved heat transfer coefficient by the proposed design and considered parameters is found comparable to the ultra-thin mini liquid cooling channels proposed by Jin et al. [137].

c) Performance comparison with the literature study

The performance of the hydrogen cooled, aluminum cold plate is compared to the performance of liquid and air cooling systems proposed in the literature for prismatic battery cooling. Figure 5.12 shows the performances of a liquid based cooling system proposed by Qian et al [9], an air based cooling system proposed by Chen et al. [60], and an evaporating fuel pool based system proposed by Al-Zareer et al. [11]. The system proposed here exhibits better performance than the three other systems considered. Although the comparison might seem to favor the proposed system performance since the proposed system by Al-Zareer et al. [11] can achieve better performance with increase in the pool height or pool geometry as shown in Al-Zareer et al. [113], it demonstrates the ability of the proposed system to compete with other cooling systems. For example, the proposed system with a velocity of 0.01 m/s and an inlet temperature of 20°C performs better than the considered parameters of liquid and air cooling systems. It can be seen that the proposed system has an end temperature equal to that of the liquid cooling system, however the proposed system has a lower temperature throughout the cycle unlike that of the liquid cooling system. The proposed system exhibits a better response to the heat generation rate of the battery compared to the mini channel water cooling system.

5.3.2 System 2 results

The proposed boiling ammonia based cooling system is investigated and its performance is evaluated through the thermal behavior of the batteries in the pack. The thermal behavior of the battery is assessed through its maximum temperature and the temperature uniformity of the battery. The effect of the height of the ammonia pool in the battery pack is varied, and its effect on the thermal behavior of the battery is investigated.

a) Battery temperature distributions

The proposed cooling system cools the battery by removing part of the heat generated by the battery using two heat transfer modes: boiling, which is characterized by a high heat transfer coefficient, and natural convection to the ammonia vapor at the battery surface not in contact with the ammonia pool. Varying the boiling ammonia pool height in the pack changes the amount of cooling provided by the boiling as well as that provided by the ammonia vapor.

The height of the ammonia pool is varied from as low as covering only 5% of the front face of the battery to covering 50% of it, and its effect on the maximum temperature of the battery is shown in Figure 5.13a. As the ammonia pool height increases in the battery pack, it is seen that the maximum temperature of the battery decreases. It is noted that the decrease in the maximum temperature is not linear with the increase in the pool height, since the main factor in reducing the maximum temperature of the battery is the amount of generated ammonia vapor and the distance it has to travel.

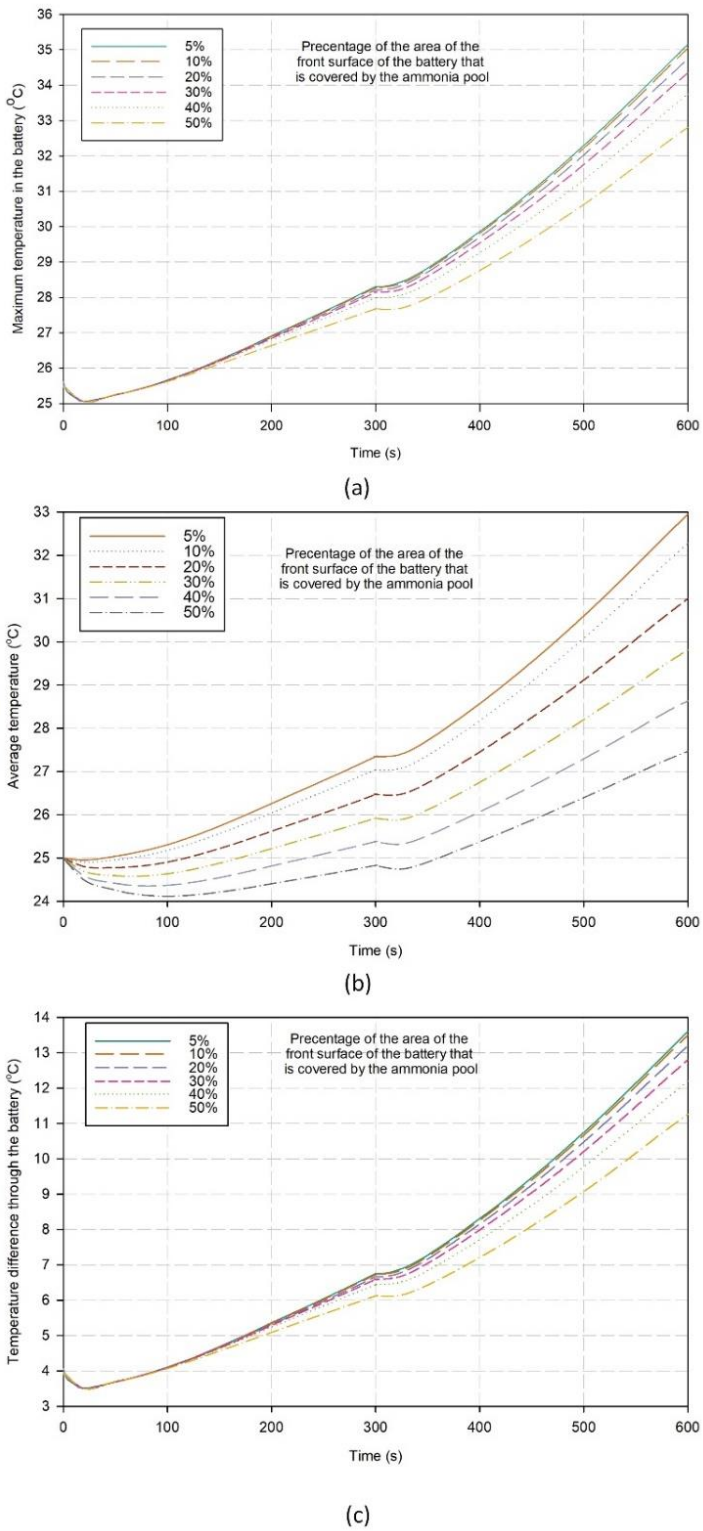

Figure 5.13 Variation with discharging and charging time of (a) maximum temperature in the battery, (b) average temperature of the battery, and (c) temperature difference across the battery, for six cases of liquid ammonia pool height in the battery pack, ranging from 5% to 50% coverage of the front surface of the battery.

The amount of ammonia vapor determines how quickly it is superheated and loses it cooling capacity, where the distance it travels also plays an important role in determining how quickly the vapor loses it cooling ability because of its temperature. However, the distance the vapor has to travel and the amount of vapor produced are both functions of the contact area between the pool and the battery surface. So increasing the contact area increases the heat exchange area, resulting in a higher boiling rate and thus a higher mass flow rate of ammonia vapor. Increasing the contact area reduces the distance the vapor travels before reaching the collection channel. Therefore, both factors can be accounted for through defining the height of the liquid ammonia in the pack through the percentage of how much the liquid ammonia covers from the surface of the battery that is in direct contact with the pool (i.e., the front surface of the battery). Increasing the area of the battery covered by liquid ammonia from 5% to 10% causes a reduction in the maximum temperature of 0.11^{o}C. However, increasing the covered area of the battery by ten times relative to the area at 5% causes a reduction of 2.34^{o}C in the maximum temperature. It is shown in Figure 5.13a that, as the height of the liquid ammonia increases, the drop in the maximum temperature decreases what appears to closely resemble an exponential manner.

The maximum temperature in the battery drops to lower than 25°C when 100% of the front area of the battery is covered with boiling ammonia, which is a 29% decrease in the maximum temperature of the battery (which is 99% of the increase in the temperature from initial temperature of the battery). Regarding the maximum temperature of the battery in the early stages of discharging, it is seen that most of the six cases considered provide nearly the same cooling performance for the 130 seconds of the 4C discharging period.

For a low coverage area of the battery surface, the main differences appear at the end of the 300 seconds 4C discharging rate, as shown in Figure 5.13a. Further understanding of the cooling ability of the proposed system, Figure 5.14 graphically exhibits the temperature differences of the battery relative to the saturation temperature of the cooling ammonia pool. Figure 5.14 also shows the surface temperature plot of the surface in contact with the cooling pool and the surface in between the two batteries. Here, the height and color are based on the temperature difference from the saturation temperature of the ammonia pool. Furthermore, Figure 5.14 is used to provide a better understanding of the cooling capabilities of the proposed system.

The temperature distribution of the battery or more importantly the temperature uniformity of the battery can be presented in terms of both its average temperature and the maximum temperature difference in the battery. Note the maximum temperature difference within the battery is not alone sufficient to describe its temperature uniformity since the maximum temperature difference does not capture how the temperature is distributed throughout the surface of the battery.

The maximum temperature difference across the battery as shown in Figure 5.13(c) is 13.6^{o}C when 5% of the front surface of the battery is covered with boiling ammonia. The improvement in the temperature uniformity of the battery is directly proportional to the improvement in the maximum temperature of the battery, since the maximum temperature difference is the maximum less the minimum battery temperatures. The change in the maximum temperature of the battery and the change of the maximum temperature difference of the battery with the variation of the height of the ammonia pool in the pack

is directly proportional. This is because the minimum temperature of the battery for all cases of ammonia pool height in the pack is nearly the same, which is very close to the boiling temperature of the ammonia pool. Figure 5.15 shows the temperature uniformity through temperature contour plots of the surfaces of the battery (front and back) at the end of the 600 second discharging and charging cycle.

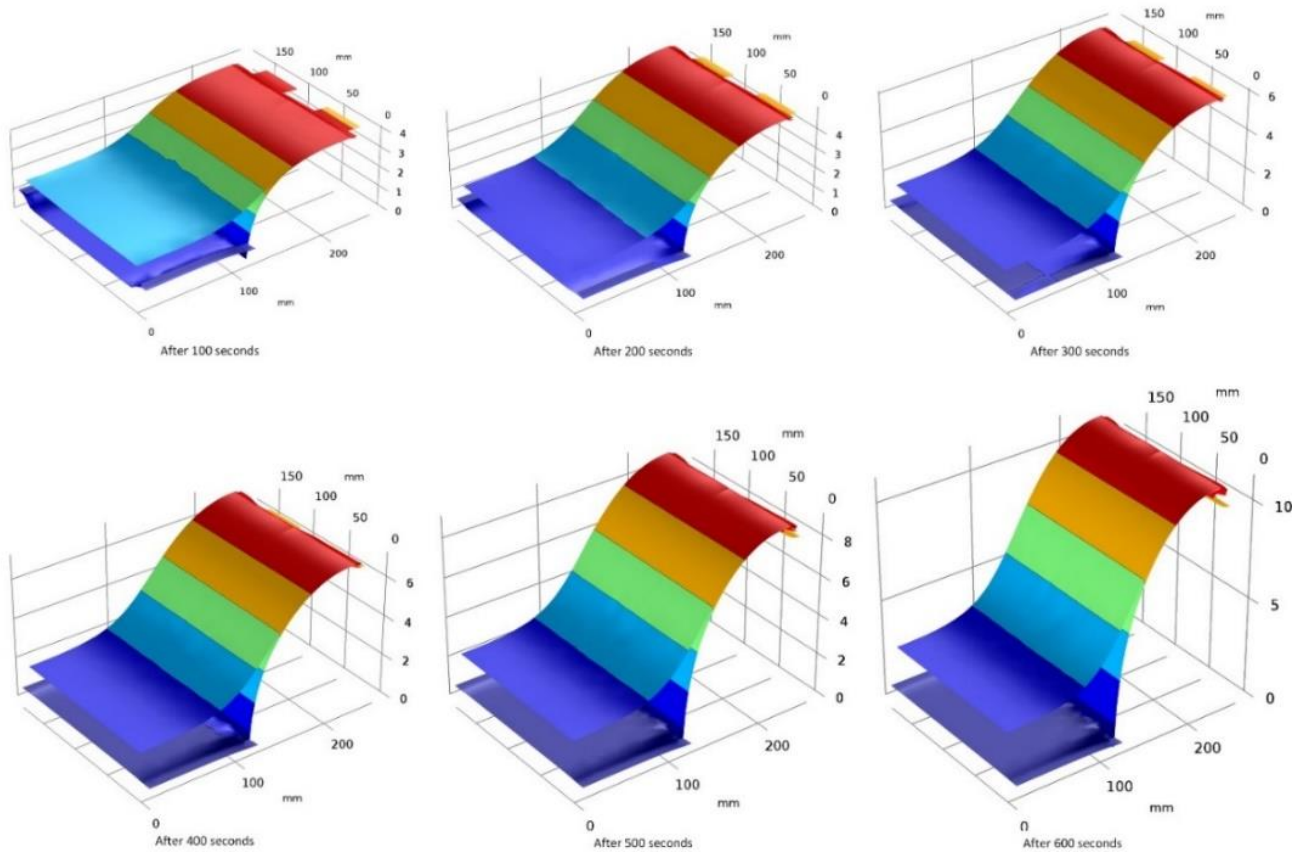

Figure 5.14 Shows a surface temperature difference with the saturation temperature of the cooling ammonia pool plot for the surface in contact with the pool and the surface in the middle of the battery through the discharging and charging time of a rate of 4C.

As shown in Figure 5.15 the temperature uniformity of the battery at the end of the cycle improves as the covered area of the battery surface by boiling ammonia in the battery pack increases. A better temperature uniformity presentation is seen in Figure 5.13(b), which shows the variation of the battery average temperature with time. Figure 5.13(b) shows that as more of the battery front surface is covered with boiling ammonia the lower becomes the average temperature of the battery. Increasing the amount of boiling ammonia in the battery pack from covering 5% of the battery front surface to covering 50% of the front face reduces the average temperature at the end of the 600 seconds discharging and charging cycle from 33.0^{o}C to 27.5^{o}C.

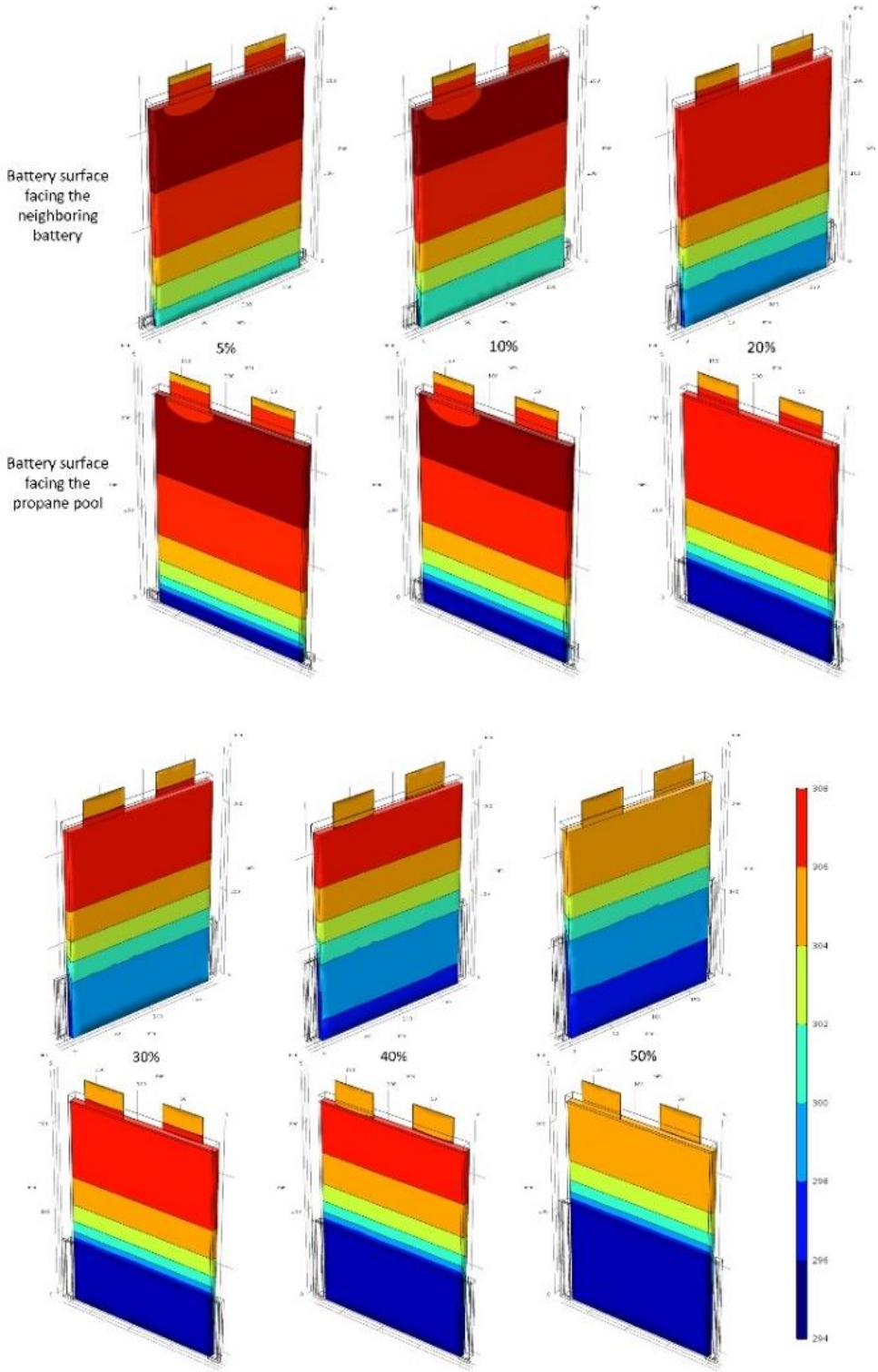

Figure 5.15 Temperature contours of the front surface (in contact with the ammonia pool) and the back surface (facing the neighboring battery) of a battery in the proposed pack design at the end of the 600 second discharging and charging cycle at 4C, for six cases of ammonia pool height

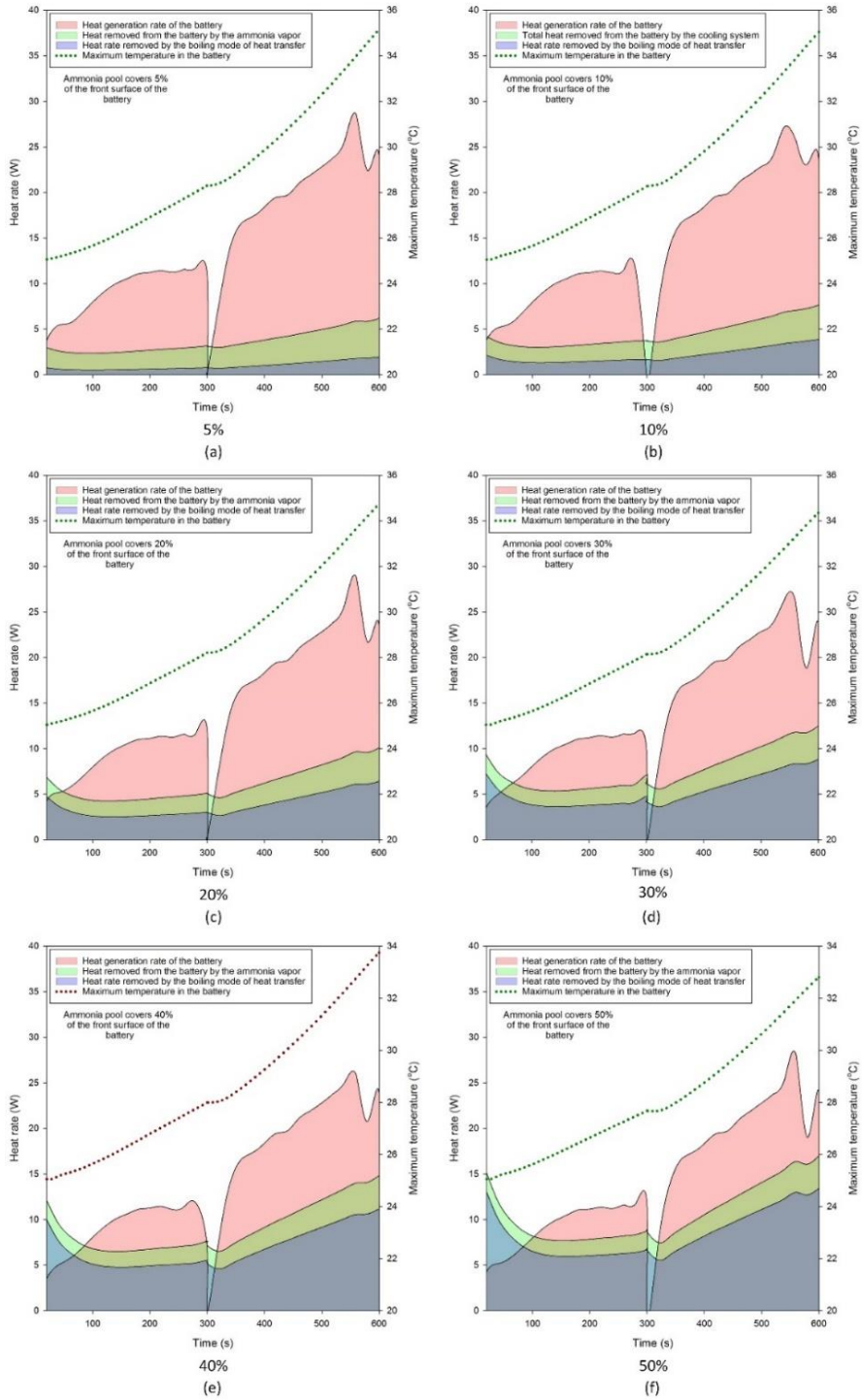

Figure 5.16 Variation with the discharging and charging time of maximum temperature, heat generation rate, total heat removed from the battery by the proposed cooling system, and fraction of the heat removed by the boiling ammonia, for fractions of the battery front surface covered by boiling ammonia pool of (a) 5%, (b) 10%, (c) 20%, (d) 30%, (e) 40%, and (f) 50%. Note that the figure starts at 20 seconds after discharging for better viewing of the curves.

b) Battery heat rate distributions

The battery heat rate distribution is investigated in terms of the battery heat generation rate, boiling heat transfer rate and the natural convection heat transfer rate by the generated vapor. Shown in Figure 5.16 is the maximum temperature, battery heat generation, heat removed by boiling, and heat removed by the natural convection for six cases of the portion of the battery front surface covered by boiling ammonia. When the boiling ammonia covers only 5% of the front surface, most of the cooling is provided by the ammonia vapor, as shown in green in Figure 5.16(a). However, increasing the contact area from 5% to 10% causes an increase in the cooling through the pool and a reduction in the cooling by the vapor as shown in Figure 5.16(b). Increasing the contact area to 20% of the front surface of the battery causes the cooling curve to jump over the heat generation curve for the first 50 seconds of the discharging and charging cycle, while increasing the contact area to 50% increases the duration at which the cooling curve overcomes the heat generation curve, to slightly over 100 seconds from the start of the cycle. While increasing the contact area increases the amount of heat removed by the pool, the effectiveness of the vapor cooling tends to remain constant after its first drop to a 10% contact area. The tendency of the vapor cooling in the cooling process of the battery to remain constant is due to the vapor cooling being limited by a certain distance, after which it cannot cool the battery further because of its temperature. None of the heights considered had a vapor traveling distance less than the cooling vapor limiting distance. However, increasing the contact area between the boiling ammonia and the battery front surface reduces the vapor cooling distance to lower than the limiting one, which reduces the area where the ammonia vapor experiences cooling. Thus it is concluded that the cooling provided by the vapor has its maximum contribution for the case when 5% of the front surface of the battery is covered by boiling ammonia. The contribution of the vapor cooling to the overall cooling capacity of the proposed system is limited and reduces the effectiveness of the boiling based proposed cooling system.

Finally, there is a safety concern in the proposed system of having the ammonia fuel in contact with the batteries in the battery pack. However, such concerns are easily addressed by having the ammonia inside a cooling plate. Having the ammonia pool in the cooling plate contribute also in avoiding any possible corrosion to the battery surfaces in the pack. An addition of the cooling plate in the system is expected to slightly affect the cooling performance, and the drop in the performance may be negligible if a high thermal conductive metal is used.

Then when using the ammonia tubes in the cold plate as the source of cooling and the results of that system are presented next.The proposed boiling ammonia based cooling system is investigated and its performance is evaluated through the thermal behavior of the batteries in the pack. The thermal behavior of the battery is assessed through its maximum temperature and the temperature uniformity of the battery. The effect of the height of the stagnant liquid ammonia in the battery pack is varied and its effect on the thermal behavior of the battery is investigated.

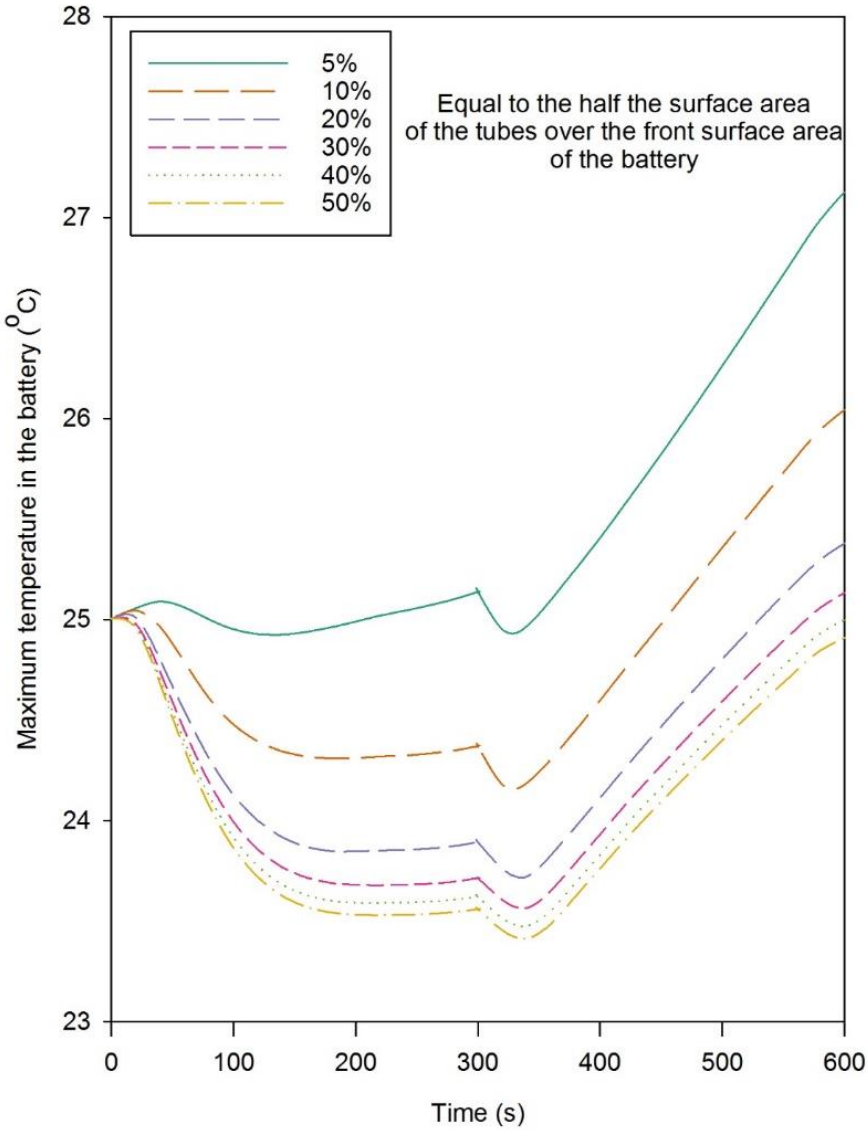

Figure 5.17 Variation with discharging and charging time of (a) maximum temperature in the battery

c) The effect of number of tubes on the battery temperature distribution

The proposed design cools the battery by boiling the stagnant liquid ammonia, which cools the aluminum cold plate that is in direct contact with the battery surface. The number of tubes in the aluminum plate is varied from one tube located in the middle of the cold plate to ten tubes separated from each other and from the sides of the plate by equal distances. From Figure 5.17 and the dimensions of the design, one tube surface area corresponds to 10% of the front surface area of the battery, two corresponds to 20% and so on up to ten tubes corresponding to 100%. Figure 5.17(a) shows the variation of the maximum temperature of the battery through the discharging and charging cycle of 600 seconds at a rate of 4C. Having one tube in the aluminum cold plate filled with stagnant liquid ammonia is sufficient to maintain the maximum temperature of the battery at less than 28°C through

the discharging and charging cycle at 4C. In the tube design, a single tube spans the vertical dimension of the battery (the longest dimension in the battery design) and is located in the middle of battery, which is the case when there is one tube in the cold plate.

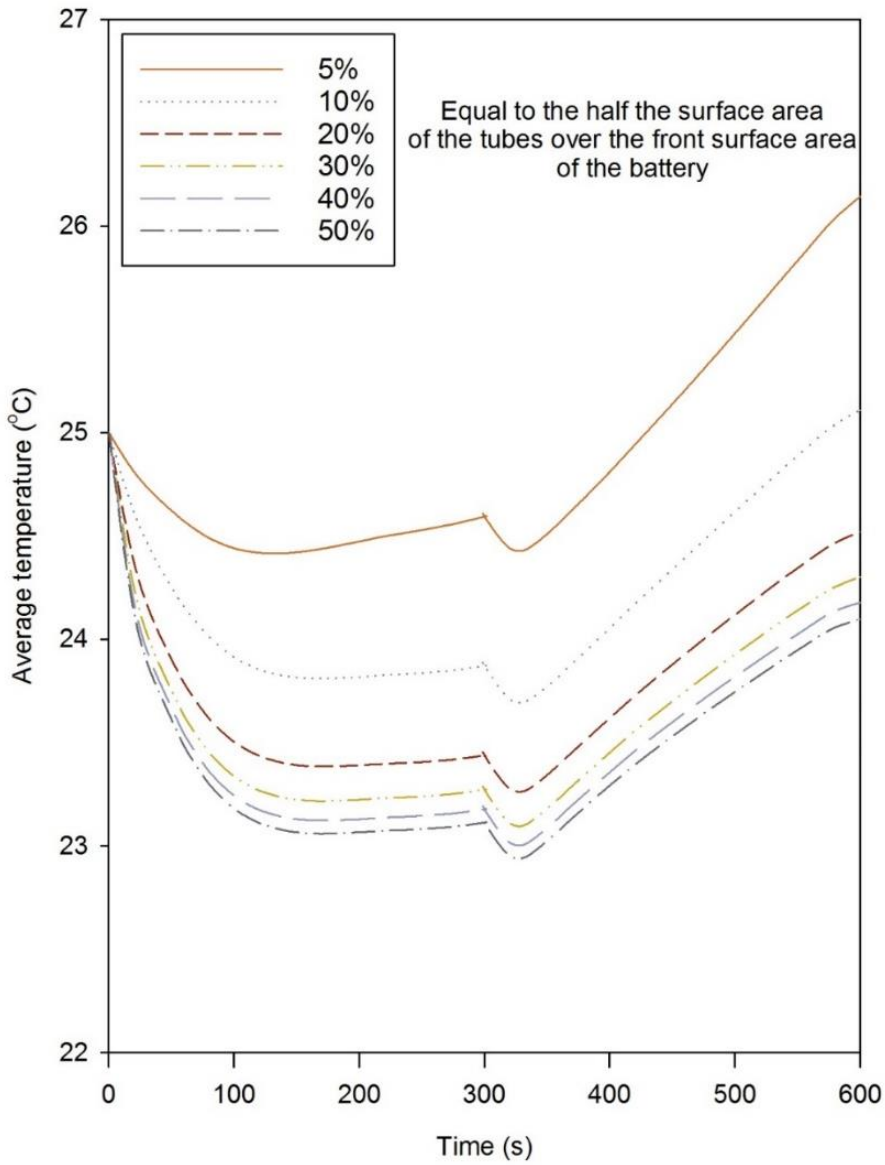

Figure 5.17 Variation with discharging and charging time of (b) average temperature of the battery,

Varying the number of tubes affects the maximum temperature of the battery, as shown in Figure 5.17. It is seen that as the number of tubes increases, the maximum temperature of the battery decreases. The improvement in the maximum temperature of the battery for the design declines notably as the number of tubes increases, as shown in Figure 5.17. The notable decline in the improvement to the maximum temperature of the battery with an increase in the number of tubes is due to the fact that the cooling system is reaching its limit in cooling the battery.

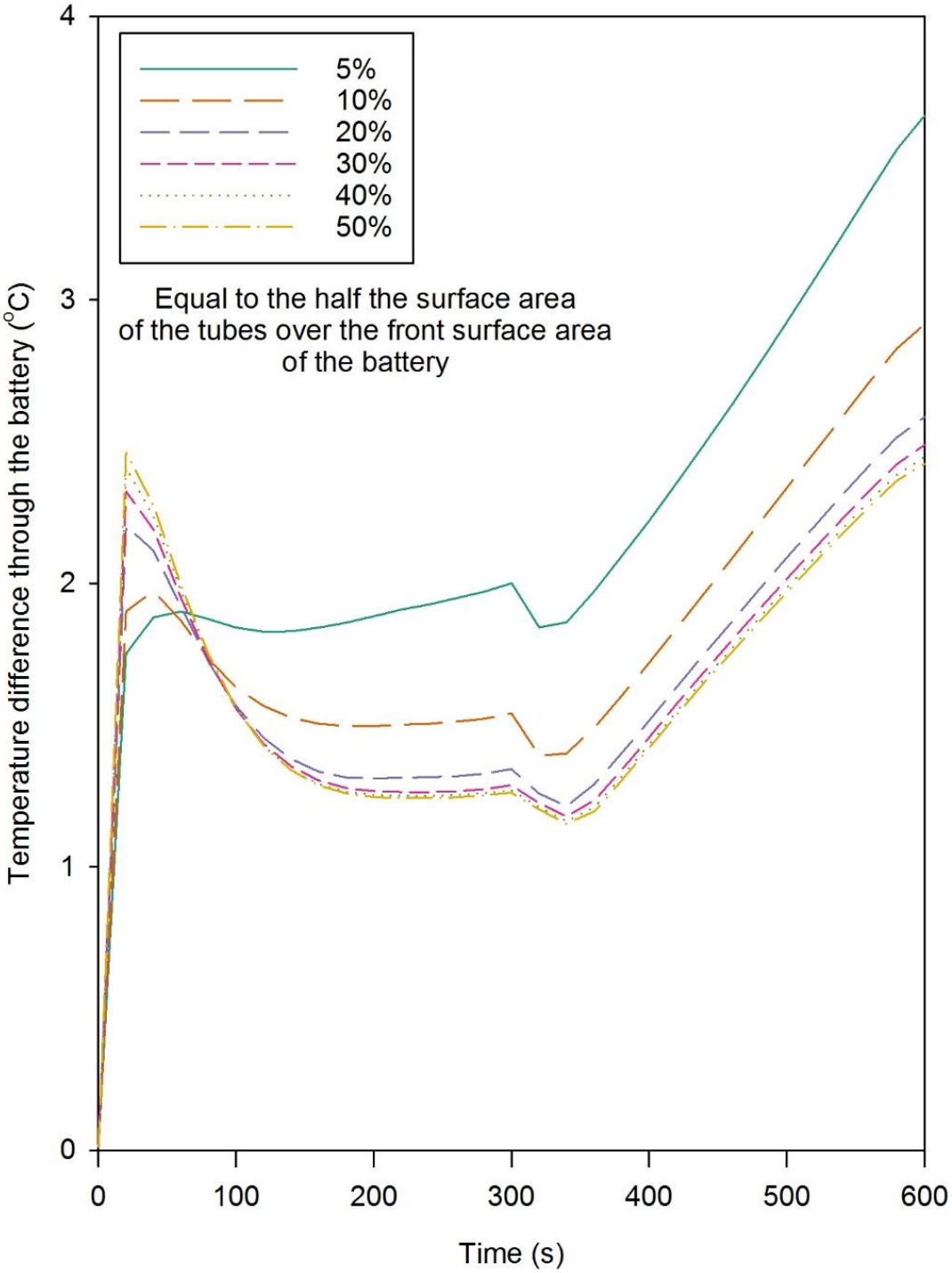

Figure 5.17 Variation with discharging and charging time of (c) maximum temperature difference across the battery, for six cases of liquid ammonia tubes in the aluminum cooling plate in the battery pack.

The temperature of the battery surface in contact with the cold plate approaches the saturation temperature of the boiling ammonia for the case when ten tubes are used in the cold plate (see Figure 5.17 (a)). When more than one tube is used the maximum

temperature of the battery is lower than its initial value. For the case when half the surface area of the tubes in the cold plate is equal to 40% of the surface area of the front face of the battery, the maximum temperature of the battery at the end of the discharging and charging cycle is equal to the battery's initial temperature.

To assess the battery temperature uniformity, the average temperature and the maximum temperature difference for six cases of numbers of tubes in the aluminum cold plate are assessed. The results are shown in Figure 5.17 (b) and 5(c). Temperature contours of the surface of the battery under the cooling effect of the cooling design at the end of the 600 second discharging and charging cycle are shown in Figure 5.18 for various numbers of tubes. The maximum temperature difference occurs at the end of the discharging and charging cycle, and is less than 4°C; this is for the case when a cold plate with one tube is used.

The improvement in the maximum temperature difference for the design declines notably as the number of tubes increase, as shown in Figure 5.17 (c). The largest improvement occurs when the number of the tubes increases from one to two. The improvement is seen to be nearly negligible when four or more tubes are placed in the cold plate. This result also can be observed at the end of the 600 discharging and charging cycle at a rate of 4C, since when using more than two tubes per cold plate there are few temperature contours (noting that all figures share the same temperature contour ranges, so lower numbers of contours denote lower temperature differences). As the number of tubes in the cold plate increases beyond four, the maximum temperature difference at the start of the discharging and charging cycle increases, as shown in Figure 5.17 (c). This is mainly attributable to the increase in the number of tubes reducing the time required to achieve the lowest maximum temperature of the battery, which in turn increases the temperature difference faster at the start of the cooling operation. The average temperature of the battery can be maintained at lower than 27°C with only one tube. The average temperature experiences the largest drop when the number of the tubes increases from one to two. The proposed system is analyzed in more detail to understand how the cooling effect it provides compares to the heat generated by the battery in the next section.

d) Battery heat rate distributions for the tube system

In order to analyze the heat rate distribution of the proposed system, Figure 5.19 shows the maximum temperature, battery heat generation, and heat removed by the ammonia boiling in the tubes versus the discharging and charging cycle for a number of tubes ranging from one to ten. Figure 5.19(a) shows the cooling provided by the proposed system when the aluminum cold plate has only one tube located in the middle. It is seen that, although the cooling provided by the proposed system exceeds the heat generation of the battery for the first 50 seconds of the discharging and charging cycle, the maximum temperature of the battery increases during that period. However, in the case of using two tubes in the cold plate, the cooling provided by the proposed system exceeds the heat generation with nearly 100% the difference in the case of using a cold plate with one tube.

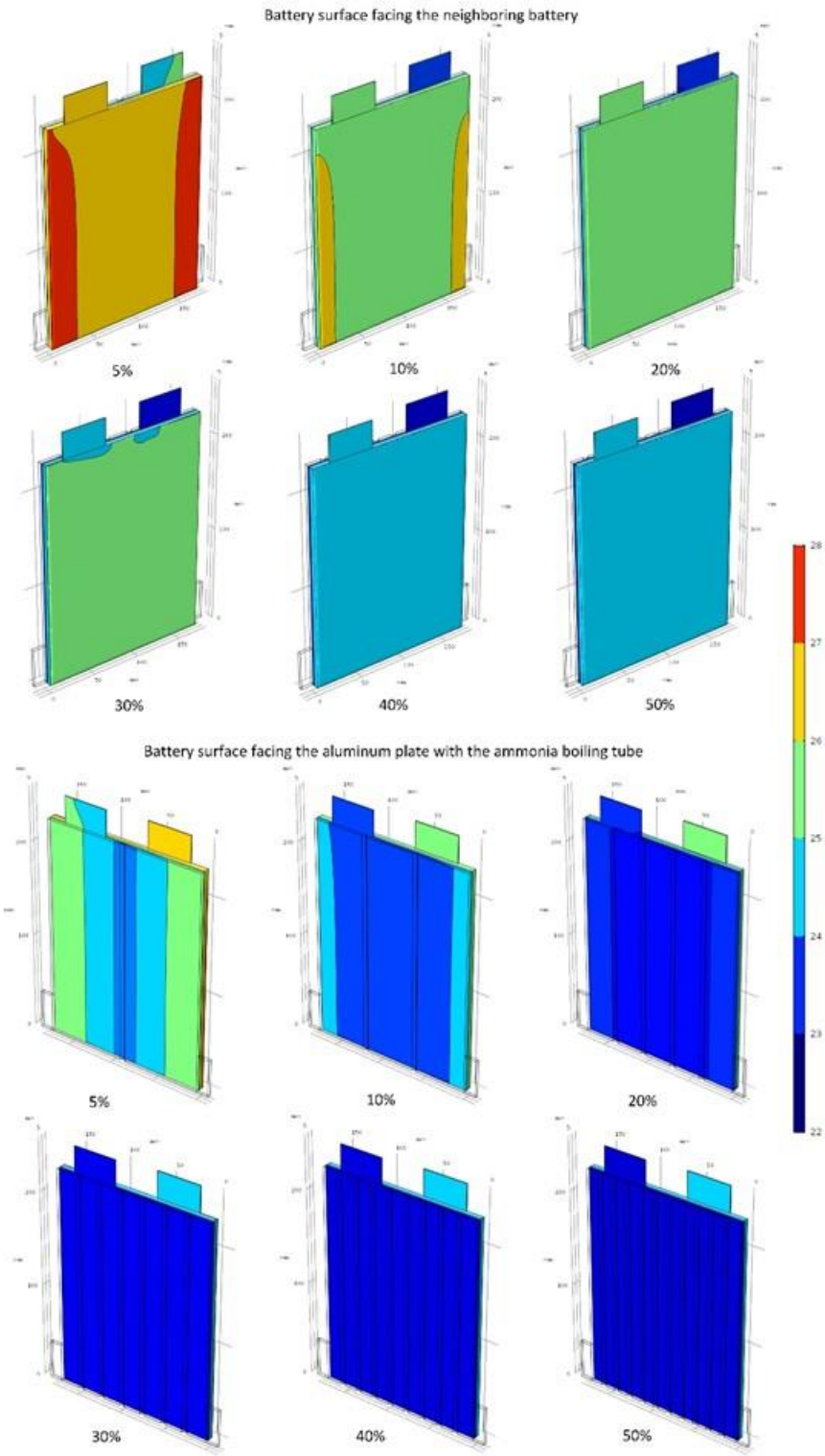

Figure 5.18 Temperature contours on the front surface (in contact with the aluminum cold plate integrated with liquid ammonia tubes) and the back surface (facing the neighboring battery) of the battery in the proposed pack design at the end of the 600 second discharging and charging cycle at 4C, for six cases of number of tubes.

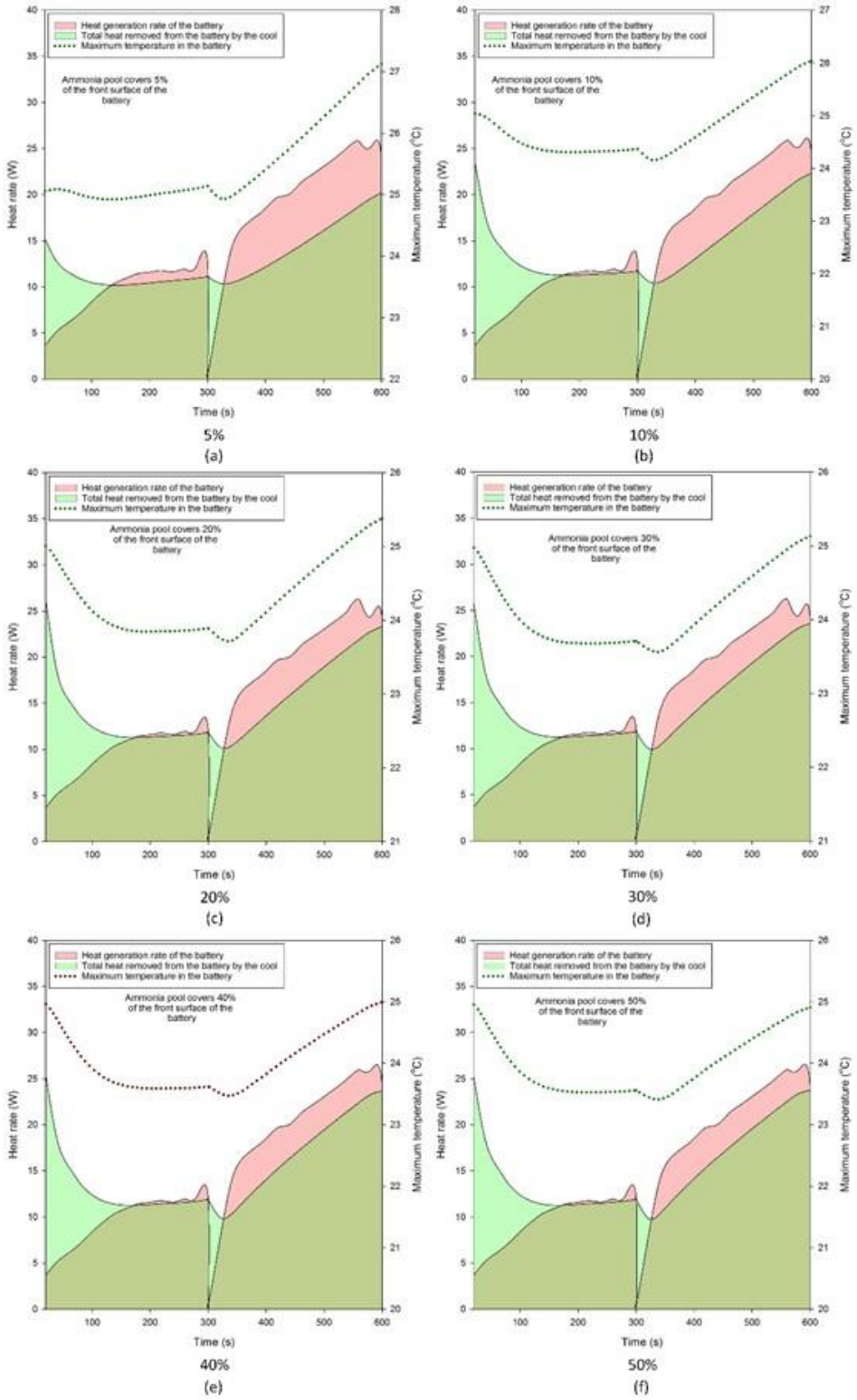

Figure 5.19 Variation with the discharging and charging time of maximum temperature, heat generation rate, total heat removed from the battery by the proposed cooling system, for various numbers of tubes.

Having a larger difference between the cooling provided by the system and the heat generation, for the case of using a two-tube cold plate compared to a single-tube cold plate, eliminates the increase in the maximum temperature of the battery, as shown in Figure 5.19(b). However, further increases in the number of tubes, as shown earlier in terms of the maximum temperature behavior, have little effect on the cooling provided by the system. This is mainly since the cold plate reaches a temperature very close to the saturation temperature of the boiling ammonia, reducing the heat transfer. As shown in the latter half of the 4C operation cycle, the difference between the heat generated and the cooling curve tends to remain constant. As shown in Figure 5.19 the increase in the cooling provided by the cooling system declines as the number of tubes in the cold plate increases, which explains the decline in the improvement in the maximum temperature of the battery.

Increasing the number of tubes in the cold plate from one to two results in the largest increase in the cooling provided by the system compared to when the number of tubes increased from two to four, four to six, and six to eight. However, for all cases of number of tubes in the cold plate, none was able to overcome the heat generation in the charging phase, which resulted in a rise in the maximum temperature of the battery.

5.3.3 System 3 results

This section continues on the developed design of the hydrogen based cooling system, where the cooling system cold plate flow channel was optimized through the iterative approach. As mentioned earlier the same design will be used for the air cooling systems where the same boundary conditions also apply.

The thermal performance of the proposed system is measured through the maximum temperature difference across the battery pack, maximum temperature of the battery, and the maximum temperature difference across the single battery. Based on the configuration of the proposed cooling system where the cold plates are distributed evenly throughout the battery pack, and since each cold plate inlet temperature is independent on the other cold plate exit coolant temperature then the temperature difference across the battery pack can be neglected.

The maximum temperature of the battery and other performance parameters are investigated through 600 seconds long simulation cycle. Where the battery is discharged for 300 seconds at a rate of 4C and then at the end of the first 300 seconds and at the same rate the battery is directly sent into a 300 seconds of charging. Note that 1C charging or discharging rate is equal to the current that will completely charge or completely discharge a battery with capacity of C in one hour. This configuration of the simulation cycle has been used to investigate the proposed thermal battery management systems performance in the literature [11,25,75,76,134–136]. Similar to the considered operating parameters that are varied to measure the performance of the air based cooling system are the same as those of the hydrogen cooling system, which are selected mainly for performance comparison. The varied operating parameters are inlet velocity of the air to each single cold plate as shown in Figure 4.4 and the air inlet temperature. Two different velocities where considered 0.01 m/s and 0.02 m/s and three inlet air temperatures, which are 10°C, 15°C and 20°C.

The performance of the battery is assessed in this section through the battery maximum battery temperature and the maximum temperature difference across the battery

pack, where the variations in these performance parameters are shown in Figure 5.20 and . Figure 5.20 shows the variation of the maximum temperature of the battery through the 600 seconds simulation cycle at a rate of 4C. As mentioned earlier the two different velocities are considered where the first considered is 0.01 m/s and then the velocity of the inlet air is increased to twice its initial value, which is 0.02 m/s. Three different hydrogen inlet temperatures were considered are 10ºC, 15ºC, and 20ºC. In addition to the considered inlet velocities and temperatures, an additional case considered is where the inlet velocity is increased to 0.05 m/s and the inlet temperature was set to 25ºC. As shown in Figure 5.20 as the inlet temperature increases the maximum temperature of the battery at the end of the simulation cycle increases and through parts of the simulation cycle.

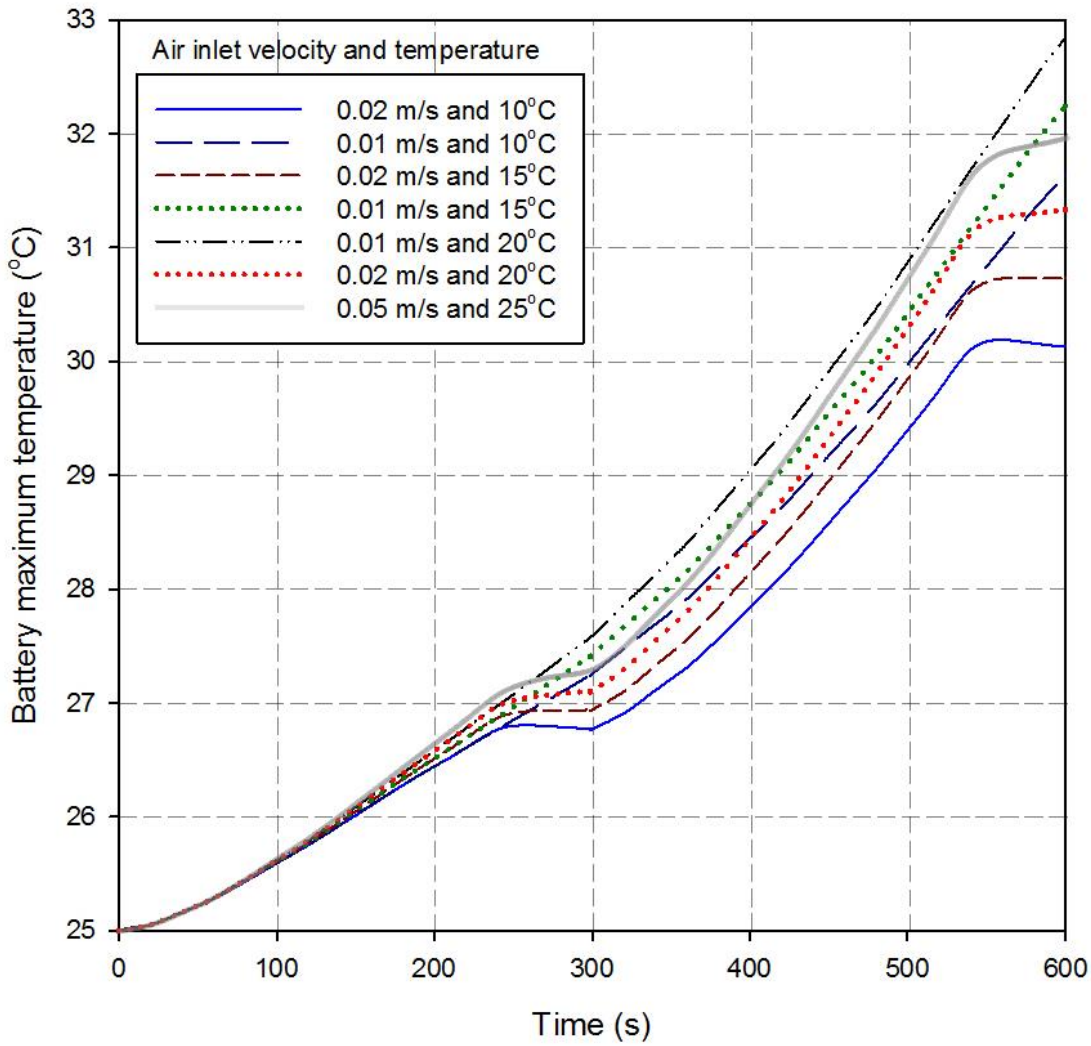

Figure 5.20 Variation with the discharging and charging time of maximum temperature for the air based cooling system at a cycle rate 4C.

Note that changing the temperature and the inlet velocity (within the considered values) results in no to negligible effect on the maximum temperature of the battery in the first 150 seconds of the cycle. Where at around 200 seconds through the simulation the differences between the simulated parameters become apparent. However, for the same

inlet velocity of the as the inlet temperature increase the maximum temperature of the battery increases as well. The increase in the maximum temperature with the inlet temperature of the coolant is expected since the temperature of the coolant will increase and lets its cooling capabilities.

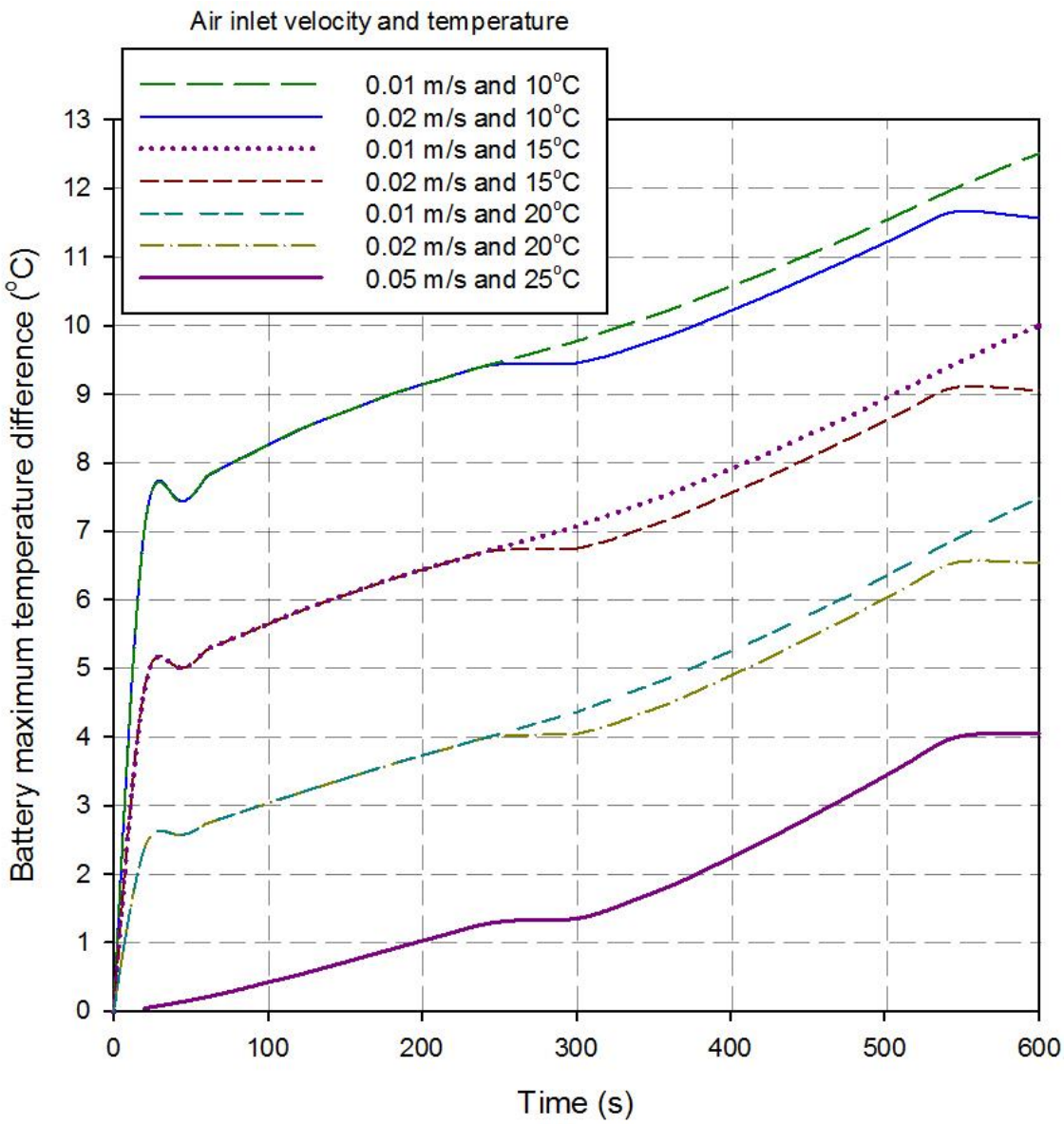

Figure 5.21 Variation of the maximum temperature difference across the battery through the discharging and charging cycle at a rate of 4C.

It is shown in Figure 5.20 that reducing the inlet velocity of the coolant results in increasing the maximum temperature of the battery. The increase in the maximum temperature with the decrease of the inlet velocity is due to that when lower inlet velocity results in increasing the temperature of the coolant at early stages through the cold plate. Raising the coolant temperature at early stages within the cold plate results in a colder areas at the inlet of the cold plate and higher temperature at the exit of the cold plate compared

to the cases with higher velocity inlet. Unlike the inlet temperature effect on the variation of the battery maximum temperature of the battery the effect of the inlet velocity within the considered ranges the variation in it shows it effect on the variation curve later around 250 seconds through the 600 seconds cycle as shown in Figure 5.20.

5.3.4 System 4 results

The battery pack design equipped with the propane based battery thermal management system results are presented first. The performance of the proposed lithium ion battery management system is investigated by examining the effect of varying several design factors. We mainly consider the maximum temperature in the pack and the temperature uniformity in the pack. The design factors examined include the height of the propane pool in the battery pack, the saturation pressure, which determines the temperature at which the propane pool boils, and discharging and charging rates. First the performance of the proposed system is investigated for prismatic battery pack design and second for a cylindrical battery pack design will be considered.

a) Pool height effect on the battery pack temperature distributions

The height of the propane pool in the battery pack is maintained through a height control system with the support of the liquid propane tank. The height of the propane liquid pool is varied to cover 5% to 30% of the front surface area of the batteries in the pack (5% to 30% of the height of the pack from the bottom) to investigate its effect on the thermal performance of the batteries in the pack. Throughout the variation of the pool height, the propane saturation pressure is maintained at 8.5 bar, and the battery pack is subject to a single 300 second discharge followed by a 300 second charge cycle, where the rate is 4C for both the charging and discharging rates. The rate of 4C was selected to test the performance of the proposed cooling system based on the loose definition in the literature of what constitutes a high charging or discharging rate. The thermal performance of the batteries in the simulated domain due to the cooling effect produced by the boiling based propane cooling system is presented in Figure 5.22 for a high discharge and charging cycle rate of 4C. In Figure 5.22, the temperature distributions of the surfaces of the batteries in contact with the propane pool and the other surface in contact to the neighboring battery in the pack are shown at the end of the complete discharging and charging cycle (i.e., after 600 seconds). The temperature of the battery surface that is in contact with the propane pool and the vapor space exhibits greater variability compared to the surface in contact with the other battery (see Figure 5.22). By raising the propane pool height in the pack from 5% to 20%, although colder temperature regions span across more surface area, a maximum temperature of around 34.9^{o}C is observed for all pool heights in the pack, as shown in Figure 5.23(a).

When the propane pool covers 30% of the battery front surface, the temperature uniformity throughout the battery improves, as shown in Figure 5.22. This suggests that increasing the height of the propane pool in the pack improves the temperature uniformity throughout the battery surfaces. This behavior can be explained through the two main heat exchange modes that are taking place.

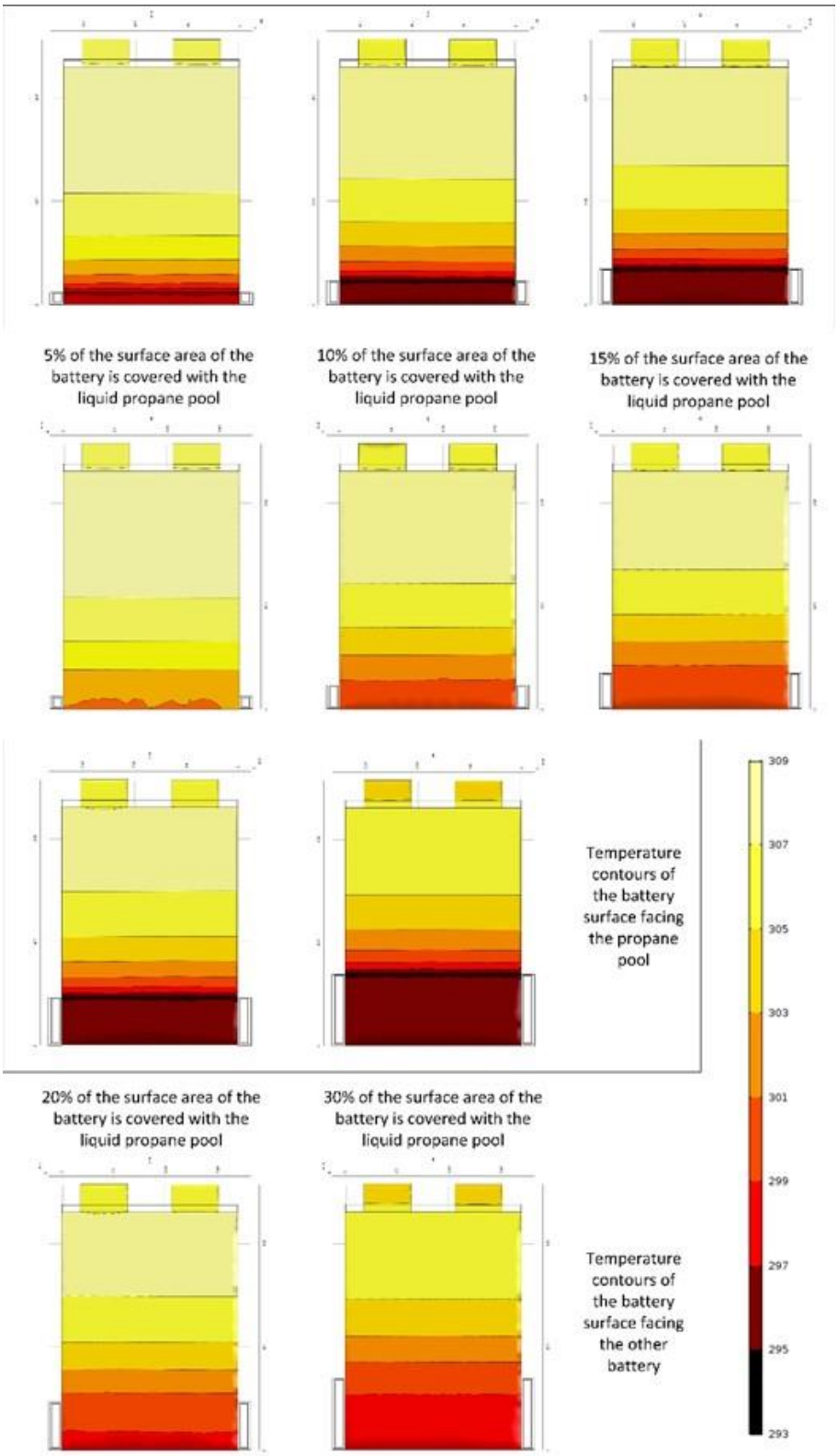

Figure 5.22 Temperature contours of the battery located at the center of the proposed pack the height of the propane pool (at saturation pressure of 8.5 bar) is varied, at the end of the discharging and charging cycle (i.e., at the end of the 600 second cycle).

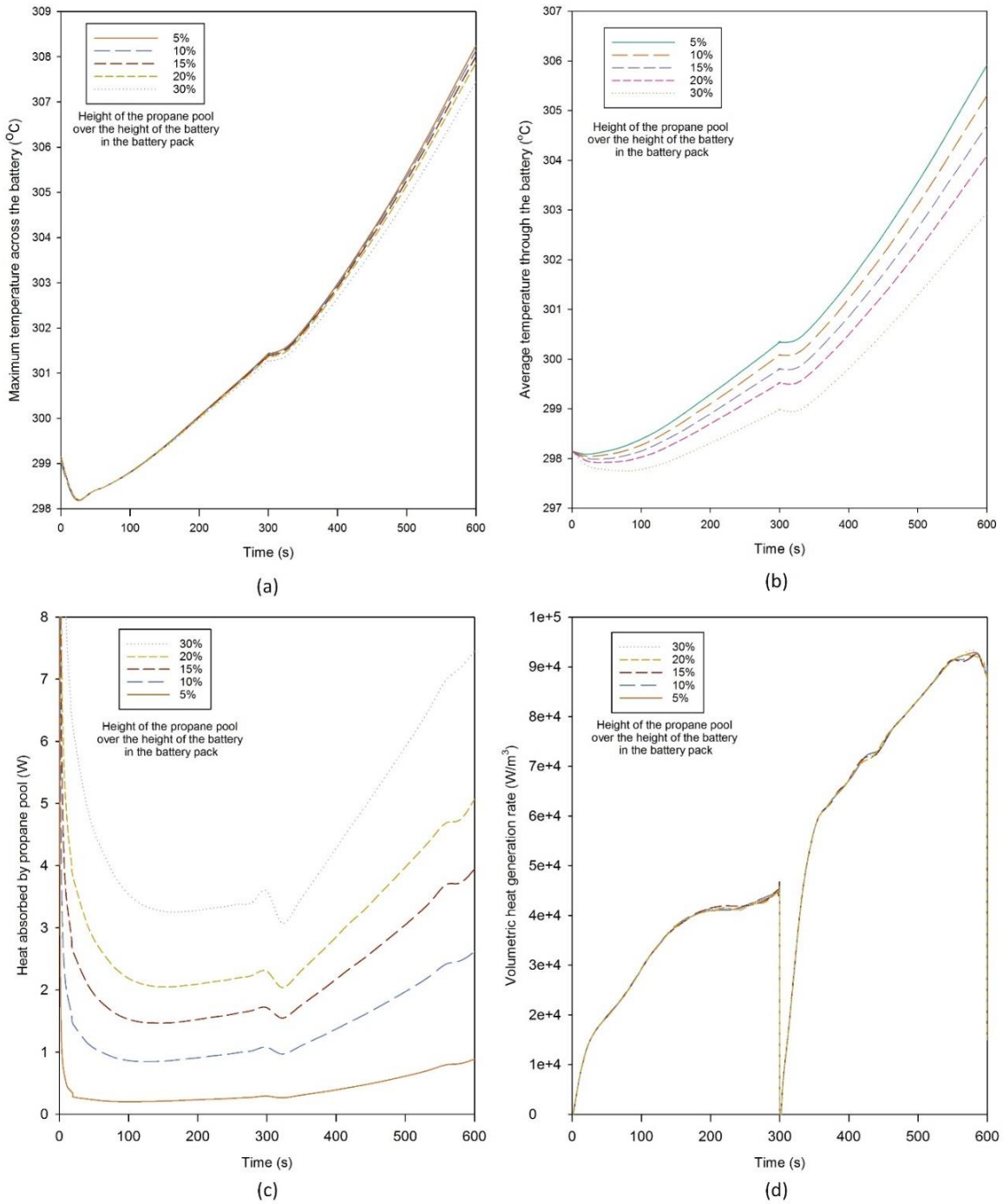

Figure 5.23 Variation of (a) maximum temperature of the battery, (b) average temperature of the battery, (c) heat absorbed by the propane pool, and (d) volumetric heat generation rate by the batteries, for various propane pool heights and discharging and charging cycle times.

The first is boiling heat transfer, the effect of which increases as the pool height covers more of the battery. The seconds is the natural convection where increasing the

amount of liquid propane results in an increase in the propane vapor flow rate and improves natural heat convection on these surfaces. The cooling effect of the propane vapor on the upper part of the battery increases as the height of the propane pool increases, since the surface area subjected to boiling increases, raising the amount of propane vapor generated. Hence, as the height of the propane pool in the pack increases to 30% or higher, enough propane is evaporated from the surface of the pool and, due to the height of that surface, cold propane manages to reach the top parts of the battery and cools it down. Having cold propane vapor reaching the uppermost part of the battery reduces the maximum temperature of the battery, as shown in Figure 5.23(a). The proposed battery pack design limits the reduction of the maximum temperature of the batteries in the pack when the pool covers 50% or less of the battery surface as shown in the small variations in the maximum temperature curves in Figure 5.23(a). Since the cooling is applied from one side of the battery leaving the other side to gain heat from the neighboring cell, and the vapor propane get superheated before reaching the upper most part of the battery.The temperature uniformity as indicated by the temperature distribution through a single battery in the pack is evaluated through the average temperature of the single battery. Figure 5.23(b) shows the variation of the average temperature of the battery in the pack through the discharging and charging cycles (at 4C rate). As the height of the propane pool increases in the pack, the lower becomes the average temperature in the pack. The decrease in average temperature shown in Figure 5.23(b) is seen to have vary linearly with the height of the propane pool in the pack relative to the total height of the pack, i.e., the height fraction.

It was found that as the height of the propane pool is increased by 1% of the height of the battery the average temperature decreases by nearly 0.12^{o}C. However, for the five propane pool height fractions considered of 5%, 10%, 15%, 20% and 30%, the average temperatures at the end of the 600 second discharging and charging cycle are 32.8^{o}C, 32.2^{o}C, 31.6^{o}C, 31.0^{o}C and 29.8^{o}C, respectively. For a better understanding of the heat absorbed by the boiling propane and the volumetric heat generation for each battery, their variations with the discharging and charging cycle time are shown in Figs. 6(c) and 6(d), respectively. Figure 5.23(c) shows that at even the heat generation rate is increasing in the 300 seconds discharging period, the heat absorbed by the pool reduces. The heat absorbed by the pool reduces in the first 300 seconds is the result that the temperature of the battery surface in contact with the pool reduces and the heat generation rate is not high enough to raise it. Through the following 300 seconds of charging the heat generation rate increases to a level that it can raise the temperature of the battery surface in contact with the pool. In response the heat absorbed by the pool increases as shown in Figure 5.23(c).

Figure 5.23(d) shows that the volumetric heat generation rate of the battery varies slightly with propane pool height, since the differences between the average temperatures of the battery for the different pool heights during the discharging and charging cycle are small. Thus, negligible differences in the volumetric generation rate are observed.

b) Pool saturation pressure effect on the battery temperatures

The saturation pressure of the propane pool, which is maintained in the pack with the help of liquid propane tank and the propane vapor pressure regulator and collector, was selected based on the corresponding saturation temperature.

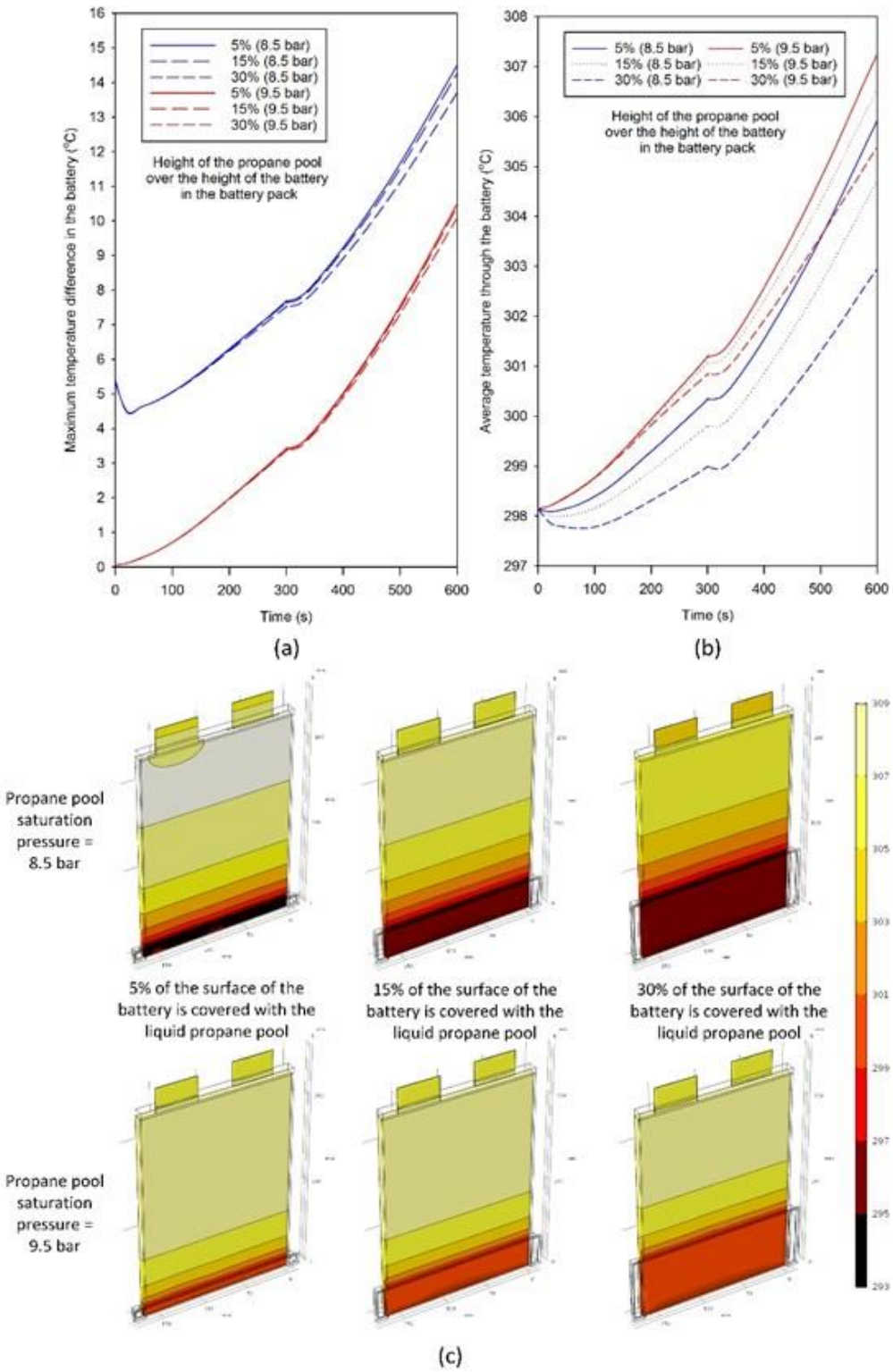

Figure 5.24 Effect of saturation pressure of the liquid propane pool on the temperature variation across the battery in terms of (a) maximum temperature difference, (b) average temperature, and (c) temperature contours on the surface of the battery (showing the surface facing the propane pool) (at the end of the 600 second cycle).

The saturation temperature was selected so as to have around a 5°C temperature difference with the initial temperature of the battery and so as to be close to the actual pressure of the propane tank in HEVs. The effect of the saturation pressure was investigated by increasing it to 9.5 bar, which corresponds to a saturation temperature of 25°C, from 8.5 bar (21°C). The effect of the pool saturation pressure on the thermal performance of the battery is presented in Figure 5.24. Figure 5.24(a) shows the maximum temperature difference in the battery, Figure 5.24(b) the average temperature through the battery and Figure 5.24(c) the temperature contours of three pool height fraction cases (5%, 15%, and 30%). Figure 5.24(a) shows that the maximum temperature difference of the battery drops around 4°C when the pressure is increased from 8.5 to 9.5 bar. As the height of the propane pool increases, the drop in temperature difference due to increasing the saturation pressure reduces, from a 4.02^{o}C temperature drop in the temperature difference at a 5% pool height fraction to a 3.62^{o}C temperature drop at 30% a pool height fraction. Figure 5.24(a) also shows that the variation in the temperature difference with the variation of the pool height is lower at a higher saturation pressure than a lower saturation pressure. In terms of the average temperature (Figure 5.24(b)), it is seen that a higher saturation pressure corresponds to a higher average temperature through the battery. From Figure 5.24(b) a pool height of 5% at a 8.5 bar saturation pressure is seen to have a similar average temperature to that of a pool height of 30% at 8.5 bar. The effects of varying the pool saturation pressure for the cases when the liquid propane pool covers 5%, 15% and 30% of the front surface of the battery are shown in Figure 5.24(c). From the temperature contours shown in Figure 5.24(c) the enhancement of the temperature difference throughout the battery can be seen, as the temperature difference between the minimum and the maximum temperatures of the battery became smaller.

c) Cycle rates effect on battery temperature distribution

The cooling performance of the proposed cooling system was investigated through the maximum temperature and temperature variation across the battery surfaces when the discharging and charging rates are varied. The resulting thermal contours of the battery surfaces for various discharging and charging rates are shown in Figure 5.25. Temperature contours are presented for the surface of the battery facing the pool and for the surface facing the neighboring battery. Six discharging and charging rates are considered: 1C, 2C, 3C, 4C, 5C and 6C. Note that a different coloring scheme was used in Figure 5.25 since a different temperature range (in the legend) was used in describing the temperature contours so that they will be not mistakenly compared with the previous contours and their temperature range presentation. Figure 5.25 shows that, as the discharging and charging rate increases, the maximum temperature increases and the temperature uniformity declines. Regarding temperature uniformity over the battery surface, note that the surface facing the liquid propane pool experience larger temperature differences than the surface in contact with the neighboring battery.

Although the surface facing the pool experiences high cooling rates as it is covered by the propane pool, resulting in a low temperature (i.e., close to the saturation temperature of the pool), the battery still experiences high temperatures on its upper parts that are above the pool surface. It is also seen that the upper parts of the battery experience the same high temperatures as the surface in contact with the neighboring battery experiences while not

exhibiting the low temperatures caused by the pool, resulting in relatively lower temperature variations through the battery surface facing the neighboring battery. For the battery surface in contact with the pool, at low discharging and charging rates (1C, 2C and 3C) boiling heat transfer is dominant and results in a constant temperature on the surface covered by the pool very close to the saturation temperature of the pool.

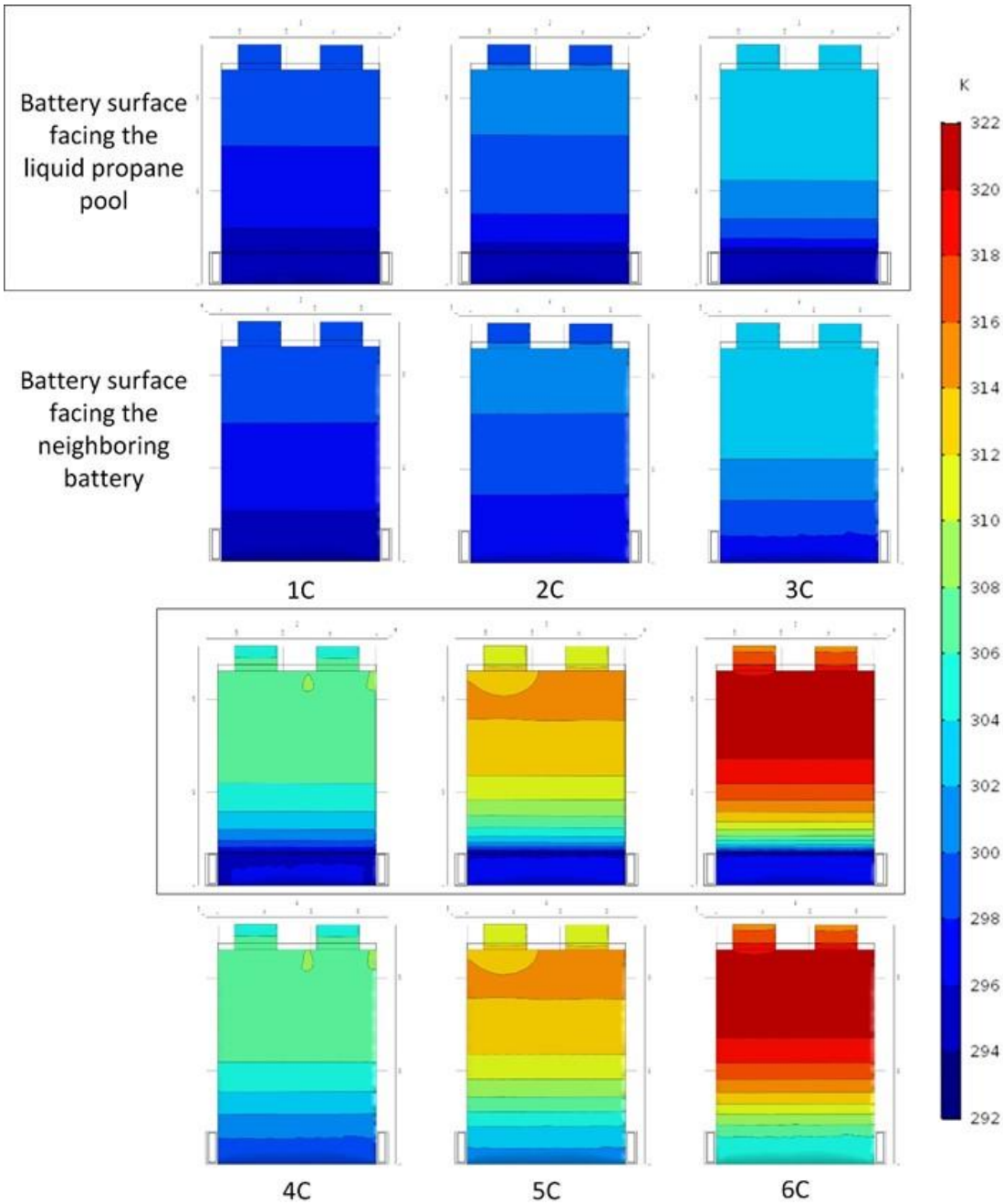

Figure 5.25 Effect of discharging and charging cycle rate on the temperature variation across the prismatic battery surface, where the upper row shows the surface in contact with propane pool and the bottom row shows the surface in contact with the neighboring battery (at the end of the 600 second cycle).

However, for higher discharge and charge rates the constant propane saturation temperature area reduces. At higher discharge rates only a small area located at the boundary of the line at which the pool surface in contact with the battery surface and that is mainly due to the very cold propane vapor that exits the surface at the saturation temperature. For the high discharging and charging rates the constant propane saturation temperature area is partially replaced with a slightly higher temperature, as shown in Figure 5.25. The maximum temperature variations through the discharging and charging cycle for various discharging and charging rates are presented in Figure 5.26. The maximum temperature at the end of the cycle (discharging for 300 seconds followed by charging for 300 seconds) was 48.5ºC at 6C compared to 41.1ºC at 5C, 34.9ºC at 4C, 30.4ºC at 3C, 27.2ºC at 2C and 25.4ºC at 1C.

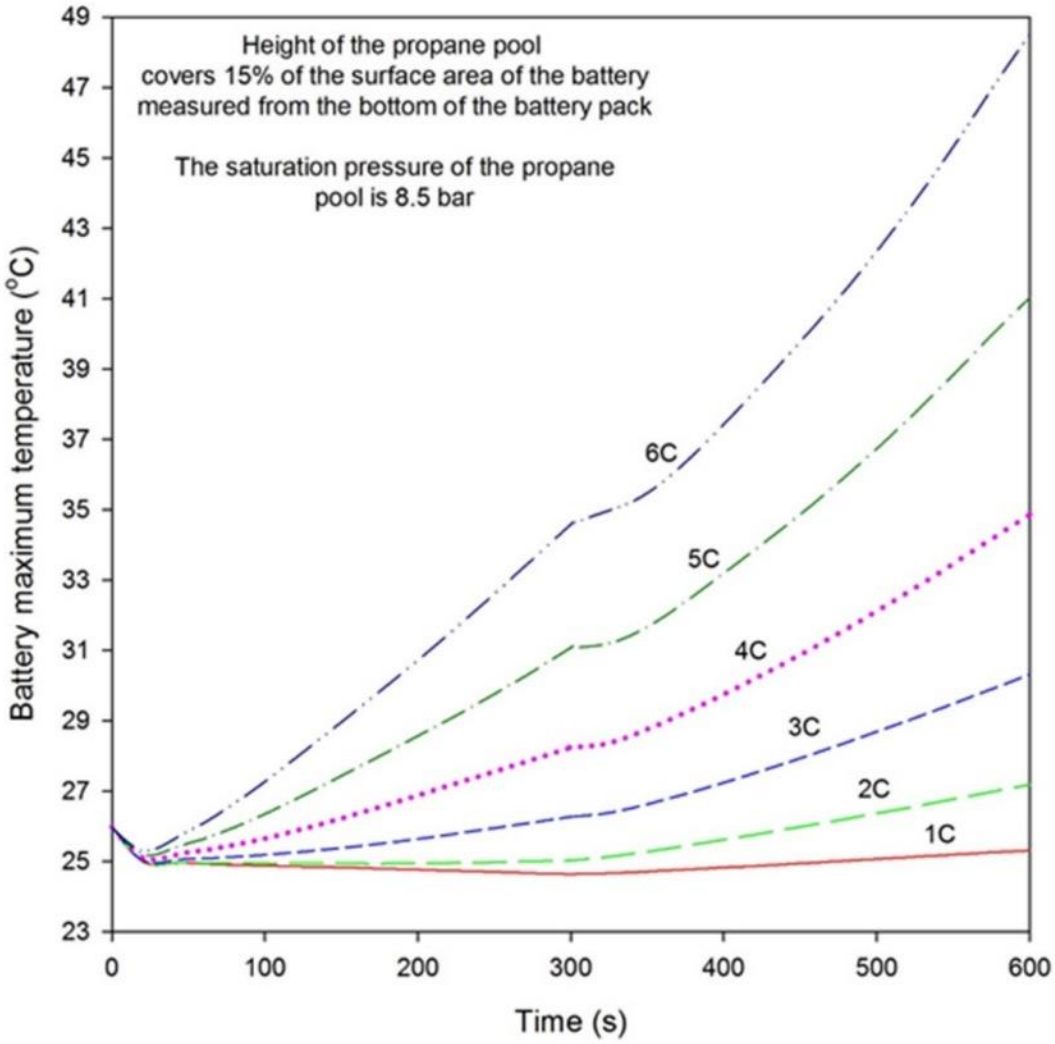

Figure 5.26 Effect of charging and discharging rates on the variation of the maximum temperature in the battery through the discharging and charging cycle.

The system performance is compared with results reported in the literature [9,134] in Figure 5.27. Note that the case when the battery was subjected to natural convection, a single battery is standing where the longest dimension is vertical, located in an open

environment. It is seen that covering 30% of the front surface of the battery with the boiling propane pool provides better performance than water cooling systems [9,134].

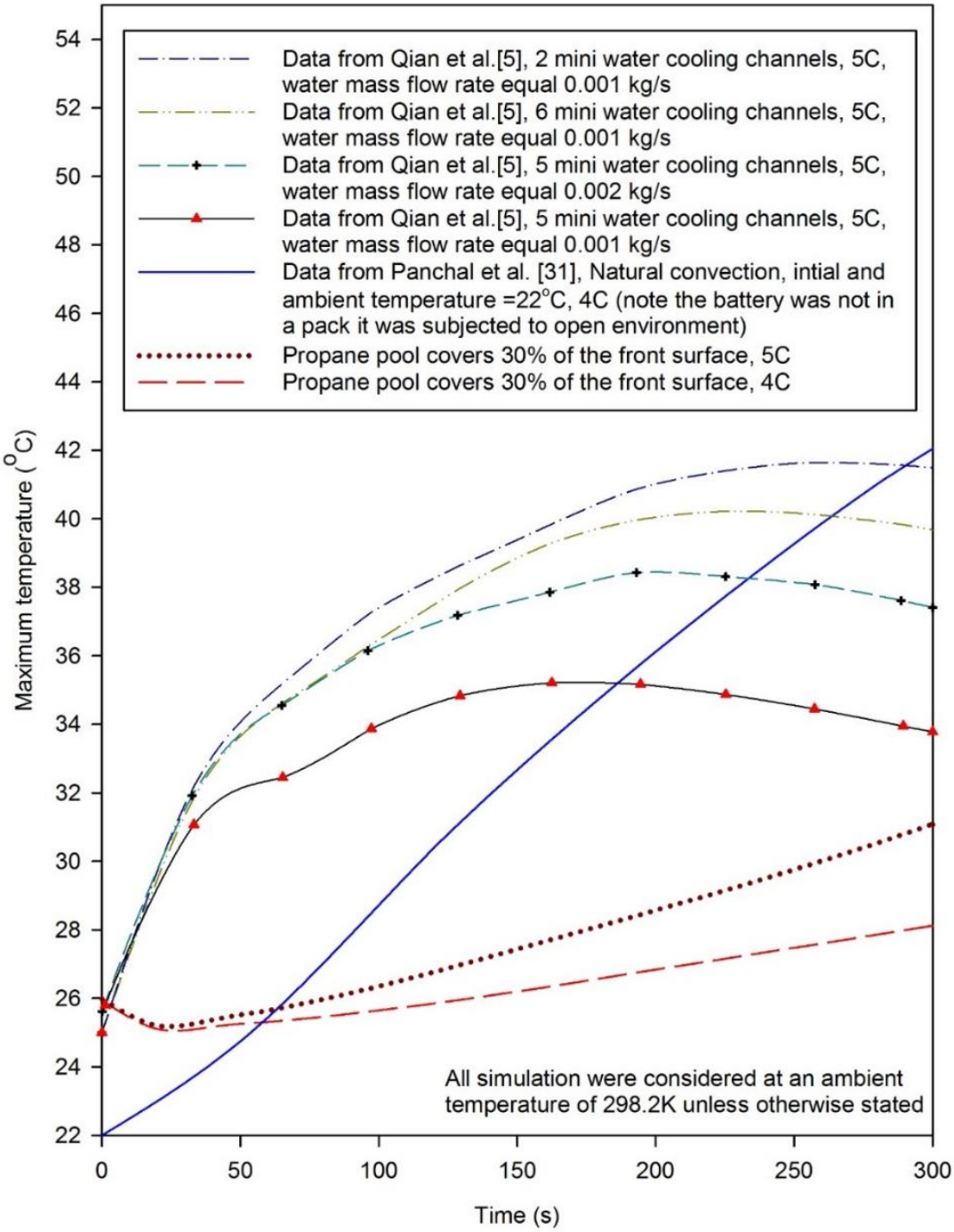

Figure 5.27 Comparison of performance of the proposed boiling based cooling system with systems reported in the open literature [9,134].

5.3.5 Comparative results of the present systems

In this section, the performance of the proposed systems for the prismatic battery pack is compared with each other and the without cooling initially and the best performing system

is comparted to the systems proposed in the literature in terms of pack performance. Pack performance is a measure of the thermal management performance however on the full pack level, which is mainly in the maximum temperature difference across the battery pack. Regarding the temperature difference across the battery, based on the configuration of the proposed cooling system where the cold plates are distributed evenly throughout the battery pack, and since each cold plate inlet temperature is independent on the other cold plate exit coolant temperature then the temperature difference across the battery pack can be neglected.

a) Temperature comparisons

In this section, the proposed systems are compared against each other, which includes all the five proposed system in this thesis, in addition to the two designs proposed for the ammonia cooling system. In order to compare between the different proposed systems and their different configurations they were set at a comparable operating parameters and simulated for a 600 seconds charging and discharging cycle at a rate of 6C. The variation of the maximum battery temperature through the simulation cycle at a rate of 6C for the five different proposed cooling systems for prismatic batteries including two designs of the cold plate and a case when there is no cooling system used are shown in Figure 5.28. As shown in Figure 5.28 the best performing system is the pool system with ammonia being the coolant and the pool covers 100% of the battery surface that is in direct contact with the cooling pool. Note that the best performance can also be achieved by the propane based system when the pool covers 100% of the battery height. The best performing system was able to reduce the maximum temperature of the battery by 45.8% compared to the case when there is no cooling system is used. A close competitor to the ammonia based system with a 100% battery height is covered with the pool is the tube based cold plate system. The tube based cold plate based system was able to achieve the closest performance to the 100% pool system as shown in Figure 5.28. Where the tube based system have the advantage of having a smaller amount of coolant in the battery pack due to the configuration of the tube system and without having the direct contact with the battery surface over the 100% pool based system. All these advantages the tube system have in addition to its high performance leads to having the tube system to be the favored from all the different proposed systems. To compare between the pool based system and the tube based system, three different variations of the pool system are compared to the one variation of the tube based system in terms of the reduction in the maximum temperature of the battery without the cooling system and the study is plotted in Figure 5.29.

As shown in Figure 5.29 the pool based system with ammonia and the battery surface is covered 100% and the tube based system have a very close performance as was earlier concluded through the variation of the maximum battery temperature in Figure 5.28. However, reducing the coverage percentage of the battery surface in the pool based system, while having a different coolant, propane which is predicted to have a comparable performance to the ammonia coolant as was shown in earlier sections of the results and discussion. It is shown that dropping the coverage percentage of the battery surface by the pool to 80% (by 20% from 100%) results in a large drop in the system performance as shown in Figure 5.29, which shows the ability of the tube based system in achieving a better performance in terms of the battery maximum temperature. Further case considered for the pool based system is with the R134a refrigerant as the coolant, which resulted in a

lower performance compared to the case where propane was the coolant for the same coverage of the surface of the battery. The lower performance achieved by the refrigerant based system is mainly that it has lower enthalpy of vaporization, which is 177.8 kJ/kg compared to propane which is 342.9 kJ/kg. Having higher enthalpy of evaporation results in having the liquid in a longer period of time in contact with the boiling surface, which results in a higher heat transfer convection.

For the other systems the air and the hydrogen based systems for the considered parameters, which are an inlet velocity of 0.05 m/s and an inlet temperature of 25°C. These parameters where considered to have an inlet temperature equal to the saturation temperature set for the pool based systems.

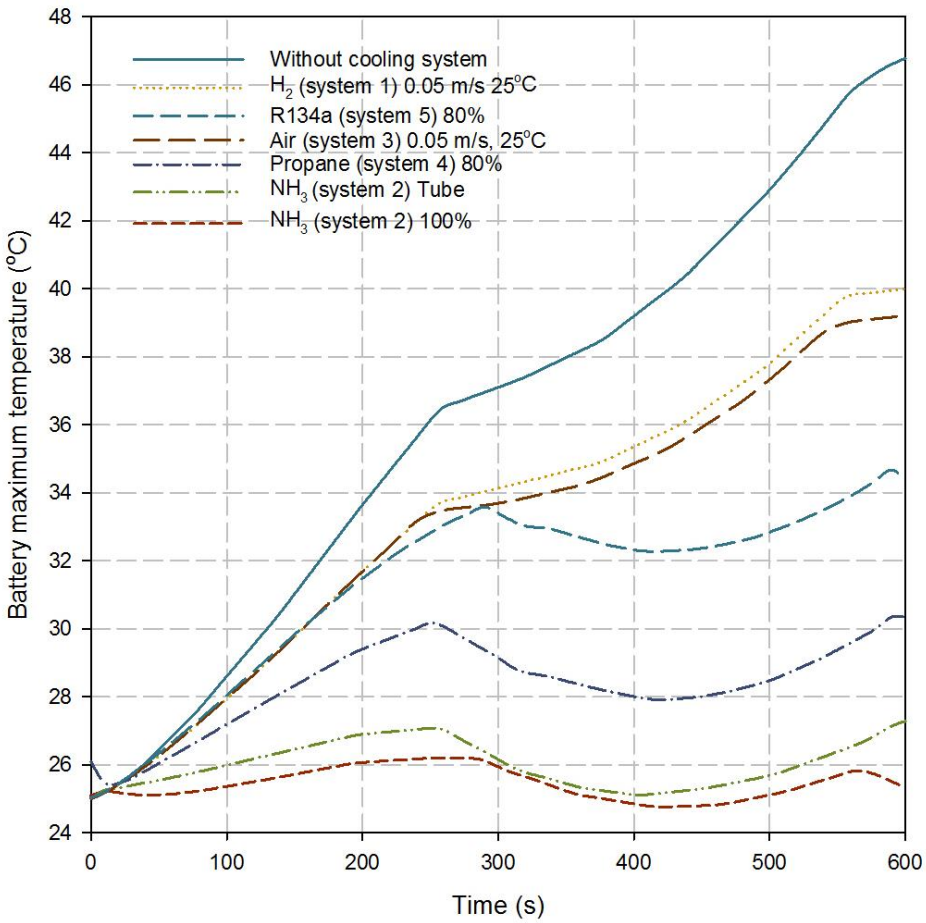

Figure 5.28 The variation of the maximum battery temperature through the simulation cycle at a rate of 6C for the five different proposed cooling systems for prismatic batteries including two designs of the cold plate

The air based system was able to achieve a better performance than the hydrogen based system at the same operating parameters as well as in the same optimized final cold plate design considered in this thesis (refer to section 5.2.1.1) as shown in Figure 5.28. The air was able to perform better than the hydrogen system in terms of the battery maximum temperature is mainly due to the higher density of the air compared to the hydrogen at the

selected inlet coolant temperature, which result in the air to have a higher inlet mass flow rate leading to a higher cooling rate.

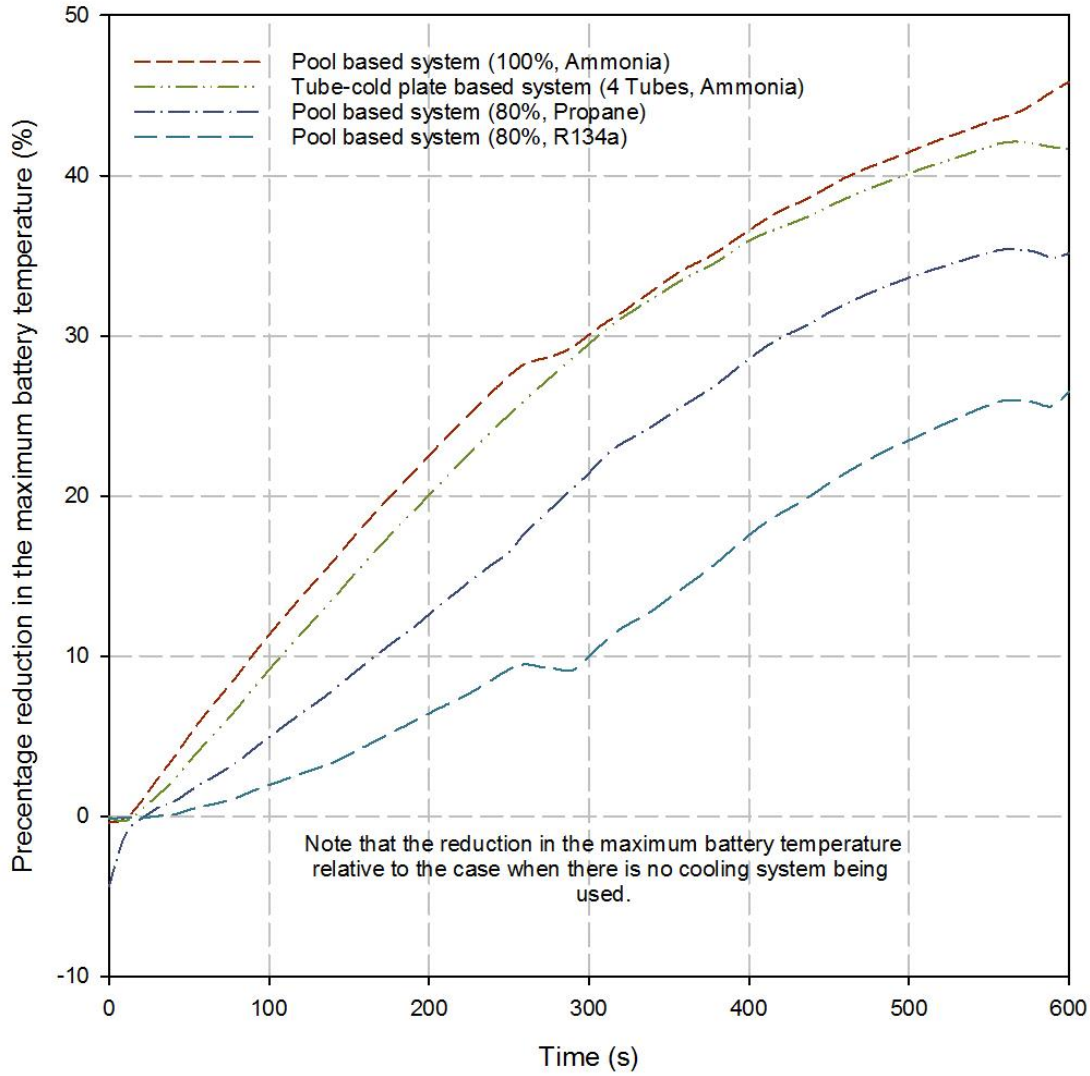

Figure 5.29 The variation of the reduction of the battery maximum temperature by the pool and the tube based systems.

In addition to the variation of the maximum temperature of the battery, the comparison between the different proposed systems in terms of the maximum temperature difference across the battery, where the considered battery is the battery with the maximum temperature in the pack. The variation of the maximum temperature difference across the battery for the five different proposed system including the two variation of the ammonia based system are shown in Figure 5.30. A very comparable performance and the best is again achieved by the 100% pool based and the tube based systems as shown in Figure 5.30. Although it might seem that the all the systems result in a larger temperature across the battery compared to the case when there is no cooling system is used, yes it is true however it should always be noted that the slightly larger temperature difference across the battery is achieved at nearly around 50% lower maximum temperature compared to the

case when there is no cooling. The maximum temperature difference is maintained across the battery within 3 to 4°C for the 100% covered battery pool system and tube based system. Reducing the percentage of the battery surface covered by the pool results in a large increase in the maximum temperature difference across the battery as shown in Figure 5.30, which mainly due having the uncovered battery surface cooled by the generated vapor. The generated vapor as was shown in the detailed analysis of each of the pool proposed systems results in increasing the maximum temperature and the maximum temperature difference of the batteries due to its low buoyance case of velocity and low mass flow rate. The air and hydrogen based system at the specified parameters achieved better performance in terms of the maximum temperature difference across the battery than 80% pool based systems.

As concluded this section of the thesis, the tube-cold plate design achieves the best performance throughout the considered operating parameters and in addition it contains at a time 20% less coolant in comparison to the competitor which is the 100% covered battery surface with the direct coolant system.

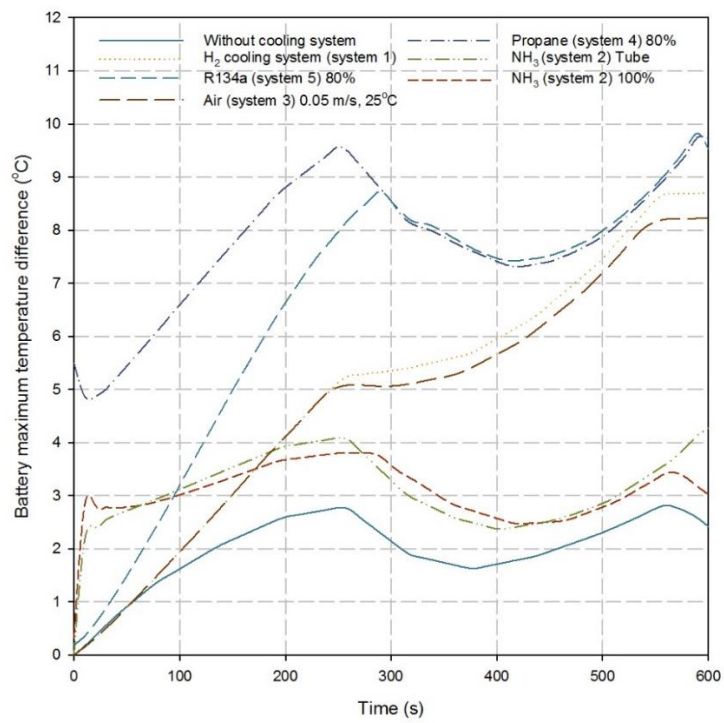

Figure 5.30 The variation of the maximum temperature difference across the battery for the five different proposed system including the two variation of the ammonia based system in addition to the case when there is no cooling system is used.

b) Efficiency comparisons

The performances of the various liquid-to-vapor based thermal management systems are assessed and compared based on the energy efficiency. The energy efficiency of a thermal management system is defined in this paper as follows:

$$\eta = \frac{Q_{rem}}{Q_{gen}+W} \tag{5.1}$$

Here, η denotes the energy efficiency of the thermal management system, Q heat, and W the electrical energy the active thermal management system consumes, such as the pumping work consumed in pumping the water. Also, the subscript rem refers to the removed heat from the battery using the thermal management system, and the subscript gen refers to the heat generation accumulation in the battery. Note that the amount of electrical energy consumed in moving the coolant in the liquid-to-vapor systems is negligible compared to that for active systems; hence we can neglect the energy consumed by the system to maintain the height of the boiling pool. The energy efficiency is assessed throughout the cycle as the cumulative heat removed from the battery over the cumulative heat generated by the battery throughout the simulation cycle 600 seconds of charging and discharging at a rate of 6C. For the simulation cycle used to calculate the energy efficiency of the various liquid-to-vapor phase change systems, the initial temperature of the battery is set to the saturation temperature of the coolant to simulate the charging and discharging of the battery from the equilibrium state.

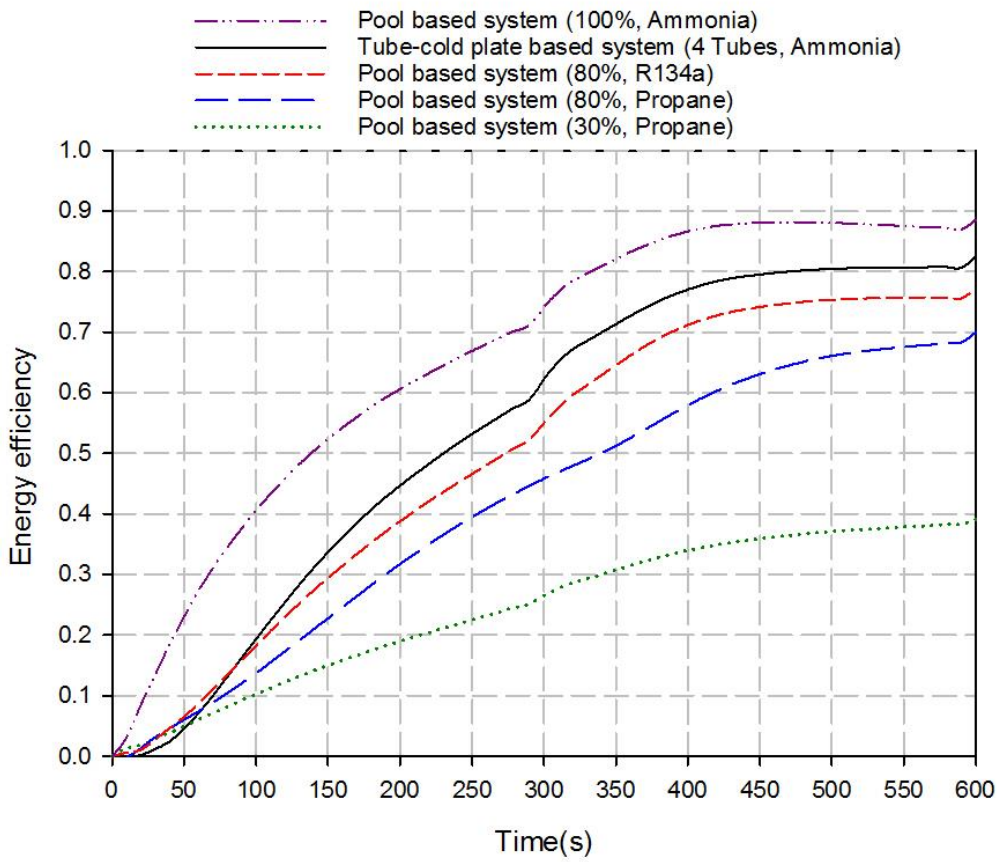

Figure 5.31 Variation of the maximum temperature of the prismatic battery when the tube based system with ammonia coolant and for other systems proposed in the literature, for a discharge cycle at a rate of 5C.

The energy efficiency variation through the charging and discharging simulation cycle at a rate of 6C is shown in Figure 5.31. It is seen for all liquid-to-vapor systems that the energy efficiency increases throughout the cycle, starting from zero due to the initial equilibrium state with the phase changing coolant. The energy efficiencies of all of the systems increase sharply throughout the starting half of the simulation cycle, as seen in

Figure 5.31. Then through the last 100 seconds of the cycle they tend to stay constant. Similar to the maximum reduction in the battery maximum temperature relative to the no cooling case, the best preforming system in terms of the energy efficiency occurs when 100% of the battery height is covered with the liquid ammonia boiling pool. The maximum energy efficiency is 88.6%, followed by the tube based system, which reaches a maximum value of 82.5%. It is seen in Figure 5.31 that the system performs better in terms of the energy efficiency as the cycle duration increases until the system energy efficiency levels off. Note in Figure 5.31 that the sudden rise in energy efficiency at the far right is due to the sudden drop in the heat generation rate and does not indicate an actual increase in the energy efficiency of the cooling system.

c) Comparisons with the literature studies

The previous section concluded that the tube based cooling system was able to achieve the largest reduction in the battery's maximum temperature relative to the case when there is no cooling system is used. For that the best performing system from the various proposed systems is compared to other systems in the literature that were simulated to achieve the required cooling an avoid thermal runway. The tube based system with ammonia in the tubes as the boiling coolant is simulated for the same simulation cycle that was used to evaluate the performance of the proposed systems in the literature and the results are shown in Figure 5.32. The simulation cycle is 600 seconds discharge cycle at a rate of 5C.

As shown in Figure 5.32 the tube based system outperform the proposed systems in the literature at their own selected operating parameters at the same simulation cycle of 5C of discharging rate for 600 seconds.

5.4 Cylindrical battery pack results

In this section the results of the proposed battery pack thermal management systems are presented in this section of those that are proposed for the cylindrical batteries.

5.4.1 System 2 results

For the proposed an ammonia boiling based thermal management system for Li-ion batteries for future ammonia based HEVs with zero carbon emissions, the effect of the thermal management system on the Li-ion battery pack thermal performance is investigated. The effects are assessed of several parameters of the proposed system on the thermal performance of the Li-ion battery pack. The thermal performance of the battery pack is taken to be characterized by the maximum temperature of the battery and the temperature uniformity throughout it. The effect of the height of the PSLA in the battery pack on the maximum temperature of the battery and the temperature distribution is investigated to determine the minimum height that provides an acceptable operating range for the high power demands anticipated for the vehicles. The effects are also investigated of other factors such as the pressure of the PSLA and charging and discharging rates.

a) Battery temperature distributions

The height of the PSLA, which covers part of the batteries in the pack, is varied from covering 5% of the total height of the battery to 30%. The pressure of the PSLA is maintained at 9.0 bar for the five cases of PSLA height in the pack. Figure 5.33 shows the

thermal performance of the ammonia based cooling system at high power charging and discharging rates (7.5C) in terms of (a) the maximum temperature, (b) the temperature difference between the minimum and the maximum temperatures, (c) the specific heat generation rate, and (d) the electric potential of the battery.

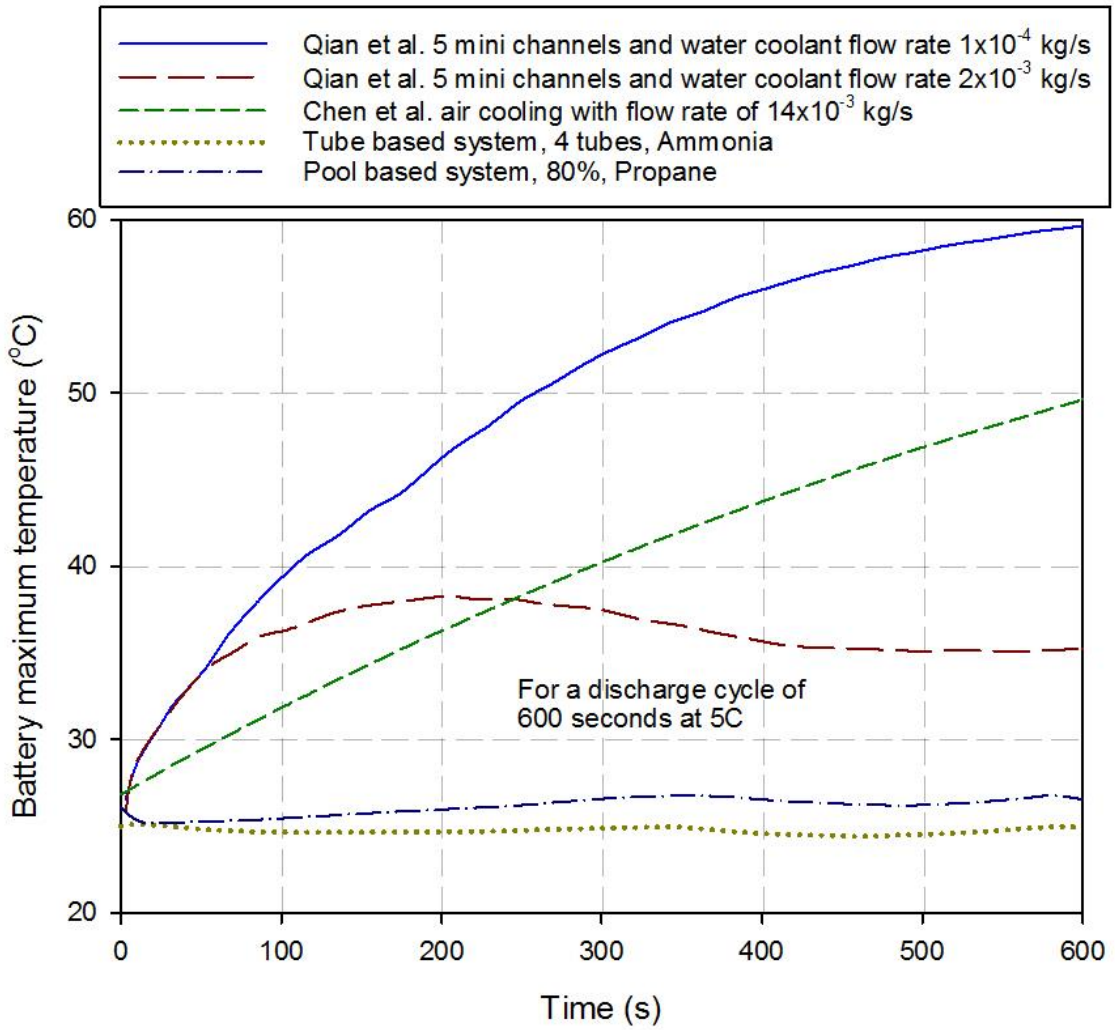

Figure 5.32 The variation of the maximum temperature of the battery prismatic battery when the tube based system with ammonia as the coolant and other systems proposed in the literature for a discharge cycle at a rate of 5C.

The maximum temperature of the battery increases rapidly with various increasing rates for different heights of the PSLA. That is, the difference between the rate of increase of the maximum temperature in the battery becomes clearer as time progresses in the charging phase, as shown in Fig. 5 (a). After two thirds of the charging process the maximum temperature increase rate starts to decrease gradually, with a more visible change for the higher PSLA height, which is the result of having greater cooling ability in the last third of the charging process since the specific heat generation rate decreases, as shown in Figure 5.33(c). For the five cases of PSLA heights in the battery pack, the maximum temperature reached in the charging phase is 37.8°C, which occurs for the case where the

PSLA covers 5% of the height of the battery. However, having 5% of the height of the battery covered with PSLA is sufficient to maintain the maximum temperature of the battery below 34ºC in the first two thirds of the high power charging rate.

After the 300 seconds of charging, the high powered discharge rate at 7.5C starts as shown in Figure 5.33. When the discharging phase begins, the maximum temperature starts to decrease rapidly, dropping by 2ºC in the first 50 seconds of the discharging phase for the case when 30% of the battery height is under the PSLA surface.

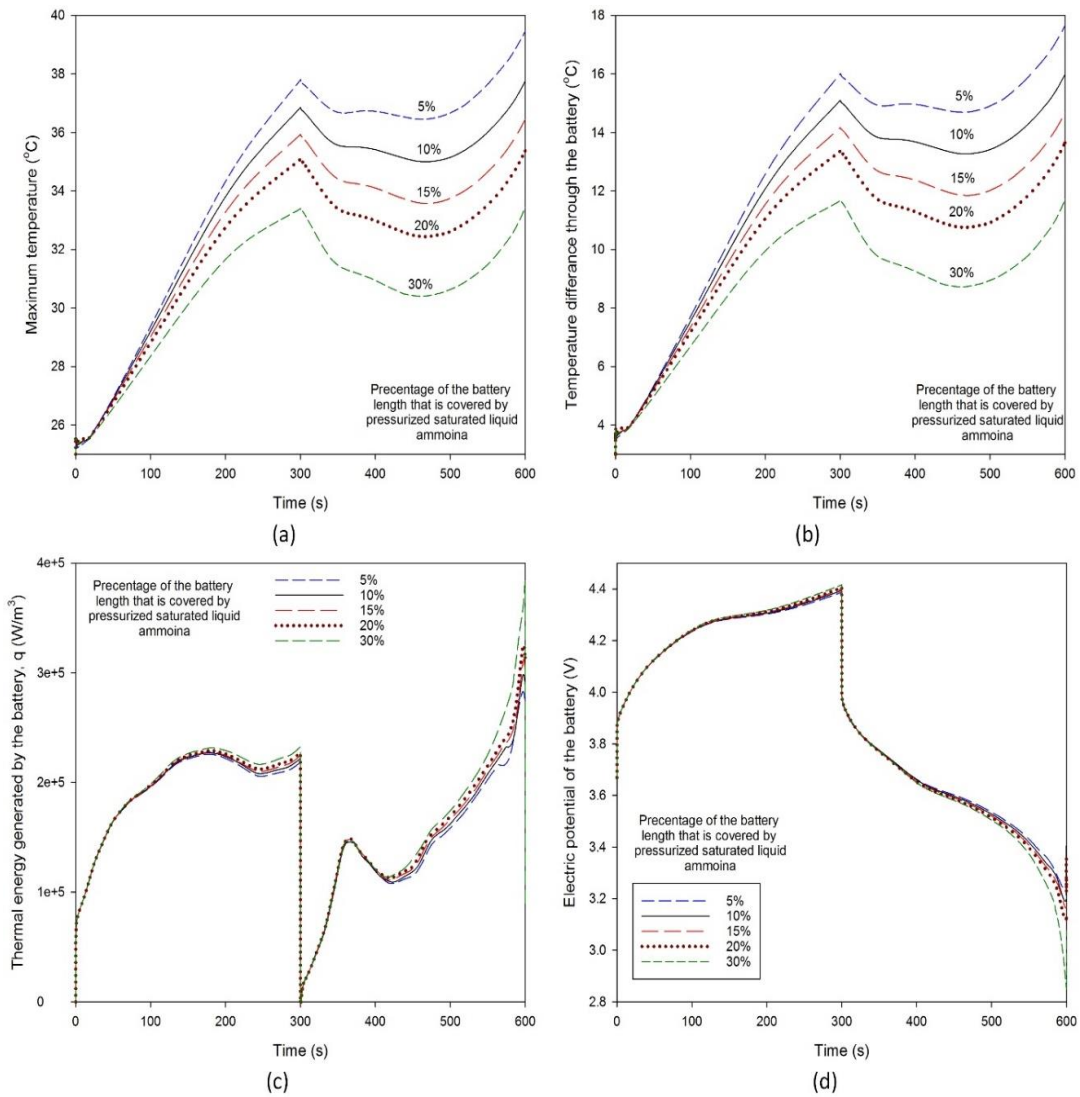

Figure 5.33 Electro-thermal performance of cooling system at a 9.0 bar saturation pressure of the PSLA. (a) Temperature difference throughout the battery, (b) maximum battery temperature, (c) specific heat generation rate, and (d) electrical potential.

This is due to the sudden drop in the heat generation rate produced by the battery, as shown in Figure 5.33(c). The maximum temperature continues to decrease to its lowest value within the discharging phase, which is 3ºC less than that at the start of the discharging process for the case where 30% of the battery height is under the PSLA surface. Following

that point, the temperature starts to increase since the heat generation rates are higher than the cooling capacity of the proposed system, as shown in Figure 5.33(a) and (c). The maximum temperature of the battery reaches a maximum of 39.4^{o}C, which is 1.6^{o}C higher than the maximum at the end of the charging phase for the case when the PSLA is covering only 5% of the total height of the battery. Figure 5.33(a) shows that as the height of the PSLA in the battery pack increases, the maximum temperature of the battery is achieved at the end of the charging and discharging cycle decreases. The maximum temperature of the battery decreases from 39.4^{o}C to 33.4^{o}C as a result of increasing the height of the PSLA from 5% to 30% of the height of the battery. When the height of the PSLA increases, it also reduces the temperature difference between that at the end of the charging phase and that at the end of the discharging phase, as shown in Figure 5.33(a). The increase in the maximum temperature between the end of the charging and the discharging phases reduces from 1.6^{o}C to 0°C when the height of the PSLA increases from 5% to 30% of the height of the battery.

The temperature uniformity in the battery pack is of high importance in order to maintain its optimum working conditions. However, due to the nature of the proposed cooling system, it is expected that the temperature variation between the batteries in the pack will be negligible. So temperature uniformity as a cooling system performance measure will be more focused on the temperature variation in each battery. Figure 5.33(b) shows the level of temperature uniformity throughout the battery in terms of the maximum temperature difference in the battery, which follows a similar trend to that of the maximum temperature shown in Figure 5.33(a). The temperature difference in the battery through the high power (7.5C) charging and discharging cycles reaches a maximum of 17.6^{o}C at the end of the discharging phase, when only 5% of the battery height is covered by PSLA. The system with 5% of the height of the battery covered by PSLA maintains temperature difference below 15°C during the first 500 seconds of the 600 seconds cycle.

The effect of varying the percentage of the height of the battery covered by PSLA on the temperature difference throughout the battery is shown in Figure 5.33(b). For the five heights of the PSLA considered (5%, 10%, 15%, 20%, and 30%), the maximum temperature difference occurred at the end of the discharging phase (600 seconds) for all cases, at values of 17.6^{o}C, 15.2^{o}C, 13.8^{o}C, 12.9^{o}C and 10.8^{o}C, respectively. The gap between the temperature difference at the end of charging and at the end of discharging decreases as the height of the PSLA increases. Increasing the height of the PSLA covering the battery from 5% to 30% reduces the gap from 1.63^{o}C to 0.03^{o}C respectively. The drop in temperature difference as the height of the PSLA increases is due to the increase of the surface area that is covered by a material with a high heat transfer coefficient (boiling heat transfer coefficient), which in turn produces more ammonia vapor that further cools the part of the battery not covered by liquid.

The temperature contours of the battery from the center of the battery pack shown in Fig. 2 for the five cases of PSLA height in the battery pack are shown in Figure 5.34(a) after 300 seconds of high power charging and after 300 seconds of high powered discharging. Figure 5.34(a) shows how increasing the height of the PSLA reduces the temperature difference in the battery. Figure 5.35 shows the variation of the temperature distribution in a single battery with time for the case when 30% of the battery height is covered by PSLA. As shown in Figure 5.35(b), the temperature distributions at the end of

charging and at the end of discharging are identical. The shape of the temperature distribution in the battery (see Figure 5.35) is maintained after the end of the battery charging period, even when the temperature starts to decline at the start of the discharging period.

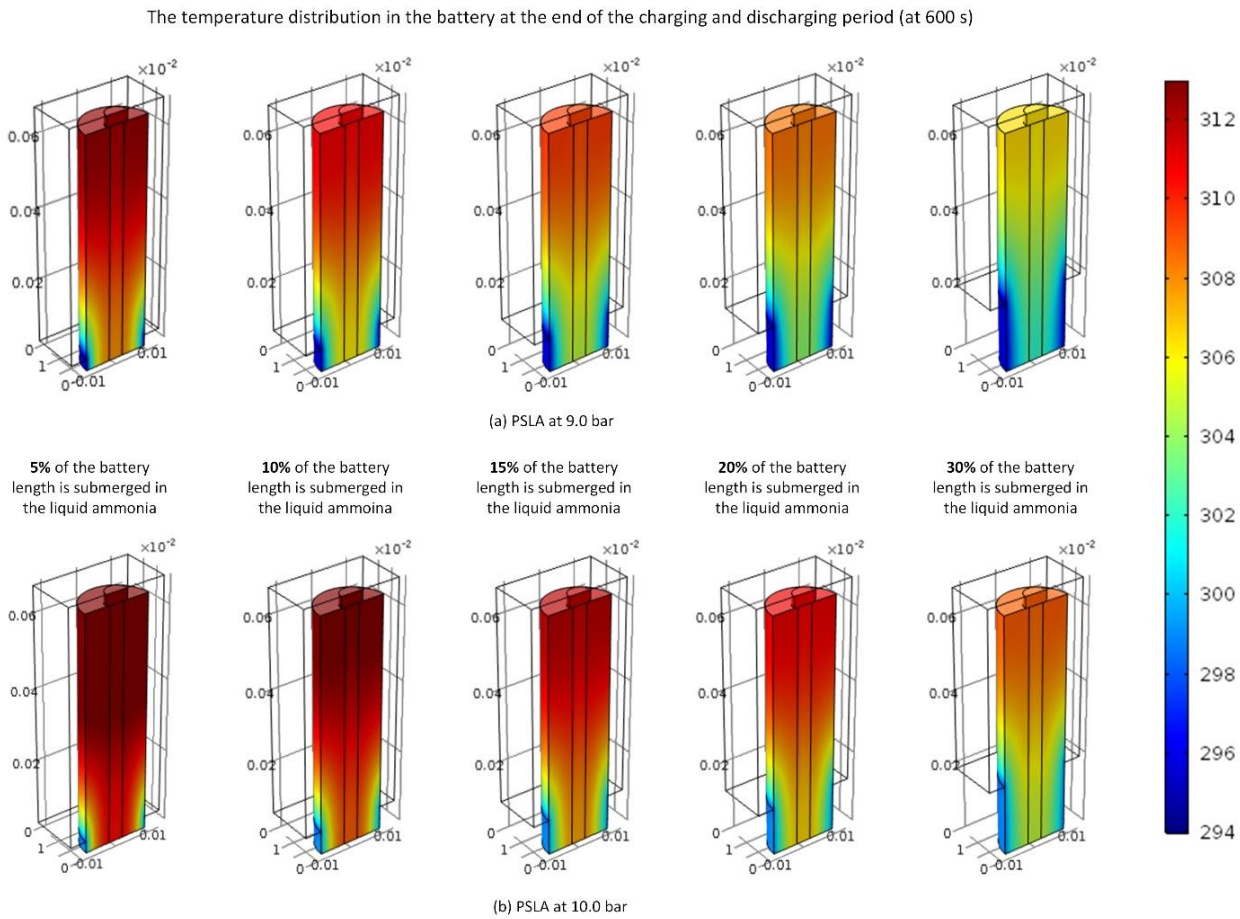

Figure 5.34 Temperature contours of the middle section of the battery in the center of the pack for five cases of liquid propane height at the end of the cycle (at 600 s).

The constant temperature of the PSLA during boiling is a function of the saturation pressure of the PSLA, and the effect of the saturation pressure on the performance of the cooling system is shown in Figure 5.36. A second pressure value is considered (10.0 bar), and the results are compared to those at 9.0 bar, considered earlier in the thesis. The saturation temperatures corresponding to pressures of 9.0 bar and 10.0 bar are 294.7 K and 298.0 K respectively. The two pressure cases are applied to all five heights of the PSLA in the battery pack, and the results are shown in Figure 5.34 and Figure 5.36. Figure 5.36 illustrates the effect of PSLA pressure on the performance of the cooling system in terms of maximum temperature of the battery and temperature difference throughout the battery. Figure 5.36 also shows that constant results are achieved in which for all five heights of PSLA the higher pressure PSLA is achieved at a lower temperature difference and higher maximum temperature of the battery, which is supported by the contour plots of the battery under the two pressures. Another result that can be observed in Figure 5.36 is that the variation of the temperature with time maintains a similar trend for both pressure values.

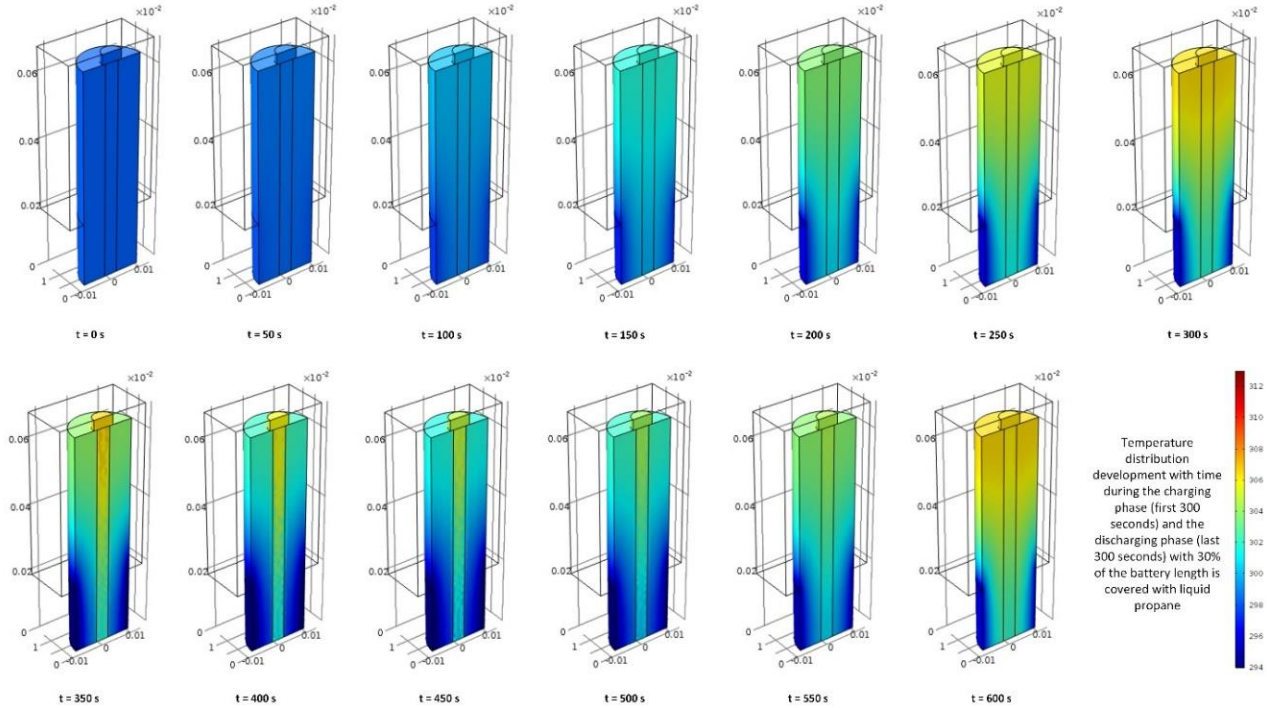

Figure 5.35 Battery temperature distribution with time during the charging and the discharging phases when 30% of the battery length is covered with liquid ammonia.

b) Cycling rate effect on the battery temperature distributions

The thermal performance of the proposed cooling system is investigated at high power charging and discharging rates of 7.5C. However, the battery packs in any HEV applications are not expected always to be charging and discharging at the high power rates. Figure 5.37 shows the effect of charging and discharging rate on the thermal performance of the battery pack. Figure 5.37 (a) and (b) show the temperature contours at the end of the cycle for three charging and discharging rates (2.5C, 5C, and 7.5C) for the cases when the pressure of the PSLA is 9.0 bar and 10.0 bar respectively and when the height of the PSLA is 5% of the height of the battery. Figure 5.37 (a) and (b) show that as the charging and discharging rates decrease the temperature difference reduces as well as the maximum temperature in the battery. When the charging and discharging rates are 2.5C, covering only 5% of the total height of the battery with PSLA at 9.0 bar is adequate to obtain a nearly constant temperature difference of around 3.5^{o}C. However, when the pressure is 10.0 bar the temperature difference is maintain below 3.0^{o}C.

5.4.2 System 4 results

The objective of this study is to propose a thermal management system for the battery packs of HEVs that use propane as a source of some of the energy required by the vehicle, and to investigate the effect of the cooling system on the thermal performance of the Li-ion battery pack. Five heights of the liquid propane in the battery pack are investigated to define the minimum height of liquid propane that provides a low temperature throughout the battery for a high discharge current, and to simulate the high power demand of the HEVs. The effect of the cooling system on the thermal performance of the battery pack is assessed through the maximum temperature and the temperature difference throughout the battery, which represents the temperature distribution for the battery.

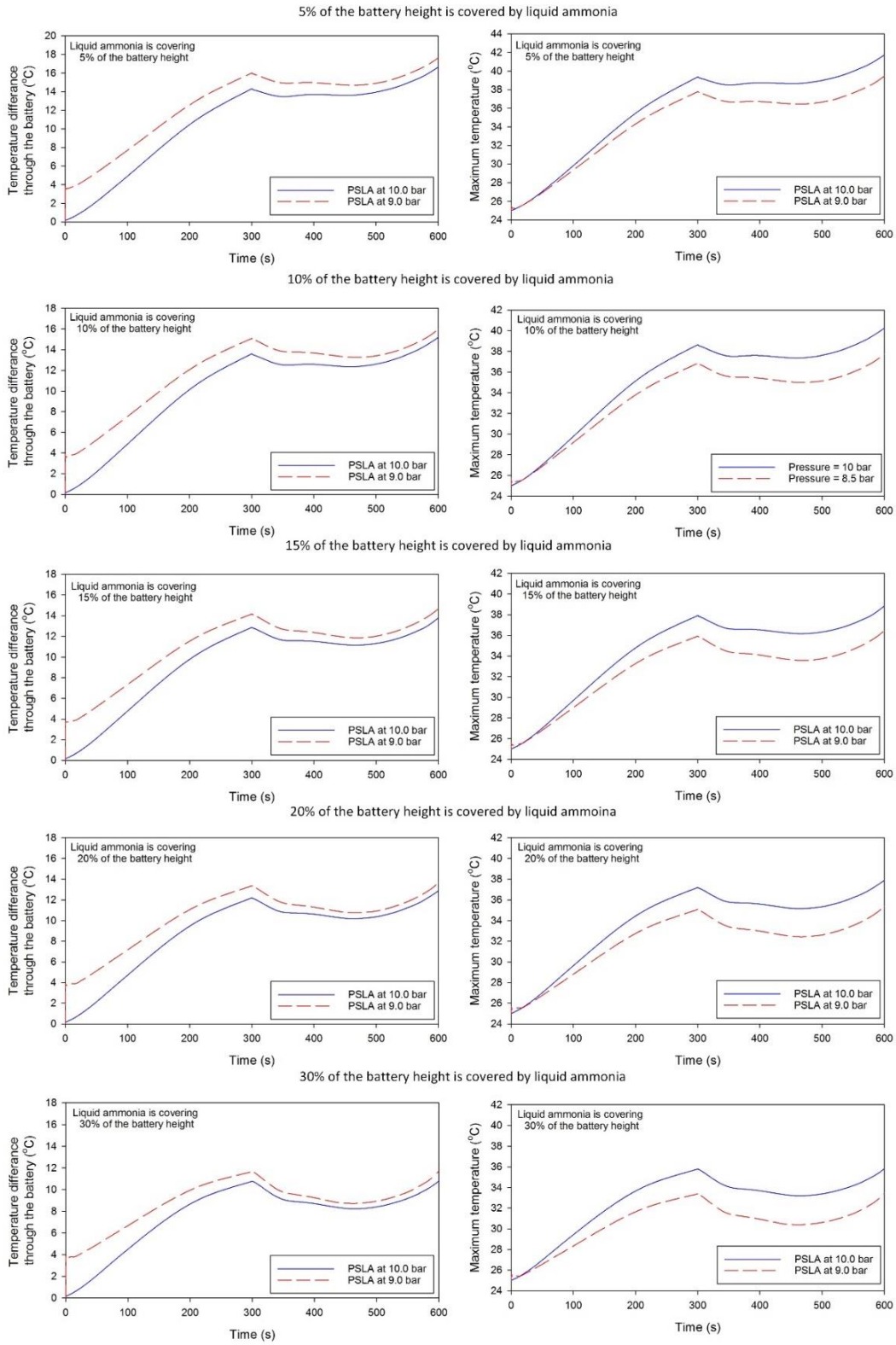

Figure 5.36 Effect of the saturation pressure of the PSLA partially covering the lithium ion batteries in the pack on the maximum temperature and the temperature difference in the battery.

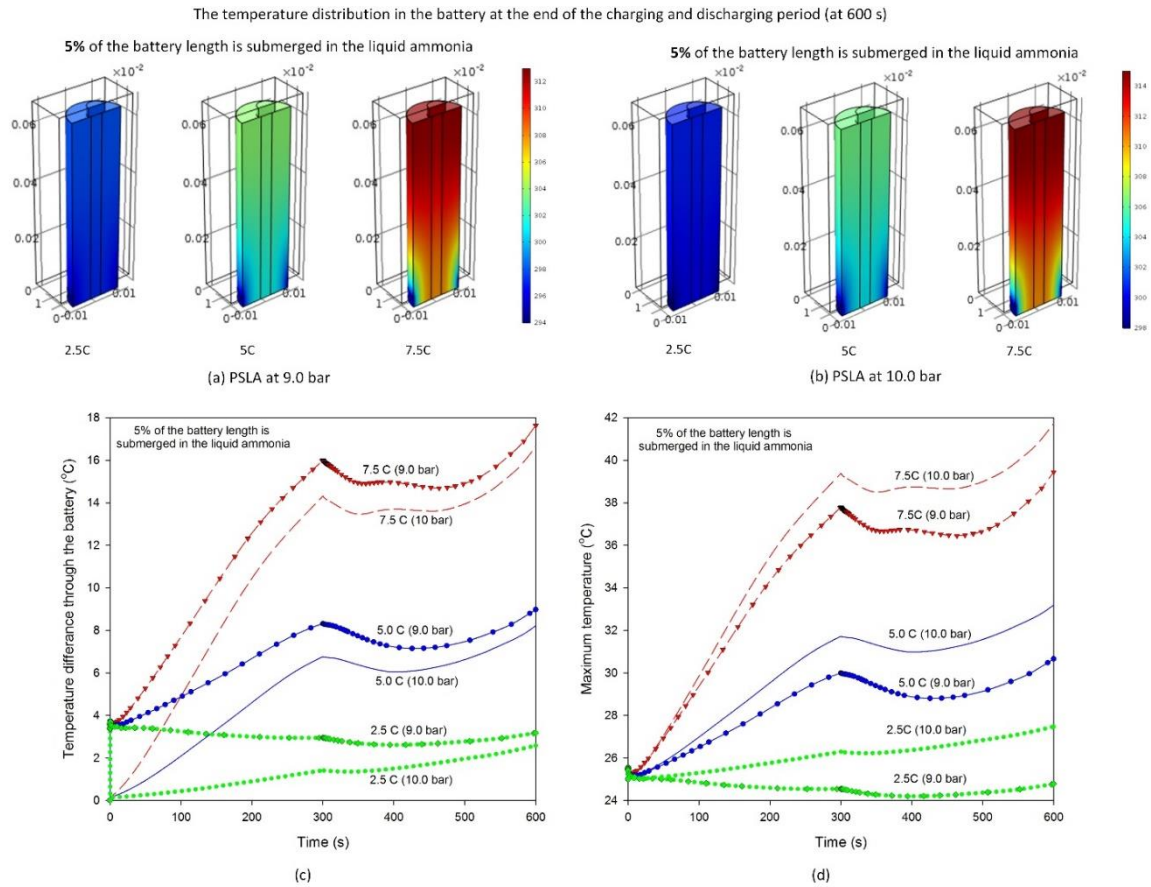

Figure 5.37 Effect of charging and discharging rates on the thermal performance of the cooling system

a) Battery temperature distributions

The height of the liquid propane surrounding the batteries was varied from 5% to 30% of the height of the battery. The pressure of the propane was maintained at 8.5 bar for all of the propane heights considered. Figure 5.38 shows the maximum temperature in the battery, the difference between the maximum and minimum temperatures in the battery, the volumetric heat generation and the electrical potential of the battery for a 300 second charging rate at 7.5C, followed by a 300 second discharge rate of 7.5C, all for several heights of liquid propane.

Figure 5.38(a) shows that the maximum temperature in the battery continues to increase during the charging phase, with the period for which the battery experiences the highest increase rate of maximum temperature occurring at around 200 seconds for the various liquid propane height in the battery pack. The increase rate of the maximum temperature decreases after two thirds of the charging period, since the heat generation rate decreases as shown in Figure 5.38(c) and the cooling by the liquid propane is still active. The maximum temperature for the five cases of liquid propane height in the pack during charging phase is 37.4^{o}C, occurring for the case when 5% of the battery height is covered by liquid propane, which is acceptable considering the high charging rate of the battery.

The maximum temperature is below 32.0ºC for half of the high charging rate period (150 seconds out of the 300 seconds).

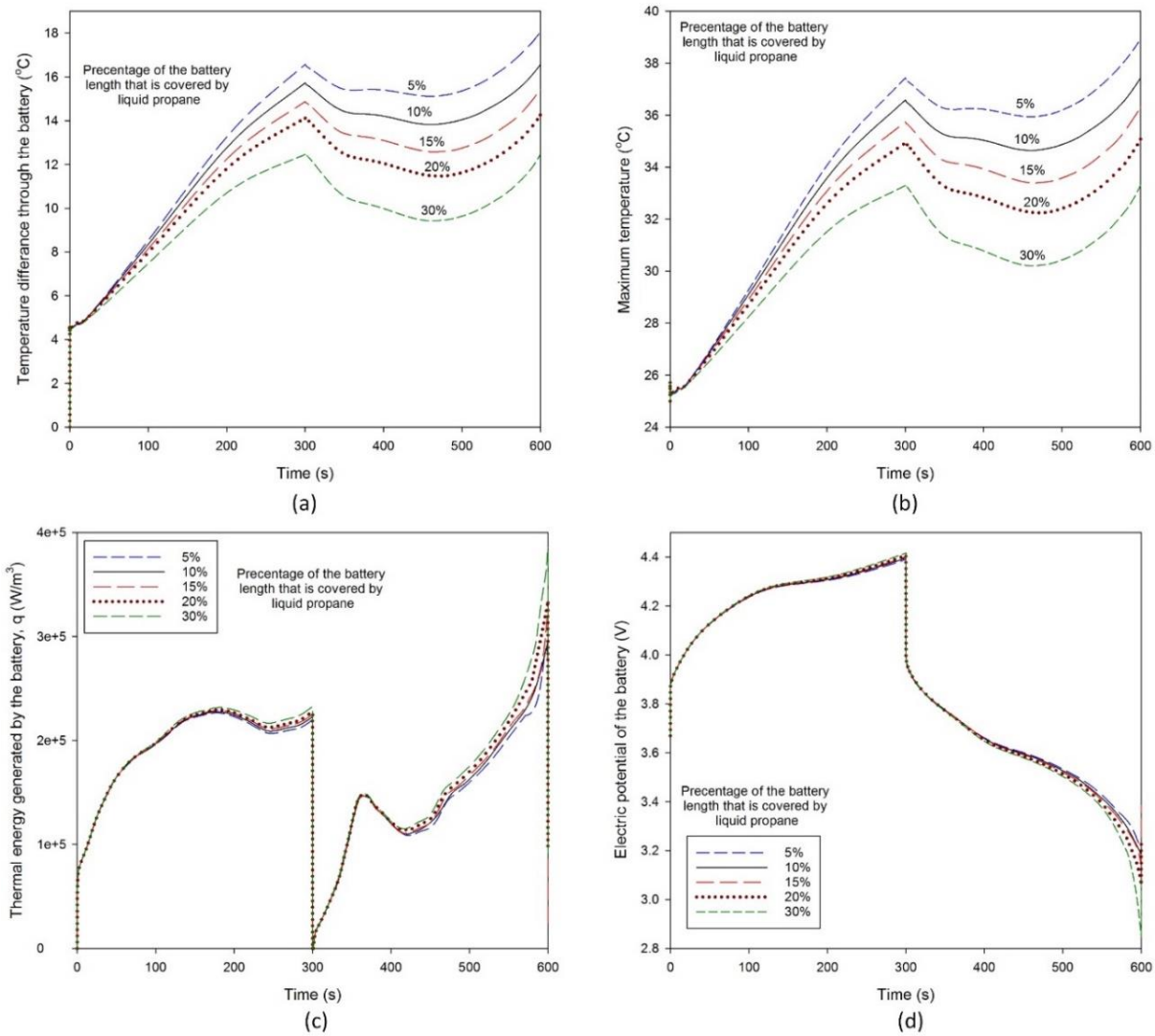

Figure 5.38 Maximum temperature (a), maximum temperature difference (b), specific thermal energy generated (c), and electric potential (d) of the lithium ion battery for various heights of the battery submerged in the liquid propane.

Figure 5.38(a) shows the thermal behavior of the battery after 300 seconds at a high charging rate of 7.5C followed by 300 seconds at a high discharge rate of 7.5C. The maximum temperature in the battery during the discharging phase starts decreasing and continues to decrease until around half of the discharging period (different point in time for different heights of liquid propane). The reason why the maximum temperature is decreasing is the sudden drop in the heat generation rates as shown in Figure 5.38(c) when the operation mode shifts from charging to discharging. However, in the last 50 seconds of the discharging period the maximum temperature in the battery starts increasing nonlinearly to reach a maximum temperature after the 600 seconds of charging and

discharging. The maximum temperature for the five cases of liquid propane height is 38.9^{o}C for the case with 5% of the battery height covered with the liquid propane pool. However, for 250 seconds of the 300 seconds of high discharge rate the temperature was below 37.5^{o}C. For the last 50 seconds, the thermal behavior of the battery can be explained by the heat generation curve shown in Figure 5.38(c). Figure 5.38(a) shows the effect increasing the height of the liquid propane in the battery pack. As the height of the propane increase in the battery pack the maximum temperature in the battery decreases. Figure 5.38(a) shows that when the height of the battery that is submerged in the liquid propane increases from 5% to 30% the maximum temperature drops by 5.6^{o}C (from 38.9^{o}C to 33.3^{o}C). Higher heat transfer occurs at the submerged surface in the form of boiling heat transfer, and as more of the battery surface is covered by the liquid propane more area is available on which boiling heat transfer is occurring. Another effect of increasing the liquid propane covered area on the maximum temperature in the battery is that it causes the rate at which the maximum temperature increases to decline, as shown in Figure 5.38(a).

The temperature distribution through each single battery and between the batteries in the pack affects significantly the performance of the batteries in the pack, and also is an indicator of the performance of the cooling system. The temperature difference between the batteries in the pack is expected to be very close to zero, since the cooling system provides cooling for each battery independently due to all batteries being submerged in the liquid propane, which is at a constant boiling temperature. The propane vapor released from the evaporation of the liquid propane flows along the length of the battery. However, regarding the temperature distribution in a single battery in the pack, the maximum temperature difference across the battery is shown in Figure 5.38(b). The behavior of this temperature difference is similar to the maximum temperature in the battery shown in Figure 5.38(a). The maximum temperature difference during the charging and discharging periods for the five cases of liquid propane height is 18.0^{o}C for the case when 5% of the length of the battery is covered with liquid propane. But the temperature difference is lower than 16.6^{o}C for the first 550 seconds of the 600 seconds cycle.

Figure 5.38(b) shows that the temperature difference across the battery decreases as the percentage of the length of the battery covered by the liquid propane increases. When the liquid propane height covered in the pack rises from 5% to 30% of the battery height, the maximum temperature difference decreases from 18.0^{o}C to 12.5^{o}C. This is because more of the battery surface area is covered by the liquid propane, subjecting a greater area to the high heat transfer coefficient of the boiling process. This causes more propane vapor to be generated, providing more cooling effect to the uncovered parts of the battery. This means that the large gap in the cooling effect between boiling and convection on the uncovered part decreases, which also helps in reducing the maximum temperature difference across the battery. Figure 5.39 shows the temperature contours of the middle section of the battery in the center of the pack for the five cases of liquid propane height, at the end of the cycle (at 600 s). It is clear that, as more of the battery is covered with propane, the lower are the maximum temperature in the battery and the temperature difference across the battery.

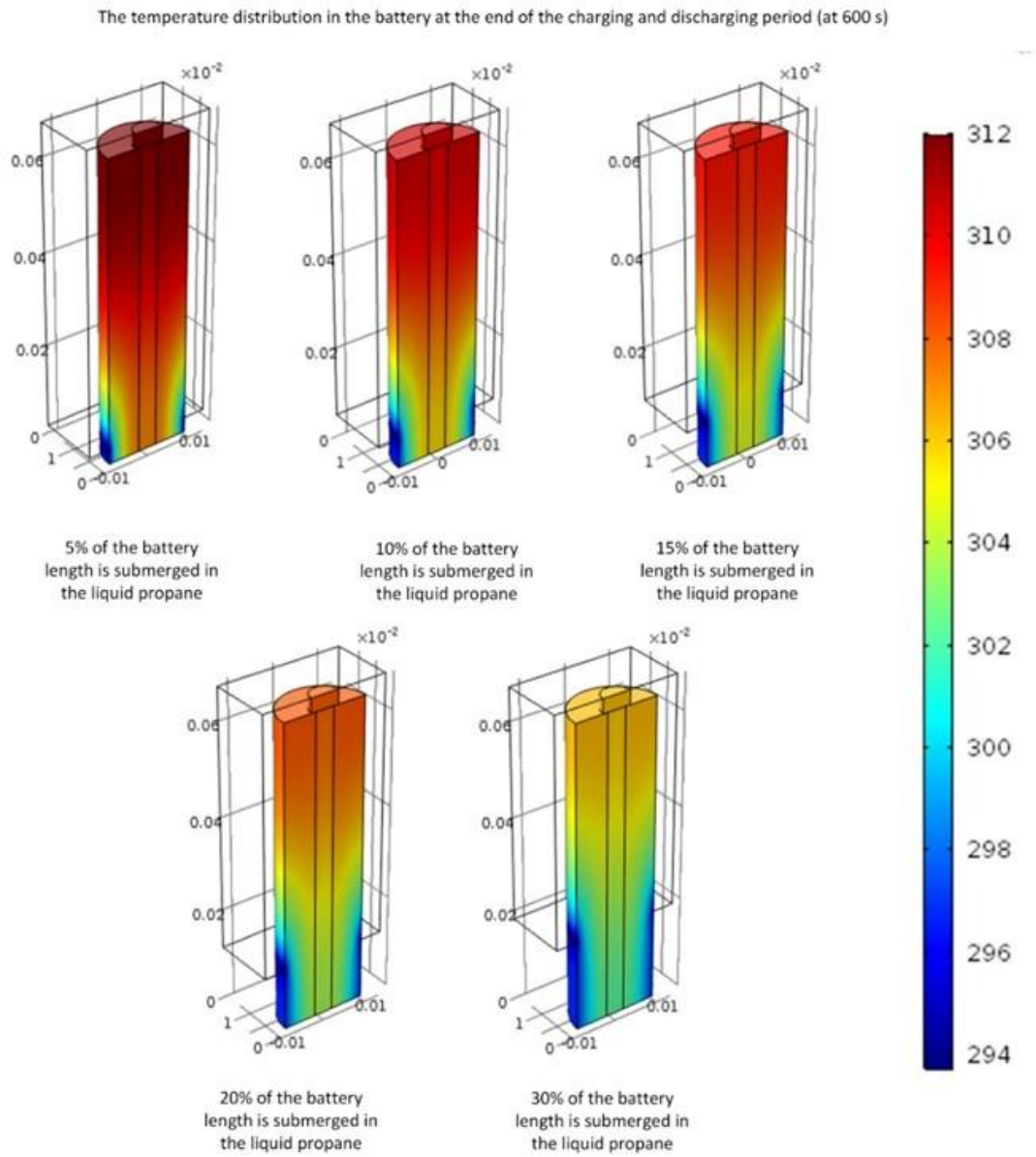

Figure 5.39 Temperature contours of the middle section of the battery in the center of the pack for the five cases of liquid propane height at the end of the cycle (at 600 s).

Figure 5.40 shows the development of the temperature distribution during the high rate charging and discharging for the case when the liquid propane covers 30% of the battery height. It is observed that, after 100 seconds from the start of the charging process (7.5C), a clear temperature distribution starts appearing and, by the end of the charging process, the temperature distribution is similar to that at the end of the discharging phase. The battery maintains the shape of the temperature distribution after charging ends and, even when the temperature starts to decrease at the beginning of discharging, the shape of the temperature distribution is almost the same.

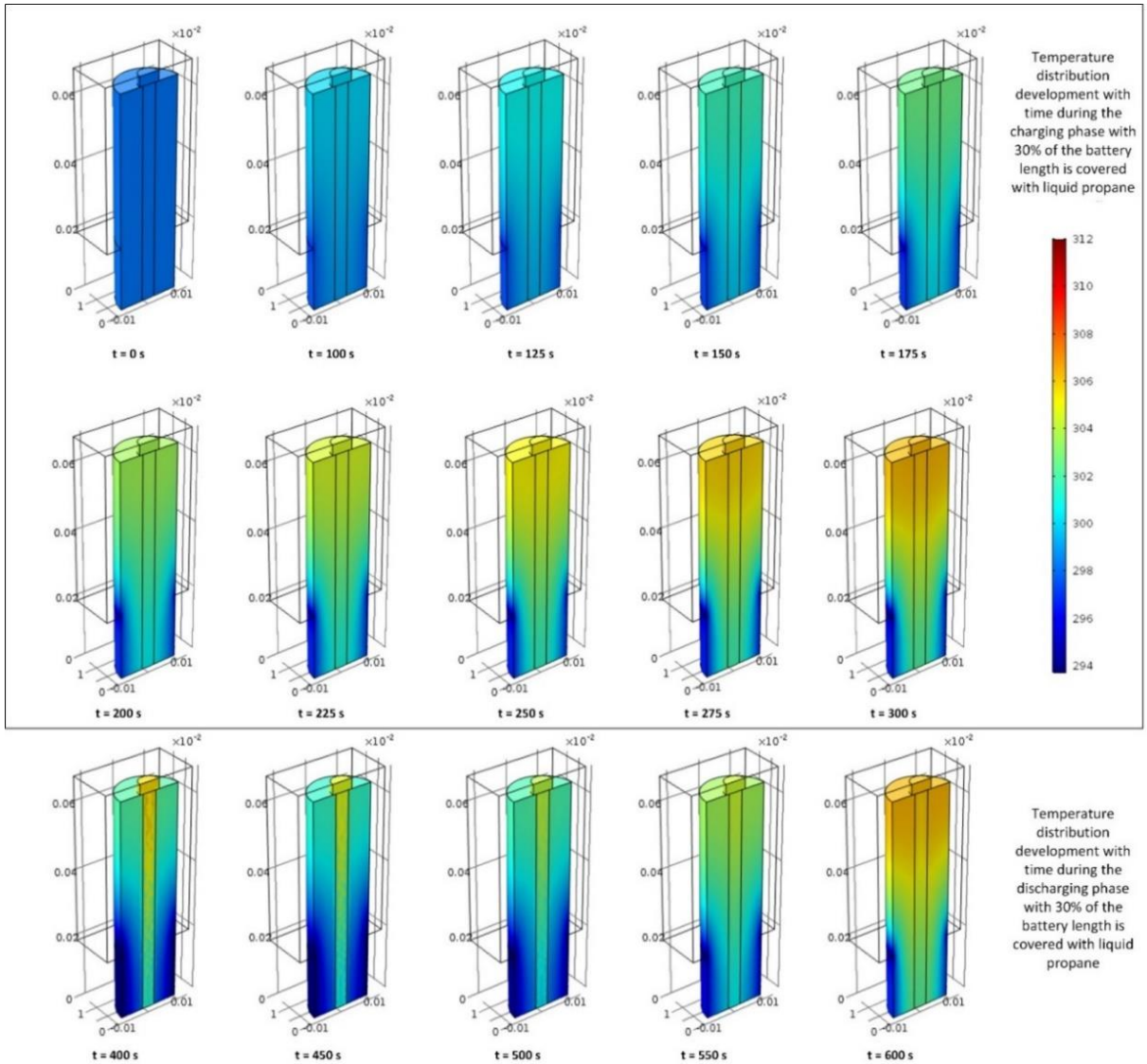

Figure 5.40 Temperature distribution variation with time during the charging and discharging phases, for 30% of the battery length covered with liquid propane.

The pressure of the liquid propane surrounding the batteries in the pack determines the saturation temperature at which the propane boils to provide the cooling effect. Two saturation pressures are considered: 8.5 bar which corresponds to a saturation temperature of 293.75 K and 10 bar which corresponds to a saturation temperature of 300.1 K. The two pressure cases are applied to the five heights of propane considered in this thesis. Figure 5.41 shows the effect of the liquid propane saturation pressure on the maximum temperature and the temperature difference across the battery. A consistent result for all the five heights of liquid propane is observed when the pressure of the liquid propane increases, which is that the maximum temperature of the battery during the charging and discharging high rate cycle is always higher for the higher pressure. However, the higher pressure maintains a lower temperature difference through the battery in all cases of liquid propane height.

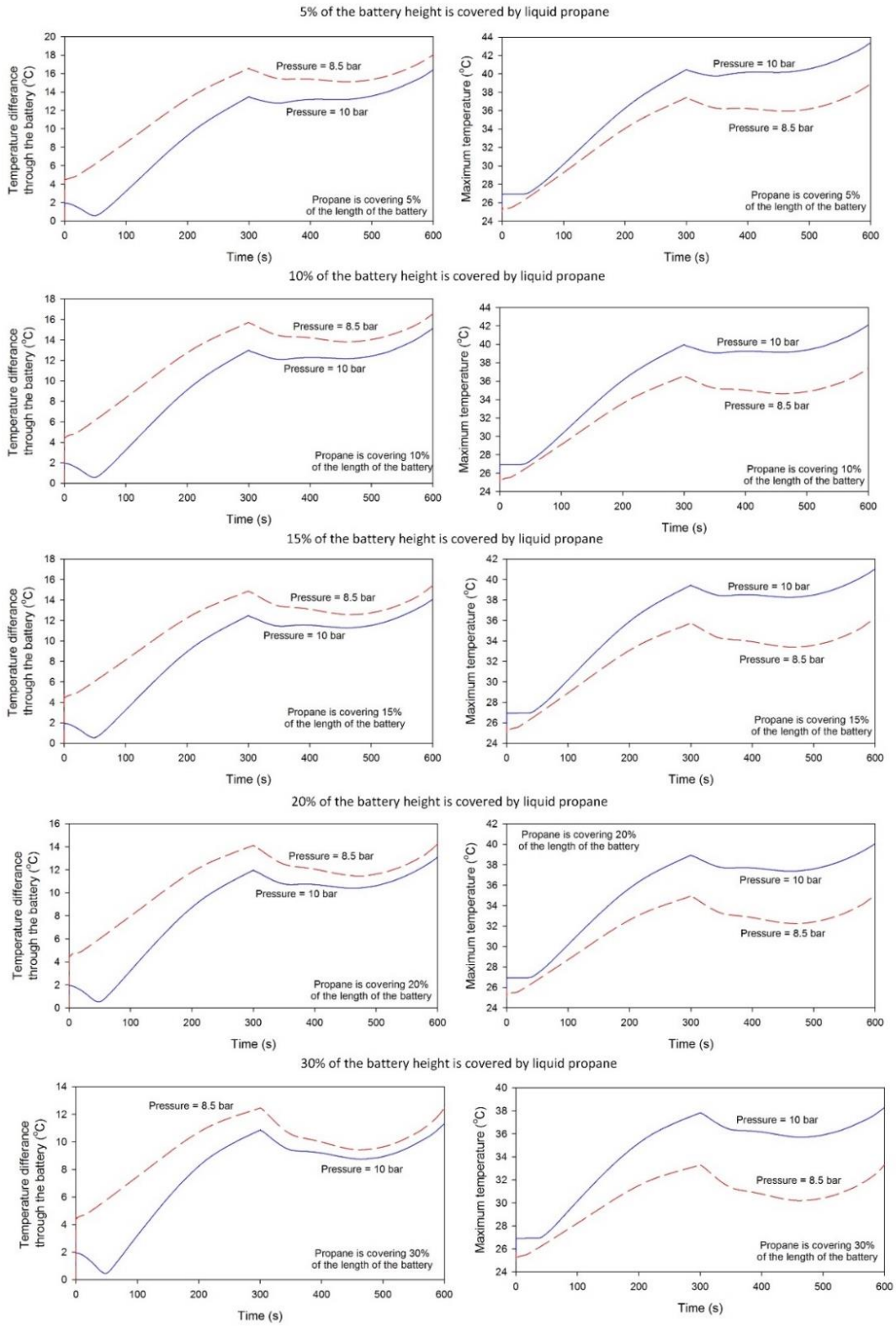

Figure 5.41. Effect of pressure of the saturated liquid propane partially covering the lithium ion batteries in the pack on the maximum temperature and the temperature difference in the battery.

The high pressure considered exhibits a temperature difference of less than 2ºC in the first 80 seconds as shown in Figure 5.41, which is the trend for nearly all cases of propane height. Figure 5.41 shows that, as more of the battery is covered by the liquid propane, less of a drop in the temperature difference is observed due to the increase in the pressure. Figure 5.41 shows that reducing the pressure for the higher liquid propane height has a larger effect on the maximum temperature than for the lower liquid propane height in the pack. At a higher elevation of the propane in the pack, the effect of the vapor propane in the convective cooling of the uncovered part of the battery is much higher than its effect at low a liquid propane height. This means that the lower temperature vapor propane reduces the temperature more effectively than the higher temperature propane, which is the case when the pressure of the liquid propane increases. This observation justifies further the difference between the maximum temperature of the battery achieved by the low and high pressure propane, shown in Figure 5.41.

The highest change in the temperature difference due to the increase in the pressure is when 5% of the battery is covered with liquid propane; then the temperature difference across the battery decreases by 1.64ºC and exhibit the lowest increase in the maximum temperature (4.46ºC).

Although the analysis of the performance of the proposed system considers an ambient temperature of 25ºC and an insulated battery pack, the system is able to perform well in cold and hot weather. In hot weather more propane evaporates due to the leakage of thermal energy to the battery pack. The increase in the amount of evaporated propane due to heat infiltration from outside, is expected to be much smaller than the propane evaporated due to the thermal energy generated by the batteries in the pack. Even if the amounts of heat entering the pack from the environment are comparable to the energy generated by the battery, the extra vapor propane is sent to power production and the worst possible scenario is to increase the size of the vapor propane collector-pressure regulator. In cold weather the liquid propane remains in the liquid phase, since the freezing point incurs negligible changes with pressure and the freezing point for liquid propane is -187.7ºC. Since the boiling of the propane is driven more by the higher temperature of the battery surface than the saturation temperature of the liquid propane covering part of the battery, no excessive cooling will occur for the batteries in the pack. In addition, the liquid propane acts as an insulator, protecting the batteries from the cold environment, and it also increases the mass and the specific heat of the battery pack. In other words, the thermal energy that needs to be removed from the pack to reduce the temperature of the pack is higher due to the presence of the propane pool.

b) The battery pack geometry and design results

The coming studies cannot be continued with the correlation based model that is why the phase changing boiling based model is developed and is used to simulate the remaining results and simulations. The thermal performance of the considered battery pack thermal management system when the coolant filling the battery pack has no supply and the pack is filled with the liquid coolant is evaluated through the maximum battery temperature within the pack and the maximum temperature difference across the pack and through a single battery. The effect of the spacing between the batteries and the charging and discharging rate is investigated.

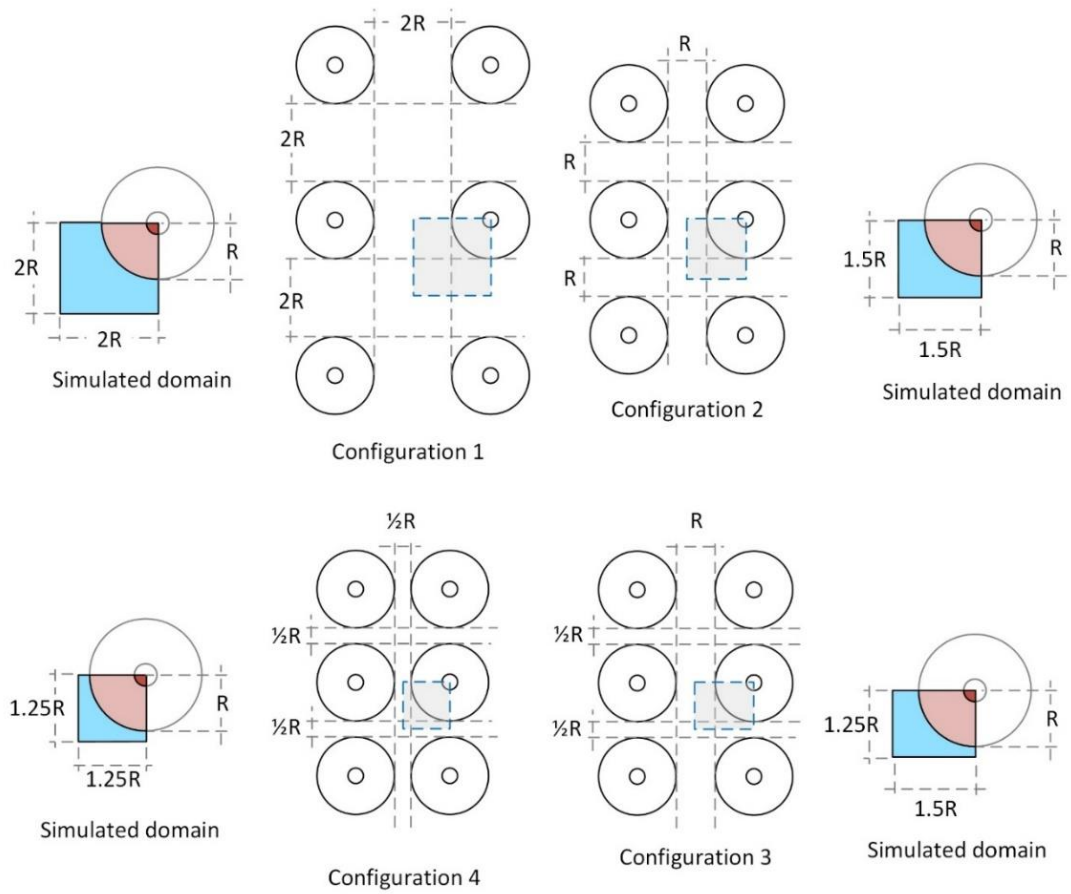

Figure 5.42 Four configurations of the cylindrical batteries in the pack and the top view of the simulated domain for each pack configuration, where the main operating parameter is the spacing between them (top view of the pack is used to demonstrate the spacing between the batteries for each configuration)

As shown in Figure 5.42, four battery configurations in the pack are considered, where the spacing between the batteries is varied from twice the battery radius in the x and y directions for the largest space considered to half the battery radius in the x and y directions for the smallest considered size. Figure 5.43(a) shows the variation of the battery maximum temperature with time through the charging and discharging cycle at a current of 4C for a cycle of 600 seconds duration. From Figure 5.43(a), it is observed that as the spacing between the batteries increases the maximum temperature of the battery reduces. For the largest considered battery spacing, the maximum temperature of the battery for a 4C charging and discharging cycle for 600 seconds reaches a value of 30.3^{o}C. When the spacing of the battery decreases to nearly half the initial spacing (from configuration 1 to 2), the maximum temperature of the battery increases to 31.5^{o}C at the end of the cycle, which is a 1.29^{o}C reduction in the maximum temperature. A further reduction of the spacing by half from a single radius spacing (configuration 2) to half a radius spacing in both directions (configuration 4) increases the maximum temperature at the end of the cycle from 31.5^{o}C to 32.6^{o}C, which is 1.09^{o}C increase. Configuration 3 is used to investigate

decreasing the spacing from one direction in the battery pack while maintaining the other spacing constant relative to configuration 2. From Figure 5.43 the battery maximum temperature increases with a reduction of the battery spacing in one direction from 31.5°C to 32.1°C, which is a 0.54°C increase.

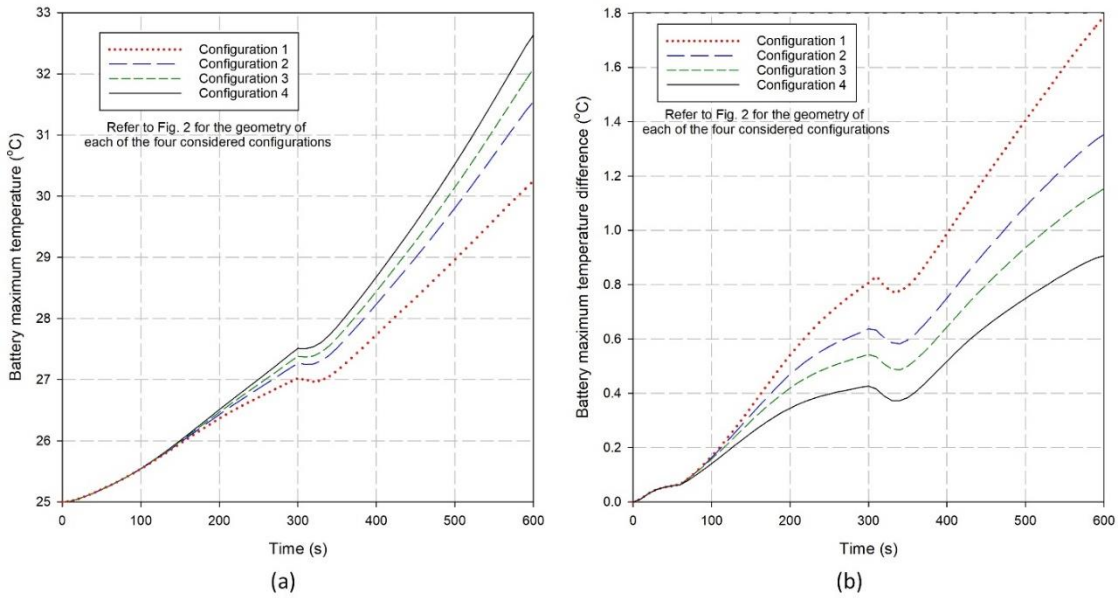

Figure 5.43 Thermal performance of the thermal battery management system under a charging and discharging cycle of 600 seconds at a 4C rate in terms of (a) battery maximum temperature and (b) battery maximum temperature difference.

Since the amount of the coolant in the pack is constant with no more coolant supply, the separation distance leads to a higher maximum battery temperature as shown in Figure 5.43(a). Smaller spacing means that there is less liquid coolant for each battery in the pack, which leads to evaporating the liquid coolant faster than configurations with larger spacing. Since the pack coolant is maintained at a constant pressure, then not all the generated vapor leaves the pack and some remains to maintain a constant pressure inside the pack. The remaining vapor is the only coolant method between the batteries. Figure 5.44 shows the variation of the coolant liquid volume fraction through the 600 seconds charging and discharging cycle. As shown in Figure 5.44, with the increase in the spacing the liquid coolant lasts for a longer period of time, leading to a lower maximum battery temperature compared to configurations with smaller spacing. The increase in the battery maximum temperature with reduction of the spacing between the batteries is not linear, as can be seen in Figure 5.43(a).

A more detailed description of the effect of the liquid volume fraction is shown in Figure 5.45. Figure 5.45 shows the iso-temperature surfaces of the battery and its surrounding coolant volume through the charging and discharging cycle for specific time steps. Figure 5.45 shows the iso-surface temperature plot at 590 seconds in the charging and discharging cycle with a rate of 4C (note that the time selected is to avoid selecting the final time step where the battery is shutting off). Note that the phase change temperature is equal to 26.94°C. As shown in Figure 5.45 the only configuration which has an iso-

temperature surface at a temperature below the boiling point and at the boiling temperature is configuration 1, which is also shown in Figure 5.44.

c) Cycling rate results

The effect of the charging and discharging rate for the four configurations is considered with three rates of 4C, 5C and 6C, as shown in Figure 5.46. Figure 5.46 shows the effect of the charging and discharging rate on the performance of the cooling system in terms of the battery maximum temperature and the coolant liquid volume fraction.

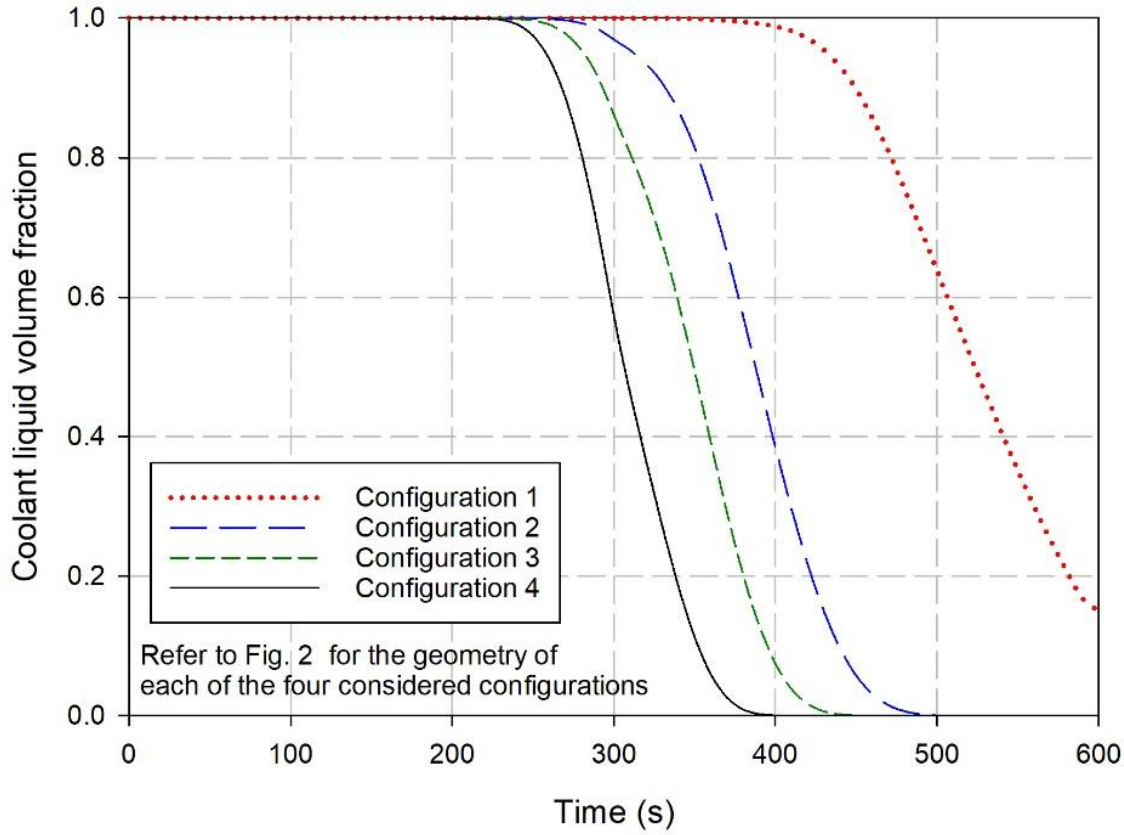

Figure 5.44 Variation of the coolant volume fraction throughout the charging and discharging cycle for the four configuration considered at a charging and discharging rate of 4C.

From Figure 5.46 it is seen that as the spacing between the batteries decreases the faster and sharper the coolant liquid volume fraction decreases to zero. Increasing the charging and discharging cycle rate results in increasing the maximum temperature in all of the four configurations considered and results in evaporating the pool faster. Figure 5.46 (a) shows that when the cycle rate is increased from 4C to 5C the pool completely evaporated at 480 seconds compared to having a liquid content larger than 15% of the volume at 4C. A further increase in the cycle rate to 6C further shortens the life of the liquid coolant in the battery pack, where at 6C the pool lasts for only 380 seconds through the 600 second cycle. The smallest battery spacing is considered in configuration 4 (Figure 5.46(d)); the boiling cooling runs out at 380 seconds, 210 seconds, and 170 seconds for the cycle rates of 4C, 5C and 6C respectively.

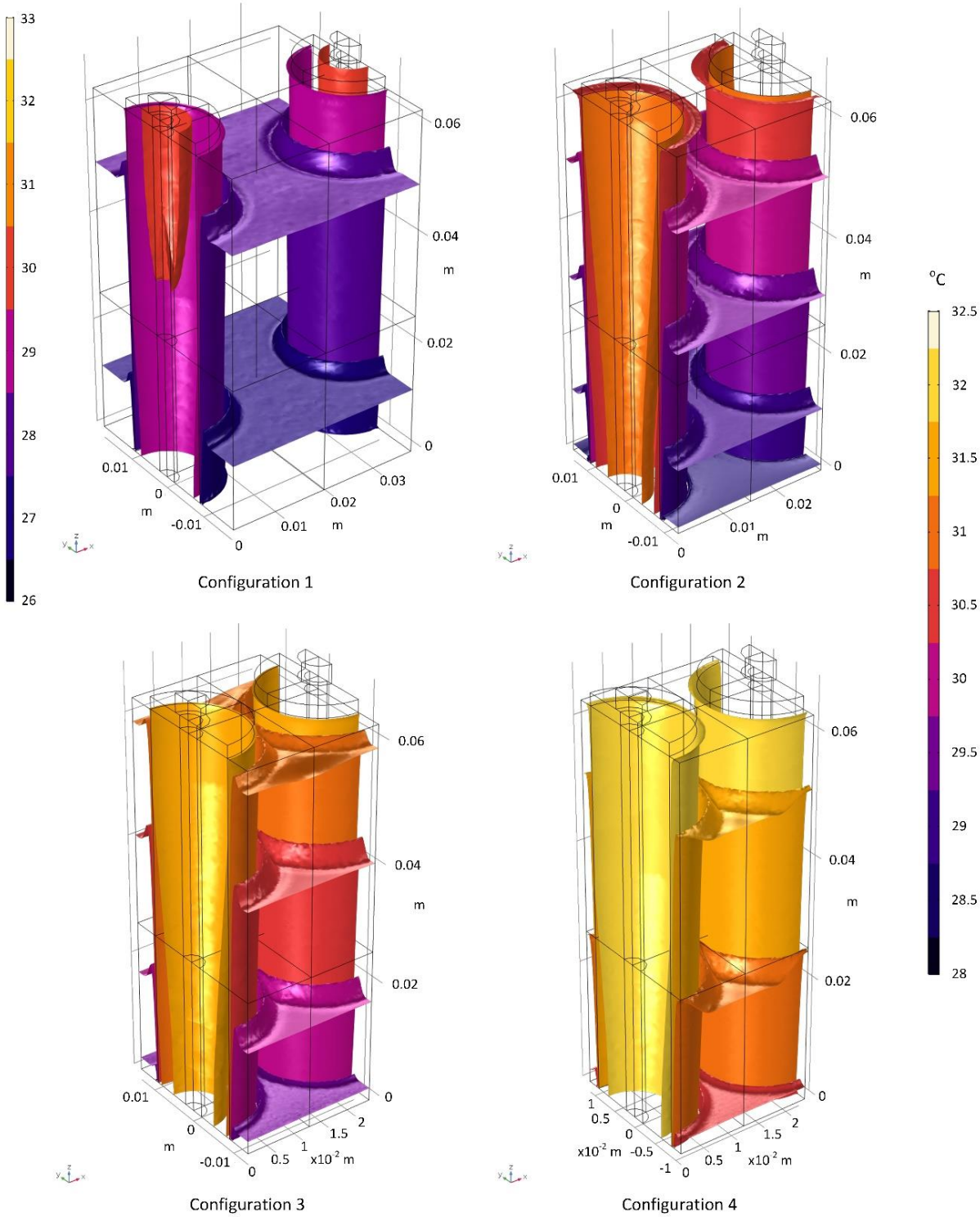

Figure 5.45 Temperature iso-surfaces (in °C) of the four configurations considered at time 590 s of the 600 s charging and discharging cycle at a rate of 4C (note that only the first configuration has it is own temperature legend, while the other three configurations has a single temperature legend shown on the right).

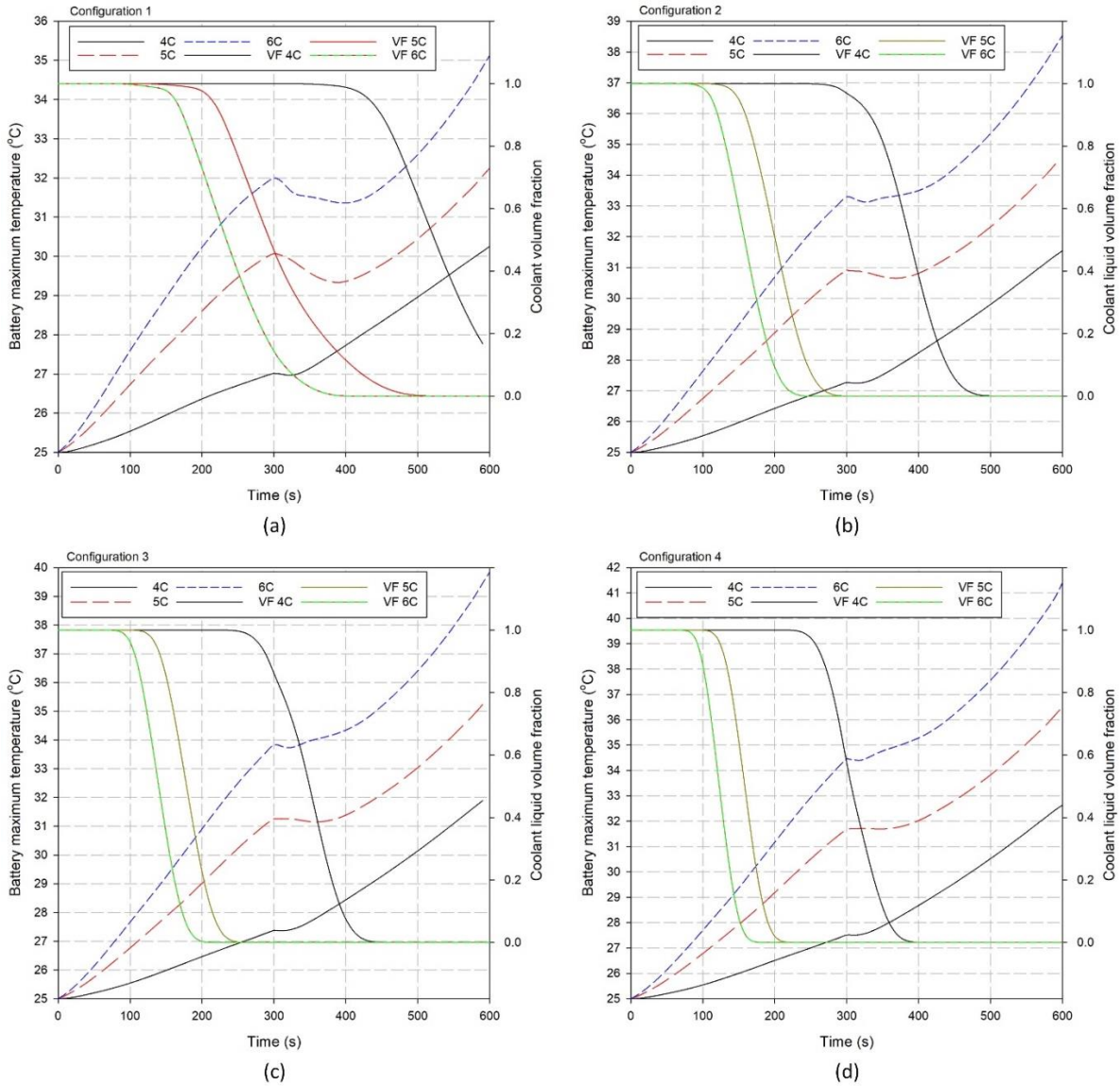

Figure 5.46 Variation of the battery maximum temperature and volume fraction (VF) of the liquid coolant surrounding the batteries in the pack throughout the charging and discharging cycle for three cycle rates and considering four configurations.

However, for the largest battery spacing considered in configuration 1, the boiling cooling does not run out for the rate of 4C, while it runs out in 470 seconds, and 380 seconds for the cycle rates of 5C and 6C respectively. The difference in maintaining the boiling cooling rate is directly reflected on the maximum temperature of the battery as shown in Figure 5.46. However, increasing the space between the batteries from half a radius to twice the radius of the battery in the x and y directions improves the maximum battery temperature at the end of the simulation cycle at 4C by 2.2^{o}C. The improvement in the maximum battery temperature by 2.2^{o}C, increases to 4.3^{o}C and 6.2^{o}C when the cycle rate increased to 5C and 6C respectively.

From the results shown in Figure 5.46, as the configuration space decreases the temperature differential increases with the increasing charging and discharging rate of the simulation cycle. The effect of the high boiling rate on the battery maximum temperature shown in Figure 5.46 can be better understood through the variation of the heat generation rate and the cooling rate shown in Figure 5.47. Figure 5.47 shows the variation of the heat generation rate for each of the considered cycle rates and the cooling rate provided by each of the four considered configurations. Figure 5.47 shows the variation of the heat generation rate by the battery and the cooling rate provided by the cooling system four configurations throughout the charging and discharging for the three cycle rates considered. The effect of the boiling cooling is most apparent in Figure 5.47 (a) where only in configuration 1 does the coolant liquid fraction remain more than zero to the end of the simulation cycle. The response and the amount of cooling the cooling system provides after the liquid pool evaporates completely is slower compared to boiling cooling, which is seen at the beginning of the cycle.

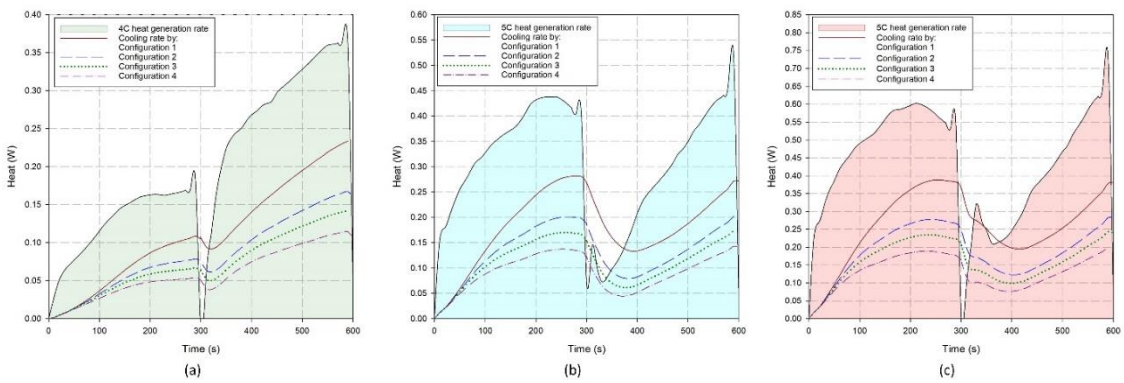

Figure 5.47 Variation of the heat generation rate by the battery and the cooling rate by the battery for four spacing configurations throughout the charging and discharging cycle time for a cycle rate of (a) 4C, (b) 5C, and (c) 6C.

The effect of the charging and discharging rate on the four considered configurations on the maximum temperature difference across the battery is shown in Figure 5.48. Figure 5.48(a) shows the maximum temperature difference across the battery for the three different charging and discharging rates considered. As the charging and discharging cycle rate increases the temperature difference across the battery increases. Having the largest battery spacing considered results in the largest temperature difference across the battery, which is mainly due to having a high cooling rate on the covered part of the battery compared to the uncovered part of the battery. However, as the spacing decreases the cooling system maintains a higher temperature uniformity across the battery even when the cooling fraction is continuously dropping and runs out faster. Having a smaller battery spacing results in having the boiling cooling rate run out faster since there is less liquid coolant for the same heat generation rate. Having a lower boiling cooling rate results in an even distribution of cooling rate across the battery, compared to having a high cooling rate on the pool covered part only (see to Figs. 1 and 7). Having an even distribution of cooling rate across the battery helps in reducing the temperature difference across the battery as shown in Figure 5.48; however, this occurs at the expense of the maximum temperature of the battery as shown in Figure 5.46.

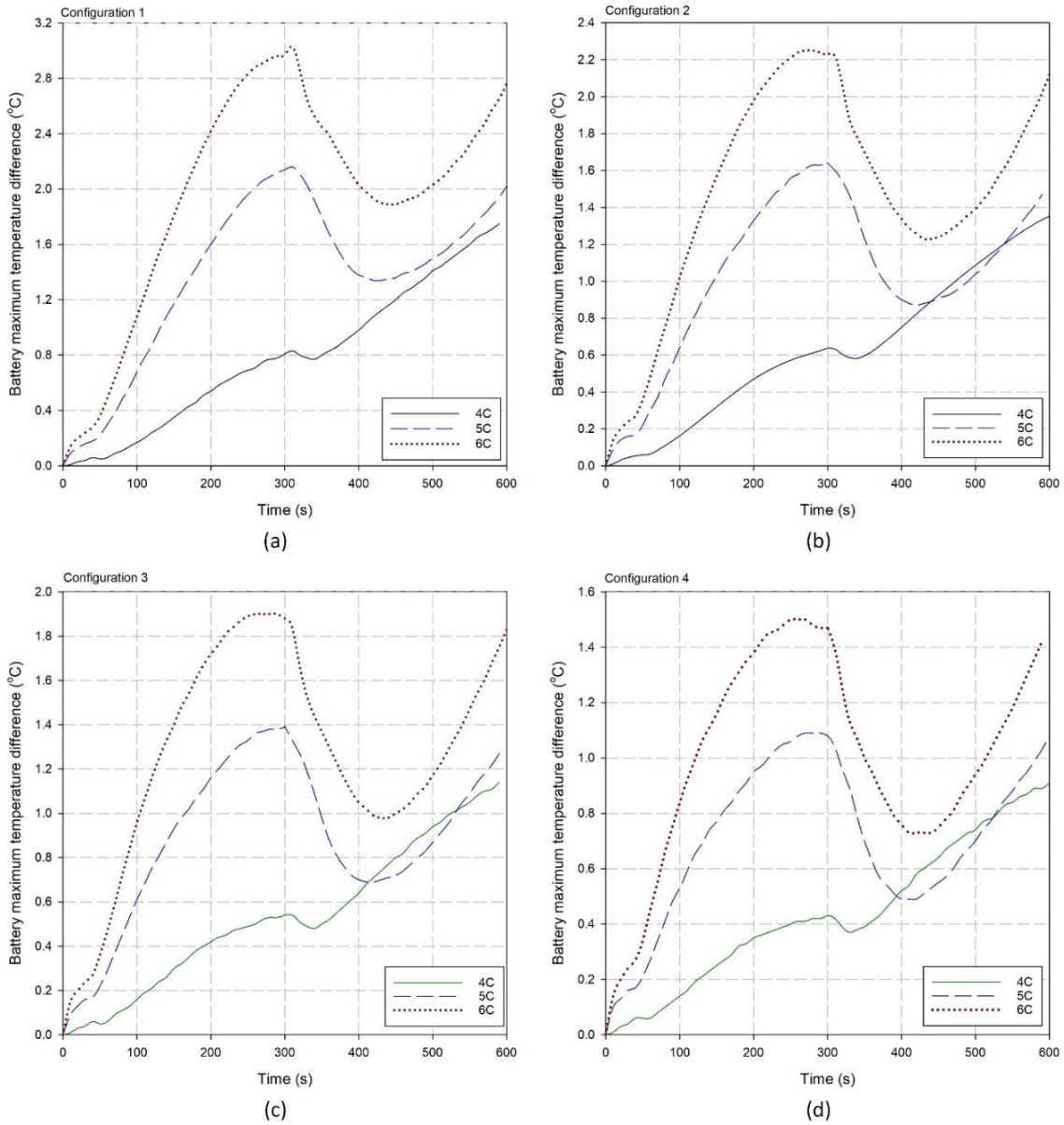

Figure 5.48 Variation of the battery maximum temperature difference across the battery throughout the charging and discharging cycle for cycle rates of 4C, 5C, and 6C for (a) configuration 1, (b) configuration 2, (c) configuration 3, and (d) configuration 4.

5.4.3 System 5 results

The performance of the proposed BCS using refrigerant R134a is assessed in terms of the thermal characteristics of the batteries in the pack during a high rate charging and discharging cycle. The effects of the variations of the height of the liquid R134a pool on the thermal behavior of the batteries in the pack are investigated. The subsequent analysis considers the performance of the proposed BCS with a realistic diving cycle. Then, the performance of the proposed cooling system is compared with air, liquid and refrigerant based cooling systems described in the literature.

a) Battery temperature distributions

The proposed system cools the battery by boiling the refrigerant R134a pool, through absorbing part of the heat generated by the battery, which in turn cools the battery surface covered by the R134a liquid pool. The uncovered part of the battery is cooled by the generated vapor from boiling through natural convection. The height of the R134a liquid pool in the pack is varied from a completely uncovered to a completely covered battery surface. Note that for the case when the battery surface is completely uncovered, it is assumed that that the surrounding space is filled with R134a vapor that can cool the battery by natural convection. The variation of the battery maximum temperature with changing height of the R134a pool is shown in Figure 5.49(a). There, it is shown that increasing the height of the R134a pool in the battery pack, i.e., increasing the battery surface area covered by the liquid R134a pool, decreases the maximum battery temperature at the end of the 600 second charging and discharging cycle. It is shown that for the first 150 seconds of the charging the battery at a 4C rate, having 0% of the surface of the battery covered by the liquid R134a results in a lower maximum temperature than the other five cases of liquid R134a heights. However, the reason for this performance is that the system is considered after it has reached equilibrium. Assessing the performance of the system after reaching the equilibrium state results in the surface of the battery reaching the saturation temperature of the R134a.

Increasing the height of the liquid R134a in the pack reduces the maximum temperature of the battery at the end of the 600 second charging and discharging cycle. However, the reduction in the maximum temperature at the end of the cycle declines as the height of the liquid R134a in the pack increases, as shown in Figure 5.49(a). Covering 20% of the battery surface starting from the bottom of the battery results in a maximum battery temperature at the end of the cycle of 35.5oC. However, increasing the coverage area from 20% to 40% reduces the maximum temperature at the end of the test cycle to 33.9oC, which represents a 2.6^{o}C improvement in the maximum temperature of the battery. Increasing the covered area from 40% to 60%, then to 80% and finally to 100% results in maximum battery temperatures of 32.7^{o}C, 31.9^{o}C, and 31.6^{o}C, respectively. It is shown that the maximum temperature of the battery improves with increasing height of the liquid R134a pool in the pack, but that magnitude of the improvement with each interval reduces as well. To understand more fully the behavior of the cooling system with variation of pool height, the effect of varying pool height on the temperature uniformity of the batteries in the pack is investigated next.

The cooling load provided by the ELP based BCS varies with the height of the liquid pool in the pack (or the covered area of the battery by the liquid pool) [11,115,116]. However, the variation and the cooling load provided by such cooling systems varies with the type of refrigerant used [11,115,116]. The cooling system in this thesis uses refrigerant R134a. In this section, the effect of reducing the spacing between the batteries on the maximum temperature in the pack is determined for various pool heights and charging and discharging rates. The cycles considered in this section are 600 seconds long, starting with 300 seconds of charging at rates of 6C, 7C and 8C and ending with 300 seconds of the cycle discharging at rates of 6C, 7C and 8C, respectively.

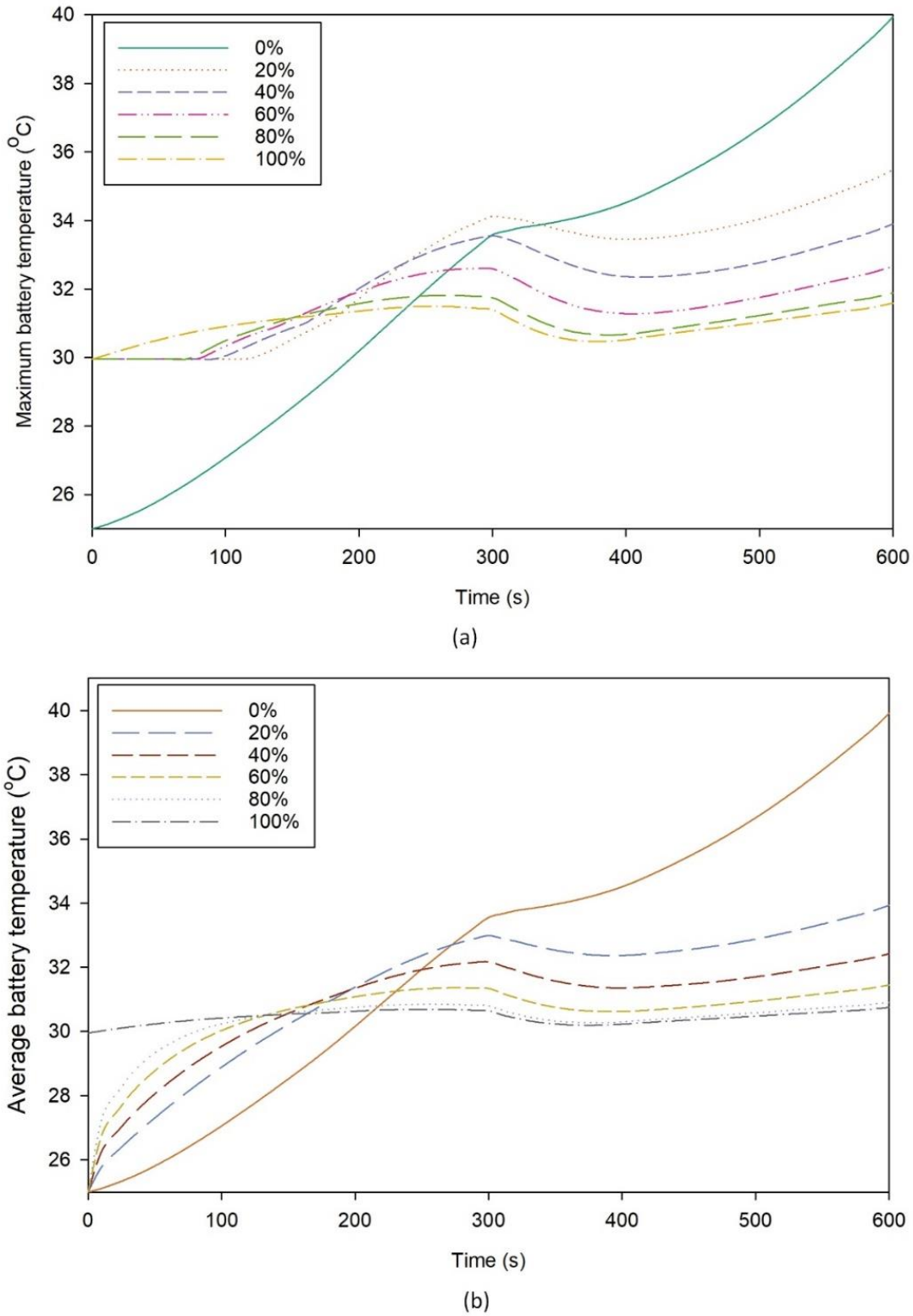

Figure 5.49 Variation with discharging and charging time of (a) maximum temperature in the battery, and (b) average temperature of the battery, for the six different cases of liquid R134a height in the battery pack.

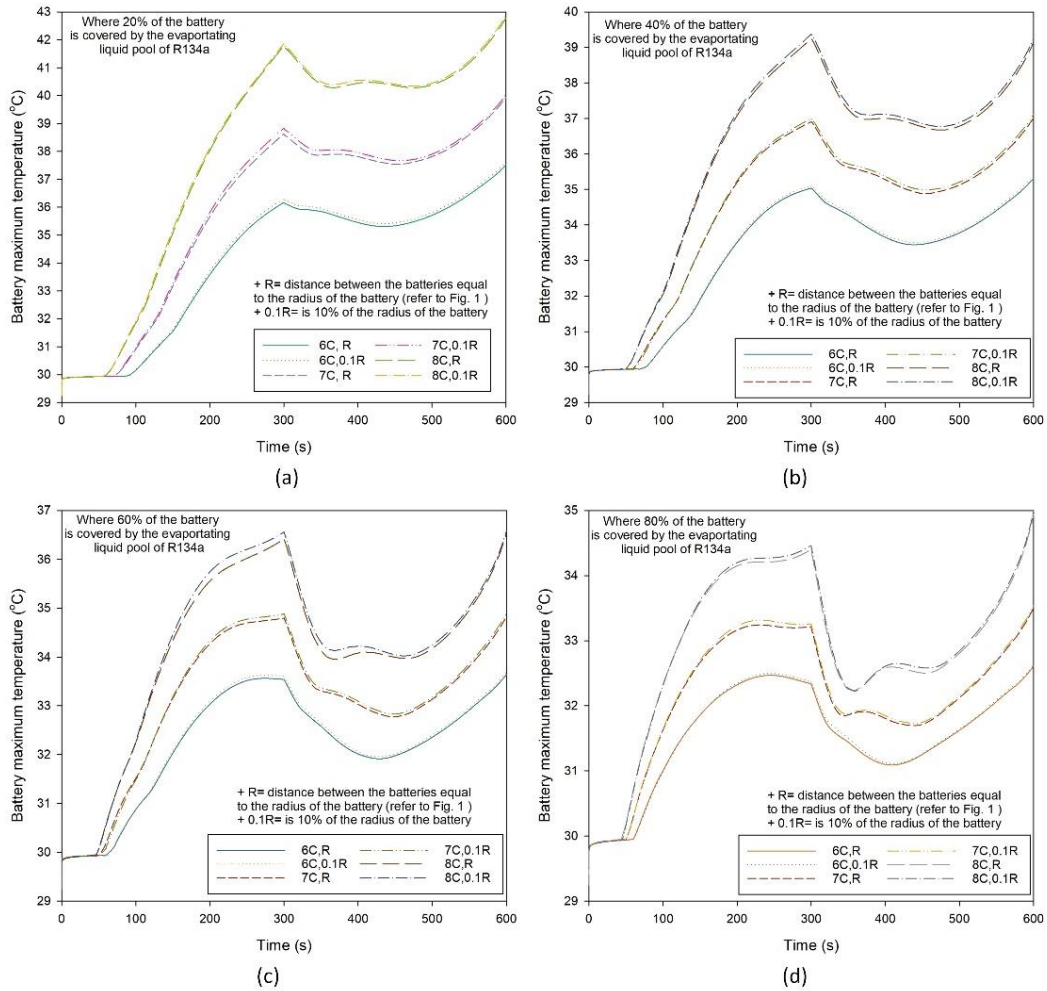

Figure 5.50 Variation with charging and discharging time of battery maximum temperature for the cases when (a) 20%, (b) 40%, (c) 60%, and (d) 80% of the battery is covered with the liquid refrigerant pool

Figure 5.50 illustrates the effect of varying the considered design and operating parameters on the battery's maximum temperature. Figure 5.50(a) shows that when the pool covers 20% of the battery the maximum temperature in the compact design (a shorter separating distance between the batteries) behaves similar to the larger spaced design. However, the compact design achieves higher maximum temperatures through the cycle, with a maximum difference of 0.2ºC for the case when the charging and discharging rate is 7C. The difference between the two designs is lower in terms of the battery maximum temperature when the cycle rate is 6C. The compact design exhibits maximum temperatures of 37.6ºC, 40.0ºC, and 42.9ºC for cycle current rates of 6C, 7C and 8C respectively. For the case where the refrigerant pool covers 40% of the battery Figure 5.50(b) shows the variation of the battery maximum temperature through the 600 second cycle. The compact design again resembles the behavior of the larger spaced design, with a small difference between the achieved temperatures. Similar to case for 20% of the battery covered, the difference in the maximum temperatures achieved between the two designs increases when the cycle current rate increases.

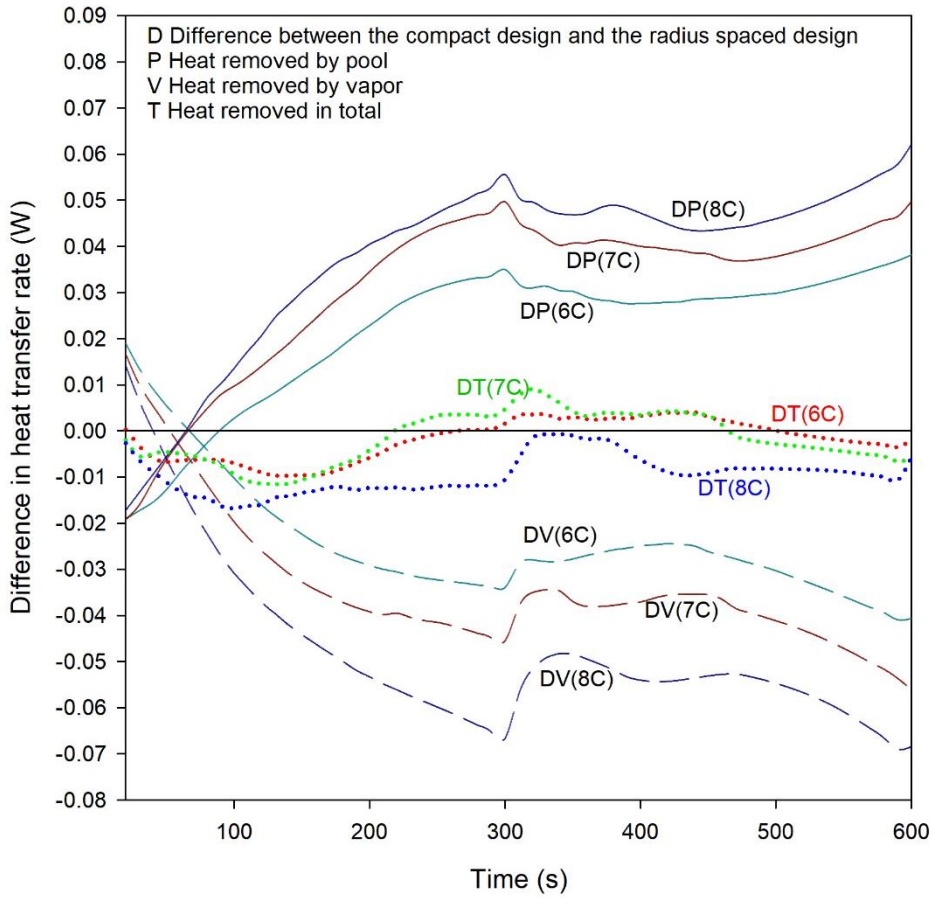

Figure 5.51 Variation with charging and discharging time of the difference in the breakdown of the heat transfer rate between the two proposed design configurations of the cooling system.

To understand the increase in the maximum temperature achieved by the compact design compared to the radius spaced design, the contribution of the pool and generated vapor is plotted in Figure 5.50(e). Negative values in Figure 5.51 mean that the compact design values are less than those of the radius spaced design. Figure 5.51 shows the difference in the heat absorbed by the pool, by the vapor and the total removed heat for the compact design and the radius spaced design. For the case when 20% of the battery is covered, as the cycle current increases, the difference between the two designs increases in terms of the cooling provided by the pool and the vapor. For the three considered cycle rates the contribution of the vapor in the total cooling load is less for the compact design than the radius spaced design. But the difference in contribution increases as the cycle current rate increases, as seen in Figure 5.51. However, the pool contributes more in the compact design than the radius spaced design, where the difference increases as the charging and discharging rates increase.

Increasing the pool height reduces the battery maximum temperature at the end of the cycle. Increasing the height of the pool in the pack decreases the maximum temperature. For the compact design, when the batteries in the pack are 20% covered with the pool the maximum temperature in the cycle increases from 37.6^{o}C to 40.0^{o}C when the cycle rate

increases from 6C to 7C, and the maximum temperature reaches 42.9^{o}C for a cycle rate of 8C. However, submerging up to 80% of the battery in the refrigerant pool reduces these temperatures to 32.6^{o}C, 33.5^{o}C, and 35.0^{o}C when the cycle rates are 6C, 7C, and 8C respectively. It is seen in Fig. 4 that, as the pool height in the pack increases, the system is abler to take advantage of the low heat generation rate occurring just after switching from charging to discharging. For the compact design and when 40% of the batteries are submerged from the point where the cycle switches from charging to discharging, the temperature drops in 50 seconds by 0.8^{o}C, 1.3^{o}C and 2.0^{o}C for 6C, 7C and 8C, respectively. This is similar to the 60% covered case, where the temperature drops increase to 1.0^{o}C, 1.5^{o}C and 2.3^{o}C.

From this section, it can be concluded that the compact design achieves similar results as the larger spaced design (radius spaced design) and mirrors the performance of the larger spaced design. However, further investigation is needed to consider the distribution of the temperature through the battery, since large temperature differences might lead to unstable cells. This topic is discussed next.

Temperature uniformity of the battery is an important factor in the performance of the battery and represents a measure of the performance of the deployed cooling system. The battery's average temperature is used to assess the battery temperature uniformity, and is shown in Figure 5.49(b). The average temperature of the battery behaves similarly to the maximum temperature of the battery, however they the average temperature lower limit is the ambient temperature except for the case where the battery is completely submerged in the R134a pool. The average temperature of the battery reaches its highest value at the end of the 600 seconds charging and discharging cycle, as shown in Figure 5.49(b). For the cases when 0%, 20%, 40%, 60%, 80% and 100% of the battery surface is covered with liquid R134a, the maximum average temperature reaches 39.9^{o}C, 33.9^{o}C, 32.4^{o}C, 31.4^{o}C, 30.9^{o}C, and 30.7^{o}C respectively. Note that for the case when 80% of the battery surface is covered with liquid R134a, the average temperature of the battery increases by less than 1°C.

A more detailed presentation of the temperature variation in the battery is provided in Figure 5.52, which plots the temperature contours on the surface of the battery for the six cases considered for the height of the R134a pool in the pack at the end of the 600 second charging and discharging cycle. Although having 0% of the surface of the battery covered by the liquid R134a results in a high level of temperature uniformity in the battery as shown in Figure 5.52, the average temperature of the battery is nearly 40°C, compared to the 30.7^{o}C when the battery is completely covered. Considering the cases other than 0% and 100% coverage, the battery temperature uniformity improves as the covered surface of the battery increases.

The temperature contours represent the boundaries between regions with different temperatures based on specified temperature increments, which means that a larger number of temperature contours on the surface of the battery indicates a lower level of temperature uniformity. The number of temperature contours on the surface of the battery decreases as the R134a covers a larger surface area of the battery, as shown in Figure 5.52. For the case when 80% of the battery surface is covered with the R134a pool, the entire side surface of the cylindrical battery reaches a temperature less than 31°C. Figure 5.53 shows the

variation of the temperature contours on the surface of the battery for the case when the R134a covers 20% of the surface of the battery. Figure 5.52 shows that maximum temperature of 35.5°C is reached after 550 seconds have elapsed of the 600 second charging and discharging cycle. The cooling system was able to achieve high temperature uniformity in the battery pack; for the first 200 seconds of the cycle the maximum temperature difference within the battery was around 3°C, compared to the maximum reached at the end of the cycle of 7°C.

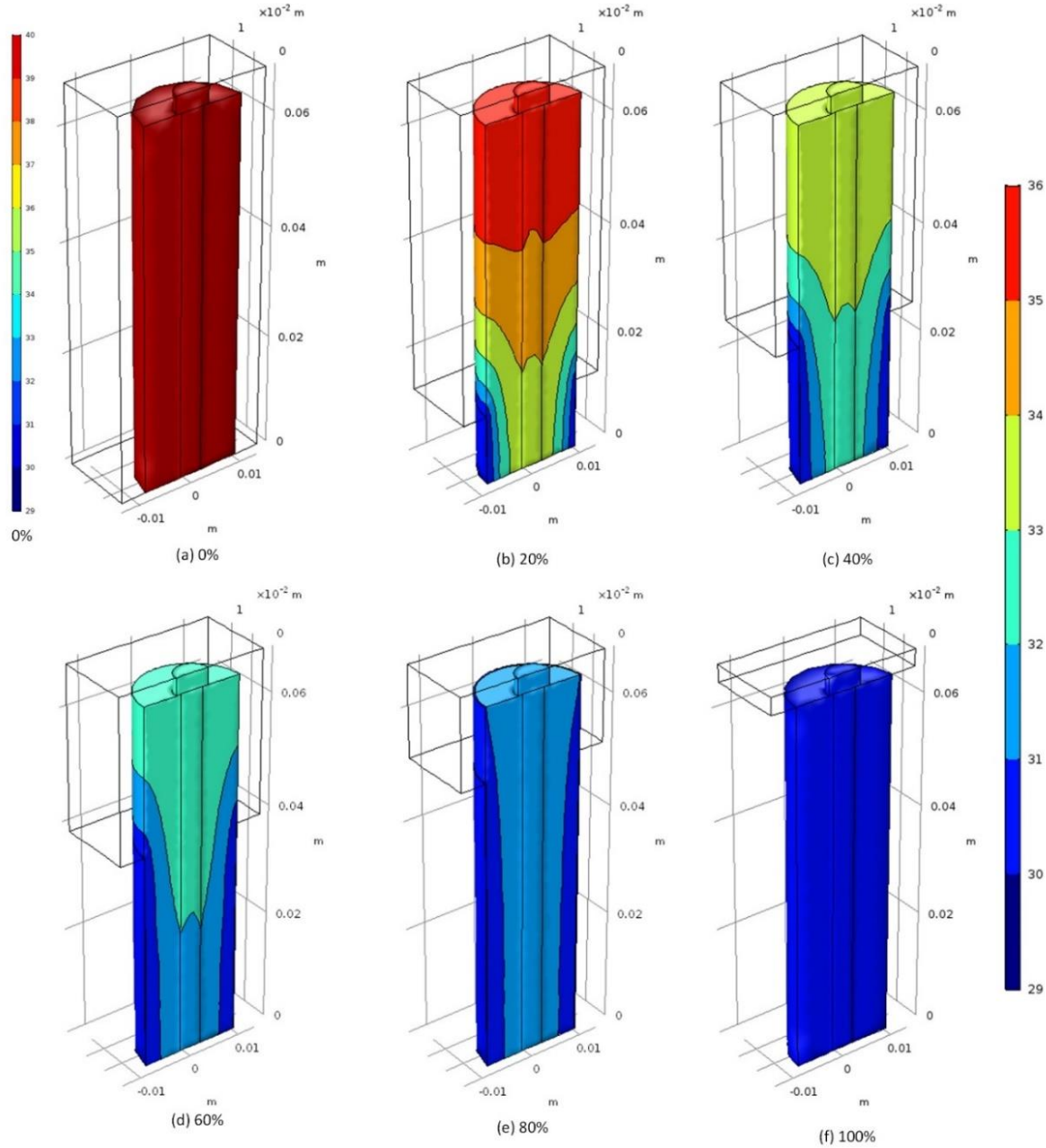

Figure 5.52 Temperature contours of the battery when (a) 0%, (b) 20%, (c) 40%, (d) 60%, (e) 80% and (f) 100% of the battery surface is covered by liquid R134a.

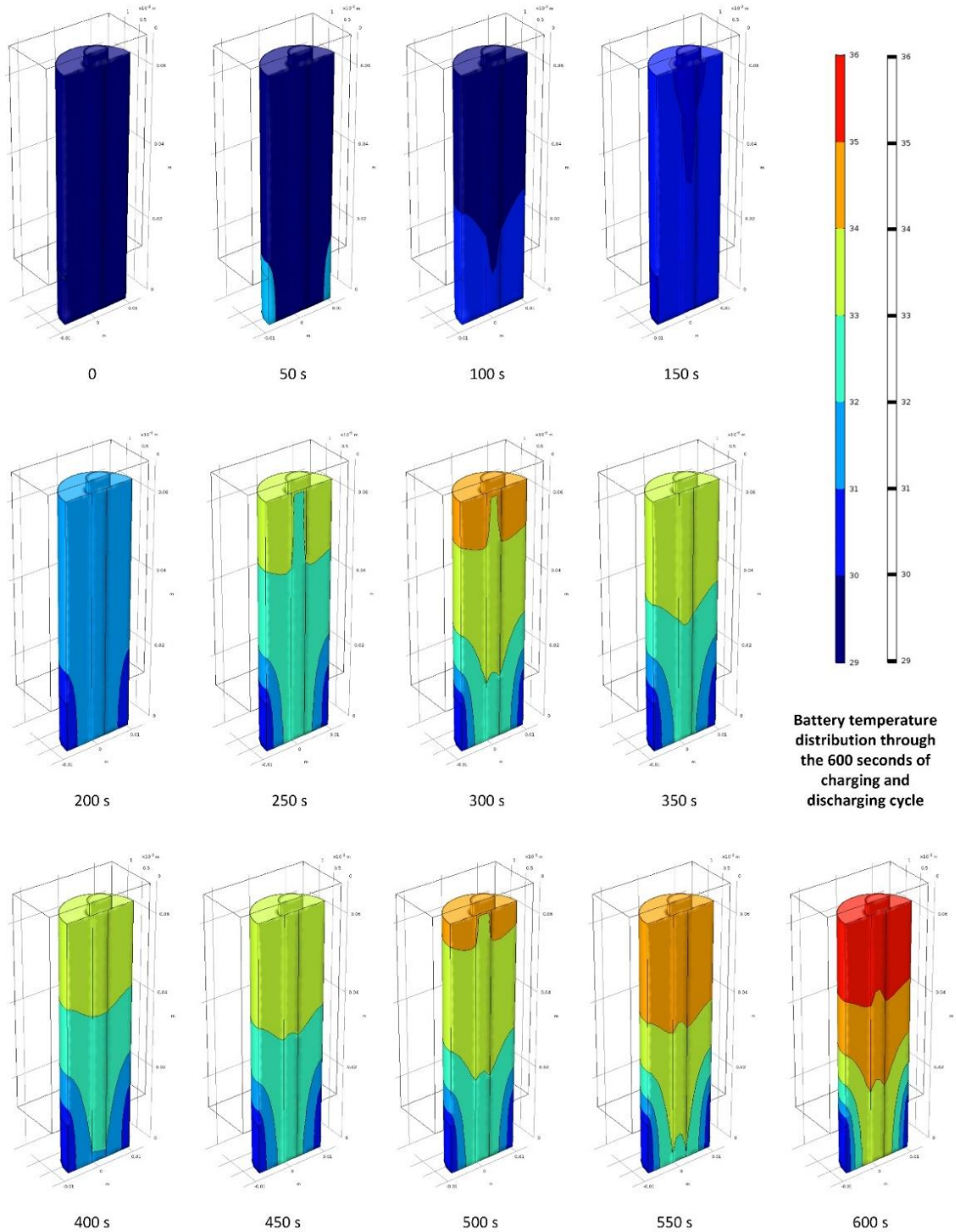

Figure 5.53 Variation of battery temperature distribution over the charging and discharging cycle for the case when 20% of the battery surface is covered by liquid R134a.

Effect of the pool height and different battery separation on the temperature distribution The temperature distribution through a single battery is an important factor for battery performance, and can be used as a performance measure of the cooling system. The

temperature distribution through a single battery can be represented by the battery's average temperature. The average temperature of the battery under various operating conditions and for the two proposed designs is shown in Figure 5.54. Increasing the compactness does not change the system behavior through the 600 second cycle, but the compact design achieves a slightly larger average temperature. Increasing the height of the pool in the pack reduces the difference between the two design as shown in Figure 5.54(d), where the difference between the two designs reaches almost zero. Increasing the height of the pool reduces the differences between the average temperature for different charging and discharging cycle rates.

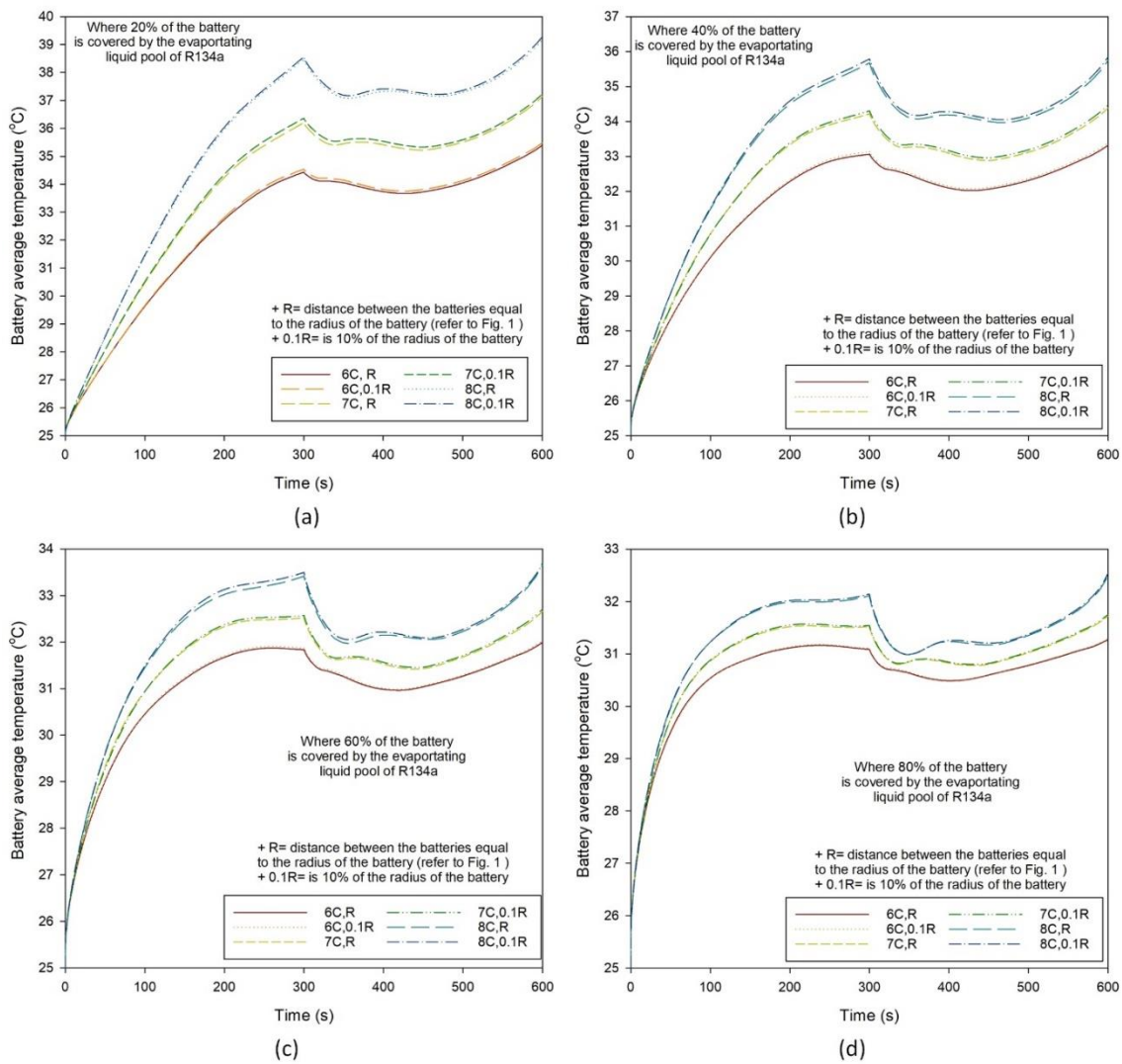

Figure 5.54 Variation with charging and discharging time of battery average temperature for the cases when (a) 20%, (b) 40%, (c) 60% and (d) 80% of the battery is covered with the liquid refrigerant pool.

The temperature distribution through the battery can also be graphically presented in terms of the temperature contours on the outer surface and middle plane passing through

the battery as shown in Figure 5.55. There, the effects are shown of raising the height of the pool in the pack on the temperature distribution through the batteries in the pack for cycle rates of 6C, 7C and 8C for the compact design. Figure 5.55(a) shows the temperature contours of the outer and the middle plane of the battery for various heights of the pool in the pack for a cycle rate of 8C.

For the case when the refrigerant pool covers 20% of the battery, increasing the cycle rate from 6C to 7C increases the average temperature at the mid cycle from 34.5^{o}C to 36.4^{o}C. A further increase in the cycle rate from 7C to 8C increases the mid cycle temperature from 36.4^{o}C to 38.6^{o}C . However, for the case when the pool covers 80% of the battery, increasing the cycle rate from 6C to 7C increases the mid cycle temperature from 31.1^{o}C to 31.5^{o}C, while a further increase in the cycle rate from 7C to 8C increases the mid cycle temperature from 31.5^{o}C to 32.1^{o}C. Reducing the increase or decrease in the average temperature for different cycle rates reflects the better temperature uniformity the system is capable of providing for various cycle rates. Further investigation of the performance of the cooling system under the optimum operating and design parameters (within the considered ranges) is done through the drive cycle study, which is presented in the next section.

The fast response rate of the proposed system can be highlighted in Figure 5.54 as the average temperature drops after 50 seconds when the cycle switches from charging to discharging. The drop in the average temperature varies with the cycle rate and the pool height in the battery pack. For the discharge rate of 8C and for the compact design, the drop in the average temperature is 1.4^{o}C, 1.6^{o}C, 1.4^{o}C, and 1.2^{o}C when the liquid pool covers 20%, 40%, 60% and 80% of the battery surface.

Figure 5.55(a) shows the temperature distribution improvement through the increase of the height of the pool for an extremely high rate of 8C. For all short cycle rates of 6C, 7C and 8C, a pool height of 80% achieves a temperature on the upper surface of the battery equal to that at the bottom of the battery as shown in Figure 5.55, which indicates a high degree of temperature uniformity. For the various considered cases, the removed heat from the battery through the pool and the vapor is compared for the two proposed configurations in Figure 5.56. As more of the battery is covered with the liquid pool, the removed heat becomes closer to the generated heat, as shown in Figure 5.56(j), (k), and (l).

b) Battery heat rate distributions

The proposed cooling system cools the battery through boiling of the liquid R134a pool and the generated R134a vapor. In order to understand the battery temperature variation throughout the test cycle, the battery heat generation rate, the heat rate removed by boiling, the heat rate removed through natural convection by the R134a vapor and the maximum temperature of the battery are plotted during the test cycle (see Figure 5.57). Note that Figure 5.57 reports the heat rates plus the maximum battery temperature for the six cases considered of percentages of the battery area covered by the liquid R134a pool. Figure 5.57(a) shows that, when the battery is not in contact with the pool, a small amount of heat is removed by the stagnant vapor surrounding the battery, which results in a rapid increase in the battery maximum temperature.

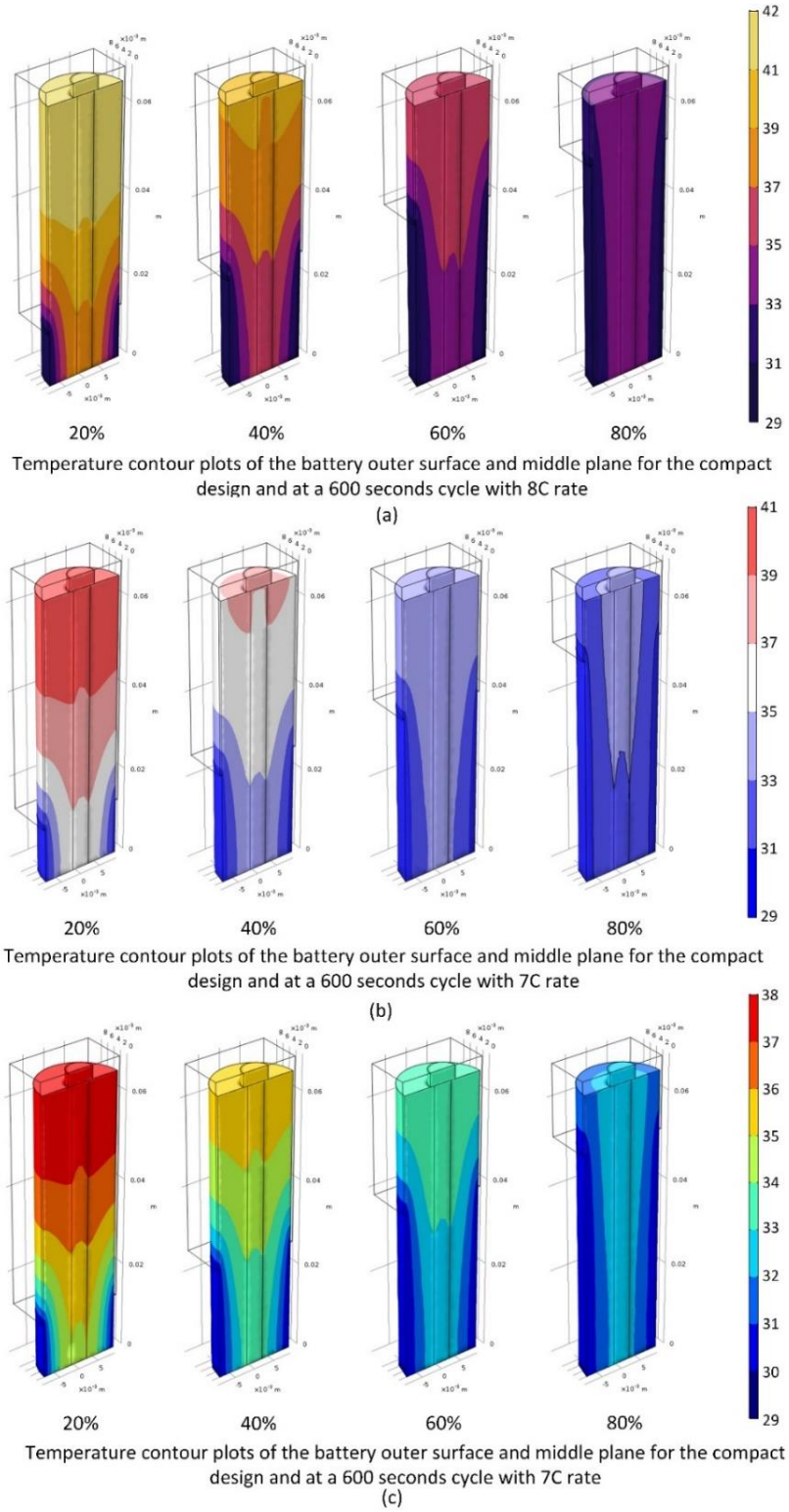

Figure 5.55 Temperature contours of the battery middle plane and outer surface for the four considered pool heights of the evaporating pool when the charging and discharging rates are (a) 6C, (b) 7C, and (c) 8C.

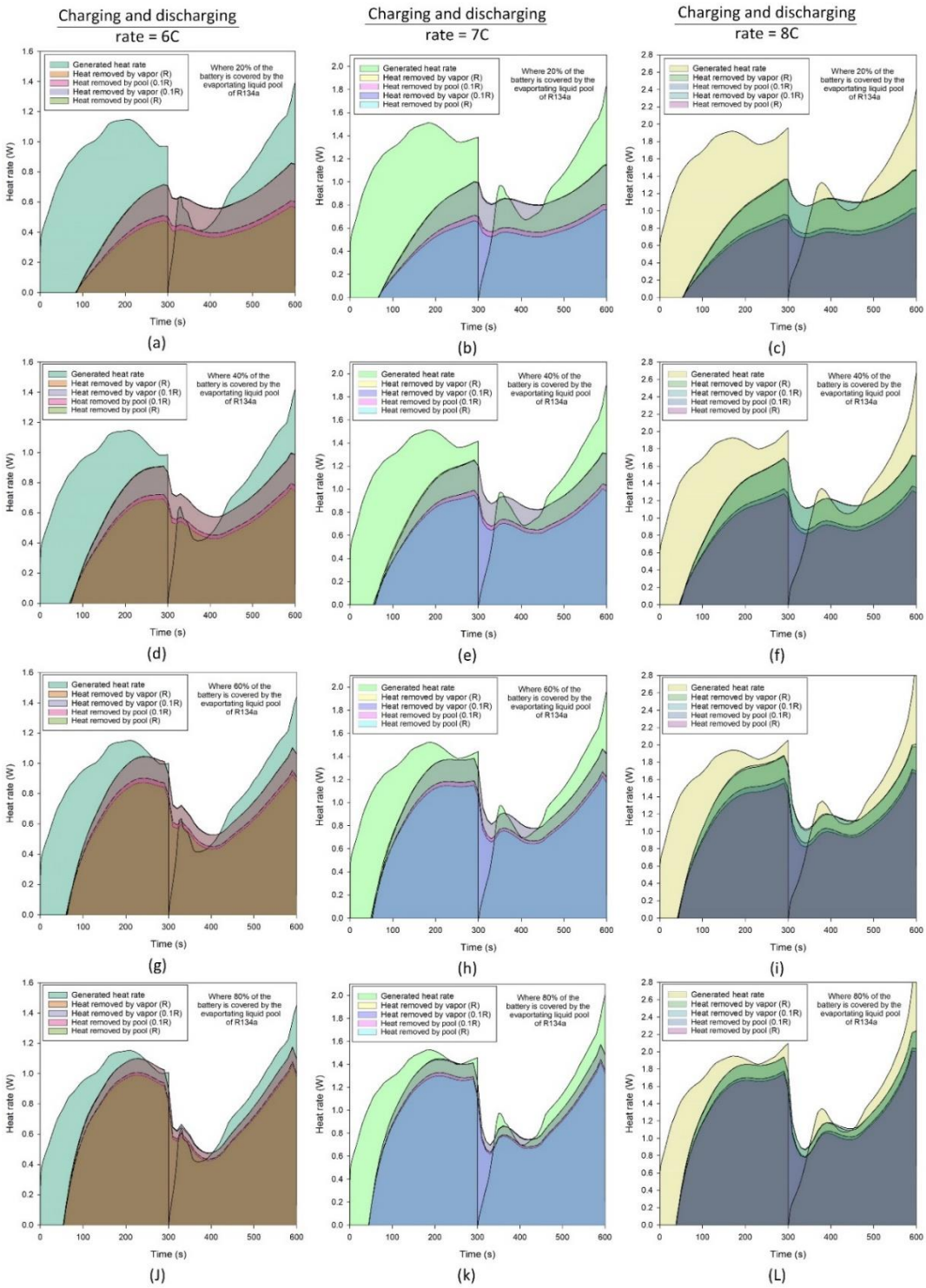

Figure 5.56 Variation of the battery heat generation rate, and heat rate removed from the battery through boiling and through natural convection by the generated R134a vapor for the two compared designs for a liquid pool height of 20% and a cycle rate of (a) 6C, (b) 7C and (c) 8C, 40% and a cycle rate of (d) 6C, (e) 7C and (f) 8C, 60% and a cycle rate of (g) 6C, (h) 7C and (i) 8C, and 80% and a cycle rate of (j) 6C, (k) 7C and (l) 8C.

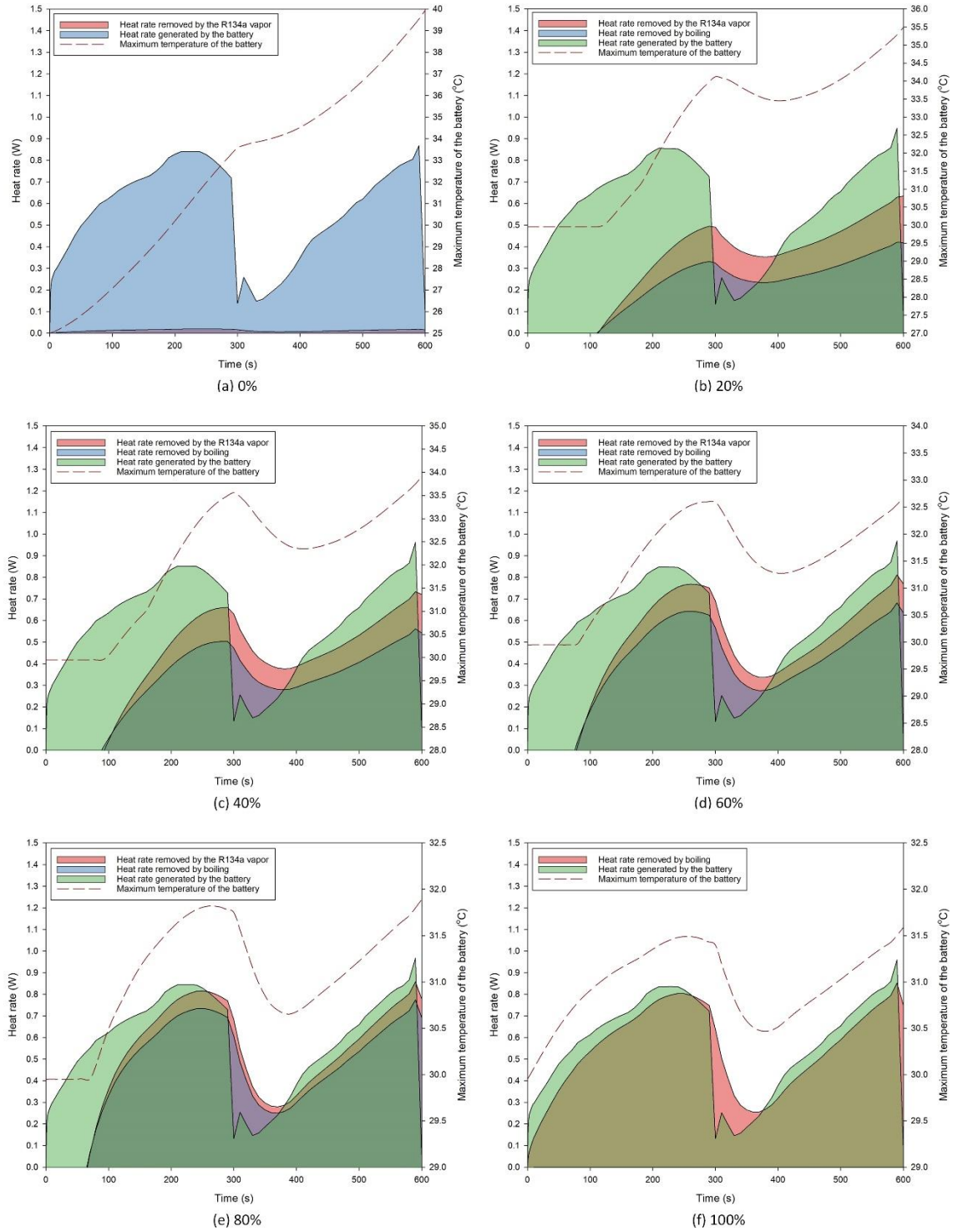

Figure 5.57 Variation of the battery heat generation rate, and heat rate removed from the battery through boiling and through natural convection by the generated R134a vapor, when (a) 0%, (b) 20%, (c) 40%, (d) 60%, (e) 80% and (f) 100% of the battery surface is covered by liquid R134a.

The variation of the heat rates and the maximum battery temperature when covering 20%, 40%, 60%, 80%, and 100% of the battery surface with liquid R134a are presented in Figure 5.57(b), (c), (d), (e), and (f) respectively. Covering more of the battery surface with the liquid R134a leads to a faster onset of cooling. When 20% of the battery is covered with the R134a pool, the cooling effect starts after 100 seconds of the test cycle compared to 95, 80, 70, 1 seconds for the test cycles when 40%, 60%, 80%, and 100% of the battery surface is covered with the R134a pool. It shown that when the heat rate becomes higher than the heat generation rate the maximum temperature of the battery decreases, and when the heat generation rate is higher the maximum temperature of the battery increases. For the case when 100% of the battery is covered with the R134a pool, the cooling effect by the generated R134a vapor is negligible compared to that of the boiling and hence it is not included in Figure 5.57(f).

c) Drive cycle results

The pollutant emissions and fuel consumptions for conventional vehicles are measured using standard driving cycles, such as the new European driving cycle (NEDC). However, vehicle manufacturing companies rely increasingly on a more realistic driving cycle such as the Artemis cycle. Through a more realistic driving cycle, the Artemis cycle emulates the actual performance of vehicles. There are three variations of the Artemis driving cycle: urban, motorway and road driving. Also, there are two versions of the motorway cycle, differing based on the maximum speed that the vehicle reaches in the cycle (130 km/h or 150 km/h).

The proposed refrigerant based cooling system performance is tested here for the Artemis motorway cycle with a maximum speed of 150 km/h for a period of 10 minutes for the case when 40% of the battery is covered with the liquid R134a pool. The parameters of a typical EV are used to determine the electrode power relative to the other electrode of the battery cell, and are listed in Table 3. Note that the three dimensional heat and mass transfer model and the one dimensional electrochemical model are used in this study. More details on the method for calculating the required electrode power corresponding to the 10-minute duration of the Artemis motorway cycle can be found in reference [24]. The thermal performance of the proposed system in terms of the maximum temperature, average temperature and minimum temperature through the second test cycle is presented in Figure 5.58(a). Figure 5.58(b) shows the state of charge, voltage, current and operation power of a single battery in the pack. From Figure 5.58(a), it is observed that the battery reaches a maximum temperature of 30°C at the end of the test cycle. In the test cycle, the average and the minimum temperatures are 30°C and 30°C respectively, demonstrating the high level of temperature uniformity achieved by the system.

The proposed system was able to remove more heat with the generated vapor compared to another refrigerant based cooling system that was proposed [19,20], which resulted in increasing the overall heat removal rate. Another advantage the proposed system over other refrigerant based cooling systems is that it is not limited to hybrid electric vehicles or based on the type of fuel they use. However, some of the disadvantages of the proposed system are that it works when the ambient temperature is lower than 30°C or if the air conditioning unit in the vehicle is cooling the vehicle cabin to a temperature lower than 30°C. The objective of this research to reduce the dependence of the refrigerant based

cooling system on the type of fuel or vehicle the system was achieved. However, further research is merited to remove the dependence of the refrigerant based cooling system on the ambient temperature and the operation of the vehicle air conditioning system, and to investigate condensation and the recycling of the R134a.

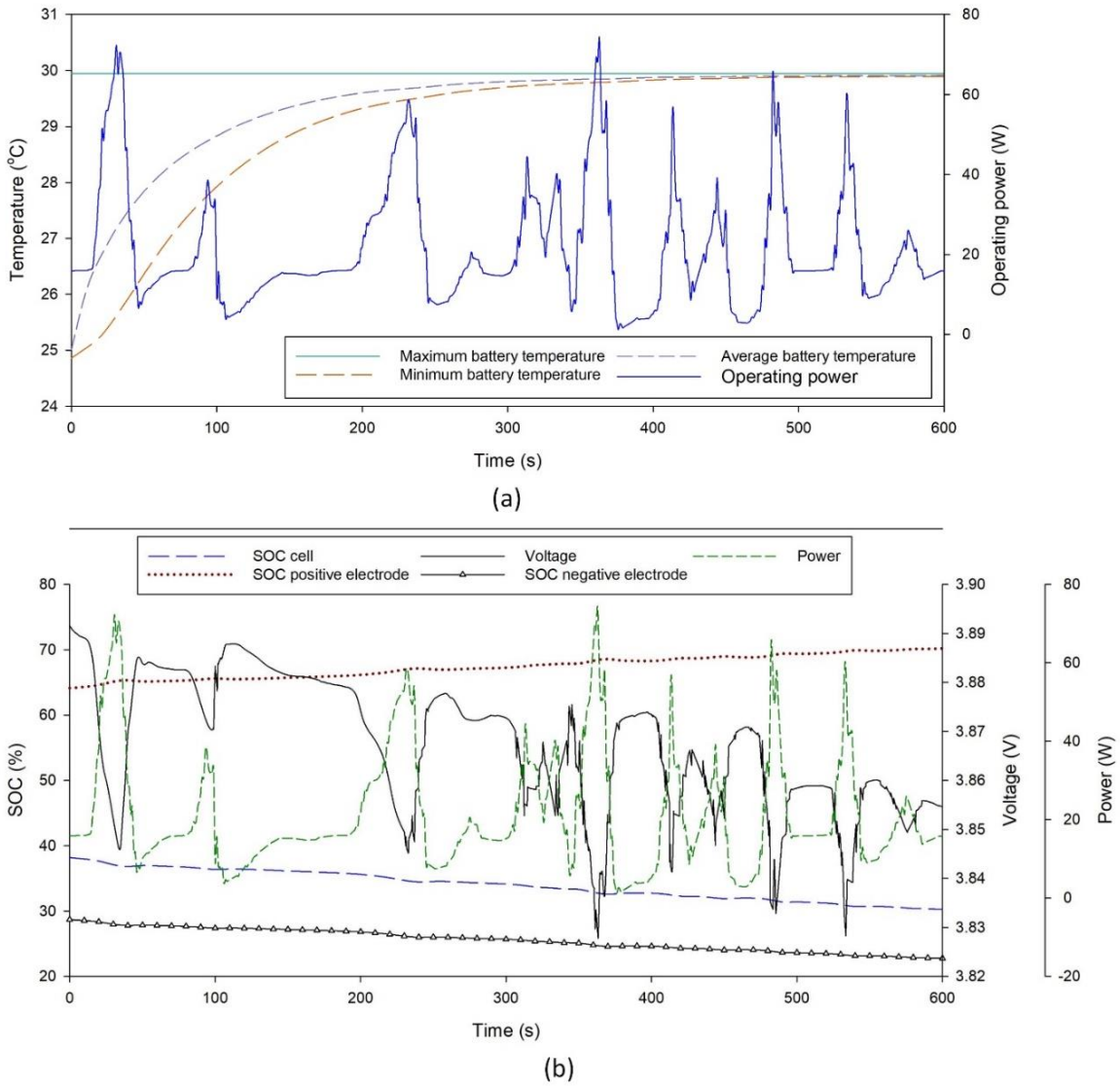

Figure 5.58 (a) Maximum temperature, average temperature and minimum temperature through the second test cycle, and (b) state of charge, voltage, current and operation power of a single battery in the pack.

A refrigerant based cooling system is proposed that manages and maintains the operating temperature of batteries within the optimum operation range, and that can compete with the most commonly used liquid and air cooling systems. The proposed system is independent on the type of vehicle, i.e., it can be used in electric vehicles, hybrid electric vehicles, and plug in hybrid electric vehicles. The proposed system exploits the high heat transfer coefficient of boiling through a direct contact boiling with the battery

surface. The proposed design performance was investigated under two 600-second test cycles. The first test cycle had a 300 seconds of charging at a rate of 4C followed by 300 seconds of discharging at a rate of 4C. The second test cycle had a duration of 600 seconds for an Artemis motorway cycle with a maximum speed of 150 km/h.

For the first test cycle, the proposed system was able to limit the temperature rise of the battery to 1.6ºC for the case when 100% of the battery surface is submerged within the liquid R134a. The maximum temperature difference in a single battery in the pack was largest when only 20% of the battery was covered by liquid R134a, at 7ºC. It was shown that due to the selected relatively high boiling temperature of the liquid R134a, the cooling effect is delayed from the start of the test cycle. The exception to the delay of the cooling effect occurs when the battery is covered completely. However, for the second test cycle, the proposed system with the batteries being covered with only 40% was able to maintain the maximum battery temperature at under 30ºC.

Further analysis of the drive cycle considers further cycles for the case when the separating distances between the batteries selected is the smaller one. The resulting battery pack thermal performance of the considered EV through the long intensity cycle is shown in Figure 5.59(a), that includes the variations of the maximum and average temperatures, cell electrode potential and cycle operating power. The maximum temperature in the pack varies within a 4ºC range throughout the cycle, while the average temperature variations are limited to 1ºC as seen in Figure 5.59(a). The maximum temperature reaches a value 35ºC, while the highest average temperature reaches was 32.5ºC. It is also seen in Figure 5.59(a) that a resting period of one sixth of the cycle is enough to stabilize the system temperature to the pool saturation temperature of 30ºC. It is also shown in Figure 5.59(a) that a period of one sixth of the cycle is enough to permit the average temperature to equal the maximum temperature. However, the long intensity cycle considered is not a realistic cycle. The proposed system thermal performance through the Artemis motorway cycle is shown in Figure 5.59(b). It is seen that after around 650 seconds the system keeps the maximum temperature around the saturation temperature of the liquid refrigerant cooling pool. However, the average temperature of the battery starts from a low of 25ºC and reaches the maximum temperature around 600 seconds through the cycle. Then both the maximum temperature and the average temperature start to raise and exceed the saturation temperature together, with a maximum temperature difference through the remainder of the cycle of 0.5ºC, which shows the high thermal uniformity within the pack. The pack maximum temperature reaches 31.3ºC at the end of the realistic drive cycle.

5.4.4 Comparative results of the present systems

In this section, the performance of the proposed systems for the cylindrical battery pack is compared with each other and the without cooling initially and the best performing system is comparted to the systems proposed in the literature in terms of pack performance. Pack performance is a measure of the thermal management performance however on the full pack level, which is mainly in the maximum temperature difference across the battery pack. While the thermal management system performance is further investigated through the variation of the maximum temperature of the battery which has the maximum temperature in the pack and others, and the variation of the maximum temperature difference in those batteries as well. The first subsection will deal with comparison between the proposed systems to each other and with the case where no cooling system is used. The following

subsection will compare the best performing system will be compared with the literature proposed systems.

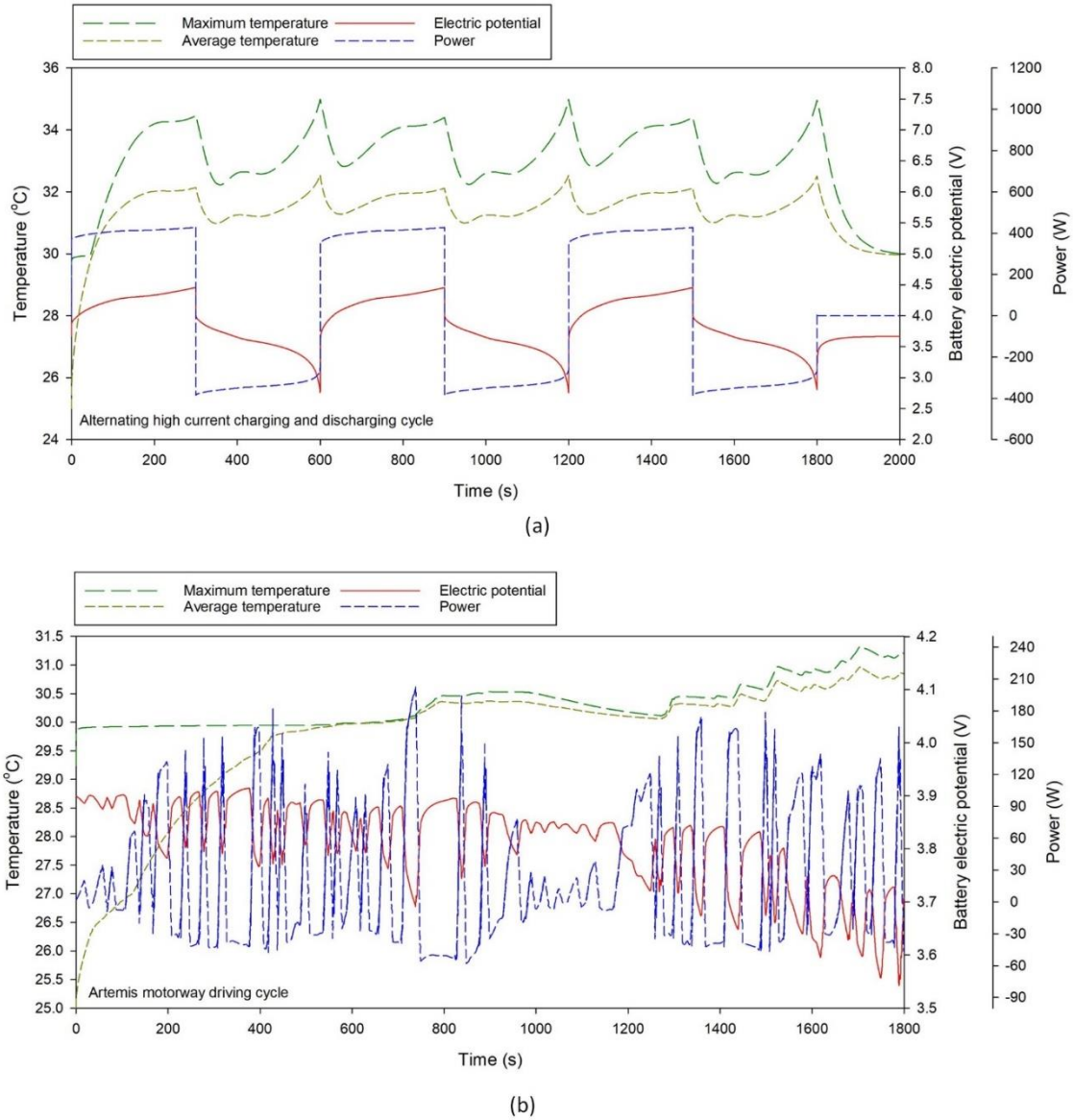

Figure 5.59 (a) Maximum temperature, average temperature, cell electrical potential and cycle power for (a) three continuous multiples of the short test cycle and (b) Artemis motorway cycle.

a) Temperature comparisons

In this section, the proposed systems are compared against each other, where the hydrogen system was not proposed since the novelty of the hydrogen proposed system as well as the air based cooling system was in using the fuel of the vehicle in the cooling process and the proposed cold plate for the prismatic battery pack. For the air based cooling system for cylindrical battery packs, various novel proposed system in the literature pack geometry is adapted. For each system the main parameters of the cooling system where maintain the

same as much the system flexibility allows, while the differences are reported in the text and in the comparison figure. Figure 5.60 shows the variation of the maximum temperature of the battery with the highest temperature in the battery pack through a charging and discharging cycle at a rate of 6C for 600 seconds.

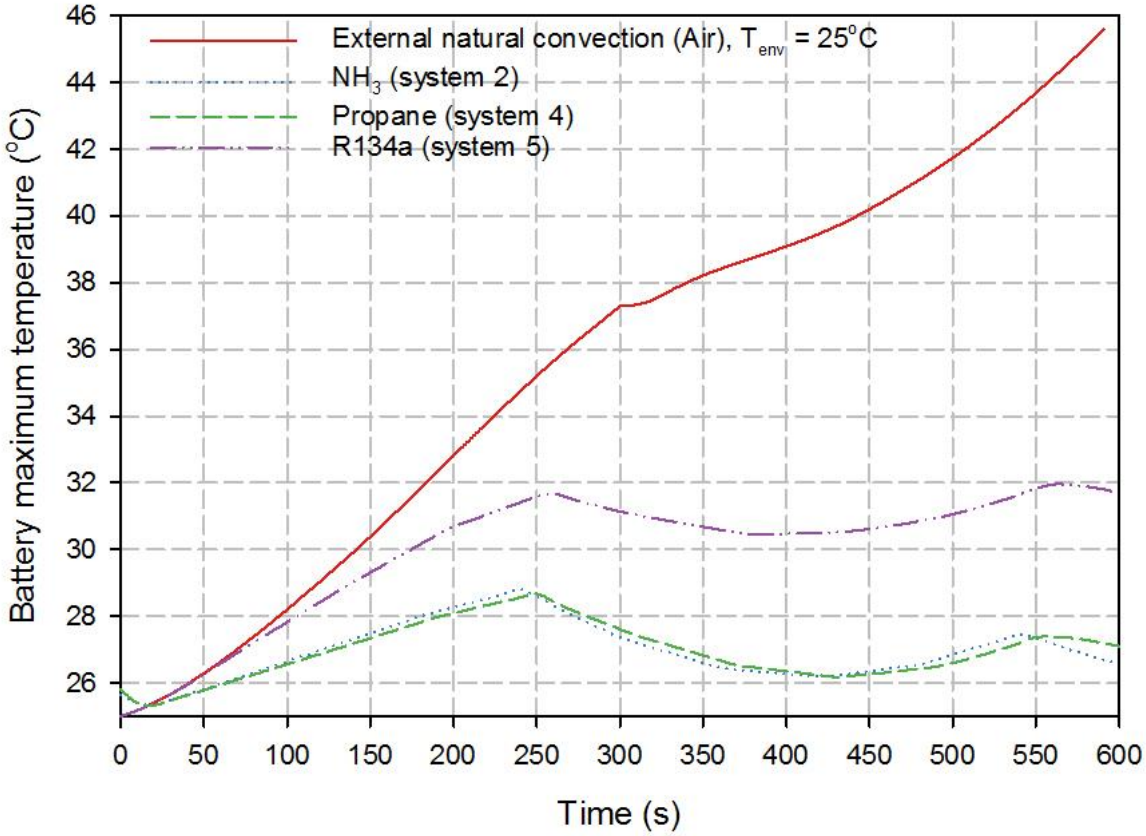

Figure 5.60 The variation of the maximum temperature of the battery with the highest temperature in the battery pack through a charging and discharging cycle at a rate of 6C for 600 seconds, where systems 2, 4 and 5 are all simulated at the same pool height of 30% of the height of the battery.

For the three different proposed cooling systems proposed in the thesis for the cylindrical batteries, the performance is compared when coolant in all three systems have the same saturation temperature of 25°C as well as the environment temperature of the battery without cooling system however with a natural convention as shown in Figure 5.60. As Figure 5.60 all boiling systems, which in this case all three proposed systems have a similar behavior in terms of the temperature variation relative to heat generation curve. The differences between the performance in terms of the achieved maximum temperature of the battery is due to the physical and thermophysical properties of the coolant itself. The best performing system is the ammonia based system, and the propane based system has a very close performance as well. Figure 5.61 shows the reduction percentage of the battery maximum temperature (relative to the case with cooling comes from the natural convection in an environment temperature) variation with time versus the charging and discharging cycle time for the three proposed systems. The ammonia and the propane based systems

where able to reduce the maximum temperature of the battery with around 40% at the end of the cycle relative to the case with no cooling system is used other than natural convection in room environment temperature. The refrigerant based system reduced the maximum temperature of the battery to 28% less at the end of the simulation cycle. As shown in Figure 5.61 the reduction of the battery temperature increases with the increase of the battery maximum temperature without the cooling system being used, which is due to the ability of the proposed systems to maintain the maximum temperature of the battery within 2 to 3°C temperature range as shown in Figure 5.60. Comparing the thermophysical properties of the three considered coolants at the same saturation temperature, the ammonia will highest enthalpy of evaporation of 1180 kJ/kg, followed by propane of 342.9 kJ/kg and last is the refrigerant R134a with 177.8 kJ/kg.

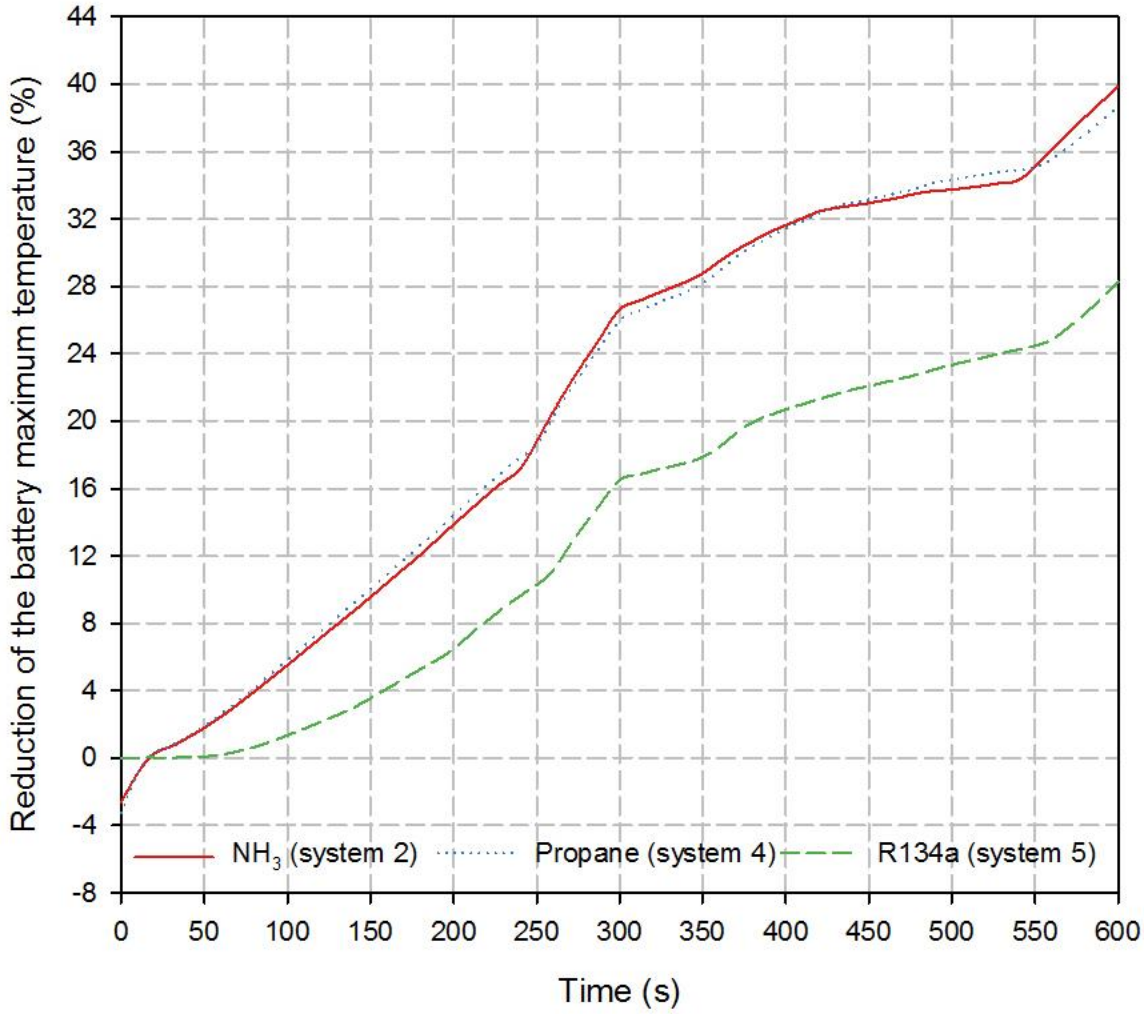

Figure 5.61 The reduction percentage of the battery maximum temperature (relative to the case with cooling comes from the natural convection in an environment temperature) variation with time versus the charging and discharging cycle time for the three proposed systems.

The role that the enthalpy of evaporation plays is the larger its value the longer it takes to phase change the liquid on the high temperature wall, which leads to having a

higher heat transfer rate since it leaves the surface in contact with liquid phase for longer period of time compared to the coolants with a lower enthalpy of evaporation. In addition to the effect of the enthalpy of evaporation, the ammonia has a high thermal capacity, which makes it one of the best refrigerants. The thermal capacity of a fluid depends on the specific heat capacity and the density of the fluid. For better understanding of the behavior of the various considered refrigerants, which are R134a, ammonia and propane temperature and enthalpy properties plot is presented in Figures 61, 62, and 63 respectively.

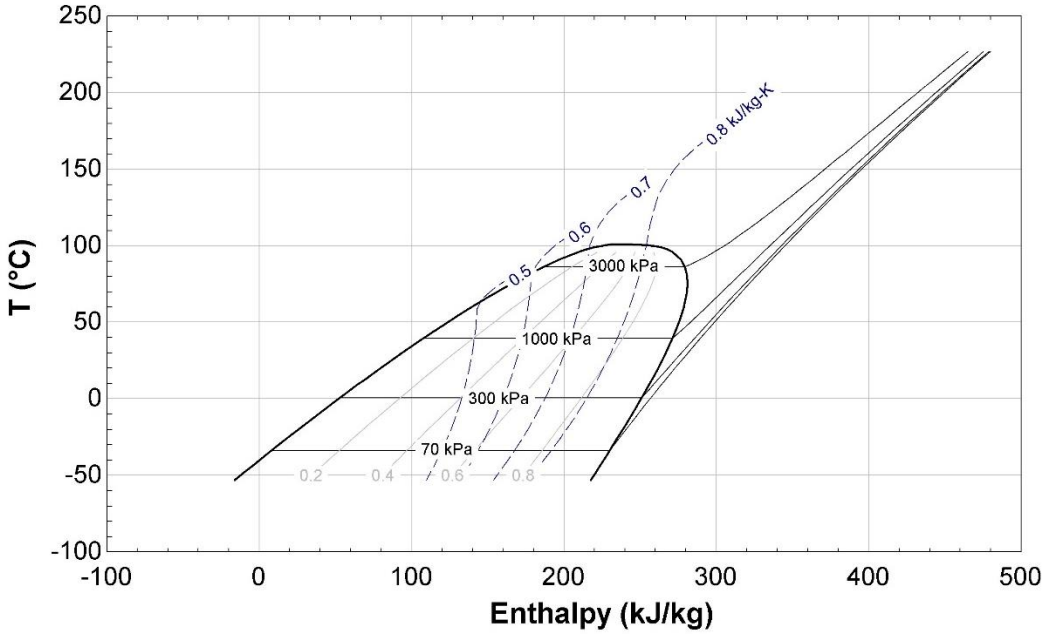

Figure 5.62 Temperature versus enthalpy property plot of refrigerant R134a.

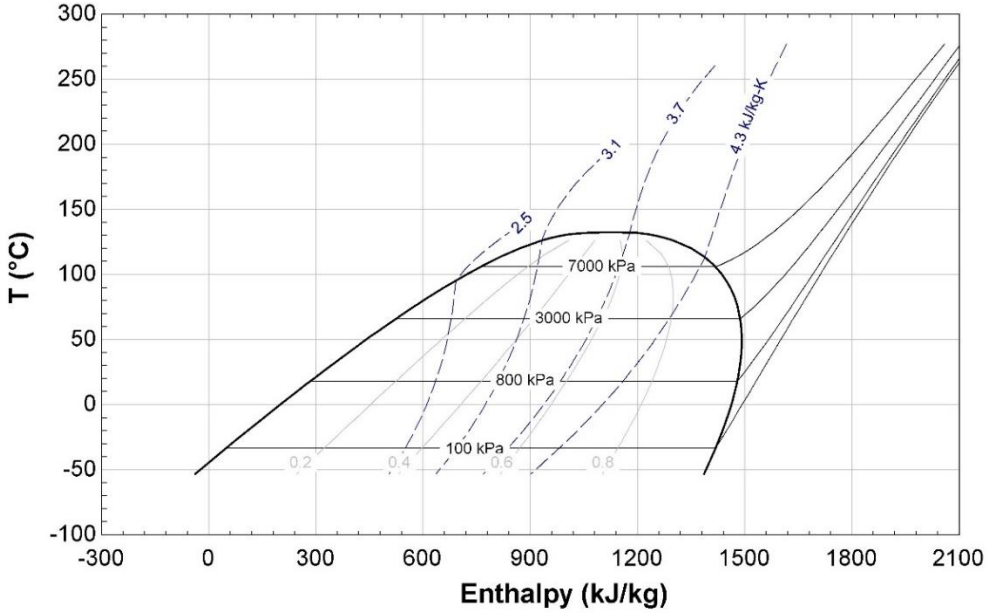

Figure 5.63 Temperature versus enthalpy property plot of ammonia.

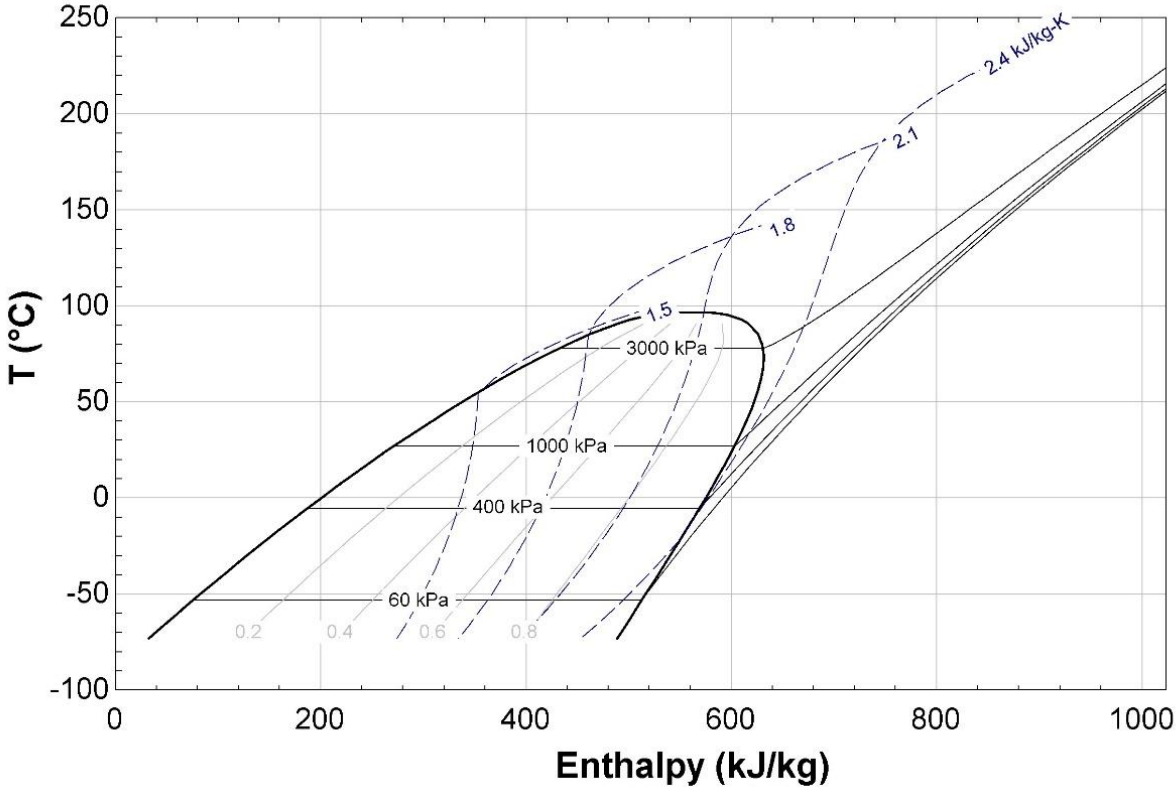

Figure 5.64 Temperature versus enthalpy property plot of propane.

In Figures 5.61, 5.62, and 5.63 the enthalpy of vaporization of ammonia is much larger than those of the R134a and that of propane as the area of under the bell shaped curve is larger for ammonia compared to the other two considered refrigerant, which gives it the advantage over them.

The systems that exploit liquid-to-vapor phase change to cool the batteries in a cylindrical battery pack are compared for the battery with the maximum temperature in the pack. The variations of the maximum temperature difference across the battery for the three proposed systems are shown in Figure 5.66, in this case the initial temperature of the battery was set to 25ºC. The ammonia based system achieves the lowest temperature difference across the battery and thus achieves the highest temperature uniformity across the battery surface as show in Figure 5.66. Another study considers the starting temperature of battery to be equal to the saturation temperature of the coolant and the resulting battery maximum temperature difference across the battery is shown in Figure 5.66. In the case where the initial battery is set to the saturation temperature of the pool, the ammonia system still achieves the lowest temperature at the end of the cycle compared to the other two systems. However, throughout the simulation cycle the propane was achieving better performance in terms of having a lower temperature difference across the battery. But at the end of the cycle both of the ammonia and propane reached the same final temperature.

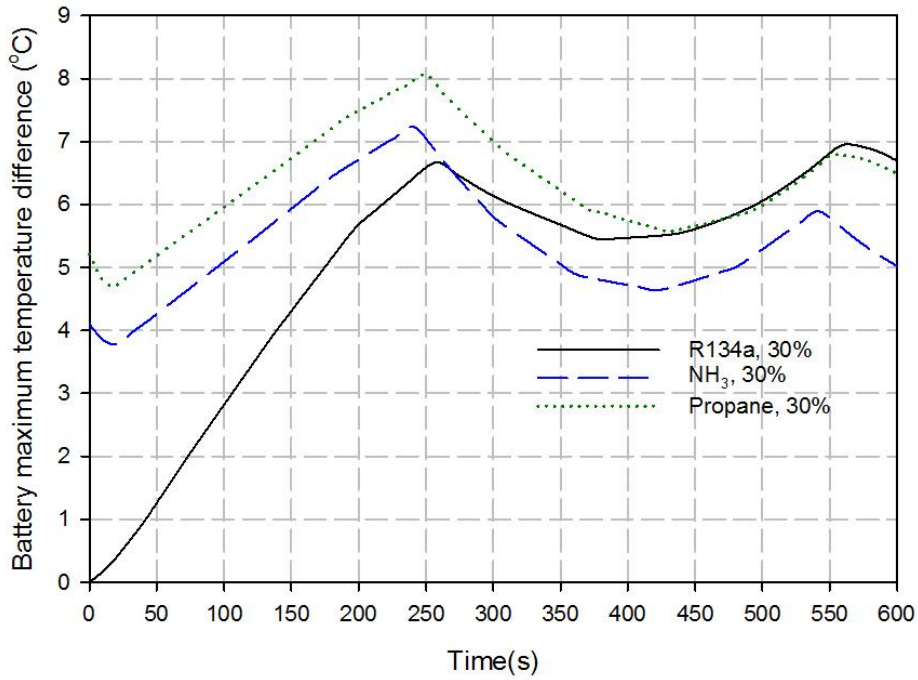

Figure 5.65 Variation of the maximum temperature difference across the cylindrical battery that has the highest maximum temperature in the battery pack, when cooled by various liquid-to-vapor phase change based thermal management systems. The initial temperature of the battery is 25°C.

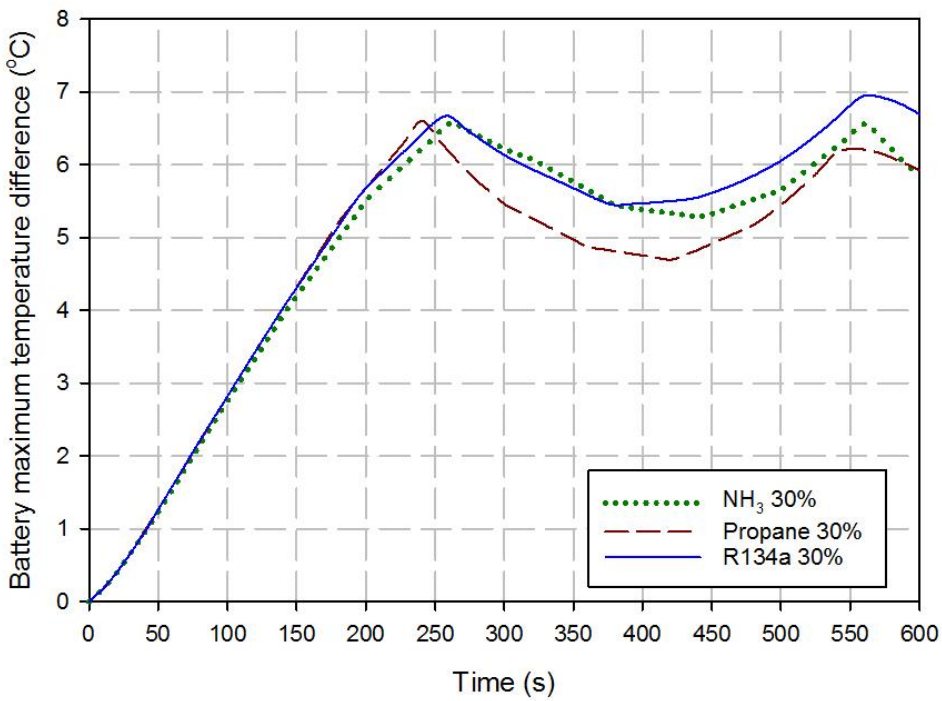

Figure 5.66 Variation of the maximum temperature difference across the cylindrical battery that has the highest maximum temperature in the battery pack, when cooled by various liquid-to-vapor phase change based thermal management systems. The initial temperature of the battery is the saturation temperature of the coolant.

b) Efficiency comparisons

The method used to determine the energy efficiencies of using the liquid-to-vapor phase change battery thermal management system to cool prismatic batteries is used in this section for cylindrical batteries. Figure 5.67 shows the variation of the energy efficiencies of various systems proposed in the literature that use liquid-to-vapor phase change to cool the batteries. Since the propane and ammonia based systems exhibit similar thermal performance in terms of the maximum battery temperature and the maximum temperature difference across the battery with the maximum temperature in the pack, they are expected to achieve similar energy efficiencies. However, as shown in Figure 5.67, the ammonia based system achieved a slightly higher efficiency. So the ammonia based system achieved the highest energy efficiency in cooling both cylindrical and prismatic batteries.

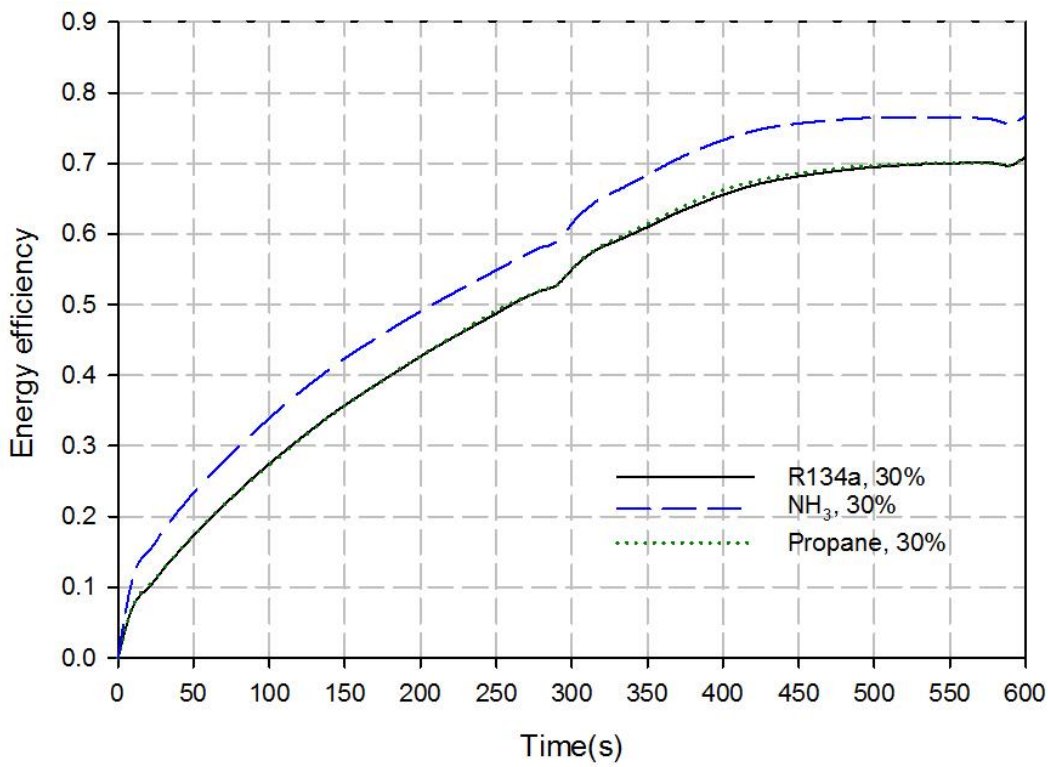

Figure 5.67 Variation of the energy efficiencies of liquid-to-vapor phase change thermal management systems for cylindrical batteries. The initial battery temperature is set to the saturation temperature of the coolant.

c) Comparison with the literature studies

The previous section concluded that the propane based cooling system was able to achieve the largest reduction in the battery's maximum temperature relative to the case when there is no cooling system is used, however natural convection is the only source of cooling in an environment with a temperature and pressure of 25°C and 1 atm respectively. In this section the propane based cooling system performance is compared with various proposed systems in the literature. In this section, the performance of the proposed system is

compared against other studies for thermal management of 18650 Li-ion battery packs, and the comparison is presented in Figure 5.68.

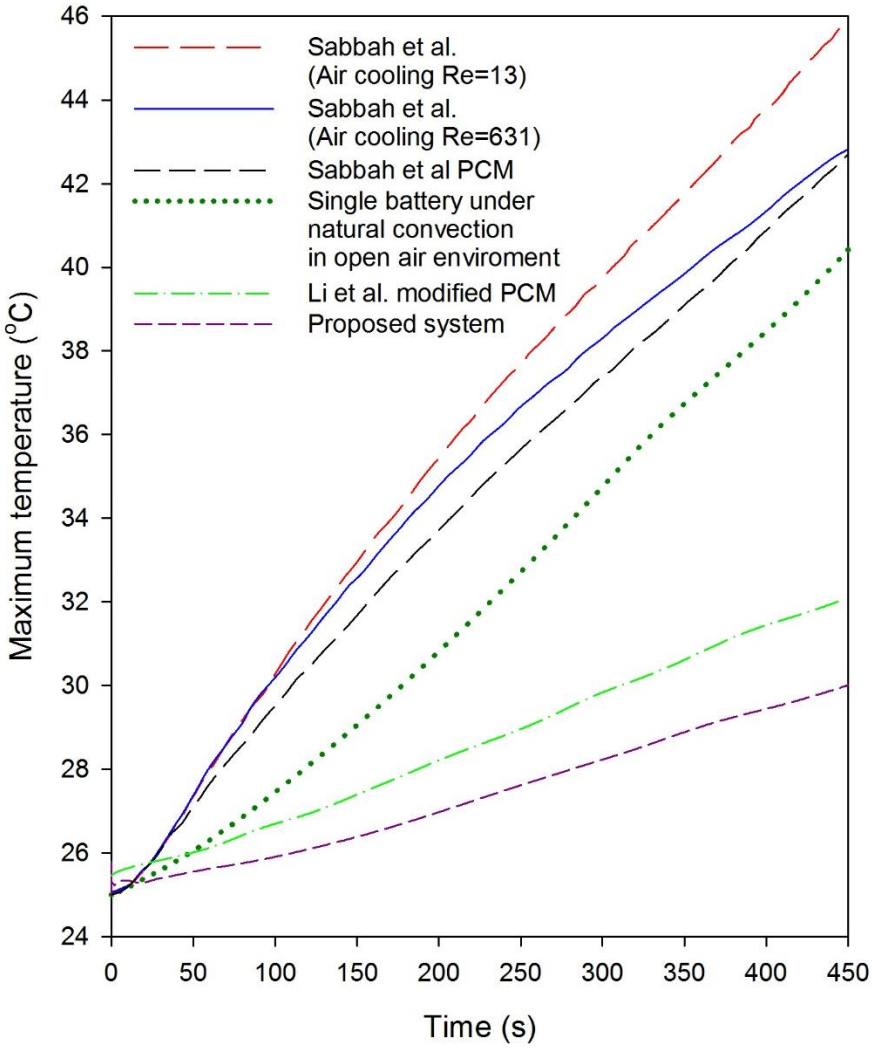

Figure 5.68 Performance compared of the proposed system against proposed systems from other studies for the thermal management of 18650 Li-ion battery packs at a discharge rate of 6.667C

The performance of the proposed propane based battery thermal management system is compared with studies that considered air cooling and PCM [52,82], at a high discharging rate of 6.667C. Li et al. [82] proposed a sandwich structure cooling system that uses a copper metal foam structure integrated with a PCM (copper foam-paraffin composite), and investigated its performance experimentally at a high power discharge rate of 6.667C, which corresponds to 10 A.. Li et al. [82] reported the results of the battery pack in terms of the average maximum temperature of the batteries in the pack. Li et al. [82] used battery model 18650, which is similar to the battery type considered in this study. Sabbah et al. [52] proposed expanded graphite that is saturated with paraffin, where the structure is designed to reduce the surface temperature of the battery. A similar discharge rate of 6.667C was also considered by Sabbah et al. Sabbah et al. assessed two air based

cooling system as comparison cases to assess the performance of the proposed cooling system.

It is pointed out that the use of the HEV fuel, propane, in this study as a PCM to passively manage the thermal performance of the Li-ion batteries in the pack has not yet been proposed. In previous studies, researchers focused on using solid metallic meshes with foam PCMs, such as copper-foam, aluminum-foam, nickel foam-paraffin and graphite-foam, as a battery thermal management system for Li-ion batteries. As shown in Figure 5.68, the proposed system is highly efficient at keeping the maximum temperature in the battery pack at less than 30°C through 450 seconds of a high discharge rate of 6.667C. Comparing the performance of the battery thermal management system proposed in this study with other previous studies considering PCM and air cooling shows that the proposed system performs better than the systems in the considered studies, with even better performance than the proposed system of Li et al. [82] using nickel foam-paraffin.

Finally, with all the advantages the proposed systems there are limitations and disadvantages. In order to better understand the proposed systems in addition to their high performance capabilities and advantages that the systems introduce to the electric and hybrid electric vehicles the limitations and the disadvantages of the proposed systems are important as well to understand the performance of these systems. The limitations and disadvantages of the proposed systems can be presented as follows:

- The fuel based systems, including the hydrogen, ammonia and propane based systems increases the danger of the thermal runway since the fuel surrounds the batteries and if thermal runway occurs and the batteries caught on fire, the fuel will combust leaving larger damage.
- The fuel based systems have the disadvantage of limiting the drive range on the fuel since when the fuel runs out the thermal management system can no longer work.

Chapter 6: Conclusions and Recommendations

This chapter presents conclusions of the work, research and results in this and then the chapter goes to the recommendation section, which provide recommendations that are inferred from the results of the thesis. Note that the recommendations also introduce ideas for further systems that can be proposed and further analysis ideas that are out of the scope of this thesis and its objectives.

6.1 Conclusions

The battery thermal management system plays an important role in the performance and safety of EVs, HEVs and any system that drives high discharge and charging rates from batteries to power a system or a group of systems. The literature review chapter showed that battery thermal management systems that are currently used by the companies that have mass production of HEVs and EVs have a limited heating capacity based on thermodynamics analysis. The literature review has shown that the novelist of the systems proposed in the literature were focusing on optimizing the currently available systems and work on efforts to get closer to their thermodynamic limits. However, by analyzing the thermodynamic limits of conventional systems it was shown that novel thermal management systems with higher thermodynamic potential are required with better heat transfer characteristics and higher efficiency.

The main novelties that this thesis offers as the main contribution to the field, are using the hybrid electric vehicle fuel as the battery pack coolant and the second is in using the high heat transfer of boiling in battery thermal management. The proposed systems are modeled, simulated and analyzed, and the performance is compared between themselves and later with the literature proposed systems. The main finding of the research, modeling, simulation and analyses of this thesis are summarized as follows:

- The proposed pool-based system is more effective for cylindrical than prismatic battery packs. A pool that covers 30% of the cylindrical battery height can reduce the maximum temperature of the battery at the end of an intense simulation cycle at a rate of 6C that lasts for 600 seconds by 13.0^{o}C to 18.6^{o}C depending on the type of the coolant used.
- To achieve the maximum prismatic battery temperature reduction of 13.0^{o}C to 18.6^{o}C by the pool based system, it is required to have a pool that covers 80% of the battery height through the same simulation cycle.
- The most effective system for cylindrical batteries is the pool based system, whereas high as 40% reduction of the maximum battery temperature is achieved when 30% of the battery height is covered by the boiling pool.
- The most effective system in reducing the maximum temperature of the battery is the tube based system. A cold plate with four tubes results in reducing the battery maximum temperature by 19.5^{o}C.
- The geometry of the flow channel embedded in the cold plate of the air and the hydrogen based systems, which used to cool the prismatic batteries in the pack is developed through an iterative approach that is based on the thermal and flow

performance of the cooling system. The area of the flow channel covers only 16% of the surface area of the battery.

- Increasing the number of tubes in the cold plate enhances the temperature distribution through the prismatic battery. Increasing the number of tubes from one to six improves the temperature distribution through the battery by reducing the maximum temperature difference across the battery by 33%.
- The air and hydrogen based system is more sensitive to the inlet temperature more than the flow rate when the flow rate changes from 0.01 m/s to 0.05 m/s. Reducing the coolant inlet temperature by 5°C reduces the battery maximum temperature by 3% and reduces the maximum temperature difference across the battery by 30%.
- The pool based and the tube based systems for both cylindrical and prismatic battery packs outperform the literature systems, mainly the liquid, air and PCM systems further through the cycle and at high rates. In one of the most advanced water cooling systems, which is the mini channels water cooling and while operating at a high mass flow rate of 0.002 kg/s per each prismatic battery the maximum temperature increased up to 13°C from the starting temperature and then reached a steady state at a temperature that is 10°C more than the starting battery temperature.
- The pool based system response was 10 seconds of the 600 seconds cycle compared to around 102 seconds for 600 seconds cycle for the mini channel cold plate cooling system.
- The most effective system in terms of reducing the maximum temperature difference across the prismatic battery is the pool based cooling system, where it maintains the temperature difference less than 3.5^{o}C compared to less than 9.0^{o}C for air and hydrogen based systems.
- Tube cold plate based system has 80% less coolant in the battery pack than the direct contact pool based system while achieving a higher reduction in the maximum battery temperature and the maximum temperature difference across the battery pack.

6.2 Recommendations

In this section a set of recommendations are provided to for further studies considerations that can be built up on the work and results presented in this thesis. The work in this thesis investigates the unexplored field of using the high heat transfer rate of boiling in battery thermal management systems and it also investigate the integration of the vehicle drive train with the battery thermal management system.

In order to further investigate the proposed systems and expand on the introduced field of thermal management systems and the recommendations can be listed as follows:

- Expanding the developed integrated model of electrochemical and thermal models to simulate a full battery pack of 300 cells including the coolant supply system to investigate the effect of the environment temperature, collusions and other environmental conditions.

- An experimental study of the integration of the hybrid vehicle drive train with the battery thermal management system is recommended to investigate the performance of the proposed systems experimentally.
- The developed one dimensional model can be extended to two dimensional or even three dimensional electrochemical model to increase the accuracy of the modeling of the electrochemical reactions. However, doing that will results in increasing the computational time extensively especially for a large battery pack.
- Developing a tube based system for cylindrical battery pack to investigate the potential improvement in the percentage reduction in the maximum battery temperature and the maximum temperature difference across the battery.
- Investigating the potential efficiency improvement in liquid based thermal management systems with integrating it with liquid to vapor phase change system.
- Performing cost and exergoeconomic cost analysis on the proposed systems, including the savings due to the integration of the vehicle derive train with the cooling of the battery packs and the use of the continuously recycled refrigerant based system.
- Performing environmental and exergoenvironmental analysis on the proposed systems, including the savings due to the integration of the vehicle derive train with the cooling of the battery packs and the use of the continuously recycled refrigerant based system.
- Investigating the performance of the proposed thermal management systems for stationary battery based systems used for energy storage of renewable energy collection systems and for EV solar panels.
- Studying the corrosive effect of the proposed coolants and their safety under vehicle collision and battery thermal runway conditions.
- Studying the cooling performance of the proposed systems for the new Li-ion batteries geometries and the promising solid state properties.
- Studying the performance of the proposed systems under the effect of variable environment temperature.

As was presented in the comparison sections of the results and discussion chapter, the proposed systems were able to achieve a better performance than most liquid and air based systems at the mentioned parameters prove that the proposed systems are promising option for hybrid and electric vehicles industry. With the help of the proposed systems the hybrid and electric vehicles disadvantage of long charging time can be reduced significantly specially with the fast system response and makes them more appealing to costumers. It is recommended that the industry focus on investigating the refrigerant based system since it can be used for both electric and hybrid electric vehicle and it has the same concept as the propane and ammonia based systems. As shown in the conclusions for cylindrical battery packs it is recommended to use and further investigate the pool based systems. However, for prismatic batteries, tube based systems. Material properties and associated problems such as corrosion should be further investigated as well. Note that the uses of the proposed systems are not limited to vehicle's battery packs, since the cooling methodology can be applied future large scale battery pack energy storage systems for houses and electricity refuel stations for electric vehicles.

References

[1] Government of Canada, Greenhouse gas sources and sinks: executive summary - Canada.ca, 2016.

[2] K. Chen, S. Wang, M. Song, L. Chen, Structure optimization of parallel air-cooled battery thermal management system, Int. J. Heat Mass Transf. 111 (2017) 943–952. doi:10.1016/j.ijheatmasstransfer.2017.04.026.

[3] R. Zhao, S. Zhang, J. Liu, J. Gu, A review of thermal performance improving methods of lithium ion battery: Electrode modification and thermal management system, J. Power Sources. 299 (2015) 557–577. doi:10.1016/j.jpowsour.2015.09.001.

[4] I. Dincer, H.S. Hamut, N. Javani, Thermal Management of Electric Vehicle Battery Systems, Wiley, 2017.

[5] L. Ungurean, G. Cârstoiu, M. V. Micea, V. Groza, Battery state of health estimation: a structured review of models, methods and commercial devices, Int. J. Energy Res. 41 (2017) 151–181. doi:10.1002/er.3598.

[6] T.M. Bandhauer, S. Garimella, T.F. Fuller, A Critical Review of Thermal Issues in Lithium-Ion Batteries, J. Electrochem. Soc. 158 (2011) R1–R25. doi:10.1149/1.3515880.

[7] T. Waldmann, M. Wilka, M. Kasper, M. Fleischhammer, M. Wohlfahrt-Mehrens, Temperature dependent ageing mechanisms in Lithium-ion batteries - A Post-Mortem study, J. Power Sources. 262 (2014) 129–135. doi:10.1016/j.jpowsour.2014.03.112.

[8] M.M. Kabir, D.E. Demirocak, Degradation mechanisms in Li-ion batteries: a state-of-the-art review, Int. J. Energy Res. 41 (2017) 1963–1986. doi:10.1002/er.3762.

[9] Z. Qian, Y. Li, Z. Rao, Thermal performance of lithium-ion battery thermal management system by using mini-channel cooling, Energy Convers. Manag. 126 (2016) 622–631. doi:10.1016/j.enconman.2016.08.063.

[10] L.H. Saw, Y. Ye, A.A.O. Tay, W.T. Chong, S.H. Kuan, M.C. Yew, Computational fluid dynamic and thermal analysis of Lithium-ion battery pack with air cooling, Appl. Energy. 177 (2016) 783–792. doi:10.1016/j.apenergy.2016.05.122.

[11] M. Al-Zareer, I. Dincer, M.A. Rosen, A novel phase change based cooling system for prismatic lithium ion batteries, Int. J. Refrig. 86 (2018) 203–217. doi:10.1016/j.ijrefrig.2017.12.005.

[12] I Dincer, M.A. Rosen, Energy Storage Systems, Therm. Energy Storage. (2010). doi:10.1002/9780470970751.ch2.

[13] N. Javani, I. Dincer, G.F. Naterer, B.S. Yilbas, Heat transfer and thermal management with PCMs in a Li-ion battery cell for electric vehicles, Int. J. Heat Mass Transf. 72 (2014) 690–703. doi:10.1016/j.ijheatmasstransfer.2013.12.076.

[14] P. Ramadass, B. Haran, R. White, B.N. Popov, Capacity fade of Sony 18650 cells cycled at elevated temperatures Part II. Capacity fade analysis, J. Power Sources. 112 (2002) 614–620.

[15] Model S | Tesla Canada. https://www.tesla.com/en_CA/models (accessed July 22, 2017).

[16] G. Berdichevsky, K. Kelty, J. Straubel, E. Toomre, The Tesla Roadster Battery System Tesla Motors, (2007).

[17] Y. Ji, Y. Zhang, C.-Y. Wang, Li-Ion Cell Operation at Low Temperatures, J. Electrochem. Soc. 160 (2013) A636–A649. doi:10.1149/2.047304jes.
[18] M. Mahmoud, R. Garnett, M. Ferguson, P. Kanaroglou, Electric buses: A review of alternative powertrains, Renew. Sustain. Energy Rev. 62 (2016) 673–684. doi:10.1016/J.RSER.2016.05.019.
[19] N.E.V.R. Dheeraj Varma, R. Vaishnava, A. Mittal, A review of energy sources and power converters for electrified vehicles, Int. J. Renew. Energy Environ. Eng. ISSN. 03 (2015) 2348–157.
[20] L. Lu, X. Han, J. Li, J. Hua, M. Ouyang, A review on the key issues for lithium-ion battery management in electric vehicles, J. Power Sources. 226 (2013) 272–288. doi:10.1016/j.jpowsour.2012.10.060.
[21] D.B. Richardson, Electric vehicles and the electric grid: A review of modeling approaches, Impacts, and renewable energy integration, Renew. Sustain. Energy Rev. 19 (2013) 247–254. doi:10.1016/J.RSER.2012.11.042.
[22] J.Y. Yong, V.K. Ramachandaramurthy, K.M. Tan, N. Mithulananthan, A review on the state-of-the-art technologies of electric vehicle, its impacts and prospects, Renew. Sustain. Energy Rev. 49 (2015) 365–385. doi:10.1016/j.rser.2015.04.130.
[23] R. von Helmolt, U. Eberle, Fuel Cell Vehicles: Fundamentals, System Efficiencies, Technology Development, and Demonstration Projects, in: Hydrog. Technol., Springer Berlin Heidelberg, Berlin, Heidelberg, 2008: pp. 273–290. doi:10.1007/978-3-540-69925-5.
[24] A. Tourani, P. White, P. Ivey, Analysis of electric and thermal behaviour of lithium-ion cells in realistic driving cycles, J. Power Sources. 268 (2014) 301–314. doi:10.1016/j.jpowsour.2014.06.010.
[25] S. Panchal, Experimental Investigation and Modeling of Lithium-ion Battery Cells and Packs for Electric Vehicles, PhD dissertation, Automotive, mechanical and manufacturing engineering department Univerisity of Ontario Institute of Technology, 2016.
[26] I. Dincer, M.A. Rosen, I. Dinçer, M.A. Rosen, Exergy: Energy, Environment and Sustainable Development, Elsevier Science, 2012. 2nd edition.
[27] Ferrari LaFerrari: First Hybrid with 963 CV - Ferrari.com. http://auto.ferrari.com/en_EN/sports-cars-models/car-range/laferrari/ (accessed July 22, 2017).
[28] D. Doughty, E.P. Roth, A General Discussion of Li Ion Battery Safety, Electrochem. Soc. (2012) 44.
[29] J.R. Selman, S. Al Hallaj, I. Uchida, Y. Hirano, Cooperative research on safety fundamentals of lithium batteries, J. Power Sources. 97–98 (2001) 726–732. doi:10.1016/S0378-7753(01)00732-7.
[30] S.A. Khateeb, M.M. Farid, J.R.R. Selman, S. Al-Hallaj, Design and simulation of a lithium-ion battery with a phase change material thermal management system for an electric scooter, J. Power Sources. 128 (2004) 292–307. doi:10.1016/j.jpowsour.2003.09.070.
[31] I. Uchida, H. Ishikawa, M. Mohamedi, M. Umeda, AC-impedance measurements during thermal runaway process in several lithium/polymer batteries, J. Power Sources. 119–121 (2003) 821–825. doi:10.1016/S0378-7753(03)00248-9.
[32] A. Jossen, V. Spath, H. Doring, J. Garch, Reliable battery operation — a challenge

for the battery management system, J. Power Sources. 84 (1999) 283–286.
[33] B.L. McKinney, G.L. Wierschem, E.N. Mrotek, Thermal Management of Lead-Acid Batteries for Electric Vehicles, in: Proc. Batter. Electr. Veh. Dev. Test. Conf., 1983. doi:10.4271/830229.
[34] Q. Lin, T. Yixiong, Q. Ruizhen, Z. Zuomin, D. Youliang, W. Jigiang, General safety considerations for high power Li/SOC1_2 batteries, Elsevier J. Power Sources. 54 (1995) 12–133.
[35] K.T. Chau, Y.S. Wong, C.C. Chan, Overview of energy sources for electric vehicles, Energy Convers. Manag. 40 (1999) 1021–1039. doi:10.1016/S0196-8904(99)00021-7.
[36] U. Köhler, J. Kümpers, M. Ullrich, High performance nickel-metal hydride and lithium-ion batteries, J. Power Sources. 105 (2002) 139–144. doi:10.1016/S0378-7753(01)00932-6.
[37] T. Horiba, K. Hironaka, T. Matsumura, T. Kai, M. Koseki, Y. Muranaka, Manganese type lithium ion battery for pure and hybrid electric vehicles, J. Power Sources. 97–98 (2001) 719–721. doi:10.1016/S0378-7753(01)00599-7.
[38] M. Majima, S. Ujiie, E. Yagasaki, K. Koyama, S. Inazawa, Development of long life lithium ion battery for power storage, J. Power Sources. 101 (2001) 53–59. doi:10.1016/S0378-7753(01)00554-7.
[39] N. Terada, T. Yanagi, S. Arai, M. Yoshikawa, K. Ohta, N. Nakajima, A. Yanai, N. Arai, Development of lithium batteries for energy storage and EV applications, J. Power Sources. 100 (2001) 80–92. doi:10.1016/S0378-7753(01)00885-0.
[40] E. Baker, H. Chon, J. Keisler, Battery technology for electric and hybrid vehicles: Expert views about prospects for advancement, Technol. Forecast. Soc. Change. 77 (2010) 1139–1146. doi:10.1016/j.techfore.2010.02.005.
[41] P.T. Moseley, Characteristics of a high-performance lead/acid battery for electric vehicles -an ALABC view, EISEVIER J. Power Sources. 67 (1997) 115–19.
[42] B. Dong, Y. Li, K. Ahmed, C.S. Ozkan, M. Ozkan, Adoption of thermal behavior as an indicator for enhancement of the EIS analysis for NCR 18650B Commercial Lithium-ion batteries system, MRS Adv. 3 (2018) 3155–3162. doi:10.1557/adv.2018.499.
[43] H. Fathabadi, A novel design including cooling media for Lithium-ion batteries pack used in hybrid and electric vehicles, J. Power Sources. 245 (2014) 495–500. doi:10.1016/j.jpowsour.2013.06.160.
[44] H. Park, A design of air flow configuration for cooling lithium ion battery in hybrid electric vehicles, J. Power Sources. 239 (2013) 30–36. doi:10.1016/j.jpowsour.2013.03.102.
[45] L. Fan, J.M. Khodadadi, A.A. Pesaran, A parametric study on thermal management of an air-cooled lithium-ion battery module for plug-in hybrid electric vehicles, J. Power Sources. 238 (2013) 301–312. doi:10.1016/j.jpowsour.2013.03.050.
[46] Y.S. Choi, D.M. Kang, Prediction of thermal behaviors of an air-cooled lithium-ion battery system for hybrid electric vehicles, J. Power Sources. 270 (2014) 273–280. doi:10.1016/j.jpowsour.2014.07.120.
[47] J. Choi, M. Jeong, J. Yoo, M. Seo, A new CPU cooler design based on an active cooling heatsink combined with heat pipes, Appl. Therm. Eng. 44 (2012) 50–56.

doi:10.1016/j.applthermaleng.2012.03.027.
[48] L.H. Saw, Y. Ye, A.A.O. Tay, Electrochemical-thermal analysis of 18650 Lithium Iron Phosphate cell, Energy Convers. Manag. 75 (2013) 162–174. doi:10.1016/j.enconman.2013.05.040.
[49] S.C. Chen, C.C. Wan, Y.Y. Wang, Thermal analysis of lithium-ion batteries, J. Power Sources. 140 (2005) 111–124. doi:10.1016/j.jpowsour.2004.05.064.
[50] R. Mahamud, C. Park, Reciprocating air flow for Li-ion battery thermal management to improve temperature uniformity, J. Power Sources. 196 (2011) 5685–5696. doi:10.1016/j.jpowsour.2011.02.076.
[51] V. Srinivasan, C.Y. Wang, Analysis of Electrochemical and Thermal Behavior of Li-Ion Cells, J. Electrochem. Soc. 150 (2003) A98–A106. doi:10.1149/1.1526512.
[52] R. Sabbah, R. Kizilel, J.R. Selman, S. Al-Hallaj, Active (air-cooled) vs. passive (phase change material) thermal management of high power lithium-ion packs: Limitation of temperature rise and uniformity of temperature distribution, J. Power Sources. 182 (2008) 630–638. doi:10.1016/j.jpowsour.2008.03.082.
[53] T. Wang, K.J. Tseng, J. Zhao, Z. Wei, Thermal investigation of lithium-ion battery module with different cell arrangement structures and forced air-cooling strategies, Appl. Energy. 134 (2014) 229–238. doi:10.1016/j.apenergy.2014.08.013.
[54] G. Karimi, X. Li, Thermal management of lithium-ion batteries for electric vehicles, Int. J. Energy Res. 37 (2013) 13–24. doi:10.1002/er.1956.
[55] Y. Inui, Y. Kobayashi, Y. Watanabe, Y. Watase, Y. Kitamura, Simulation of temperature distribution in cylindrical and prismatic lithium ion secondary batteries, Energy Convers. Manag. 48 (2007) 2103–2109. doi:10.1016/j.enconman.2006.12.012.
[56] J. Xun, R. Liu, K. Jiao, Numerical and analytical modeling of lithium ion battery thermal behaviors with different cooling designs, J. Power Sources. 233 (2013) 47–61. doi:10.1016/j.jpowsour.2013.01.095.
[57] J. Reyes-Marambio, F. Moser, F. Gana, B. Severino, W.R. Calderón-Muñoz, R. Palma-Behnke, P.A. Estevez, M. Orchard, M. Cortés, A fractal time thermal model for predicting the surface temperature of air-cooled cylindrical Li-ion cells based on experimental measurements, J. Power Sources. 306 (2016) 636–645. doi:10.1016/j.jpowsour.2015.12.037.
[58] N.S. Spinner, K.M. Hinnant, R. Mazurick, A. Brandon, S.L. Rose-Pehrsson, S.G. Tuttle, Novel 18650 lithium-ion battery surrogate cell design with anisotropic thermophysical properties for studying failure events, J. Power Sources. 312 (2016) 1–11. doi:10.1016/j.jpowsour.2016.01.107.
[59] T. Yang, N. Yang, X. Zhang, G. Li, Investigation of the thermal performance of axial-flow air cooling for the lithium-ion battery pack, Int. J. Therm. Sci. 108 (2016) 132–144. doi:10.1016/j.ijthermalsci.2016.05.009.
[60] S. Hong, X. Zhang, K. Chen, S. Wang, Design of flow configuration for parallel air-cooled battery thermal management system with secondary vent, Int. J. Heat Mass Transf. 116 (2018) 1204–1212. doi:10.1016/j.ijheatmasstransfer.2017.09.092.
[61] Green Car Congress: BMW Group presents prototype of i8 plug-in hybrid; first use of new 3-cylinder engine http://www.greencarcongress.com/2013/08/i8-20130807.html (accessed January 3, 2018).

[62] The Chevrolet Volt Cooling/Heating Systems Explained - GM-VOLT : Chevy Volt Electric Car Site GM-VOLT : Chevy Volt Electric Car Site, http://gm-volt.com/2010/12/09/the-chevrolet-volt-coolingheating-systems-explained/ (accessed January 3, 2018).
[63] Concept_One | Rimac Automobili, http://www.rimac-automobili.com/en/supercars/concept_one/ (accessed January 3, 2018).
[64] Z. Rao, Z. Qian, Y. Kuang, Y. Li, Thermal performance of liquid cooling based thermal management system for cylindrical lithium-ion battery module with variable contact surface, Appl. Therm. Eng. 123 (2017) 1514–1522. doi:10.1016/j.applthermaleng.2017.06.059.
[65] S. Panchal, R. Khasow, I. Dincer, M. Agelin-Chaab, R. Fraser, M. Fowler, Thermal design and simulation of mini-channel cold plate for water cooled large sized prismatic lithium-ion battery, Appl. Therm. Eng. 122 (2017) 80–90. doi:10.1016/j.applthermaleng.2017.05.010.
[66] W.B. Gu, C.Y. Wang, Thermal-Electrochemical Modeling of Battery Systems, J. Electrochem. Soc. 147 (2000). doi:10.1149/1.1393625.
[67] T.F. Fuller, M. Doyle, J. Newman, Simulation and Optimization of the Dual Lithium Ion Insertion Cell, J. Electrochem. Soc. 141 (1994) 1–9. doi:10.1149/1.2054684.
[68] M. Doyle, T.F. Fuller, J. Newman, Modeling of Galvanostatic Charge and Discharge of the Lithium/Polymer/Insertion Cell, J. Electrochem. Soc. 140 (1993) 1526. doi:10.1149/1.2221597.
[69] S. Basu, K.S. Hariharan, S.M. Kolake, T. Song, D.K. Sohn, T. Yeo, Coupled electrochemical thermal modelling of a novel Li-ion battery pack thermal management system, Appl. Energy. 181 (2016) 1–13. doi:10.1016/j.apenergy.2016.08.049.
[70] T. Li, Y.G. Lv, J. Liu, Y.X. Zhou, A powerful way of cooling computer chip using liquid metal with low melting point as the cooling fluid, Forsch. Im Ingenieurwesen/Engineering Res. 70 (2006) 243–251. doi:10.1007/s10010-006-0037-1.
[71] K. Ma, J. Liu, Liquid metal cooling in thermal management of computer chips, Front. Energy Power Eng. China. 1 (2007) 384–402. doi:10.1007/s11708-007-0057-3.
[72] K.Q. Ma, J. Liu, Heat-driven liquid metal cooling device for the thermal management of a computer chip, J. Phys. D. Appl. Phys. 40 (2007) 4722–4729. doi:10.1088/0022-3727/40/15/055.
[73] X.-H. Yang, S.-C. Tan, J. Liu, Thermal management of Li-ion battery with liquid metal, Energy Convers. Manag. 117 (2016) 577–585. doi:10.1016/j.enconman.2016.03.054.
[74] C. Wang, G. Zhang, L. Meng, X. Li, W. Situ, Y. Lv, M. Rao, Liquid cooling based on thermal silica plate for battery thermal management system, Int. J. Energy Res. 41 (2017) 2468–2479. doi:10.1002/er.3801.
[75] S. Panchal, I. Dincer, M. Agelin-Chaab, R. Fraser, M. Fowler, Experimental and theoretical investigations of heat generation rates for a water cooled LiFePO4 battery, Int. J. Heat Mass Transf. 101 (2016) 1093–1102. doi:10.1016/j.ijheatmasstransfer.2016.05.126.

[76] S. Panchal, R. Khasow, I. Dincer, M. Agelin-Chaab, R. Fraser, M. Fowler, Numerical modeling and experimental investigation of a prismatic battery subjected to water cooling, Numer. Heat Transf. Part A Appl. 71 (2017) 626–637. doi:10.1080/10407782.2016.1277938.
[77] D. Lisbona, T. Snee, A review of hazards associated with primary lithium and lithium-ion batteries, Process Saf. Environ. Prot. 89 (2011) 434–442. doi:10.1016/J.PSEP.2011.06.022.
[78] Q. Wang, P. Ping, X. Zhao, G. Chu, J. Sun, C. Chen, Thermal runaway caused fire and explosion of lithium ion battery, J. Power Sources. 208 (2012) 210–224. doi:10.1016/J.JPOWSOUR.2012.02.038.
[79] J. Xu, C. Lan, Y. Qiao, Y. Ma, Prevent thermal runaway of lithium-ion batteries with minichannel cooling, Appl. Therm. Eng. 110 (2017) 883–890. doi:10.1016/j.applthermaleng.2016.08.151.
[80] M.R. Giuliano, A.K. Prasad, S.G. Advani, Experimental study of an air-cooled thermal management system for high capacity lithium–titanate batteries, J. Power Sources. 216 (2012) 345–352. doi:10.1016/J.JPOWSOUR.2012.05.074.
[81] M.Y. Ramandi, I. Dincer, G.F. Naterer, Heat transfer and thermal management of electric vehicle batteries with phase change materials, Heat Mass Transf. 47 (2011) 777–788. doi:10.1007/s00231-011-0766-z.
[82] W.Q.Q. Li, Z.G.G. Qu, Y.L.L. He, Y.B.B. Tao, Experimental study of a passive thermal management system for high-powered lithium ion batteries using porous metal foam saturated with phase change materials, J. Power Sources. 255 (2014) 9–15. doi:10.1016/j.jpowsour.2014.01.006.
[83] J. Yan, K. Li, H. Chen, Q. Wang, J. Sun, Experimental study on the application of phase change material in the dynamic cycling of battery pack system, Energy Convers. Manag. 128 (2016) 12–19. doi:10.1016/j.enconman.2016.09.058.
[84] Z. Zhang, J. Cheng, X. He, Numerical simulation of flow and heat transfer in composite PCM on the basis of two different models of open-cell metal foam skeletons, Int. J. Heat Mass Transf. 112 (2017) 959–971. doi:10.1016/j.ijheatmasstransfer.2017.05.012.
[85] S.A. Khateeb, S. Amiruddin, M. Farid, J.R. Selman, S. Al-Hallaj, Thermal management of Li-ion battery with phase change material for electric scooters: Experimental validation, J. Power Sources. 142 (2005) 345–353. doi:10.1016/j.jpowsour.2004.09.033.
[86] C. Guo, W. Zhang, Numerical simulation and parametric study on new type of high temperature latent heat thermal energy storage system, Energy Convers. Manag. 49 (2008) 919–927. doi:10.1016/J.enconman.2007.10.025.
[87] Z. Rao, S. Wang, G. Zhang, Simulation and experiment of thermal energy management with phase change material for ageing $LiFePO_4$ power battery, Energy Convers. Manag. 52 (2011) 3408–3414. doi:10.1016/j.enconman.2011.07.009.
[88] C.Y. Zhao, W. Lu, Y. Tian, Heat transfer enhancement for thermal energy storage using metal foams embedded within phase change materials (PCMs), Sol. Energy. 84 (2010) 1402–1412. doi:10.1016/J.solener.2010.04.022.
[89] F. Samimi, A. Babapoor, M. Azizi, G. Karimi, Thermal management analysis of a Li-ion battery cell using phase change material loaded with carbon fibers, Energy.

96 (2016) 355–371. doi:10.1016/j.energy.2015.12.064.
[90] A.H.N. Shirazi, F. Mohebbi, M.R. Azadi Kakavand, B. He, T. Rabczuk, Paraffin Nanocomposites for Heat Management of Lithium-Ion Batteries: A Computational Investigation, J. Nanomater. 2016 (2016) 1–10. doi:10.1155/2016/2131946.
[91] P. Goli, S. Legedza, A. Dhar, R. Salgado, J. Renteria, A.A. Balandin, Graphene-enhanced hybrid phase change materials for thermal management of Li-ion batteries, J. Power Sources. 248 (2014) 37–43. doi:10.1016/j.jpowsour.2013.08.135.
[92] M. Mehrali, S. Tahan Latibari, M.A. Rosen, A.R. Akhiani, M.S. Naghavi, E. Sadeghinezhad, H.S.C. Metselaar, M. Mohammadi Nejad, M. Mehrali, From rice husk to high performance shape stabilized phase change materials for thermal energy storage, RSC Adv. 6 (2016) 45595–45604. doi:10.1039/C6RA03721F.
[93] C. Huang, Q. Wang, Z. Rao, Thermal conductivity prediction of copper hollow nanowire, Int. J. Therm. Sci. 94 (2015) 90–95. doi:10.1016/J.ijthermalSCI.2015.02.017.
[94] M. Malik, I. Dincer, M.A. Rosen, Review on use of phase change materials in battery thermal management for electric and hybrid electric vehicles, Int. J. Energy Res. 40 (2016) 1011–1031. doi:10.1002/er.3496.
[95] W. Wu, X. Yang, G. Zhang, K. Chen, S. Wang, Experimental investigation on the thermal performance of heat pipe-assisted phase change material based battery thermal management system, Energy Convers. Manag. 138 (2017) 486–492. doi:10.1016/j.enconman.2017.02.022.
[96] A. Alrashdan, A.T. Mayyas, S. Al-Hallaj, Thermo-mechanical behaviors of the expanded graphite-phase change material matrix used for thermal management of Li-ion battery packs, J. Mater. Process. Technol. 210 (2010) 174–179. doi:10.1016/J.jmatprotec.2009.07.011.
[97] T. Wang, S. Wang, L. Geng, Y. Fang, Enhancement on thermal properties of paraffin/calcium carbonate phase change microcapsules with carbon network, Appl. Energy. 179 (2016) 601–608. doi:10.1016/J.apenergy.2016.07.026.
[98] Q. Wang, Z. Rao, Y. Huo, S. Wang, Thermal performance of phase change material/oscillating heat pipe-based battery thermal management system, Int. J. Therm. Sci. 102 (2016) 9–16. doi:10.1016/j.ijthermalsci.2015.11.005.
[99] R. Zhao, J. Gu, J. Liu, An experimental study of heat pipe thermal management system with wet cooling method for lithium ion batteries, J. Power Sources. 273 (2015) 1089–1097. doi:10.1016/j.jpowsour.2014.10.007.
[100] A. Greco, D. Cao, X. Jiang, H. Yang, A theoretical and computational study of lithium-ion battery thermal management for electric vehicles using heat pipes, J. Power Sources. 257 (2014) 344–355. doi:10.1016/j.jpowsour.2014.02.004.
[101] F. Bai, M. Chen, W. Song, Z. Feng, Y. Li, Y. Ding, Thermal management performances of PCM/water cooling-plate using for lithium-ion battery module based on non-uniform internal heat source, Appl. Therm. Eng. 126 (2017) 17–27. doi:10.1016/j.applthermaleng.2017.07.141.
[102] J. Zhao, P. Lv, Z. Rao, Experimental study on the thermal management performance of phase change material coupled with heat pipe for cylindrical power battery pack, Exp. Therm. Fluid Sci. 82 (2017) 182–188. doi:10.1016/j.expthermflusci.2016.11.017.

[103] M. Chen, F. Bai, W. Song, J. Lv, S. Lin, Z. Feng, Y. Li, Y. Ding, A multilayer electro-thermal model of pouch battery during normal discharge and internal short circuit process, Appl. Therm. Eng. 120 (2017) 506–516. doi:10.1016/j.applthermaleng.2017.03.135.
[104] D. Bernardi, E. Pawlikowski, J. Newman, A General Energy Balance for Battery Systems, J. Electrochem. Soc. . 132 (1985) 5–12. doi:10.1149/1.2113792.
[105] G. Jiang, J. Huang, M. Liu, M. Cao, Experiment and simulation of thermal management for a tube-shell Li-ion battery pack with composite phase change material, Appl. Therm. Eng. 120 (2017) 1–9. doi:10.1016/j.applthermaleng.2017.03.107.
[106] S. Shi, Y. Xie, M. Li, Y. Yuan, J. Yu, H. Wu, B. Liu, N. Liu, Non-steady experimental investigation on an integrated thermal management system for power battery with phase change materials, Energy Convers. Manag. 138 (2017) 84–96. doi:10.1016/j.enconman.2017.01.069.
[107] M. Al-Zareer, I. Dincer, M.A. Rosen, A Review of Novel Thermal Management Systems for Batteries, Int. J. Energy Res. (2018) 1–24. doi:10.1002/er.4095.
[108] R. Kandasamy, X.-Q. Wang, A.S. Mujumdar, Application of phase change materials in thermal management of electronics, Appl. Therm. Eng. 27 (2007) 2822–2832. doi:10.1016/j.applthermaleng.2006.12.013.
[109] M. Lachheb, M. Karkri, F. Albouchi, F. Mzali, S. Ben Nasrallah, Thermophysical properties estimation of paraffin/graphite composite phase change material using an inverse method, ENERGY Convers. Manag. 82 (2014) 229–237. doi:10.1016/j.enconman.2014.03.021.
[110] Z. Xiangfa, X. Hanning, F. Jian, Z. Changrui, J. Yonggang, Preparation and thermal properties of paraffin/porous silica ceramic composite, Compos. Sci. Technol. 69 (2009) 1246–1249. doi:10.1016/j.compscitech.2009.02.030.
[111] P. Zhang, Y. Hu, L. Song, J. Ni, W. Xing, J. Wang, Effect of expanded graphite on properties of high-density polyethylene/ paraffin composite with intumescent flame retardant as a shape-stabilized phase change material, Sol. Energy Mater. Sol. Cells. 94 (2009) 360–365. doi:10.1016/j.solmat.2009.10.014.
[112] M. Al-Zareer, I. Dincer, M.A. Rosen, Heat and Mass Transfer Modeling and Assessment of a New Battery Cooling System, Int. J. Heat Mass Transf. 126 (2017) 765–778. doi:10.1016/j.ijheatmasstransfer.2018.04.157.
[113] M. Al-Zareer, I. Dincer, M.A.M.A. Rosen, Heat transfer modeling of a novel battery thermal management system, Numer. Heat Transf. Part A Appl. 73 (2018) 277–290. doi:10.1080/10407782.2018.1439237.
[114] M. Al-Zareer, I. Dincer, M.A. Rosen, Development and evaluation of a new ammonia boiling based battery thermal management system, Electrochim. Acta. 280 (2018) 340–352. doi:10.1016/j.electacta.2018.05.093.
[115] M. Al-Zareer, I. Dincer, M.A. Rosen, Electrochemical modeling and performance evaluation of a new ammonia-based battery thermal management system for electric and hybrid electric vehicles, Electrochim. Acta. 247 (2017) 171–182. doi:10.1016/j.electacta.2017.06.162.
[116] M. Al-Zareer, I. Dincer, M.A. Rosen, Novel thermal management system using boiling cooling for high-powered lithium-ion battery packs for hybrid electric vehicles, J. Power Sources. 363 (2017) 291–303.

doi:10.1016/j.jpowsour.2017.07.067.
[117] M.F. Ezzat, I. Dincer, Development, analysis and assessment of fuel cell and photovoltaic powered vehicles, Int. J. Hydrogen Energy. 43 (2018) 968–978. doi:10.1016/j.ijhydene.2017.05.065.
[118] B.K. Boggs, G.G. Botte, On-board hydrogen storage and production: An application of ammonia electrolysis, J. Power Sources. 192 (2009) 573–581. doi:10.1016/j.jpowsour.2009.03.018.
[119] Toyota Canada: Toyota to Increase "Mirai" Production, (2014). http://www.toyota.ca/toyota/en/company-info/news/post/toyota-to-increase-mirai-production (accessed September 13, 2016).
[120] Toyota, 2016 Mirai Product Information, 2016.
[121] M.F. Ezzat, I. Dincer, Development, analysis and assessment of a fuel cell and solar photovoltaic system powered vehicle, Energy Convers. Manag. 129 (2016) 284–292. doi:10.1016/j.enconman.2016.10.025.
[122] C. Zamfirescu, I. Dincer, Ammonia as a green fuel and hydrogen source for vehicular applications, Fuel Process. Technol. 90 (2009) 729–737. doi:10.1016/j.fuproc.2009.02.004.
[123] I. Dincer, C. Zamfirescu, Methods and apparatus for using ammonia as sustainable fuel, refrigerant and nox reduction agent, US8272353 B2, 2011. doi:CA2654823A1, CA2654823C, US20110011354.
[124] G.W. Rowley, Fuel vaporizer for fuel injected engines, (2010).
[125] M. Doyle, Comparison of Modeling Predictions with Experimental Data from Plastic Lithium Ion Cells, J. Electrochem. Soc. 143 (1996) 1890–1903. doi:10.1149/1.1836921.
[126] A. Bates, S. Mukherjee, N. Schuppert, B. Son, J.G. Kim, S. Park, Modeling and simulation of 2D lithium-ion solid state battery, Int. J. Energy Res. 39 (2015) 1505–1518. doi:10.1002/er.3344.
[127] A.A. Pesaran, Battery thermal models for hybrid vehicle simulations, J. Power Sources. 110 (2002) 377–382. doi:10.1016/S0378-7753(02)00200-8.
[128] A. Bolukbasi, D. Ciloglu, Pool boiling heat transfer characteristics of vertical cylinder quenched by SiO_2–water nanofluids, Int. J. Therm. Sci. 50 (2011) 1013–1021. doi:10.1016/j.ijthermalsci.2011.01.011.
[129] J. Murallidharan, G. Giustini, Y. Sato, B. Ničeno, V. Badalassi, S.P. Walker, Computational Fluid Dynamic Simulation of Single Bubble Growth under High-Pressure Pool Boiling Conditions, Nucl. Eng. Technol. 48 (2016) 859–869. doi:10.1016/J.NET.2016.06.004.
[130] Y. Sato, B. Niceno, Nucleate pool boiling simulations using the interface tracking method: Boiling regime from discrete bubble to vapor mushroom region, Int. J. Heat Mass Transf. 105 (2017) 505–524. doi:10.1016/j.ijheatmasstransfer.2016.10.018.
[131] S. Lal, Y. Sato, B. Niceno, Direct numerical simulation of bubble dynamics in subcooled and near-saturated convective nucleate boiling, Int. J. Heat Fluid Flow. 51 (2015) 16–28. doi:10.1016/J.ijheatfluidflow.2014.10.018.
[132] S. Mehendale, A new heat transfer coefficient correlation for pure refrigerants and near-azeotropic refrigerant mixtures flow boiling within horizontal microfin tubes, Int. J. Refrig. 86 (2017) 292–311. doi:10.1016/j.ijrefrig.2017.11.017.

[133] S. Ebrahim, F.-B. Cheung, A. Alshayji, Numerical Simulation of Pool Film Boiling Heat Transfer during Quenching of Heated Cylindrical Rods, Proceedings of the 2017 COMOSL conference in Boston.
[134] S. Panchal, I. Dincer, M. Agelin-Chaab, R. Fraser, M. Fowler, Transient electrochemical heat transfer modeling and experimental validation of a large sized $LiFePO_4$/graphite battery, Int. J. Heat Mass Transf. 109 (2017) 1239–1251. doi:10.1016/j.ijheatmasstransfer.2017.03.005.
[135] H. Lundgren, P. Svens, H. Ekström, C. Tengstedt, J. Lindström, M. Behm, G. Lindbergh, Thermal Management of Large-Format Prismatic Lithium-Ion Battery in PHEV Application, J. Electrochem. Soc. 163163 (2016) 309–317. doi:10.1149/2.09411602jes.
[136] G. Vertiz, M. Oyarbide, H. Macicior, O. Miguel, I. Cantero, P. Fernandez De Arroiabe, I. Ulacia, Thermal characterization of large size lithium-ion pouch cell based on 1d electro-thermal model, J. Power Sources. 272 (2014) 476–484. doi:10.1016/j.jpowsour.2014.08.092.
[137] L.W.W. Jin, P.S.S. Lee, X.X.X. Kong, Y. Fan, S.K.K. Chou, Ultra-thin minichannel LCP for EV battery thermal management, Appl. Energy. 113 (2014) 1786–1794. doi:10.1016/j.apenergy.2013.07.013.

Appendix

Copyright Permission

The high similarity of this thesis is exclusively due to the six published journal papers by the candidate, which are based on this thesis. As a result, some critical information, equations and illustrations which cannot be revised without losing the fundamental essence of the work were maintained. The similarity of the thesis and each of those papers is listed below. For this reason, permissions were duly obtained from the publishers to include this information in the thesis.

The following are the obtained permissions from the publishers for the reuse of the published work based on this PhD thesis.

1) **Wiley: (International Journal of Energy Research)**

Article C, in the Copyright transfer agreement:

"3. *Final Published Version. The Owner hereby licenses back to the Contributor the following rights with respect to the final published version of the Contribution (the "Final Published Version"):"*

> **"b.** *Re-use in other publications. The right to re-use the Final Published Version or parts thereof for any publication authored or edited by the Contributor (excluding journal articles) where such re-used material constitutes less than half of the total material in such publication. In such case, any modifications must be accurately noted.*"

2) **Elsevier:**

Article: Submission declaration and verification in the Guide for authors:

"*Submission of an article implies that the work described has not been published previously (except in the form of an abstract, a published lecture or academic thesis, see 'Multiple, redundant or concurrent publication' for more information), that it is not under consideration for publication elsewhere, that its publication is approved by all authors and tacitly or explicitly by the responsible authorities where the work was carried out, and that, if accepted, it will not be published elsewhere in the same form, in English or in any other language, including electronically without the written consent of the copyright-holder. To verify originality, your article may be checked by the originality detection service Crossref Similarity Check.*"

Similarity of the thesis with each of the published work that is based on the thesis

Paper 1: M. Al-Zareer, I. Dincer, M.A. Rosen, Performance assessment of a new hydrogen cooled prismatic battery pack arrangement for hydrogen hybrid electric vehicles, Energy Conversion and Management. 173 (2018) 303-319.

Similarity: 12%

Paper 2: M. Al-Zareer, I. Dincer, M.A. Rosen, Electrochemical modeling and performance evaluation of a new ammonia-based battery thermal management system for electric and hybrid electric vehicles, Electrochimica Acta. 247 (2017) 171–182.

Similarity: 7%

Paper 3: M. Al-Zareer, I. Dincer, M.A. Rosen, Novel thermal management system using boiling cooling for high-powered lithium-ion battery packs for hybrid electric vehicles, J. Power Sources. 363 (2017) 291–303

Similarity: 4%

Paper 4: M. Al-Zareer, I. Dincer, M.A. Rosen, A novel phase change based cooling system for prismatic lithium ion batteries, International Journal Refrigeration. 86 (2018) 203–217.

Similarity: 9%

Paper 5: M. Al-Zareer, I. Dincer, M.A. Rosen, Heat and mass transfer modeling and assessment of a new battery cooling system, International Journal of Heat and Mass Transfer. 126 (2018) 765–778.

Similarity: 6%

Paper 6: M. Al-Zareer, I. Dincer, M.A. Rosen, A review of novel thermal management systems for batteries, International Journal of Energy Research. 42 (2018) 3182–3205.

Similarity: 12%